



**UCGE Reports
Number 20246**

Department of Geomatics Engineering

**Intelligent MEMS INS/GPS Integration For Land
Vehicle Navigation**

(URL: <http://www.geomatics.ucalgary.ca/research/publications/GradTheses.html>)

by

Jau-Hsiung Wang

September 2006

SCHULICH
School of Engineering



UNIVERSITY OF CALGARY

Intelligent MEMS INS/GPS Integration For Land Vehicle Navigation

by

Jau-Hsiung Wang

A DISSERTATION

SUBMITTED TO THE FACULTY OF GRADUATE STUDIES
IN PARTIAL FULFILMENT OF THE REQUIREMENTS FOR THE
DEGREE OF DOCTOR OF PHILOSOPHY

DEPARTMENT OF GEOMATICS ENGINEERING

CALGARY, ALBERTA

SEPTEMBER 2006

© Jau-Hsiung Wang 2006

Abstract

Although Global Positioning System (GPS) has been widely used to land vehicle navigation systems, GPS is unable to provide continuous and reliable navigation solutions in the presence of signal fading and/or blockage such as in urban areas. With the advent of the Micro-Electro-Mechanical System (MEMS) Inertial Navigation System (INS), a low-cost MEMS INS/GPS integration system becomes available to provide improved navigation performance by integrating the long-term GPS accuracy with the short-term INS accuracy. The challenges to low-cost MEMS INS/GPS integration arise from dealing with the corrupted GPS data in signal-degraded environments, the large instrument errors experienced with low-grade MEMS sensors and the distorted magnetic measurements from an embedded electronic compass. This dissertation develops intelligent data fusion and processing techniques for such a low-cost integration system by incorporating the Artificial Intelligence (AI) with the Kalman filtering.

Two cascaded Kalman filters implemented upon a loosely coupled integration scheme are applied to perform data fusion in the velocity/attitude and position domain, respectively. Three AI-based methods are developed for GPS data assessment, INS error control and compass error modelling to enhance the Kalman-filter-based integration. Specifically, a fuzzy GPS data classification system is developed to optimize INS/GPS data fusion through adjusting the measurement covariances of the Kalman filters according to GPS signal degradation conditions. A dynamics knowledge aided inertial navigation algorithm along with a fuzzy expert vehicle dynamics identification system is created to reduce and control INS error drift through simplifying system models and extending measurement update schemes of the Kalman filters. A neural-networks-based compass calibration algorithm is developed to provide the correct compass heading updates to the Kalman filters in the presence of disturbance.

The developed algorithms have been tested and evaluated in various GPS conditions, which include open areas, complete GPS outages and urban areas, using a low-cost Xsens

MT9 MEMS IMU and SiRF Star II conventional/high sensitivity GPS receivers. The obtained results have confirmed the effectiveness of the AI-based methods and the significant performance improvement by the intelligent integration algorithm. For GPS outages around 3 minutes, the intelligent integration system is able to maintain satisfactory position accuracy with the maximum error less than 30 m. In the typical North American urban canyons, the intelligent integration system can provide continuous and reliable navigation solutions with the horizontal position accuracy of around 15 m. Overall results confirm the benefits and advantages of applying the developed AI methods to assist the low-cost MEMS INS/GPS integration for land vehicle navigation.

Acknowledgements

First of all, I would like to express my sincere gratitude to my supervisor, Dr. Yang Gao, for his constant encouragement and guidance in all the time of my studies at The University of Calgary. Without the supervision and the support from him, this study cannot be done.

I would like to thank some of my colleagues in the PMIS group, Dr. Yufeng Zhang and Dr. Kongzhe Chen, for providing the PPP/INS geo-referencing solution for the performance analysis of field tests. Dr. Yufeng Zhang is also thanked for the valuable discussion with the inertial navigation system and the Kalman filter design.

I also wish to acknowledge Dr. Naser El-Sheimy, Dr. Henry Leung, Dr. Abraham Fapojuwo and Dr. Christopher Jekeli for taking time to read my dissertation and giving valuable comments.

This research is partially supported by the Natural Sciences and Engineering Research Council of Canada (NSERC), the Geomatics for Informed Decisions (GEOIDE) and other scholarship sponsors including the Dean's Special Doctoral Scholarship, the University of Calgary Travel Grant, the Sangster Award, the Institute of Navigation Best Paper Award and Alberta Section Graduate Award, the International MultiConference of Engineers and Computer Scientists Best Student Paper Award and the Department of Geomatics Engineering Graduate Research Scholarship, Special Award and Travel Grant.

Special thanks go to my family, especially my wife Wen-Ya, for their patience and love that enabled me to complete this dissertation.

Dedication

To three most important females behind me:

my wife - Wen-Ya,

my daughter - Jocelyn,

and my mother - Li-Ching.

Table of Contents

Abstract	ii
Acknowledgements	iv
Dedication	v
Table of Contents	vi
List of Tables	xi
List of Figures	xiii
List of Symbols	xvii
List of Abbreviations	xxii
Chapter 1 Introduction	1
1.1 Background.....	1
1.2 Literature Review.....	4
1.2.1 Integration of MEMS INS with GPS Using Kalman Filter	4
1.2.2 Control of Stand-Alone INS Error Drift	5
1.2.3 Optimization of INS and GPS Data Fusion	7
1.3 Research Objectives and Contributions	7
1.4 Dissertation Outline	9
Chapter 2 Land Vehicle Navigation Sensor Overview	12
2.1 Overview of Global Positioning System.....	12
2.1.1 GPS Principles	13
2.1.2 GPS Errors	17
2.1.2.1 Satellite Orbit Errors	17
2.1.2.2 Satellite Clock Errors	17

2.1.2.3 Receiver Clock Errors.....	18
2.1.2.4 Ionospheric Errors.....	18
2.1.2.5 Tropospheric Errors	19
2.1.2.6 Multipath Errors.....	19
2.1.2.7 Receiver Noise.....	21
2.1.2.8 Error Budget.....	21
2.1.3 High Sensitivity GPS	22
2.2 Overview of Inertial Navigation System	24
2.2.1 INS Principles	24
2.2.1.1 Navigation Equations.....	25
2.2.1.2 Mechanization Equations.....	27
2.2.1.3 Initial Alignment.....	30
2.2.2 INS Errors	32
2.2.2.1 Initial Alignment Errors.....	32
2.2.2.2 Inertial Sensor Errors	32
2.2.2.3 Computational Errors.....	34
2.2.3 MEMS INS	34
2.3 Overview of Magnetic Compass.....	36
2.3.1 Compass Principles.....	36
2.3.2 Compass Errors.....	38
2.3.2.1 Transformation Errors.....	38
2.3.2.2 Magnetic Measurement Errors.....	39
2.3.2.3 Misalignment Errors	39
Chapter 3 Data Fusion and Processing Methodologies	41
3.1 Kalman Filter	41
3.1.1 Discrete Kalman Filter.....	42
3.1.2 Innovation-Based Adaptive Kalman Filter	46
3.1.3 INS/GPS Integration Using Kalman Filter	48
3.2 Fuzzy Logic	50
3.2.1 Fundamentals of Fuzzy Logic.....	51

3.2.1.1 Fuzzy Sets and Membership Functions	51
3.2.1.2 Logical Operations and If-Then Rules.....	52
3.2.1.3 Defuzzification.....	54
3.2.2 Fuzzy Inference System.....	55
3.3 Neural Networks	57
3.3.1 Fundamentals of Neural Networks	57
3.3.1.1 Models of A Neuron	57
3.3.1.2 Network Architecture.....	59
3.3.1.3 Learning Processes.....	61
3.3.1.4 Benefits of Neural Networks	62
3.3.2 Multilayer Feedforward Neural Networks.....	63
Chapter 4 Development of AI-Based Methods for Integration Enhancement	69
4.1 Limitation of MEMS INS/GPS Integration Using Kalman Filter	69
4.2 Fuzzy Logic Rule-Based GPS Data Classification.....	71
4.2.1 GPS Signal Quality Measures.....	73
4.2.2 Geo-Signal Degradation Measures	81
4.2.3 Design of Fuzzy Logic Rule-Based Data Classification System.....	85
4.3 Dynamics Knowledge Aided Inertial Navigation Algorithm	90
4.3.1 Land Vehicle Motion Model.....	91
4.3.2 Vehicle Dynamics-Derived Observations.....	95
4.3.2.1 Stationary Mode.....	96
4.3.2.2 Straight-Line Motion Mode	97
4.3.2.3 Cornering Motion Mode	98
4.3.2.4 Summary	100
4.3.3 Design of Fuzzy Expert Vehicle Dynamics Identification System	100
4.4 Neural Networks Compass Calibration	106
4.4.1 Magnetic Compass Error Model.....	107
4.4.2 Design of Neural Networks Compass Calibration System	109
4.4.3 Simulation Verification.....	111
Chapter 5 Development of An Intelligent Integration Algorithm	115

5.1 Cascaded Integration Scheme	115
5.2 Design of AI-Enhanced Velocity/Attitude and Position Filters	116
5.2.1 Velocity and Attitude Filter	117
5.2.1.1 Dynamics Model	117
5.2.1.2 Measurement Model	120
5.2.1.2.1 GPS Observations	120
5.2.1.2.2 Dynamics-Derived Observations	122
5.2.1.2.3 Compass Observation	127
5.2.2 Position Filter	129
5.2.2.1 Dynamics Model	129
5.2.2.2 Measurement Model	130
5.2.2.2.1 Model with GPS	130
5.2.2.2.2 Model without GPS	133
5.3 Construction of An Intelligent Integration Algorithm	134
Chapter 6 Test Results in Open Areas	138
6.1 Test Description	138
6.2 Results with GPS Updates	142
6.2.1 Performance Analysis of Integrated Navigation	143
6.2.1.1 Accelerometer Bias Estimation Accuracy	143
6.2.1.2 Attitude Accuracy	147
6.2.1.3 Velocity and Position Accuracy	149
6.2.2 Performance Analysis of Compass Heading Error Modelling	151
6.3 Results without GPS Updates	153
6.3.1 Performance Analysis of Dynamics-Derived Observations	153
6.3.2 Performance Analysis of Compass Heading Calibration	157
6.3.3 Performance Analysis of Stand-Alone Inertial Navigation	159
6.3.3.1 Aiding from Dynamics-Derived Observations Only	159
6.3.3.1.1 Attitude Accuracy	159
6.3.3.1.2 Velocity and Position Accuracy	162
6.3.3.2 Aiding from Dynamics-Derived and Calibrated Compass Observations	164

6.3.3.2.1 Attitude Accuracy	164
6.3.3.2.2 Velocity and Position Accuracy.....	166
6.4 Summary of Test Results.....	167
Chapter 7 Test Results in Urban Areas	169
7.1 Test Description.....	169
7.2 GPS Data Classification Performance	172
7.2.1 Results of HSGPS	172
7.2.2 Results of GPS.....	178
7.3 Integration System Performance.....	184
7.3.1 Results of MT9/HSGPS.....	184
7.3.2 Results of MT9/GPS	189
7.4 Summary of Test Results.....	194
Chapter 8 Conclusions and Recommendations	196
8.1 Conclusions.....	197
8.2 Recommendations.....	201
References	204

List of Tables

Table 1.1: Required Navigation Performance (RNP) parameters	3
Table 2.1: Typical pseudorange measurement errors for single-frequency single point positioning.....	22
Table 2.2: Signal power budget	23
Table 3.1: Two if-then rules.....	57
Table 4.1: Parameters of reference functions of the expected C/N0 (SiRF Star II Xtrac HSGPS).....	81
Table 4.2: Parameters of reference functions of the expected C/N0 (SiRF Star II conventional GPS)	81
Table 4.3: If-then rules used in the fuzzy inference system for GPS/HSGPS data classification.....	89
Table 4.4: Vehicle dynamics aided observations.....	100
Table 4.5: If-then rules used in the fuzzy inference system for vehicle dynamics identification	102
Table 4.6: Expert rules for stationary/non-stationary identification.....	105
Table 4.7: Expert rules for straight-line/cornering motion identification.....	105
Table 4.8: Calibrated compass heading accuracy (12.5% data deteriorated by disturbances)	113
Table 4.9: Calibrated compass heading accuracy (6.25% data deteriorated by disturbances)	114
Table 4.10: Calibrated compass heading accuracy (25% data deteriorated by disturbances)	114
Table 5.1: Adaptive $\sigma_{\delta V_f^{GPS}}$ values under different signal degradation conditions	122
Table 5.2: Adaptive $\sigma_{\delta \psi^N}$ values under different dynamics	128
Table 5.3: AI-enhanced adaptive measurement noise covariance for GPS position	133
Table 6.1: SiRF HSGPS specifications.....	139
Table 6.2: MT9 specifications	140

Table 6.3: Accelerometer bias estimation accuracy	147
Table 6.4: Attitude estimation accuracy (INS/GPS integration)	149
Table 6.5: Velocity and position estimation accuracy (INS/GPS integration)	151
Table 6.6: Dynamics-derived observation accuracy	157
Table 6.7: Calibrated compass heading accuracy	158
Table 6.8: Attitude estimation accuracy (stand-alone INS with dynamics aid)	162
Table 6.9: Velocity and position estimation accuracy (stand-alone INS with dynamics aid)	164
Table 6.10: Attitude estimation accuracy (stand-alone INS with dynamics aid and compass aid).....	165
Table 6.11: Velocity and position estimation accuracy (stand-alone INS with dynamics aid and compass aid).....	167
Table 7.1: HSGPS position accuracy after data classification (route-A).....	177
Table 7.2: HSGPS position accuracy after data classification (route-B).....	178
Table 7.3: GPS position accuracy after data classification (route-A).....	183
Table 7.4: GPS position accuracy after data classification (route-B).....	183
Table 7.5: Integrated MT9/HSGPS vs. HSGPS position accuracy (route-A)	188
Table 7.6: Integrated MT9/HSGPS vs. HSGPS position accuracy (route-B).....	189
Table 7.7: Integrated MT9/GPS vs. GPS position accuracy (route-A).....	193
Table 7.8: Integrated MT9/GPS vs. GPS position accuracy (route-B).....	194

List of Figures

Figure 2.1: Heading determination using a triad of magnetometers.....	38
Figure 3.1: Discrete Kalman filter algorithm.....	45
Figure 3.2: Loosely coupled INS/GPS integration algorithm.....	48
Figure 3.3: Tightly coupled INS/GPS integration algorithm.....	49
Figure 3.4: Features of the membership function	52
Figure 3.5: Block diagram of the fuzzy inference system	55
Figure 3.6: Graphical Mamdani (max-min) inference method	56
Figure 3.7: Nonlinear model of a neuron.....	59
Figure 3.8: Single-layer feedforward networks	60
Figure 3.9: Multi-layer feedforward networks.....	60
Figure 3.10: Signal flow of the back-propagation learning applied to a multilayer feedforward neural network.....	68
Figure 4.1: Test set-up in a low signal-degraded environment.....	75
Figure 4.2: Test set-up in a medium signal-degraded environment.....	75
Figure 4.3: Test set-up in a high signal-degraded environment.....	76
Figure 4.4: C/N0 scatter diagram under open-sky and low signal-degraded environments (SiRF Star II Xtrac HSGPS)	76
Figure 4.5: C/N0 scatter diagram under open-sky and medium signal-degraded environments (SiRF Star II Xtrac HSGPS).....	77
Figure 4.6: C/N0 scatter diagram under open-sky and high signal-degraded environments (SiRF Star II Xtrac HSGPS)	77
Figure 4.7: C/N0 scatter diagram under open-sky and low signal-degraded environments (SiRF Star II conventional GPS).....	78
Figure 4.8: C/N0 scatter diagram under open-sky and medium signal-degraded environments (SiRF Star II conventional GPS).....	78
Figure 4.9: C/N0 scatter diagram under open-sky and high signal-degraded environments (SiRF Star II conventional GPS).....	79

Figure 4.10: Profile of reference functions of the expected C/N0 (SiRF Star II Xtrac HSGPS).....	80
Figure 4.11: Profile of reference functions of the expected C/N0 (SiRF Star II conventional GPS)	81
Figure 4.12: Distribution of the geo-signal degradation measures in various signal-degraded environments (SiRF Star II Xtrac HSGPS).....	84
Figure 4.13: Distribution of the geo-signal degradation measures in various signal-degraded environments (SiRF Star II conventional GPS)	84
Figure 4.14: Architecture of the fuzzy logic GPS data classification system.....	86
Figure 4.15: Membership functions used in the fuzzy inference system for HSGPS data classification.....	87
Figure 4.16: Membership functions used in the fuzzy inference system for GPS data classification.....	88
Figure 4.17: Membership functions used in the fuzzy inference system for vehicle dynamics identification	103
Figure 4.18: Decision flow of the vehicle dynamics identification system.....	105
Figure 4.19: Nonlinear relationship between compass headings and true headings.....	109
Figure 4.20: Architecture of the neural networks compass calibration system	110
Figure 4.21: Magnetic field measurement locus in 2-D	112
Figure 4.22: Performance of the neural networks nonlinear mapping.....	112
Figure 5.1: Cascaded INS/GPS integration scheme	116
Figure 5.2: Architecture of the intelligent integration algorithm.....	137
Figure 6.1: System set-up for open area tests	139
Figure 6.2: Equipment set-up on the test vehicle.....	141
Figure 6.3: Open area test trajectory.....	141
Figure 6.4: Estimation results of accelerometer bias (x-axis).....	143
Figure 6.5: Estimation results of accelerometer bias (y-axis).....	144
Figure 6.6: Estimation results of true accelerometer bias (x-axis)	145
Figure 6.7: Estimation results of true accelerometer bias (y-axis)	146
Figure 6.8: Estimation results of pitch (INS/GPS integration).....	148
Figure 6.9: Estimation results of roll (INS/GPS integration)	148

Figure 6.10: Estimation results of heading (INS/GPS integration)	149
Figure 6.11: Estimation results of velocity (INS/GPS integration)	150
Figure 6.12: Estimation results of position (INS/GPS integration)	150
Figure 6.13: Measured magnetic fields for neural networks training	152
Figure 6.14: Results of neural networks training	152
Figure 6.15: Results of vehicle dynamics identification	154
Figure 6.16: Dynamics-derived pitch observations	155
Figure 6.17: Dynamics-derived roll observations	155
Figure 6.18: Dynamics-derived velocity observations	156
Figure 6.19: Errors of dynamics-derived observations	156
Figure 6.20: Calibrated and un-calibrated compass headings	158
Figure 6.21: Estimation results of pitch (stand-alone INS with dynamics aid)	160
Figure 6.22: Estimation results of roll (stand-alone INS with dynamics aid)	160
Figure 6.23: Estimation results of heading (stand-alone INS with dynamics aid)	161
Figure 6.24: Estimation results of velocity (stand-alone INS with dynamics aid)	163
Figure 6.25: Estimation results of position (stand-alone INS with dynamics aid)	163
Figure 6.26: Comparison of heading estimation using different approaches (zoom-in)	166
Figure 7.1: Urban area test trajectory (route-A)	170
Figure 7.2: Urban area test trajectory (route-B)	171
Figure 7.3: Satellites tracked in a route-A test	171
Figure 7.4: Satellites tracked in a route-B test	172
Figure 7.5: HSGPS positions and classification results, route-A tests, April 23, 2005 ...	173
Figure 7.6: HSGPS positions and classification results, route-A tests, April 26, 2005 ...	174
Figure 7.7: HSGPS positions and classification results, route-B tests, April 23, 2005 ...	175
Figure 7.8: HSGPS positions and classification results, route-B tests, April 26, 2005 ...	176
Figure 7.9: GPS positions and classification results, route-A tests, April 23, 2005	179
Figure 7.10: GPS positions and classification results, route-A tests, April 26, 2005	180
Figure 7.11: GPS positions and classification results, route-B tests, April 23, 2005	181
Figure 7.12: GPS positions and classification results, route-B tests, April 26, 2005	182
Figure 7.13: MT9/HSGPS integrated positions, route-A tests, April 23, 2005	185
Figure 7.14: MT9/HSGPS integrated positions, route-A tests, April 26, 2005	186

Figure 7.15: MT9/HSGPS integrated positions, route-B tests, April 23, 2005	187
Figure 7.16: MT9/HSGPS integrated positions, route-B tests, April 26, 2005	188
Figure 7.17: MT9/GPS integrated positions, route-A tests, April 23, 2005	190
Figure 7.18: MT9/GPS integrated positions, route-A tests, April 26, 2005	191
Figure 7.19: MT9/GPS integrated positions, route-B tests, April 23, 2005	192
Figure 7.20: MT9/GPS integrated positions, route-B tests, April 26, 2005	193

List of Symbols

Symbol	Definition
$(\bullet)(t)$	Quantity \bullet as a function of time
$(\bullet)_k$	Quantity \bullet at the k^{th} epoch
$(\bullet)^-$	Quantity \bullet before a measurement update
$\hat{(\bullet)}$	Estimated quantity \bullet
$\bar{(\bullet)}$	Corrected quantity \bullet
$\tilde{(\bullet)}$	True quantity \bullet
$\dot{(\bullet)}$	Time derivative of \bullet
$\partial(\bullet)$	Partial derivative of \bullet
$\delta(\bullet)$	Perturbation from the nominal value of \bullet
$E[\bullet]$	Mathematical expectation of \bullet
A	Acceleration vector
A	Amplitude of the direct signal
A_{norm}	Norm of the three-axis accelerations
Az	Azimuth angles
C	Covariance matrix of the innovation sequence
C_B^N	Transformation matrix describing the relationship between Euler rates and gyro measurements
DA	Linear dynamics parameter
DI	Dynamics indicator
E	Satellite elevation
	Cost function
E_{av}	Average squared error energy
F	Dynamics matrix

\mathbf{F}_{ENU}	Average fading C/N0 vector on the local ENU coordinate frame
FR	Fading satellite ratio
\mathbf{G}	Gravity vector
	Shaping matrix
$\tilde{\mathbf{G}}$	Satellite geometry matrix
G_a	Antenna gain
\mathbf{H}	Design matrix
J	Linear jerk measure
\mathbf{K}	Kalman gain matrix
L	Latitude
M	Cross-coupling coefficients
	Magnetic field
$M\omega_z$	Cornering dynamics parameter
N_F	Number of fading satellites
N_U	Number of satellites used for navigation
NF	Receiver noise figure
\mathbf{P}	Position vector
	Error covariance matrix
P	Pseudorange measurement
\mathbf{Q}	Process noise matrix
$\mathbf{Q}(t)$	Spectral density matrix
\mathbf{R}	Measurement noise matrix
\mathbf{R}_b^a	Transformation matrix from frame b to a
$\mathbf{R}_a(b)$	Matrix of rotation through the angle b about the axis a
$(R_b^a)_{r,c}$	Element of the r^{th} row and the c^{th} column of the matrix \mathbf{R}_b^a
S	Scale factor

S_R	Received signal power
\mathbf{V}	Velocity vector
W	Pitching and rolling measure
b	Receiver clock bias Accelerometer bias Gyro bias Neuron bias
c	Speed of electromagnetic wave in vacuum
\mathbf{d}	Desired response vector of the neural networks
d_{ion}	Ionospheric delay
d_{trop}	Tropospheric delay
$d\rho$	Satellite orbital error
dt	Satellite clock error
dT	Receiver clock error
f	Fading C/N0
g	Gravitational constant
\mathbf{o}	Actual response vector of the neural networks
p	PRN sequence of the C/A code
q	Spectral density
s	Composite signal
\mathbf{u}	Forcing function vector
\mathbf{v}	Measurement noise vector
\mathbf{w}	Driven response vector
w	Random noise Synaptic weight
\mathbf{x}	State vector Input vector of the neural networks
x, y, z	Coordinates
y	Neuron output
y^*	Defuzzified scalar quantity

\mathbf{z}	Measurement vector
α	Momentum constant Angle between the forward axis of the vehicle and the magnetic North
α_m	Relative power of the multipath signal
δ	Local gradient Declination angle
δ_m	Delay of the multipath signal with respect to the direct signal
ε_p	Measurement noise and multipath residual
ϕ	Roll
γ	Normal gravity vector
η	Learning rate
φ	Activation function
μ	Membership function of a fuzzy set
μ_B^*	Aggregated output
\mathbf{v}	Innovation sequence
v	Local field
θ	Pitch
θ_m	Phase of the multipath signal relative to the direct signal
ρ	Geometric range
σ	Standard deviation
ω_0	Frequency of the direct signal
$\boldsymbol{\omega}_{bc}^a$	Vector of rotation rates of frame c , relative to frame b , expressed in frame a
ω_e	Earth's rate
ω_{norm}	Norm of the x-axis and y-axis angular velocities
ψ	Yaw (heading)
Δt	Time interval

Δw	Weight correction
\mathcal{L}^{-1}	Inverse Laplace transform
Ω_{bc}^a	Skew-symmetric form of vector ω_{bc}^a
Φ	Transition matrix
Λ	Attitude vector

List of Abbreviations

Abbreviation	Full term
AI	Artificial Intelligence
AKF	Adaptive Kalman Filter
C/A-code	Coarse/Acquisition code
C/N0	Carrier-to-Noise Density Ratio
DA	Data Acquisition
DGPS	Differential Global Positioning System
DoD	Department of Defense
DOP	Dilution Of Precision
DR	Dead-Reckoning
ENU	East-North-Up
FDE	Fault Detection and Exclusion
GDOP	Geometry Dilution Of Precision
GNSS	Global Navigation Satellite System
GPS	Global Positioning System
HSGPS	High Sensitivity Global Positioning System
IMUs	Inertial Measurement Units
INS	Inertial Navigation System
LBS	Location Based Service
MEMS	Micro-Electro-Mechanical System
MFNs	Multi-Layer Feedforward Networks
MFNN	Multilayer Feedforward Neural Network
MR	Magneto-Resistive
NED	North-East-Down
P-code	Precise code
PMIS	Positioning and Mobile Information System
PPM	Parts Per Million

PPP	Precise Point Positioning
PRN	Pseudo-Random Noise
PVT	Position, Velocity and Time
QR	Quality Rating
RAIM	Receiver Autonomous Integrity Monitoring
RF	Radio Frequency
RMS	Root-Mean-Square
RNs	Recurrent Networks
RNP	Required Navigation Performance
SFNs	Single-Layer Feedforward Networks
SPP	Single Point Positioning
TEC	Total Electron Content
TOA	Time-Of-Arrival
USERE	User Equivalent Range Error
ZUPT	Zero velocity UPdaTe

Chapter 1

Introduction

Land vehicle navigation is the fastest growing section of the in-vehicle electronics market. According to the CSM Worldwide, the global in-vehicle navigation systems market will grow to \$5.4 billion by 2010 which represents 66% growth over today's market, estimated at \$3.2 billion on May 20, 2005 (Telematics Update, 2005). Currently, overall navigation system installation in Japan is at about 16% of vehicle production while Europe and North America lag the Japanese market with overall installation rates of 8% and 3%, respectively (Telematics Update, 2005). As the price for navigation systems drops, navigation systems will go from optional luxury equipment to standard amenities on generic cars, which helps continue the growth of navigation systems in the global market. Towards this goal, however, an important issue is to maintain reasonable navigation performance along with the cost demand. This dissertation investigates a low-cost integrated approach to provide continuous and reliable land vehicle navigation in all operational environments.

1.1 Background

The most fundamental task of a vehicular navigation system is to continuously maintain accurate track of the vehicle's position (French, 1987). Basically, two types of navigation technologies, dead-reckoning (DR) and position fixing, are available for position determination. The principle of the dead-reckoning technology is to determine the current position of the vehicle based on the knowledge of the previous position and the measurement of the motion. The typical DR sensors used for land vehicle navigation are odometer, magnetic compass and Inertial Navigation System (INS). DR sensors are self-contained and autonomous navigators independent on operational environments but the sensor errors will lead to unbounded position error growing with time. In contrast,

position fixing technology which determines the vehicle position by measuring the distance between the vehicle and the reference points based on radio signals can provide absolute position and velocity information with bounded accuracy. The most commonly used position fixing technology is the Global Navigation Satellite System (GNSS) such as Global Positioning System (GPS). GPS has been adopted widely in vehicular navigation systems due to its cost-effect performance. However, the major drawback of GPS is that at least four satellites must be visible to the GPS receiver. In real operational environments such as urban canyons, GPS positioning accuracy and availability will degrade due to the poor satellite geometry, multipath and satellite signal outages.

There are four main parameters that can be used to measure the performance of a navigation system: accuracy, integrity, continuity and availability (Ashkenazi et al., 1995; Ochieng et al., 1999). These quantities are referred to as the Required Navigation Performance (RNP) parameters and their definition are given in Table 1.1. The RNP parameters are originally applied in aviation and have been extend to marine and land vehicle navigation. According to Hofmann-Wellenhof et al. (2003), autonomous navigation in urban areas requires continuous positioning information with accuracy of 2~5 metres (2D-95%). For location based service (LBS), the accuracy requirement varies with applications, e.g. positioning accuracy of 10~20 metres (2D-95%) is required for fleet management. Unfortunately, neither DR nor GPS can fulfill these requirements in stand-alone mode. Although DR sensors can provide continuous navigation solutions in all environments, they suffer from navigation error growth over time and eventually cannot sustain the accuracy requirement. In contrast, GPS is able to provide sufficiently accurate position solutions but it cannot fulfill the continuity and availability requirements in some land vehicle environments such as urban canyons. Although currently developed high sensitivity technologies have improved the GPS availability in signal-degraded environments, the position solutions provided by the high sensitivity GPS in such environments could be unreliable and suffer from the hundred-metre level error. Thus, to fulfill these requirements, integration of DR and GPS is required and has become a common approach worldwide for land vehicle navigation (French, 1995). INS/GPS integration is typically the most popular approach since it can provide three-

dimension attitude, velocity and position information and is also applicable to portable systems. Given complementary nature of INS and GPS, the integration system can provide superior system performance in terms of accuracy, integrity and availability than each system in stand-alone mode (Greenspan, 1996).

Table 1.1: Required Navigation Performance (RNP) parameters (after Ochieng et al., 1999)

Accuracy	defined as the degree of conformance of an estimated or measured position at a given time, to the truth.
Integrity	defined as the ability of the navigation system to provide timely warnings to users when the system must not be used for navigation.
Continuity	defined as the ability of the total system to perform its function without interruption during an intended period of operation.
Availability	defined as the percentage of time during which the service is available for use taking into account all the outages whatever their origins. The service is available if accuracy, integrity and continuity requirements are satisfied.

Advances in microelectronics, computer, and sensor technologies permit the development of commercial low-cost Inertial Measurement Units (IMUs) and GPS receivers for vehicular navigation markets. Recently, a single-frequency GPS chipset receiver with the cost of less than 200 USD is available in the markets. The continuous development of the Micro-Electro-Mechanical System (MEMS) technology has made low-cost inertial sensors available to land vehicle navigation. A single point positioning (SPP) GPS/MEMS INS integration system has become one of the most attractive low-cost solutions to land vehicle navigation. However, the challenges when working with MEMS INS/SPP GPS are to develop a robust integration algorithm that can deal with the large instrument errors experienced with low-grade MEMS INS and the corrupted GPS data in signal-degraded environments. This dissertation focuses on the development of a new integration algorithm that enables the low-cost MEMS INS/SPP GPS integration system to provide reliable and accurate navigation solutions for land vehicle applications.

1.2 Literature Review

For decades, integration of INS with GPS has been investigated in many literatures. The Kalman filtering methodology has been successfully applied for INS/GPS integration using either loosely or tightly coupled integration strategies (Wei and Schwarz, 1990; Cannon, 1991; Salychev, 1998; El-Sheimy and Schwarz, 1999; Jekeli, 2000; Scherzinger, 2000 and Petovello, 2003). The Kalman filter offers a powerful method for linear data fusion and estimation that are optimal in the statistical sense if the system and measurement models and their stochastic properties are known (Gelb, 1974). For low-cost MEMS INS/GPS integration, however, these requirements are difficult to meet due to the poor quality of the instrument measurements. The traditional integration algorithm finds new challenges dealing with rapid INS error drift during GPS outages and INS/GPS data fusion in GPS signal-degraded environments. In the following sections, we will first discuss the current research regarding MEMS INS/GPS integration using the Kalman filter. Then, the available methods to reduce INS error drift during GPS outages are reviewed, followed by the discussion of fusion optimization techniques for MEMS INS/GPS.

1.2.1 Integration of MEMS INS with GPS Using Kalman Filter

In the last few years, several researchers have investigated the MEMS INS/GPS integration using the Kalman filter. Salychev et al (2000) and Nayak (2000) applied a loosely coupled integration strategy to integrate the MotionPak™ MEMS IMU with pseudorange differential GPS (DGPS). Brown and Lu (2004) and Jaffe et al. (2004) developed Kalman filter-based MEMS INS/SPP GPS integrated navigation systems using tightly coupled integration strategy. Shin (2005) applied the unscented Kalman filter and extended Kalman filter for low-cost MEMS INS/DGPS integration. The above researches focused on evaluating the system performance under benign operational conditions such as open-sky environments and assessing the INS prediction accuracy during simulated GPS outages. The test results have demonstrated that the navigation performance degrades rapidly following loss of the GPS aiding data due to the large INS bias variation and noise.

Currently, Hide and Moore (2005) and Godha (2006) investigated the performance of the MEMS INS/DGPS integrated vehicular navigation systems in real life suburban/urban environments. Hide and Moore (2005) demonstrated that the horizontal position error within around 20 m using the tightly coupled integration of Crossbow AHRS400 MEMS IMU and DGPS is attainable when the system was tested in the city of Nottingham, UK where the surrounding buildings are generally only 3 to 4 stories tall. Godha (2006) demonstrated the similar performance obtained in downtown Calgary, Canada using the tightly coupled integration of Crista MEMS IMU and DGPS and 27-state INS filter with height and velocity constraints. However, the use of DGPS and tightly coupled integration scheme suggested by these two researches will increase the cost of system implementation and operation in real applications since it requires base stations, additional communication links and more powerful processors.

1.2.2 Control of Stand-Alone INS Error Drift

As stated previously, for a low-cost MEMS INS/GPS integration system, navigation performance degrades rapidly following loss of the GPS aiding data if prediction of navigation error only relies on the Kalman filter. A number of approaches have been proposed to reduce the stand-alone INS error drift and they are grouped into: special error prediction techniques, aiding from vehicle dynamics knowledge and the use of auxiliary sensors.

Neural networks, neuro-fuzzy models and fuzzy inference systems have been proposed to predict INS drift errors and have shown their effectiveness on navigation error reduction (Ibrahim et al., 2000; Chiang, 2004; El-Sheimy et al., 2004; Wang, 2004a). The basic idea behind the neuro-fuzzy modelling or fuzzy reasoning approaches is to predict navigation errors based on an input/output pattern memorized during a training or learning process. To maintain good performance of the neuro-fuzzy prediction, the training data should cover all the input and output data ranges and the neuro-fuzzy model should be retrained in real-time to deal with minor changes in the operating environmental conditions (Haykin, 1999). For a low-cost MEMS INS with a relatively

high instrument bias, noise and random error, sensor errors are highly sensitive to operational environments and the input/output patterns change dynamically. Thus, it is more difficult to accurately predict navigation errors using the neuro-fuzzy model or the fuzzy inference system when low-cost MEMS inertial sensors are used. For a MEMS INS/SPP GPS integration system, the stand-alone INS error after neural networks correction could reach the hundred-metre level during 30-second GPS outages (Chiang, 2004).

Another approach available in literatures to reduce INS error drift is based on the constraints of land vehicle motion. Zero velocity updates (ZUPTs) are the most commonly used techniques to provide effective INS error control when the stationary of a vehicle is available (Salychev, 1998; El-Sheimy, 2003). In addition, Brandt and Gardner (1998), Dissanayake et al. (2001) and Shin (2001) applied the nonholonomic constraints that govern the motion of a vehicle on a surface to bound the mechanization errors in a tactical grade IMU. Collin et al. (2001), Ojeda and Borenstein (2002) and Wang and Gao (2004c) used complementary motion detection characteristics of accelerometers and gyroscopes to keep the tilt estimation bounded. The basic idea is to use the accelerometer-derived tilt angle for the attitude update while vehicle is static or moving linearly at a constant speed. Among these methods, however, only ZUPTs can provide direct error control of the forward velocity of the vehicle but they are not frequently available sometimes. For low-cost MEMS IMU with large instrument errors, the control of INS error using these methods is insufficient for longer periods of GPS outage.

Auxiliary DR sensors such as odometers and magnetic compasses have also been used to reduce INS error drift. Odometers can provide absolute velocity information but they are vehicle dependent and much difficult to interface with other sensors (Stephen, 2000). As the advances in electronic and manufacture techniques, small-size and low-cost electronic compasses are available to aid INS by providing absolute heading information (Ladetto et al., 2001; Langley, 2003; Wang and Gao 2003b). In practical applications there usually exist unwanted local magnetic fields that will distort compass measurements; hence a calibration procedure is essential. For land vehicle navigation under strong magnetic

disturbance environments, however, the traditional calibration method (Bowditch, 1995; Caruso, 1997; Gebre-Egziabher et al., 2001) may diverge or fail and in turn the accuracy of compass calibration is degraded.

1.2.3 Optimization of INS and GPS Data Fusion

Another challenge to MEMS INS/GPS integration is to perform optimal and adaptive data fusion especially in signal-degraded environments so that the corrupted GPS data will not deteriorate the integration performance to a large extent. Several adaptive methods to optimize INS/GPS data fusion have been proposed in literatures. Karatsinides (1994) identified and rejected the unreasonable GPS data by formulating the measurement noise statistics dynamically based on the residuals between INS and GPS. Mohamed and Schwarz (1999) and Hide et al. (2003) applied adaptive Kalman filtering techniques for INS/GPS integration in benign environments. Swanson (1998), Sasiadek et al. (2000) and Loebis et al. (2003) used fuzzy-rule-based adaptation scheme to tune the data fusion gain (Kalman gain) based on the residuals between INS and GPS. Rahbari et al. (2005) developed an expert system to adaptively tune the measurement noise covariance of the Kalman filter for an INS/DGPS integration system according to the manoeuvring condition of the aircraft. These adaptive data fusion algorithms, however, are not designed for and tested by land vehicle navigation in signal-degraded environments. Currently, Salycheva (2004) applied innovation-based adaptive filtering techniques to integrate a tactical-grade IMU with high sensitivity GPS (HSGPS) for vehicular navigation in urban areas. The work on adaptive fusion of low-cost MEMS INS and GPS or HSGPS data in signal-degraded environments still needs to explore.

1.3 Research Objectives and Contributions

Given the lack of research and the challenges to the integration of low-grade MEMS INS with SPP GPS for land vehicle navigation in all operational environments, this dissertation is devoted to develop effective error control and integration algorithms for this kind of low-cost system so that it can provide reliable and accurate vehicular

navigation solutions. Improving the stand-alone INS navigation performance and optimizing the INS/GPS data fusion in signal-degraded environments are the major focuses. As the low-cost electronic compasses are increasingly embedded in today's MEMS IMU to provide heading aids, a robust calibration algorithm feasible for land vehicle environments is required and also explored in this dissertation.

To accomplish these objectives, this dissertation has investigated and incorporated artificial intelligence (AI) techniques including fuzzy logic, expert system and neural networks with the Kalman filter to develop an intelligent integration algorithm. AI technologies can be seen as the advanced versions of the estimation, the classification, and the inference methods and have found successful applications in a wide variety of fields, such as nonlinear mapping, data classification, and decision analysis (Kandel, 1992; Jang et al., 1997; Haykin, 1999; Luo et al., 2002). With the advantages of processing ambiguous or imprecise data and the capabilities of formulating human intelligence, AI methods can provide a powerful way for low-cost MEMS INS/SPP GPS data processing and fusion.

The major contributions of this dissertation to the field of low-cost MEMS INS/SPP GPS integration for land vehicle navigation can be summarized as follows:

1. Development of a fuzzy logic rule-based GPS data classification system. This system is able to classify GPS data according to the signal degradation conditions so that GPS data can be properly weighted in data fusion. A fuzzy logic rule-based system has been applied to classify signal degradation conditions based on the combination of signal quality and geometry information. (Wang and Gao, 2004d; Wang and Gao, 2006)
2. Development of a dynamics knowledge aided inertial navigation algorithm. This algorithm is capable of improving inertial navigation performance through the aiding from vehicle dynamics knowledge. Besides the commonly used ZUPTs and nonholonomic constraints, this algorithm develops additional dynamics-aid

observations including stationary attitude, straight-line roll and cornering velocity updates to control the INS error drift more effectively. A fuzzy expert system has also been developed to identify the status of vehicle dynamics so that these dynamics-aid observations can be properly applied to update the Kalman filter. (Wang and Gao, 2004c; Wang et al., 2005; Wang and Gao, 2005b)

3. Development of a neural networks compass calibration algorithm. This algorithm is able to provide robust compass calibration even in the magnetic disturbance-rich environments such as land vehicle environments so that compass heading can benefit the integration system. Artificial neural networks are applied to model the nonlinear relationship between the compass heading and the true heading when external heading reference is available and subsequently applied to convert the compass heading into correct heading. (Wang et al., 2005; Wang and Gao, 2005c)
4. Modification and incorporation of the conventional/adaptive Kalman filter with the developed AI-based methods in a loosely coupled integration approach to enhance the low-cost MEMS INS/SPP GPS integration. With the AI enhancement, the Kalman filter is allowed to use simplified dynamics models as well as extended and adaptive measurement update schemes to generate the improved navigation solutions. (Wang and Gao, 2005a; Wang and Gao, 2006b; Wang and Gao, 2006c)
5. Development and testing of a software program implementing the proposed AI-based methods and the intelligent integration algorithm. The navigation performance has been verified through field tests under different environments from open areas to urban areas with signal degradation.

1.4 Dissertation Outline

Chapter 1 presents the motivation, objectives and major contributions of this dissertation to the integration of low-cost MEMS INS with SPP GPS for land vehicle navigation.

Chapter 2 provides an overview of the navigation sensors used in this dissertation including GPS, INS and magnetic compass. The principle, the error source and the characteristics of each sensor are addressed with attentions given those relevant to the low-cost applications. Discussions on the increasingly used HSGPS and MEMS INS are also given.

In Chapter 3, two different data fusion and processing methods that have been used throughout the dissertation are described. They are the model-based Kalman filter algorithm and the model-free AI methodologies including fuzzy logic and neural networks.

Chapter 4 gives a comprehensive analysis of the limitation of the Kalman filter to low-cost MEMS INS/SPP GPS integration and the design of AI-based enhancement methods including a fuzzy logic rule-based GPS data classification system, a dynamics knowledge aided inertial navigation algorithm, and a neural networks compass calibration algorithm.

Chapter 5 describes the development of the intelligent integration algorithm which integrates the AI-based methods developed in Chapter 4 with the conventional/adaptive Kalman filter using a cascaded loosely coupled integration scheme. The design of the modified Kalman filter and the architecture and operation of the intelligent integration algorithm are described in details.

Chapter 6 presents the test and performance analysis results of the proposed intelligent integration algorithm in open area applications. The evaluation of the integration performance without GPS outages and the evaluation of the stand-alone inertial navigation performance with simulated GPS outages are given in this chapter.

In Chapter 7, the test and performance analysis results of the intelligent integration system under urban environments are presented. The GPS data classification performance and the attainable position accuracy of the intelligent integrated solutions are discussed.

Chapter 8 concludes the major results and findings obtained in this research and gives recommendations for future work.

Chapter 2

Land Vehicle Navigation Sensor Overview

Multisensor systems can provide more reliable and accurate navigation solutions by integrating redundant or complementary information. The most commonly used navigation sensors in land vehicle applications include GPS, INS and magnetic compass. GPS can provide good long-term navigation accuracy but is limited by the requirement of at least four visible GPS satellites. INS can provide good short-term navigation accuracy but the navigation error will grow over time unboundedly. Magnetic compass can offer direct and drift-free heading information but is subject to nearby ferrous effects and magnetic disturbances. Prior to designing multisensor data fusion algorithms, it is very important to understand and analyze each sensor's features. An overview of GPS, INS and magnetic compass in terms of their principles and error characteristics is presented in this chapter.

2.1 Overview of Global Positioning System

GPS is a satellite-based radio navigation system developed by the United States Department of Defense (DoD) to provide accurate position, velocity and time (PVT) estimates worldwide under all weather conditions. A complete description of GPS can be found in Leick (1995), Kaplan (1996), Parkinson and Spilker (1996), Hofmann-Wellenhof et al. (2001) and Misra and Enge (2001). In the following, we will place our focus on an overview of C/A-code based SPP GPS positioning widely used for low-cost land vehicle applications. The GPS principles and the error sources of code-based GPS positioning are presented first, followed by an introduction of high sensitivity GPS technology that has been increasingly applied to GPS applications in challenging environments.

2.1.1 GPS Principles

GPS positioning is based on the range from known positions of satellites in space to unknown positions on land, at sea, in air and space (Hofmann-Wellenhof et al., 2001). It consists of three segments: the Space Segment, the Control Segment, and the User Segment. The Space Segment consists of a baseline constellation of 24 satellites distributed in six orbital planes inclined at 55 degrees relative to the equatorial plane. The Control Segment steers satellite operations and maintains system functionalities. The User Segment consists of the GPS receivers and user communities.

Each satellite sends radio signals embracing time-of-arrival (TOA) ranging and satellite PVT information for determining user's PVT information. Each GPS signal comprises three components: a radio frequency (RF) carrier, a unique binary pseudo-random noise (PRN) code and a binary navigation message. Currently, two L-band frequencies: the primary L1 (1575.42 MHz) and secondary L2 (1227.60 MHz) are used to carry GPS signals. Two types of PRN code, namely the Coarse/Acquisition code (C/A-code) on L1 and the Precise code (P-code) on L1 and L2, are used to allow the receiver to determine the signal transit time instantaneously. The P-code is encrypted by the Y code for U.S. military use only while the C/A-code is available to any user. These PRN codes are designed specially to allow all satellites to transmit at the same frequency without interfering with each other. Using modulo-2 addition, each code is combined with the 50 Hz navigation message consisting of data on the satellite health status, ephemeris and almanacs.

The GPS receiver receives and converts satellite signals into position, velocity, and time information. As previously stated, GPS determines the receiver position based on the TOA ranging principle that lies in measuring the propagation time of a radio frequency signal broadcast from a GPS satellite with a known position to a receiver. By decoding the navigation message, a GPS receiver can obtain the data of the satellite's position, velocity, time and health. By measuring the travel time of the coded signal and multiplying it by its velocity, a GPS receiver can derive the user-to-satellite range. By measuring the phase of the incoming carrier, the precise range to a satellite can be

measured with an ambiguous number of cycles. In both case, since the clocks of the receiver and satellite are employed and they are not perfectly synchronized, the synchronization error (receiver clock bias) will bias the user-to-satellite range measurements, resulting in so called pseudorange measurements. To estimate the three coordinates of the user position and the receiver clock bias, pseudorange measurements from at least four satellites are needed and the resulting equation to be solved is written as follows (Misra and Enge, 2001; Lachapelle, 2002):

$$P^{(k)} = \sqrt{(x^{(k)} - x)^2 + (y^{(k)} - y)^2 + (z^{(k)} - z)^2} + b \quad k = 1, 2, \dots, K \quad (2-1)$$

where K is the total number of satellite used;
 $P^{(k)}$ is the pseudorange measurement of satellite k ;
 $(x^{(k)}, y^{(k)}, z^{(k)})$ are the known coordinates of satellite k ;
 (x, y, z) are the user coordinates to be determined; and
 b is the receiver clock bias.

The common approach to solve Eq. (2-1) is to linearize it about an approximate user position and to solve iteratively using least squares or Kalman filtering algorithms. For the determination of the user velocity, the Doppler shift measured routinely in the carrier tracking loop of a GPS receiver is used. The Doppler shift is the frequency difference between the received and transmitted signals. By multiplying it by the wavelength of the transmitted signal, the range rate as a projection of the relative velocity vector on the user-to-satellite vector can be obtained. Given the satellite velocity, the user velocity can be estimated based on the measured range rate using the same principle as the position estimation from pseudoranges.

The quality of the position or velocity estimates depends basically upon two factors (Misra and Enge, 2001):

1. The number of satellites being tracked and their spatial distribution characterized by the satellite geometry strength.
2. The quality of the pseudorange or pseudorange rate measurements.

The satellite geometry strength determines how large the position or velocity errors will be induced by the user-to-satellite pseudorange or pseudorange rate measurement errors. Roughly speaking, if the satellites are clustered in one side of the user due to the blockage of a significant part of the sky, the geometry will be bad and as a result the pseudorange errors will be significantly magnified in the position domain. The relationship between the position accuracy and the range measurement accuracy is given as (Seeber, 1993):

$$\sigma_P = \text{DOP} \times \sigma_r \quad (2-2)$$

where σ_P is the standard deviation of the user position and σ_r is the standard deviation of the range measurement. DOP is the Dilution of Precision and several widely used DOPs are defined from the satellite geometry matrix $\tilde{\mathbf{G}}$. For example, the Geometry Dilution of Precision (GDOP) can be defined as follows (Misra and Enge, 2001):

$$\text{GDOP} = \left\{ \text{trace} \left\{ \left(\tilde{\mathbf{G}}^T \tilde{\mathbf{G}} \right)^{-1} \right\} \right\}^{\frac{1}{2}} \quad (2-3)$$

$$\tilde{\mathbf{G}} = \begin{bmatrix} -\cos E^{(1)} \sin Az^{(1)} & -\cos E^{(1)} \cos Az^{(1)} & -\sin E^{(1)} & 1 \\ \vdots & \vdots & \vdots & \vdots \\ -\cos E^{(K)} \sin Az^{(K)} & -\cos E^{(K)} \cos Az^{(K)} & -\sin E^{(K)} & 1 \end{bmatrix} \quad (2-4)$$

where K is the total number of the observed satellites, and E and Az are satellite elevation and azimuth angles, respectively.

The quality of the pseudorange and pseudorange rate measurements are affected by a variety of biases and errors. The error sources can be grouped into three categories:

satellite-related errors, signal propagation errors and receiver-related errors. The satellite-related errors include satellite clock and ephemeris errors. The signal propagation errors are introduced by interference and the atmospheric propagation effect due to the ionosphere, the troposphere and multipath. The receiver-related errors include the noises introduced by the antenna, amplifiers, cables and the receiver affecting the precision of a measurement.

The code pseudorange measurement to a satellite can be modeled as follows (Misra and Enge, 2001; Lachapelle, 2002):

$$P = \rho + d\rho + c(dt - dT) + d_{ion} + d_{trop} + \varepsilon_p \quad (2-5)$$

where P is the pseudorange measurement (m);
 ρ is the geometric range between the GPS satellite and receiver antenna (m);
 $d\rho$ is the satellite orbital error (m);
 dt is the satellite clock error (s);
 dT is the receiver clock error (s);
 d_{ion} is the ionospheric delay (m);
 d_{trop} is the tropospheric delay (m);
 ε_p is the measurement noise including multipath residual (m); and
 c is the speed of electromagnetic wave in vacuum (m/s).

Similar to the pseudorange measurement, the pseudorange rate measurement to a satellite can be modeled as follows (Misra and Enge, 2001; Lachapelle, 2002):

$$\dot{P} = \dot{\rho} + d\dot{\rho} + c(\dot{dt} - \dot{dT}) + \dot{d}_{ion} + \dot{d}_{trop} + \dot{\varepsilon}_p \quad (2-6)$$

where \dot{P} is the phase rate Doppler measurement (m/s);
 $\dot{\rho}$ is the geometric range rate (m/s);
 $d\dot{\rho}$ is the satellite orbital drift (m/s);

- \dot{d}_i is the satellite clock drift;
- \dot{d}_T is the receiver clock drift;
- \dot{d}_{ion} is the ionospheric drift (m/s);
- \dot{d}_{trop} is the tropospheric drift (m/s); and
- $\dot{\epsilon}_p$ is the pseudorange rate error induced by receiver noise and multipath (m/s).

Detail of these errors and their characteristics are addressed in the following section.

2.1.2 GPS Errors

2.1.2.1 Satellite Orbit Errors

The satellite orbit error occurs due to the fact that the true satellite position is unknown. The satellite position is described by the ephemeris parameters estimated by the control segment based on the previous motion of the satellite and the knowledge of the Earth's gravity field. There exist errors from both the estimation of the current parameters and the prediction of their values for the future. The prediction error grows with the time since the last parameters upload. With typical data uploads once a day by the control segment, a current estimate of the root-mean-square (RMS) range error due to the ephemeris parameters is about 1.5 m (Misra and Enge, 2001).

2.1.2.2 Satellite Clock Errors

The satellite clock error is due to the instabilities in GPS satellite oscillators. The clock bias, drift and drift-rate are monitored with respect to the GPS reference clock maintained by the GPS Master Control Station. A prediction model is used to generate the clock parameters to be uploaded to the satellites. These parameters are then broadcast to the receivers via the navigation message for error correction of the satellite clock. Similar to the ephemeris, with typical data uploads once a day by the control segment, a current estimate of the RMS range error due to the clock error parameters is about 1.5 m (Misra and Enge, 2001).

2.1.2.3 Receiver Clock Errors

This error is the offset between the receiver clock and the GPS reference clock. The clock offset changes over time due to the clock drift which is related to the quality of the oscillator used in the receiver. As mentioned previously, the receiver clock error is usually estimated along with receiver coordinates using at least four pseudorange measurements.

2.1.2.4 Ionospheric Errors

The ionospheric error is due to the presence of free electrons in the atmosphere extending from about 50 to 1000 kilometres above the Earth's surface. These free electrons influence the propagation of microwave signals as they pass through the layer. The presence of free electrons is resulted from the Sun's radiation and thus ionospheric effects change widely between day and night and seasonally according to the solar activity. There are also irregular short-term ionospheric scintillation effects due to high levels of solar and geomagnetic activities. The ionospheric scintillation will cause a rapid variation in the amplitude and/or phase of a GPS signal. The frequency of occurrence of such event is low and varies with location and levels of solar activity (Klobuchar, 1996).

The code phase is delayed and the carrier phase is advanced by the same amount while a GPS signal propagates through the ionosphere. The magnitude of the ionospheric error is a function of the total electron content (TEC) and the signal frequency. Dual-frequency GPS users can estimate the ionospheric error and eliminate it from the measurements. For single frequency SPP users, the ionospheric error can be compensated by using an empirical model (e.g. the Klobuchar model) whose parameter values are broadcast by the satellites (Klobuchar, 1996). The broadcast model is estimated to reduce the RMS range measurement error due to uncompensated ionospheric error by about 50% and the remaining error is about 1~5 m.

2.1.2.5 Tropospheric Errors

The tropospheric error is the result of the refraction of GPS signals by the lower part of the Earth's atmosphere composed of dry gases and water vapor at altitudes up to about 50 kilometres above the Earth's surface. Most of the tropospheric delay (about 80-90%) is due to the dry atmosphere. The composition of the dry atmosphere varies with latitude, altitude and season, and is relatively stable. The water vapor content depends on the local weather and can change quickly.

The tropospheric delay due to the dry and wet effects is typically 2.3 m and 1-80 cm at the zenith, respectively (Spilker, 1996). As the delay will increase with the tropospheric path length, lower elevation satellite signals have a much larger delay by up to a factor of ten. In general, the tropospheric delay ranges from 2 to 25 m for any satellite signal. Fortunately, the tropospheric delay can be corrected by about 80-90% in a single point GPS receiver by using the tropospheric model such as the Hopfield or Saastamoinen model (Spilker, 1996).

2.1.2.6 Multipath Errors

Multipath is the occurrence of a signal reaching an antenna via two or more paths (Misra and Enge, 2001). Mostly it occurs due to the reflection and diffraction of satellite signals off nearby objects, such as buildings, tree foliage or the ground surface. These reflected or diffracted signals will distort the direct signal and result in errors in code range and carrier phase measurements. The composite multipath signal can be expressed as (Braasch, 1994):

$$s(t) = -Ap(t)\sin(\omega_0 t) - \sum_m \alpha_m Ap(t + \delta_m)\sin(\omega_0 t + \theta_m) \quad (2-7)$$

where $s(t)$ is the composite signal;

A is the amplitude of the direct signal;

$p(t)$ is the PRN sequence of the C/A code;

ω_0 is the frequency of the direct signal;

- α_m is the relative power of the multipath signal;
- δ_m is the delay of the multipath signal with respect to the direct signal; and
- θ_m is the phase of the multipath signal relative to the direct signal.

In general, the impact of multipath depends on the amplitude, delay and phase of the multipath signal with respect to the direct signal. Multipath signals are always delayed and usually weaker compared to the direct signals. Depending on the phase of the multipath signal, multipath signals can introduce both negative and positive error on the pseudorange measurement. The code range and carrier phase measurements are affected by multipath in different way. The multipath error on the phase measurement is equal to the difference between the composite signal carrier phase and the direct signal carrier phase with zero mean in all multipath environment and ± 4.75 cm at maximum (Ray, 2000). For the code measurement, multipath affects the code correlation property and in turn induces range errors. The multipath signal will delay or advance the correlation peak depending on its phase. The magnitude of the multipath error on the code range depends on the reflector distance and its strength, the correlator spacing and the receiver bandwidth. The maximum multipath error in the C/A-code range using a wide correlator is ± 150 m, which corresponds to 0.5 chip length (Ray, 2000). The code multipath errors are usually in the order of 10 m to 100 m depending on environmental conditions.

Modern GPS receivers use multipath mitigation techniques to reduce multipath errors based on special receiver and antenna design. One of the most popular technique based on receiver design is the Narrow Correlator technique which narrows the spacing of the early and late correlators in a noncoherent delay lock loop to lessen the effect of multipath (Van Dierendonck et al., 1992). For example, if 0.1 chip correlator spacing is used, multipath with relative delays of approximately 1 chip or greater is rejected entirely and maximum multipath error is reduced by a factor of 10. As multipath must pass through the antenna, multipath errors can be reduced by using an antenna with elevation-dependent gain pattern which can lower the contributions of reflective signals. For land vehicle applications in urban areas, however, the performance of multipath mitigation may be limited due to the tracking of echo-only signals especially for high sensitivity

GPS receivers. Echo-only signals will induce unbounded pseudorange errors and in turn result in large blunders in GPS positions.

2.1.2.7 Receiver Noise

The receiver noise is typically due to the high frequency thermal noise along with the effects of dynamic stresses on the tracking loops (Ward, 1996). It can be considered as a white noise as it is uncorrelated and has zero mean over time. The noise level is a function of the code correlation method, receiver dynamics and signal strength which varies with the satellite elevation angle. The C/A-code receiver noise is generally in the order of a few decimetres while the phase noise is in the order of a few millimetres in most modern receivers (Misra and Enge, 2001).

2.1.2.8 Error Budget

GPS errors can be classified as either random error or systematic error according to their error characteristics. The satellite orbit and clock errors grow slowly with time since the last clock and ephemeris parameters upload; The ionospheric and tropospheric errors, corrected with models or not, may persist for tens of minutes or longer (Olynik, 2002). These errors are classified as systematic error. As to the multipath error and receiver noise, they are random in nature and vary with time and environments and would be classified as random error. The error budget of these error sources on pseudorange measurements for single-frequency single point positioning in a moderate environment after model-based correction of ionospheric and tropospheric errors is presented in Table 2.1. The combined error, known as the user equivalent range error (UERE), can be defined as the root-sum-square of all errors and in this case is about 6 metres. For land vehicle applications in various GPS environments, the multipath error may vary from 1 m to 100 m. As the satellite-based and atmospheric propagation errors are changing slowly and less than 5 m, the multipath error becomes the major error source that determine the accuracy of the pseudorange measurement.

For the accuracy of the phase rate (Doppler) measurement, the error sources include the satellite orbit and clock drifts as well as the changes in the ionospheric and tropospheric delays and in multipath. As the satellite-based and atmospheric propagation error drifts are small and can be reduced by models based on parameters included in the broadcast navigation message, their effects on the Doppler measurement are generally small. As the multipath effect on the phase is small, the multipath error in the Doppler shift measured routinely in the carrier tracking loop of a GPS receiver is not significant, especially compared to the pseudorange multipath error. An estimate of the attainable accuracy of the Doppler shift is 0.001 Hz, which corresponds to the phase rate accuracy of 0.3 m/s if the Doppler shift is measured in the C/A-code tracking loop (Hofmann-Wellenhof et al., 2001). In weak GPS signal environments, Doppler accuracy of better than 2 m/s are possible but the Doppler measurement may be biased (Petovello et al., 2003).

Table 2.1: Typical pseudorange measurement errors for single-frequency single point positioning (Misra and Enge, 2001)

Error Source	RMS Range Error
Satellite clock and ephemeris parameters	3 m
Atmospheric propagation modeling	5 m
Receiver noise and multipath	1 m

2.1.3 High Sensitivity GPS

The high sensitivity GPS receiver (HSGPS) is the improved version of the conventional GPS receiver in terms of the capability of acquiring and tracking weak GPS signals. The power of GPS signals degrades during its propagation from the satellite to the Earth. The satellite transmitting power is about 13.4 dB-W but the power collected by a typical receiver in open-sky conditions is only about -164 dB-W to -156 dB-W. The signal power budget is listed in Table 2.2. In signal-degraded conditions, the signal attenuation due to propagation through various materials and signal reflection can significantly degrade signal power. HSGPS receivers are designed to be able to track weak signals with a power level in the range of -188 dB-W to -182 dB-W (Ray, 2002).

Table 2.2: Signal power budget (Lachapelle, 2002)

SV antenna power (dB-W)	13.4
SV antenna gain	13.4
Effective isotropic radiated power	26.8
User antenna gain (hemispherical)	3.0
Free space loss (L1)	-184.4
Atmospheric attenuation loss	-2.0
Depolarization loss	-3.4
User minimum receiver power (dB-W)	-160.0

The ability to acquire and track weak GPS signals depends on the capability of the receiver to maximize the coherent integration interval and to minimize residual frequency errors during the coherent integration period (MacGougan, 2003). In general, the coherent integration interval is limited to 20 ms due to the timing of the navigation message signal modulation. Residual frequency error sources include oscillator instability, user motion induced Doppler effects and thermal noise. Thermal noise often dominates the carrier tracking error and thermal noise jitter can be reduced by increasing the coherent integration. Thus, by using long coherent integration periods and further non-coherent accumulation, weak signal tracking in degraded GPS environments becomes possible. In order to use long coherent integration periods, the a priori knowledge of time, approximate position and satellite ephemeris is required to enable high sensitivity tracking capability. In general, high sensitivity methods are implemented in either aided or unaided modes. The aided GPS receiver acquires the a priori information about time, approximate position and satellite ephemeris through wireless communication networks. The unaided receiver acquires the same assistance data by tracking four or more GPS satellites with strong signals during initialization periods. As long as the timing, approximate position, and satellite ephemeris are accurate enough, the unaided receiver can have the same functional capability as the aided GPS receiver.

With the capability of tracking weak GPS signals, HSGPS is highly beneficial in terms of solution availability, but simultaneously is limited by large measurement errors due to the

use of the degraded signals such as the attenuated, reflected or echo-only signals. The attenuated line-of-sight signals due to propagation through a material will degrade the signal strength and in turn increase the associated measurement noise. The long-delayed multipath will further cause large errors in pseudorange measurements. When a direct GPS signal is blocked and a reflected signal reaches the antenna, the HSGPS receiver could still track the echo-only signal. This situation can cause measurement errors greater than the maximum multipath error of ± 150 m for wide correlator receivers. In addition, as HSGPS receivers are able to function with both low power and nominal power GPS signals, it increases the probability of acquiring a false correlation peak due to cross-correlation signals which subsequently leads to large measurement errors. Thus, in harsh GPS environments such as downtown canyons and forests, HSGPS solutions are subject to low reliability due to the large measurement errors caused by the increased measurement noise, severe multipath, echo-only signal tracking and cross-correlation.

2.2 Overview of Inertial Navigation System

INS is a dead-reckoning navigation system which determines the attitude, velocity and position of a moving body from the knowledge of the previous states and the measurements of the motion. Inertial navigation has been widely used for the guidance of aircraft, missiles, ships and land vehicles. Since detailed introduction to INS can be found in Titterton and Weston (1997), Salychev (1998), Jekeli (2000) and Schwarz and Wei (2001), this section will focus on an overview of the INS principles and INS error sources. The derivation of navigation states from INS measurements is presented first, followed by the analysis of INS error characteristics. Finally, an introduction of MEMS INS that has been increasingly applied to personal and vehicular navigation is given.

2.2.1 INS Principles

INS is a self-contained navigation system which calculates the change in attitude, velocity and position of a moving body by performing successive mathematical integrations of the measured acceleration and angular velocity with respect to time

(Titterton and Weston, 1997). With the knowledge of the initial attitude, velocity and position, the trajectory of a moving body with respect to a reference frame can be determined. A modern INS (strapdown INS) consisting of three-axis accelerometers and three-axis gyroscopes is usually mounted to be coincident with the axis of the moving body, referred to as the body frame. The body frame (b-frame) is an orthogonal axis set that is aligned with the roll, pitch and yaw axes of the vehicle, i.e., the forward (x), transverse (y) and down (z) direction of the vehicle. Accelerometers provide measurements of the specific force along its axes. Gyroscopes provide measurements of rotation motion of the body with respect to the inertial reference frame and can be used to determine the orientation of the accelerometers. Given this information, it is possible to resolve the accelerometer measurements into the inertial reference frame and in turn to determine the translational motion of the moving body within that frame after the integration process takes place. In order to navigate around the Earth, navigation information is commonly required in the local level frame (navigation frame). The navigation frame is a local geographic frame which has its origin at the location of the navigation system and axes aligned with the directions of north (n), east (e) and down (d) (Titterton and Weston, 1997). Thus, the transformation from the output of INS into the attitude, velocity and position information is usually described by the inertial navigation and mechanization equations in the navigation frame. The navigation equations describe the dynamics of body motion while the mechanization equations are used to derive the position, velocity and attitude increments by solving the equations of motion. Combined with the initial conditions of the system obtained from INS alignment and external sensors, these computed increments can then provide the attitude, velocity and position information needed for navigation.

2.2.1.1 Navigation Equations

The navigation equations in the navigation frame expressed by Cartesian coordinate system can be described as follows (Titterton and Weston, 1997; Schwarz and Wei, 2001):

$$\begin{bmatrix} \dot{\mathbf{P}}_N \\ \dot{\mathbf{V}}_N \\ \dot{\mathbf{R}}_B^N \end{bmatrix} = \begin{bmatrix} \mathbf{R}_B^N \mathbf{A}_B - \left(2\boldsymbol{\omega}_{IE}^N + \boldsymbol{\omega}_{EN}^N \right) \times \mathbf{V}_N + \mathbf{G}_N \\ \mathbf{R}_B^N \left(\boldsymbol{\Omega}_{IB}^B - \boldsymbol{\Omega}_{IN}^B \right) \end{bmatrix} \quad (2-8)$$

where a dot represents a time derivative and \times represents a cross product and

\mathbf{P}_N is the position vector in the navigation frame;

\mathbf{V}_N is the velocity vector in the navigation frame;

\mathbf{R}_B^N is the transformation matrix from body frame to navigation frame;

\mathbf{A}_B is the accelerometer measurement vector in the body frame;

$\boldsymbol{\omega}_{IE}^N$ is the Earth rotation rate vector expressed in the navigation frame;

$\boldsymbol{\omega}_{EN}^N$ is the orientation change rate vector of the navigation frame expressed in the navigation frame;

$\boldsymbol{\Omega}_{IB}^B$ is the skew-symmetric form of the body rotation rate (gyro measurement) vector, $\boldsymbol{\omega}_{IB}^B$, expressed in the body frame;

$\boldsymbol{\Omega}_{IN}^B$ is the skew-symmetric form of the rotation rate vector $\boldsymbol{\omega}_{IN}^B$, which describe the combined rate of the Earth rotation and the orientation change of the navigation frame expressed in the body frame; and

\mathbf{G}_N is the gravity vector expressed in the navigation frame.

In the above equations, \mathbf{A}_B and $\boldsymbol{\Omega}_{IB}^B$ represents the measured motion of the body; $\boldsymbol{\omega}_{IE}^N$, $\boldsymbol{\omega}_{EN}^N$, $\boldsymbol{\Omega}_{IN}^B$ and \mathbf{G}_N are the given Earth's effects which can be computed based on the Earth rotation rate and geographic location information; and \mathbf{P}_N , \mathbf{V}_N and \mathbf{R}_B^N are the navigation information to be solved. The transformation matrix from body frame to navigation frame, \mathbf{R}_B^N , can be expressed by three successive rotations about different axes taken in turn as follows (Titterton and Weston, 1997):

$$\begin{aligned}
\mathbf{R}_B^N &= (\mathbf{R}_N^B)^T = \mathbf{R}_z^T(\psi) \mathbf{R}_y^T(\theta) \mathbf{R}_x^T(\phi) \\
&= \begin{bmatrix} \psi_c & -\psi_s & 0 \\ \psi_s & \psi_c & 0 \\ 0 & 0 & 1 \end{bmatrix} \begin{bmatrix} \theta_c & 0 & \theta_s \\ 0 & 1 & 0 \\ -\theta_s & 0 & \theta_c \end{bmatrix} \begin{bmatrix} 1 & 0 & 0 \\ 0 & \phi_c & -\phi_s \\ 0 & \phi_s & \phi_c \end{bmatrix} \\
&= \begin{bmatrix} \theta_c \psi_c & -\phi_c \psi_s + \phi_s \theta_s \psi_c & \phi_s \psi_s + \phi_c \theta_s \psi_c \\ \theta_c \psi_s & \phi_c \psi_c + \phi_s \theta_s \psi_s & -\phi_s \psi_c + \phi_c \theta_s \psi_s \\ -\theta_s & \phi_s \theta_c & \phi_c \theta_c \end{bmatrix}
\end{aligned} \tag{2-9}$$

where the subscripts s and c refer to sine and cosine and

ϕ , θ , ψ are the roll, pitch and yaw angles which represent the attitude of the moving body;

$\mathbf{R}_z(\psi)$ is the matrix of rotation through the yaw angle ψ about the z axis;

$\mathbf{R}_x(\phi)$ is the matrix of rotation through the roll angle ϕ about the x axis; and

$\mathbf{R}_y(\theta)$ is the matrix of rotation through the pitch angle θ about the y axis.

2.2.1.2 Mechanization Equations

As the navigation equations model the relationship between INS raw measurements and the changes of navigation states, in the mechanization process these equations are solved to derive the navigation states. The mechanization equations consist of three steps: sensor error compensation, attitude computation and velocity and position computation.

1. Sensor error compensation: The INS raw measurements, $\boldsymbol{\omega}_{IB}^B$ and \mathbf{A}_B , are corrupted by sensor errors such as bias, noise, and scale factor error. The deterministic parts of error can be obtained from laboratory calibrations or estimated during the navigation process and in turn removed from the measurements based on the error equations presented in Eq. (2-25) and Eq. (2-26). The corrected gyro and accelerometer measurement vectors are denoted by $\overline{\boldsymbol{\omega}}_{IB}^B$ and $\overline{\mathbf{A}}_B$, respectively.
2. Attitude computation: Based on the last row of Eq. (2-8), the total angular rate vector of the body frame relative to the navigation frame, $\boldsymbol{\omega}_{NB}^B$, can be obtained by:

$$\boldsymbol{\omega}_{NB}^B = \overline{\boldsymbol{\omega}}_{IB}^B - \mathbf{R}_B^N (\boldsymbol{\omega}_{IE}^N + \boldsymbol{\omega}_{EN}^N) \quad (2-10)$$

The updated transformation matrix can then be obtained by a first order approximation as:

$$\mathbf{R}_B^N(t_{k+1}) = \mathbf{R}_B^N(t_k) (\mathbf{I} + \boldsymbol{\Omega}_{NB}^B \Delta t) \quad (2-11)$$

where $\boldsymbol{\Omega}_{NB}^B$ is the skew-symmetric form of the angular rate vector $\boldsymbol{\omega}_{NB}^B$ and $\Delta t = t_{k+1} - t_k$ is the time increment for the time interval (t_k, t_{k+1}) .

Finally, the attitude information can be derived directly from the transformation matrix in the following manner (Titterton and Weston, 1997).

$$\phi = \tan^{-1} \left(\frac{\left(R_B^N \right)_{3,2}}{\left(R_B^N \right)_{3,3}} \right) \quad (2-12)$$

$$\theta = \sin^{-1} \left(- \left(R_B^N \right)_{3,1} \right) \quad (2-13)$$

$$\psi = \tan^{-1} \left(\frac{\left(R_B^N \right)_{2,1}}{\left(R_B^N \right)_{1,1}} \right) \quad (2-14)$$

where $\left(R_B^N \right)_{r,c}$ is the element of the r^{th} row and the c^{th} column of the \mathbf{R}_B^N matrix.

Practically, the propagation of the transformation matrix is usually computed with the quaternion attitude representation to avoid singularity problems (Schwarz and Wei, 2001; El-Sheimy, 2003). For land vehicle applications, the singularity is not an issue since the pitch and roll angles of a land vehicle of 90 degrees are impossible.

3. Velocity and position computation: Based on the updated attitude information, the corrected accelerometer measurement vector in the body frame can be rotated to the navigation frame through Eq. (2-15) or Eq. (2-16).

$$\mathbf{A}_{N_f} = \mathbf{R}_B^N(t_k) \left(\mathbf{I} + \frac{1}{2} \boldsymbol{\Omega}_{NB}^B \Delta t \right) \overline{\mathbf{A}}_B \quad (2-15)$$

$$\mathbf{A}_{N_f} = \mathbf{R}_B^N(t_{k+1}) \left(\mathbf{I} - \frac{1}{2} \boldsymbol{\Omega}_{NB}^B \Delta t \right) \overline{\mathbf{A}}_B \quad (2-16)$$

where \mathbf{A}_{N_f} denotes the acceleration vector in the navigation frame obtained from the accelerometer measurements.

Considering the Earth's rotation and gravity effects, the total acceleration vector in the navigation frame, \mathbf{A}_N , can then be computed through:

$$\mathbf{A}_N = \mathbf{A}_{N_f} - (2\boldsymbol{\omega}_{IE}^N + \boldsymbol{\omega}_{EN}^N) \times \mathbf{V}_N + \boldsymbol{\gamma}_N \quad (2-17)$$

where $\boldsymbol{\gamma}_N$ is the normal gravity vector which varies with the geodetic latitude and ellipsoidal height. It can be computed using a nonlinear model given in such as Schwarz and Wei (2001).

The updated velocity can then be computed by directly adding the total acceleration as follows:

$$\mathbf{V}_N(t_{k+1}) = \mathbf{V}_N(t_k) + \mathbf{A}_N(t_{k+1}) \Delta t \quad (2-18)$$

Finally, the updated position vector can be computed by using trapezoidal integration as follows:

$$\mathbf{P}_N(t_{k+1}) = \mathbf{P}_N(t_k) + (\mathbf{V}_N(t_k) + \mathbf{V}_N(t_{k+1})) \frac{\Delta t}{2} \quad (2-19)$$

2.2.1.3 Initial Alignment

As the computation of attitude, velocity and position using mechanization equations is a dead-reckoning process, the initial conditions of the vehicle need to be known. Typically, the initial velocity and position are given by external sensors such as GPS while the initial attitude are obtained through initial alignment procedures including accelerometer levelling and gyro compassing. The accelerometer levelling procedure is first performed to calculate the initial pitch and roll, followed by the gyro compassing procedure used to compute the initial heading (yaw) as described below.

1. Accelerometer levelling: Under static conditions, the accelerometer measurements containing gravity field only can be combined with the known gravity information to derive the pitch and roll as follows (El-Sheimy, 2003):

$$\theta = \sin^{-1} \left(\frac{A_{Bx}}{g} \right) \quad (2-20)$$

$$\phi = -\sin^{-1} \left(\frac{A_{By}}{g} \right) \quad (2-21)$$

where A_{Bx} and A_{By} are the measured acceleration on the x and y axes, respectively. g is the down-channel component of the gravity vector in the navigation frame, referred to the gravitational constant.

To reduce the accelerometer noise effects, averaging the pitch and roll estimates over an interval is usually taken. The accuracy of these estimates is dependent on the accelerometer biases.

2. Gyro compassing: The principle of gyro compassing is based on the fact that the measurements of two orthogonal components of the Earth's rotation rate in a horizontal plane can establish a coarse heading determination mechanization. Under static conditions, the gyro measurements are due only to the Earth's rotation and the true values of the x-axis and y-axis angular rates projected on the horizontal plane, $\tilde{\omega}_{B_x}$ and $\tilde{\omega}_{B_y}$, can be expressed as follows:

$$\tilde{\omega}_{B_x} = \omega_e \cos L \cos \psi \quad (2-22)$$

$$\tilde{\omega}_{B_y} = \omega_e \cos L \sin \psi \quad (2-23)$$

where ω_e is the Earth's rotation rate and L is the latitude.

By taking the ratio of the Eq. (2-23) over Eq. (2-22), the heading information can be computed as follows:

$$\psi = \tan^{-1} \left(\frac{\tilde{\omega}_{B_y}}{\tilde{\omega}_{B_x}} \right) \quad (2-24)$$

Practically, $\tilde{\omega}_{B_x}$ and $\tilde{\omega}_{B_y}$ in Eq. (2-24) are computed by projecting the measured angular velocities in the body frame onto the horizontal plane using the pitch and roll estimates obtained from the accelerometer levelling.

To reduce the gyro noise effects, averaging the heading estimates over an interval is usually taken. The accuracy of heading estimates is proportional to the quality of the gyro measurements and the square root of the alignment time (El-Sheimy, 2003). For low-cost MEMS INS, however, the Earth's rotation rate is unobservable from the gyro measurement and thus the heading alignment is infeasible. An alternative approach to resolve the initial heading information is to use an external heading

sensor, such as a magnetic compass or using GPS velocities under dynamic conditions for in-flight heading alignment. The performance of the compass heading and the GPS-derived heading are discussed in Chapter 5.

2.2.2 INS Errors

As a dead-reckoning system which determines the current navigation states from the knowledge of the previous states and the measurements of the motion, INS is affected by three types of errors: initial alignment error, inertial sensor error and computational error. These errors are passed from one estimate to the next and result in the overall navigation errors drifting with time. Thus, understanding the characteristics of these errors and developing methods to compensate them in the navigation computation is essential for INS implementation.

2.2.2.1 Initial Alignment Errors

As previously stated, initial alignment is the process whereby the initial attitude, velocity and position of an inertial navigation system are determined based on measurements from the inertial sensors and external sensors. Thus, the alignment accuracy is mainly limited by the effects of sensor errors. Initial alignment errors cannot be estimated and calibrated because they are unobservable. Initial position errors cause constant position biases while the initial velocity and attitude errors result in position error drifting with time and the square of time, respectively.

2.2.2.2 Inertial Sensor Errors

Inertial sensors are subject to errors which limit the accuracy of the inertial measurements. In general, the accelerometer and gyro measurements about an input axis (x axis), A_{Bx} and ω_{Bx} , can be modelled as (Titterton and Weston, 1997):

$$A_{Bx} = \tilde{A}_{Bx} + b_{A_{Bx}} + S_{A_{Bx}} \tilde{A}_{Bx} + M_{A_{By}} \tilde{A}_{By} + M_{A_{Bz}} \tilde{A}_{Bz} + w_{A_{Bx}} \quad (2-25)$$

$$\omega_{Bx} = \tilde{\omega}_{Bx} + b_{\omega_{Bx}} + S_{\omega_{Bx}} \tilde{\omega}_{Bx} + M_{\omega_{By}} \tilde{\omega}_{By} + M_{\omega_{Bz}} \tilde{\omega}_{Bz} + w_{\omega_{Bx}} \quad (2-26)$$

where ‘ \sim ’ denotes the true value of the measurement and

- $b_{A_{Bx}}, b_{\omega_{Bx}}$ are the x-axis accelerometer and gyro biases;
- $S_{A_{Bx}}, S_{\omega_{Bx}}$ are the x-axis accelerometer and gyro scale factor errors;
- $M_{A_{By}}, M_{A_{Bz}}$ are the cross-coupling coefficients for the x-axis accelerometer;
- $M_{\omega_{By}}, M_{\omega_{Bz}}$ are the cross-coupling coefficients for the x-axis gyro; and
- $w_{A_{Bx}}, w_{\omega_{Bx}}$ are the x-axis accelerometer and gyro random noises.

The bias and scale factor error are the major error sources for inertial sensors. According to IEEE standards (IEEE Std 528-2001), the inertial sensor bias is defined as the average over a specified time of the sensor output measured at specified operating conditions that are independent of input acceleration or rotation. A scale factor is the ratio of a change in output to a change in the input to be measured. Both errors include some or all of the following components: fixed terms, temperature induced variations, turn-on to turn-on variations and in-run variations (Titterton and Weston, 1997). The fixed component of the error is present each time when the sensor is turned on and is predictable. A large extent of the temperature induced variations can be corrected with suitable calibration. The turn-on errors vary from sensor turn-on to turn-on but remain constant without power-off. Therefore, they can be obtained from laboratory calibrations or estimated during the navigation process. Sensitive to dynamics changes and vibrations, the in-run random errors are unpredictable and vary throughout the periods when the sensor is powered on (Farrell, 2005). The in-run random errors therefore cannot be removed from measurements using deterministic models and should be modeled by a stochastic process such as random walk process or Gaussian Markov process.

The cross-coupling error is the error due to sensor sensitivity to inputs about axes normal to an input reference axis (IEEE Std 528-2001). Such error arises through non-orthogonality of the sensor triad and is usually expressed as parts per million (PPM). For

low-cost MEMS INS, the cross-coupling error is relatively small and negligible compared to other error sources.

The random noise is an additional signal resulting from the sensor itself or other electronic equipments that interfere with the output signals being measured (El-Sheimy 2003). It is often considered time-uncorrelated with zero mean and modeled by a stochastic process. INS noise level can be characterized by the average of the standard deviation of static measurements over few seconds (Petovello, 2003).

Of above error sources, the bias has the largest impact on INS navigation performance after the mechanization process. The accelerometer bias will result in position error drifting with the square of time while the gyro bias will lead to position error drifting with the cube of time.

2.2.2.3 Computational Errors

In attitude computation, the update of the transformation matrix is approximated by using the truncated version of the propagation equation in order to produce an algorithm which can be implemented in real time. The truncation of the high order term therefore results in attitude computation errors. Reducing the update interval can substantially decrease the computational errors. This approach is feasible for most applications since high turn rates of a vehicle are not normally sustained for long periods.

2.2.3 MEMS INS

“Micro-Electro-Mechanical System (MEMS) is the integration of mechanical elements, sensors, actuators, and electronics on a common silicon substrate through the utilization of microfabrication technology.” (Huff, 1999) MEMS technology enables the realization of complete systems-on-a-chip and therefore allows the development of low-cost microsensors and microactuators. Inertial MEMS development is being driven by the high-volume, commercial market for modest performance applications below \$10 US dollars per axis (Connelly et al., 2000). The largest near-term use of MEMS gyros and

accelerometers is in automotive applications such as for seat belt tensioners, air bags, anti-skid braking systems and vehicle navigation systems.

A typical MEMS accelerometer uses a silicon mass suspended by a silicon beam to form a spring mass damper mechanism whereby capacitive sensing is used to measure the motion of the mass. The displacement of the proof mass is proportional to the change of capacitance and then capacitance change is being sensed and used to measure the amplitude of the force that led to this displacement (Kraft, 1997). The majority of MEMS gyros currently under development operates in a vibratory mode and measures the angular rate based on the coupling of mechanical energy between a vibrating motor element and a sensor element through Coriolis acceleration (Tung, 2000). The vibrating motor controls the sensing element to oscillate in plane with constant amplitude. When an angular rate is applied about the input axis, the sensing element will experience a Coriolis acceleration that forces the masses to translate in and out of the plane of oscillation. This resultant out-of-plane motion is measured via the capacitive pick-off, thus providing a signal proportional to the rate input.

Both MEMS accelerometers and gyros can be fabricated by using either surface or bulk micromachining. Surface micromachined sensors using a thinner and smaller mass of the sensing element have smaller size and lower cost than the bulk micromachined sensors. But the bulk micromachined sensors can provide higher accuracy due to the use of large proof mass. Larger sensors can provide higher performance by increased sensitivity, reduced distortion, and improved relative control of device geometry (Connelly et al., 2000). As fabricated with small size and low cost, MEMS inertial sensors have relatively large measurement errors and instabilities compared to the tactical-grade INS. Due to the high level of the MEMS INS instrument error and noise, some input signals such as the Earth's rotation rate and INS error terms such as the initial alignment error and computational error are relatively small and negligible. Given the low measurement quality in MEMS inertial sensors, completely estimating the deterministic errors and accurately modelling the random errors are difficult and often infeasible. As a result, MEMS INS has poor stand-alone accuracy and is not applicable as a sole navigation

system. Integration of MEMS INS with GPS demands the development of non-traditional approaches and algorithms (Salychev et al., 2000).

2.3 Overview of Magnetic Compass

Thanks to the Earth's magnetic field, the magnetic compass has been used to determine heading direction for centuries. Advances in technology have enabled the development of the electronic compasses which offer many advantages over conventional needle type compasses in terms of vibration resistance, error compensation and direct interface to other navigation systems. Today, the electronic compasses have been widely integrated with modern navigation systems such as GPS and INS to provide direct heading information (Ladetto et al., 2001; Langley, 2003; Wang and Gao 2003b). This section will describe the operational principle of an electronic compass, how the measured magnetic fields are converted into useful heading information. The error sources and their characteristics are also presented.

2.3.1 Compass Principles

The principle of magnetic compassing is based on the measurement of the Earth's magnetic field. Generated by the core of the Earth, the Earth's magnetic field flows out of the magnetic South Pole and back in through the magnetic North Pole. The Earth's magnetic field therefore has a component parallel to the Earth surface that always points toward the magnetic North. By resolving this component, the direction of the magnetic sensor with respect to the magnetic North can be determined. An electronic compass typically uses the magnetoresistive (MR) magnetometer to measure magnetic fields. This sensor is composed of thin strips of permalloy whose electrical resistance varies with applied magnetic field changes (Caruso, 1997). Recent MR magnetometers offer sensitivities less than 0.1 milligauss and have a response time below 1 microsecond.

In practical application, the moving vehicle or platform to which the electronic compass is attached are most often not confined to the Earth's surface. It is essential to use three-

axis magnetometers mounted orthogonally in an electronic compass so that the Earth's magnetic field can be fully rotated back to a horizontal orientation. Figure 2.1 describes this configuration and the coordinate systems. The magnetic compass is aligned with the body frame consisting of three orthogonal axes where x is in the direction of forward motion of the vehicle, z is in the down direction to the road surface, and y is in the direction of transverse motion of the vehicle, perpendicular to the plane formed by x and z axes. The attitude of the vehicle is represented by three Euler angles, roll (ϕ), pitch (θ) and yaw (heading) (ψ), which are the rotation angles about x , y and z axes, respectively. With the knowledge of tilt (pitch and roll) angles, the measured magnetic field vector can be projected on a horizontal plane parallel to the Earth's surface in the following manner (Caruso, 1997).

$$\begin{bmatrix} M_{x_H} \\ M_{y_H} \end{bmatrix} = \begin{bmatrix} \cos \theta & \sin \theta \sin \phi & -\cos \phi \sin \theta \\ 0 & \cos \phi & \sin \phi \end{bmatrix} \begin{bmatrix} M_x \\ M_y \\ M_z \end{bmatrix} \quad (2-27)$$

where M_x , M_y and M_z are the magnetometer measurements of the body frame, M_{x_H} and M_{y_H} are the magnetometer measurements of the body frame projected on the horizontal plane formed by x_H and y_H axes.

The angle α between the forward axis of the vehicle and the magnetic North can be calculated by resolving the horizontal component of the magnetometer measurements as follows (Caruso, 1997):

$$\alpha = \begin{cases} 90 & , M_{x_H} = 0, M_{y_H} < 0 \\ 270 & , M_{x_H} = 0, M_{y_H} > 0 \\ 180 - \tan^{-1} \left(\frac{M_{y_H}}{M_{x_H}} \right) \times \frac{180}{\pi} & , M_{x_H} < 0 \\ -\tan^{-1} \left(\frac{M_{y_H}}{M_{x_H}} \right) \times \frac{180}{\pi} & , M_{x_H} > 0, M_{y_H} < 0 \\ 360 - \tan^{-1} \left(\frac{M_{y_H}}{M_{x_H}} \right) \times \frac{180}{\pi} & , M_{x_H} > 0, M_{y_H} > 0 \end{cases} \quad (2-28)$$

Finally, by adding or subtracting a proper declination angle δ to correct for true North, the vehicle heading ψ can be determined. The declination angle can differ by ± 25 degrees or more and can be determined from a lookup table based on the geographic location. It should be noticed that the declination angle will change secularly according to the variations of the Earth's geomagnetic field (Whitcomb 1989).

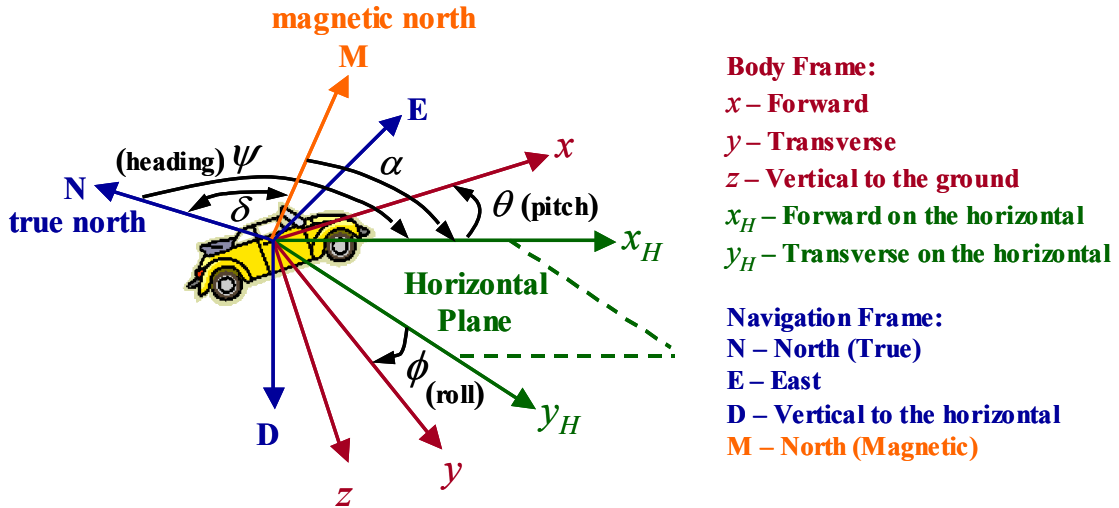


Figure 2.1: Heading determination using a triad of magnetometers

2.3.2 Compass Errors

As the compass heading determination involves the transformation of magnetic measurements from the sensor triad to the horizontal plane, the error sources of the compass heading include transformation errors, magnetic measurement errors and misalignment errors which are described in the following.

2.3.2.1 Transformation Errors

The transformation error is due to the use of inaccurate tilt information while projecting the three-axis magnetometer measurements on the horizontal plane. This error is dependent on the performance of the tilt sensor such as inclinometers or INS and is usually unpredictable. Thus, this error cannot be accounted for and removed from the compass heading and is considered as non-Gaussian random error.

2.3.2.2 Magnetic Measurement Errors

The magnetic measurement error is resulted from the distortion of the Earth's magnetic field by nearby ferrous effects, sensor noise and magnetic interferences. In practical application, compasses are mounted in vehicles and platforms that most likely have ferrous materials nearby. These nearby ferrous materials will generate permanent magnetic fields (hard irons) or varying magnetic fields (soft irons) to distort the Earth's magnetic field. Hard irons add a constant magnitude field component (bias) along each axis of the sensor output and result in a shift in the origin of the 2-D magnetic field locus (Caruso, 2000). Soft irons affect the magnetometer output with a varying amount depending on the compass orientation. The varying bias effects will distort the shape of the 2-D magnetic field locus from a circle into an ellipse. Hard and soft iron distortions are the major error sources for magnetic compassing and compensating for these effects is essential to application. They can be modeled as bias and scale factor error in magnetometer measurements (Caruso, 1997; Langley, 2003).

On the other hand, sensor noise and magnetic interferences are random in nature and cannot be modeled systematically. Noise is typically assumed to be a zero-mean Gaussian process and can be eliminated with a low pass filter. Magnetic interferences generated by such as electronic devices, however, are unpredictable and could bias the magnetometer output significantly. Errors introduced by magnetic interferences usually change with time and environments according to the activities of the interference sources. Such errors are generally considered as blunders which will corrupt the measurement statistics and therefore compensating for hard and iron effects in interference-rich environments such as land vehicle environments becomes a challenge.

2.3.2.3 Misalignment Errors

These errors are introduced by two types of misalignments: non-orthogonality of the sensor triad and imperfect alignment between the sensor triad and the body axis of the vehicle or platform. Both misalignments will cause cross coupling of the magnetometer measurements leading to compass heading error. Misalignment errors can be minimized

by calibration of the sensor triad in manufacture and careful installation of the sensor in application. Compared to other errors, misalignment errors are relatively small and usually ignored.

Chapter 3

Data Fusion and Processing Methodologies

Sensors' measurements or data need to be properly interpreted, processed and fused in order to generate refined navigation information. The model-based Kalman filter and the model-free artificial intelligence (AI) methods are two different data processing and data fusion techniques. The Kalman filter offers a powerful method for linear data fusion and estimation that are optimal in the statistical sense if the system models are known. AI methods including fuzzy logic and neural networks provide a nonlinear mechanism for high-level inference, data classification, and functional mapping. This dissertation applies the Kalman filter for MEMS INS/GPS integration and the AI techniques for data quality assessment, navigation error compensation, sensor error modelling, and fusion scheme optimization to enhance the performance of the Kalman filter-based data fusion. This chapter will present the fundamentals of these algorithms.

3.1 Kalman Filter

The Kalman filter is a linear recursive data processing algorithm that processes all available measurements, regardless of their precision, to estimate the current value of the variables of interest, with use of (1) knowledge of the system and measurement device dynamics, (2) the statistical description of the system noises, measurement errors, and uncertainty in the dynamics models, and (3) available information about initial conditions of the variables of interest (Maybeck, 1979). If the input data fits the predefined linear dynamics and statistical models and prior knowledge is known, the Kalman filter can provide an optimal, in a minimum variance sense, estimate of the state vector (Gelb, 1974). Accordingly, the Kalman filter has become the most common technique for estimating the state of a linear system particularly in navigation systems. Since the estimation process is implemented on a computer, the discrete form of the Kalman filter

is generally used. The following sections will describe the algorithm of the conventional and adaptive Kalman filter as well as the implementation strategies of INS/GPS integration using the Kalman filter.

3.1.1 Discrete Kalman Filter

Consider the random process to be estimated can be modeled by the following linear dynamics model with a series of differential equations.

$$\dot{\mathbf{x}} = \mathbf{F}\mathbf{x} + \mathbf{G}\mathbf{u} \quad (3-1)$$

where \mathbf{x} is the vector of state variables;

\mathbf{F} is a dynamics matrix;

\mathbf{G} is a type of shaping filter; and

\mathbf{u} is a vector forcing function whose elements are white noise.

The discrete time form of Eq. (3-1) can be obtained from the state-space solution of the above differential equation which can be written as (Brown and Hwang, 1992):

$$\mathbf{x}(t_{k+1}) = \Phi(t_{k+1}, t_k)\mathbf{x}(t_k) + \int_{t_k}^{t_{k+1}} \Phi(t_{k+1}, \tau)\mathbf{G}(\tau)\mathbf{u}(\tau)d\tau \quad (3-2)$$

or in the form of

$$\mathbf{x}_{k+1} = \Phi_k\mathbf{x}_k + \mathbf{w}_k \quad (3-3)$$

where \mathbf{x}_{k+1} , \mathbf{x}_k are the process state vectors at time t_{k+1} and t_k , respectively;

\mathbf{w}_k is the driven response at t_{k+1} due to the white noise input of the forcing function during the (t_k, t_{k+1}) interval; and

Φ_k is a transition matrix relating \mathbf{x}_k to \mathbf{x}_{k+1} .

Based on the assumption that the input noise in the continuous model is white, \mathbf{w}_k will be a white sequence in the discrete model with zero mean and time-uncorrelated property as follows:

$$E[\mathbf{w}_k] = 0 \quad (3-4)$$

$$E[\mathbf{w}_k \mathbf{w}_i^T] = \begin{cases} \mathbf{Q}_k, & i = k \\ 0, & i \neq k \end{cases} \quad (3-5)$$

where $E[\bullet]$ is the mathematical expectation.

The process noise covariance matrix \mathbf{Q}_k associated with \mathbf{w}_k can be written as (Brown and Hwang, 1992):

$$\begin{aligned} \mathbf{Q}_k &= E[\mathbf{w}_k \mathbf{w}_k^T] \\ &= E \left\{ \left[\int_{t_k}^{t_{k+1}} \Phi(t_{k+1}, \xi) \mathbf{G}(\xi) \mathbf{u}(\xi) d\xi \right] \left[\int_{t_k}^{t_{k+1}} \Phi(t_{k+1}, \eta) \mathbf{G}(\eta) \mathbf{u}(\eta) d\eta \right]^T \right\} \\ &= \int_{t_k}^{t_{k+1}} \int_{t_k}^{t_{k+1}} \Phi(t_{k+1}, \xi) \mathbf{G}(\xi) E[\mathbf{u}(\xi) \mathbf{u}^T(\eta)] \mathbf{G}(\eta) \Phi(t_{k+1}, \eta) d\xi d\eta \end{aligned} \quad (3-6)$$

Since the noise sequence \mathbf{u} is white, the covariance calculation can be reduced to the form of (Gelb, 1974)

$$\mathbf{Q}_k = \int_{t_k}^{t_{k+1}} \Phi(t_{k+1}, \tau) \mathbf{G}(\tau) \mathbf{Q}(\tau) \mathbf{G}(\tau) \Phi(t_{k+1}, \tau) d\tau \quad (3-7)$$

where $\mathbf{Q}(t) = E[\mathbf{u}(t) \mathbf{u}^T(t)]$ is the spectral density matrix for the forcing function input.

The transition matrix is calculated using the inverse Laplace transform as follows (Gelb, 1974):

$$\Phi_k = \mathcal{L}^{-1}[(s\mathbf{I} - \mathbf{F})^{-1}] \quad (3-8)$$

where \mathcal{L}^{-1} represents the inverse Laplace transform and s is the Laplace transform parameter. If \mathbf{F} can be assumed constant over the Δt interval of interest, the transition matrix is simply the matrix exponential of $\mathbf{F}\Delta t$, that is,

$$\Phi_k = e^{\mathbf{F}\Delta t} = \mathbf{I} + \mathbf{F}\Delta t + \frac{(\mathbf{F}\Delta t)^2}{2!} + \dots \quad (3-9)$$

Consider the observation (measurement) of the process that has a linear relationship with the system state vector

$$\mathbf{z}_k = \mathbf{H}_k \mathbf{x}_k + \mathbf{v}_k \quad (3-10)$$

where \mathbf{z}_k is a measurement vector at time t_k ;

\mathbf{H}_k is a design matrix giving the noiseless connection between the measurement and the state vector at time t_k ; and

\mathbf{v}_k is a measurement noise vector.

The measurement noise is assumed to be a white sequence with zero mean and time-uncorrelated property and uncorrelated with process noise.

$$E[\mathbf{v}_k] = 0 \quad (3-11)$$

$$E[\mathbf{v}_k \mathbf{v}_i^T] = \begin{cases} \mathbf{R}_k, & i = k \\ 0, & i \neq k \end{cases} \quad (3-12)$$

$$E[\mathbf{v}_k \mathbf{v}_i^T] = 0, \quad \text{for all } k \text{ and } i \quad (3-13)$$

where $\mathbf{R}_k = E[\mathbf{v}_k \mathbf{v}_k^T]$ is the measurement noise covariance matrix.

To derive an optimal estimate of the process state, the Kalman filter uses a linear blending of the measurement and the prior estimate in accordance with the equation:

$$\hat{\mathbf{x}}_k = \hat{\mathbf{x}}_k^- + \mathbf{K}_k (\mathbf{z}_k - \mathbf{H}_k \hat{\mathbf{x}}_k^-) \quad (3-14)$$

where $\hat{\mathbf{x}}_k$ is the update estimate, $\hat{\mathbf{x}}_k^-$ is the prior estimate, and \mathbf{K}_k is the optimal Kalman gain matrix that is determined by minimizing the mean-square estimation error.

$$\text{trace}(\mathbf{E}[(\mathbf{x}_k - \hat{\mathbf{x}}_k)(\mathbf{x}_k - \hat{\mathbf{x}}_k)^T]) \equiv \min \quad (3-15)$$

Details of the derivation of \mathbf{K}_k are available in Kalman (1960), Gelb (1974), or Brown and Hwang (1992). The summary of the discrete Kalman filter algorithm is shown in Figure 3.1.

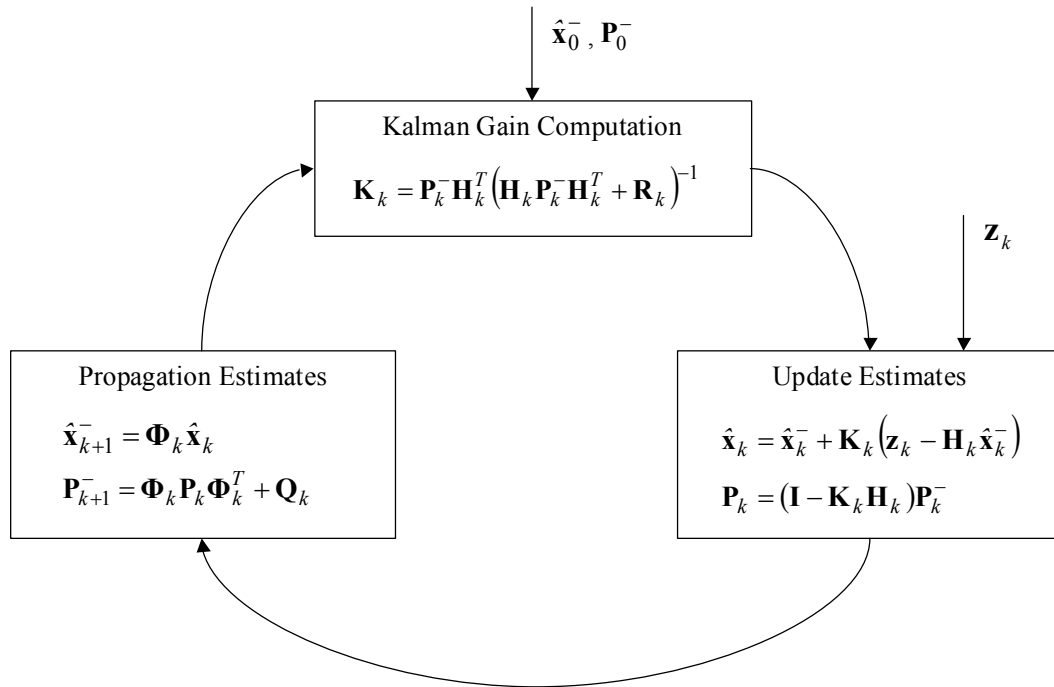


Figure 3.1: Discrete Kalman filter algorithm

3.1.2 Innovation-Based Adaptive Kalman Filter

As stated previously, the Kalman filter relies on complete a priori knowledge of the process and measurement noise statistics. In most practical situations, these statistics have time varying characteristics and are not exactly known. The use of wrong a priori statistics in the designed Kalman filter can lead to large estimation errors or even divergence of the filter. Several adaptive Kalman filter algorithms have been proposed in literatures to reduce these errors by adapting the stochastic properties of the filter online to the real data (Magill, 1965; Mehra, 1970; Mehra, 1972). The innovation-based adaptive estimation approach has been found more suitable for INS/GPS integration systems (Salychev, 1998; Mohamed and Schwarz, 1999).

The principle of the innovation-based adaptive Kalman filter is to make the filter residuals (innovation sequences) consistent with their theoretical covariances (Mehra, 1972). The innovation sequence \mathbf{v}_k at epoch k is defined as the difference between the actual measurement \mathbf{z}_k and the predicted measurement $\mathbf{H}_k \hat{\mathbf{x}}_k^-$, namely:

$$\mathbf{v}_k = \mathbf{z}_k - \mathbf{H}_k \hat{\mathbf{x}}_k^- \quad (3-16)$$

Under the assumed conditions specified in Eq. (3-5), (3-12), and (3-13), the innovation sequence is a Gaussian white noise sequence with known covariance matrix, namely:

$$E[\mathbf{v}_k] = 0 \quad (3-17)$$

$$E[\mathbf{v}_k \mathbf{v}_k^T] = \mathbf{C}_k = \mathbf{H}_k \mathbf{P}_k^- \mathbf{H}_k^T + \mathbf{R}_k = \mathbf{H}_k (\mathbf{\Phi}_{k-1} \mathbf{P}_{k-1} \mathbf{\Phi}_{k-1}^T + \mathbf{Q}_{k-1}) \mathbf{H}_k^T + \mathbf{R}_k \quad (3-18)$$

where \mathbf{C}_k is the theoretical covariance matrix of the innovation sequence.

When both of the process and measurement noise covariances are unknown, \mathbf{P}_k^- and \mathbf{P}_{k-1} do not necessarily represent the actual error covariances and thus the estimation process

may not converge (Mehra, 1972). The case in which the process noise covariance is assumed known and the measurement noise covariance is estimated by the above method can be handled more successfully (Mehra, 1972). For INS/GPS integration under signal degradation conditions, a priori knowledge of the measurement errors from GPS is much difficult to obtain and should be online estimated. In processing the real observations, the actual covariance matrix of the innovation sequence $\hat{\mathbf{C}}_k$ can be estimated by its sample covariance, namely:

$$\hat{\mathbf{C}}_k = \frac{1}{N} \sum_{i=k-N+1}^k \mathbf{v}_i \mathbf{v}_i^T \quad (3-19)$$

where N is an empirically chosen window size for the purpose of statistical smoothing.

An adaptive measurement noise covariance $\hat{\mathbf{R}}_k$ can be estimated by substituting the actual covariance matrix of the innovation sequence into Eq. (3-18) as follows:

$$\hat{\mathbf{R}}_k = \frac{1}{N} \sum_{i=k-N+1}^k \mathbf{v}_i \mathbf{v}_i^T - \mathbf{H}_k \mathbf{P}_k^- \mathbf{H}_k^T \quad (3-20)$$

The innovation-based adaptive Kalman filter based on Eq. (3-19) and Eq. (3-20) is more suitable for INS/GPS integration in land vehicle applications. It should be noted that a negative definite $\hat{\mathbf{R}}_k$ could be obtained at the beginning of estimation due to small sample data available in the estimation of $\hat{\mathbf{C}}_k$; therefore, the following normalization procedure should be considered (Salychev, 1998):

$$diag(\hat{\mathbf{R}}_k) = 0, \text{ if } diag(\hat{\mathbf{R}}_k) < 0.$$

3.1.3 INS/GPS Integration Using Kalman Filter

The Kalman filtering methodology has been extensively applied for optimal fusion of data from GPS and INS and the bridging of GPS outages. The most commonly used integration scheme in literatures is loosely and tightly coupled integration strategy (Wei and Schwarz, 1990; Salychev, 1998; Scherzinger, 2000 and Petovello, 2003). The loosely coupled integration algorithm usually applies two decentralized Kalman filter in a cascaded scheme. As shown in Figure 3.2, the INS and the GPS receiver operate as independent systems and process data parallelly. INS raw measurements (acceleration and angular velocity) are processed in the INS mechanization to derive INS attitude, velocity and position. GPS raw observations (code, Doppler and phase) are processed in the GPS Kalman filter to derive GPS velocity and position. The INS Kalman filter utilizes the differences between the INS and GPS velocities and positions as the measurements and the INS error equations as the system model. When GPS is available, the INS Kalman filter estimates all observable INS sensor and navigation errors to compensate system outputs. When GPS is unavailable, INS sensor and navigation errors will be predicted based on the system model. (Salychev, 1998)

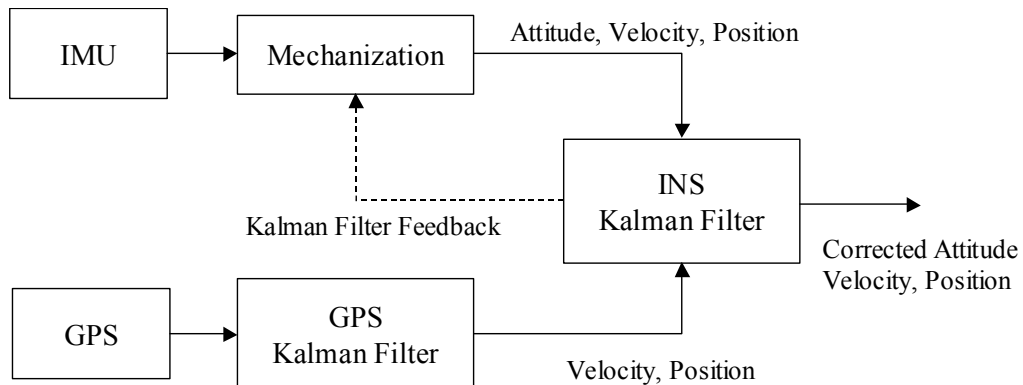


Figure 3.2: Loosely coupled INS/GPS integration algorithm

In the tightly coupled integration scheme a centralized Kalman filter is applied to process INS data and GPS raw measurements together as shown in Figure 3.3. Similarly to the loosely coupled integration algorithm, the INS navigation states are first derived from the INS raw measurements based on the INS mechanization. Then, in the INS/GPS Kalman

filter the INS sensor and navigation errors as well as GPS range and range rate errors are estimated using the pseudoranges and delta ranges calculated by the INS and measured by a GPS receiver as the system measurements. The estimated INS errors will be applied to correct the INS navigation states.

According to whether the estimated sensor errors are fed back to correct the measurements, both loosely and tightly coupled integration algorithm can be implemented with an open loop or closed loop. The closed-loop implementation, which generally enhances the navigation performance because the previous estimation results are used to minimize the approximation error due to system model linearization, are mostly applied in INS/GPS integration systems (Skaloud, 1999 and El-Sheimy, 2003).

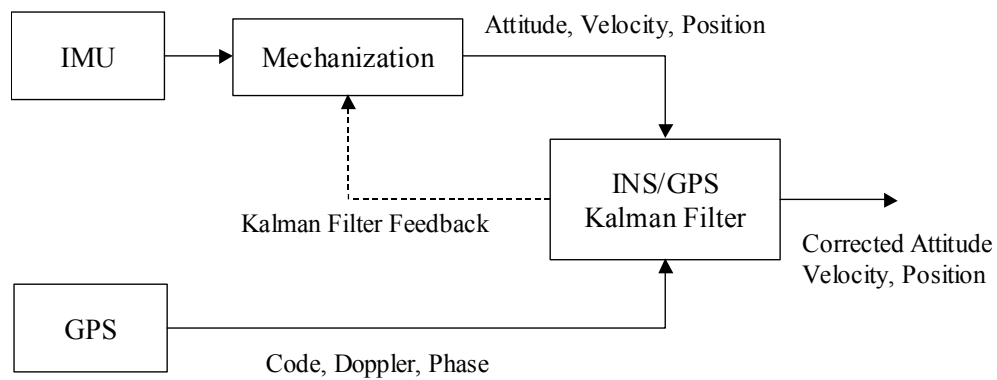


Figure 3.3: Tightly coupled INS/GPS integration algorithm

The loosely coupled integration system has both advantages and disadvantages compared to the tightly coupled one. In the aspect of system implementation, the loosely coupled integration system has higher flexibility and modularity as well as less computation and complexity due to the independent operation and the smaller dimensions of the individual Kalman filter. In the aspect of system accuracy, the tightly coupled integration system provides globally optimal estimation accuracy because all the states for the entire system are defined in one global state vector with a corresponding global description of the process noise. However, the accuracy does not deteriorate much when a sub-optimal cascaded loosely coupled integration system with a proper assessment of GPS filter outputs is used (Wei and Schwarz, 1990). In terms of system availability, the loosely

coupled integration system requires at least four GPS satellites to provide GPS updates for INS corrections while the tightly coupled method can still work with as few as one GPS satellite. For system robustness, the loosely coupled integration system has higher fault detection performance than the tightly coupled one because the independent filter solutions are available from two separate filters (Gao et al., 1993).

For land vehicle applications, GPS is frequently operating in signal-degraded environments (e.g. urban canyons, forests) in which GPS measurements deteriorate significantly due to multipath and echo-only signals and become erroneous and unreliable. The integration system, therefore, should have better fault-tolerance and blunder isolation capability. Due to the cost and operation concerns, the integration system should be easily implemented with low complexity and high flexibility so that different types of INS and GPS can be used. In addition, with the increasing use of HSGPS, the availability of GPS solutions in challenging environments can be significantly improved. Thus, the loosely coupled closed-loop integration scheme is considered as a more suitable approach for low-cost INS/GPS integration in land vehicle applications and has been applied in this dissertation.

3.2 Fuzzy Logic

The concept of fuzzy logic was first conceived by Zadeh (1965). As the complexity of a system increases, it becomes more difficult to make a precise statement about its behavior and fuzzy logic provides a framework to deal with such problems naturally (Zadeh, 1965). Resembling human decision making by using if-then rules and handling ambiguous and imprecise information by using fuzzy set theory, fuzzy logic provides a successful way of dealing with complex systems. Fuzzy logic has found successful applications in decision making, data classification, pattern recognition, automatic control and etc. (Tanaka, Okuda, and Asai, 1976; Bezdek, Ehrlich and Full, 1984; Pal and King, 1981). In this dissertation, the fuzzy logic has been applied for GPS data classification and vehicle dynamics identification where human reasoning and ambiguous data are inextricably involved. This section describes the fundamentals of fuzzy logic and fuzzy inference system while its applications to INS/GPS integration are to be described in Chapter 4.

3.2.1 Fundamentals of Fuzzy Logic

3.2.1.1 Fuzzy Sets and Membership Functions

A fuzzy set is a set without a crisp boundary but a gradual transition form characterized by membership functions. Such a set provides a natural way to deal with problems in which the source of imprecision is the absence of sharply defined criteria of class membership rather than the presence of random variables (Zadeh, 1965). A fuzzy set A in X is defined as follows:

$$A = \{(x, \mu_A(x)) | x \in X\} \quad (3-21)$$

where $\mu_A(x)$ is called the membership function for the fuzzy set A . The membership function maps the each element of X to a membership degree between 0 and 1. It is usually expressed by a linguistic term such as “the velocity is high” to embody the fuzziness for a particular fuzzy set.

A membership function can be featured by the terms of core, support and boundaries as shown in Figure 3.4. The core of a membership function for a fuzzy set A is defined as the region of the universe with full membership in the set. The support of a membership function for a fuzzy set A is defined as the region of the universe with nonzero membership in the set. The boundaries comprise the elements of universe such that $0 < \mu_A(x) < 1$. These elements define the shape of membership function and the fuzziness of the set. Many strategies such as intuitive, algorithmic and logical approaches can be used to assign membership functions for fuzzy variables. The design of membership functions can be simply derived from human knowledge or common sense reasoning or more sophisticated techniques, e.g., neural networks (Jang, 1993) or genetic algorithms (Karr and Gentry, 1993).

It should be noted that the fuzziness dealt with by fuzzy set theory are totally different from the randomness dealt with by probability theory. The fuzziness represents the

ambiguity of an event, whereas randomness represents the uncertainty in the occurrence of the event (Ross, 1995).

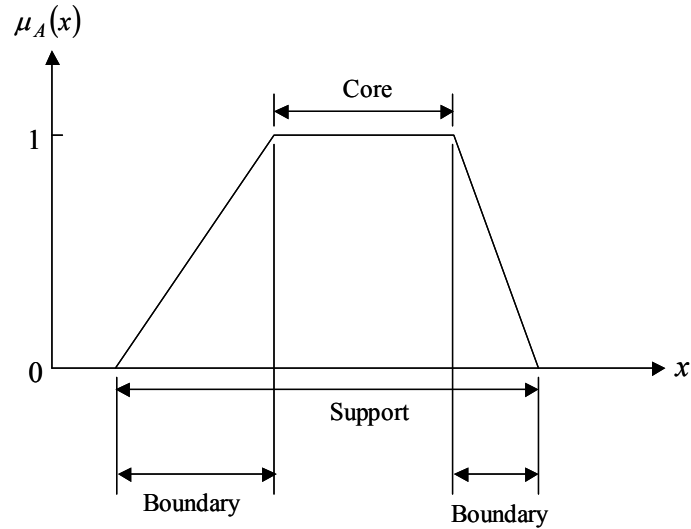


Figure 3.4: Features of the membership function

3.2.1.2 Logical Operations and If-Then Rules

After handling the ambiguous input data using fuzzy set theory, a fuzzy process performs logical operations on a formulation of if-then rules to derive fuzzy outputs. The standard Boolean logic, AND, OR and NOT, are the most basic operations used on classical sets. The input and output of these operations are crisp values, either 0 or 1. In fuzzy logic, however, the input values representing the degree of membership could be a real number between 0 and 1. Thus, the standard Boolean logic operations should be modified to equivalent functions for fuzzy set operations. One of the most popular ways is to use the *min-max* operation. The AND operation of two fuzzy sets A and B is a fuzzy set $C = A \cap B$, whose membership function is defined as $\mu_C(x) = \min(\mu_A(x), \mu_B(x))$. The OR operation of two fuzzy sets A and B is a fuzzy set $D = A \cup B$, whose membership function is defined as $\mu_D(x) = \max(\mu_A(x), \mu_B(x))$. The NOT operation of a fuzzy set A is denoted by \bar{A} , whose membership function is defined as $\mu_{\bar{A}}(x) = 1 - \mu_A(x)$. Many other fuzzy set operations such as *max-product*, *max-max* or *min-min* have been mentioned in literatures. Each of them has its own significance and applications. The *min-max*

operation is the one initially defined by Zadeh in his original paper and has found effective expression of the approximate reasoning using natural language if-then rules. Thus, this research uses the *min-max* approach for fuzzy logic operations.

The if-then rule is a type of nature language expressions to represent human knowledge. The if-then rule formulates human knowledge into a conditional statement that comprises fuzzy logic as follows:

$$\text{If } x \text{ is } A \text{ (premise) then } y \text{ is } B \text{ (conclusion)} \quad (3-22)$$

where A and B are linguistic values defined by fuzzy sets on the ranges (universes of discourse) X and Y , respectively.

The if-then rule typically expresses an inference such that if we know the premise, then we can derive another fact called a conclusion. The premise of a rule can have multiple parts connected using logical operators such as AND, OR and NOT. All parts of the premise are calculated simultaneously and resolved to a single number using the corresponding fuzzy logic operations. The conclusion of a rule can also have multiple parts in which all conclusions are affected equally by the result of the premise.

In most applications, fuzzy reasoning involves more than one rule. To obtain the overall conclusion from the individual consequents contributed by each rule, the process of aggregation of rules is required. In general, two simple aggregation strategies, conjunction of rules and disjunction of rules, are used in literatures (Vadiee, 1993). For the case where the rules must be jointly satisfied, the rules are connected by “and” connectives and the aggregated output is formed by the fuzzy intersection of all individual rule conclusions. In this case the membership function of the aggregated output, $\mu_y(y)$, is defined as:

$$\mu_y(y) = \min(\mu_{y^1}(y), \mu_{y^2}(y), \dots, \mu_{y^r}(y)) \quad \text{for } y \in Y \quad (3-23)$$

where $\mu_{y^1}(y), \mu_{y^2}(y), \dots, \mu_{y^r}(y)$ are the membership functions of the individual rule conclusions.

For the case where the satisfaction of at least one rule is required, the rules are connected by “or” connectives and the aggregated output is formed by the fuzzy union of all individual rule conclusions. In this case the membership function of the aggregated output, $\mu_y(y)$, is defined as:

$$\mu_y(y) = \max(\mu_{y^1}(y), \mu_{y^2}(y), \dots, \mu_{y^r}(y)) \quad \text{for } y \in Y \quad (3-24)$$

3.2.1.3 Defuzzification

After the approximate reasoning using if-then rules, a fuzzy process outputs a fuzzy set defined on the universe of discourse of the output variable. In many applications where the output of a fuzzy process needs to be a single scalar quantity, the defuzzification is required to convert a fuzzy quantity into a precise quantity. Hellendoorn and Thomas (1993) have investigated several popular methods for defuzzification such as max-membership principle, centroid method, weighted average method, centre of sums and etc. This research applies the centroid method for the defuzzification process, as it is the most prevalent and widely adopted defuzzification method. The centroid method is given by the following algebraic expression.

$$y^* = \frac{\int \mu_y(y)ydy}{\int \mu_y(y)dy} \quad (3-25)$$

where y^* is the defuzzified scalar quantity; and $\mu_y(y)$ is the membership function of the aggregated output.

3.2.2 Fuzzy Inference System

The fuzzy inference system is a computing framework for formulating the mapping from a given input to an output based on the concept described in the previous section: fuzzy set theory, fuzzy logic operators, if-then rules, and defuzzification. A block diagram of a fuzzy inference system is shown in Figure 3.5. In a typical fuzzy inference system the crisp inputs are first converted to the input fuzzy sets using the membership functions. Then the input fuzzy sets are mapped into a consequent fuzzy set based on the adopted fuzzy logic operators, if-then rules and aggregation strategy. Finally, the consequent fuzzy set is converted into a scalar quantity as the system output using a defuzzification method.

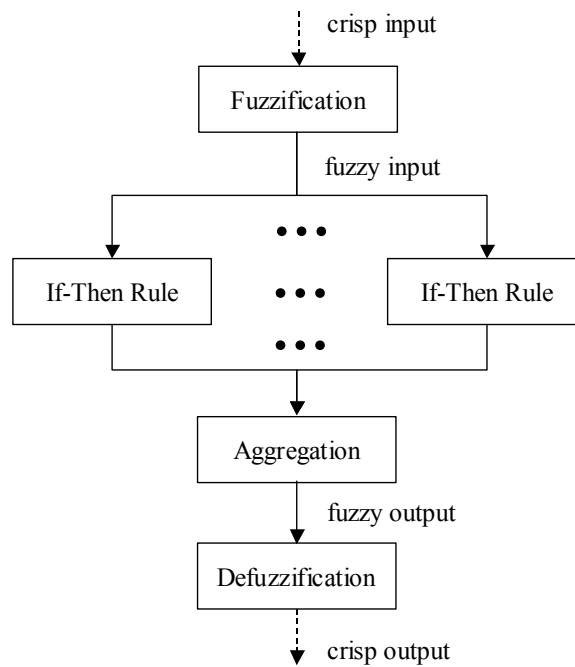


Figure 3.5: Block diagram of the fuzzy inference system

According to the implemented fuzzy implication operations, rules and their aggregation and defuzzification procedures, different types of fuzzy inference systems, such as Mamdani, Sugeno and Tsukamoto, have been employed in various applications (Jang, Sun and Mizutani, 1997). Mamdani's fuzzy inference method that is the most commonly seen fuzzy methodology has been applied in this research. The Mamdani's fuzzy inference basically uses the *max-min* fuzzy logic operator to obtain the consequent

membership functions for each rule. Figure 3.6 illustrates the graphical analysis of the Mamdani's fuzzy inference with the conjunctive aggregation strategy for the two if-then rules shown in Table 3.1. In Figure 3.6 and Table 3.1, the symbols A_{11} and A_{12} refer to the first and second fuzzy antecedents of the first rule, respectively, and the symbol B_1 refers to the fuzzy consequent of the first rule; the symbols A_{21} and A_{22} refer to the first and second fuzzy antecedents of the second rule, respectively, and the symbol B_2 refers to the fuzzy consequent of the second rule. The minimum function illustrated in Figure 3.6 arises because the antecedent pairs of the given if-then rules shown in Table 3.1 are connected by a logical AND connective. The minimum membership value for the antecedent propagates through to the consequent and the truncated membership function for the consequent of each rule is obtained. Based on the disjunctive aggregation strategy the maximum operation of the truncated membership functions for each rule is performed to generate an aggregated membership function. In summary, the aggregated output μ_B^* can be given by the following equation.

$$\mu_B^* = \max(\min(\mu_{A_{11}}(x_1^*), \mu_{A_{12}}(x_2^*)), \min(\mu_{A_{21}}(x_1^*), \mu_{A_{22}}(x_2^*))) \quad (3-26)$$

where x_1^* and x_2^* are the input values for input variables x_1 and x_2 , respectively.

Finally, a crisp value y^* for the aggregated output can be calculated using an appropriate defuzzification method.

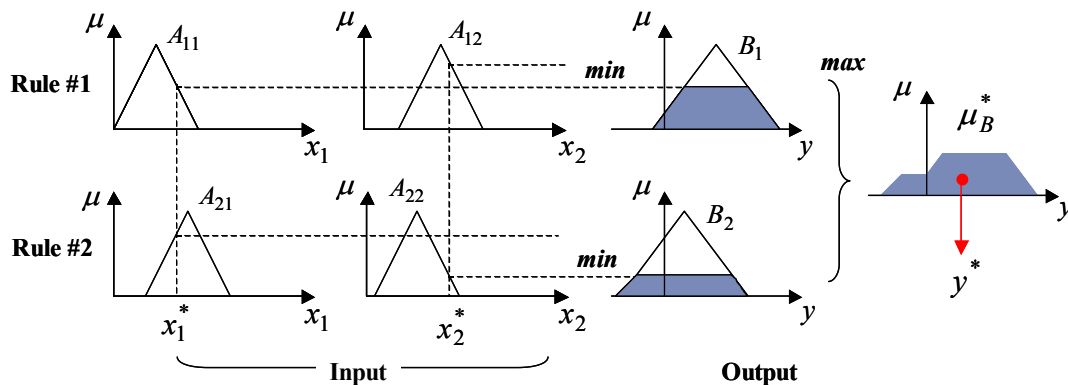


Figure 3.6: Graphical Mamdani (max-min) inference method

Table 3.1: Two if-then rules

Rule #1:	If x_1 is A_{11} and x_2 is A_{12} then y is B_1
Rule #2:	If x_1 is A_{21} and x_2 is A_{22} then y is B_2

3.3 Neural Networks

A neural network is a machine designed to mimic human brain mechanisms to simulate intelligent behavior. It resembles the brain in two respects: knowledge is acquired by the network from its environment through a learning process; interneuron connection strengths, known as synaptic weights, are used to store the acquired knowledge (Aleksander and Morton, 1990). With massively parallel distributed structures and learning and generalization abilities, a neural network is a powerful information processor for solving complex problems that are difficult for conventional model-based approaches. Neural networks have been successfully applied in various fields of application including pattern recognition, nonlinear functional mapping, classification, speech, vision and control systems (Mendel and McLaren, 1970; Barto et al., 1983). In this dissertation neural networks have been applied for a nonlinear input-output mapping between the compass heading and the true heading and sequentially used for compass calibration. This section describes the fundamentals of neural networks and the multilayer feedforward neural networks that are used for the input-output mapping.

3.3.1 Fundamentals of Neural Networks

3.3.1.1 Models of A Neuron

A neuron is an information-processing unit for basic operations of a neural network. Shown in Figure 3.7 is the model of a neuron which contains three basic elements (Haykin, 1999):

1. Synapses: Each of synapses characterized by a weight of its own is used for weighting the input signal. A signal x_i at the input of synapse i connected to neuron

j is multiplied by the synaptic weight w_{ji} . The synaptic weight could be a positive or negative value.

2. An adder: It is used for summing the weighted input signals as a linear combiner. As shown in Figure 3.7, the neuronal model also includes an externally applied bias, denoted by b_j . The bias is used to increase or lower the input of the activation function. Accounting for the bias effect by adding a new synapse with input as $x_0 = 1$ and weight as $w_{j0} = b_j$, we can formulate the adder operation as the following equation.

$$v_j = \sum_{i=0}^m w_{ji} x_i \quad (3-27)$$

where m indicates the total number of input signal and v_j is the aggregation of the weighted inputs for neuron j , also called the local field.

3. An activation function: The activation function performs a transformation to limit the permissible amplitude range of the output signal to some finite value. Typically, the normalized amplitude of the output of a neuron is in the range of $[0,1]$ (binary) or $[-1,1]$ (bipolar). The transformation is expressed by the following equation.

$$y_j = \varphi(v_j) \quad (3-28)$$

where y_j is the output of the neuron j .

The activation function can be linear or nonlinear. Different types of activation functions, such as threshold function, piecewise-linear function and sigmoid function, can be used according to applications. In general, nonlinear activation function is recommended to enhance the network capability of function approximation and noise-immunity (Ham and Kostanic, 2001).

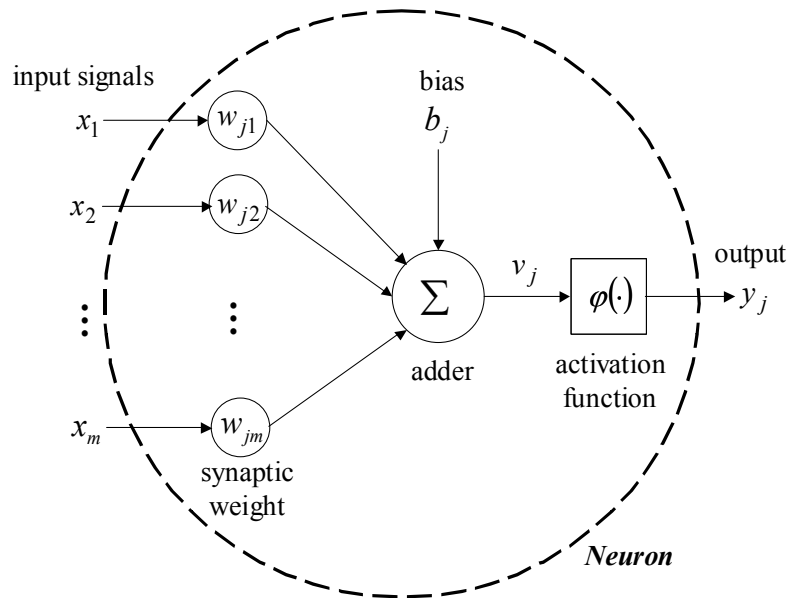


Figure 3.7: Nonlinear model of a neuron

In summary, the input-output relationship of a neuron can be described as follows:

$$y_j = \varphi \left(\sum_{i=0}^m w_{ji} x_i \right) \quad (3-29)$$

3.3.1.2 Network Architecture

To comprise neural networks, neurons are organized in the form of layers with inter-layer or/and intra-layer connections. According to the manner in which the neurons of a neural network are structured, three fundamentally different network architectures can be classified (Haykin, 1999):

1. **Single-Layer Feedforward Networks (SFNs):** SFNs have an input layer and an output layer without intra-layer connection as shown in Figure 3.8. The nodes in the input layer accept the input signals and distribute them to the neurons in the output layer where the information processing shown in Figure 3.7 is performed.

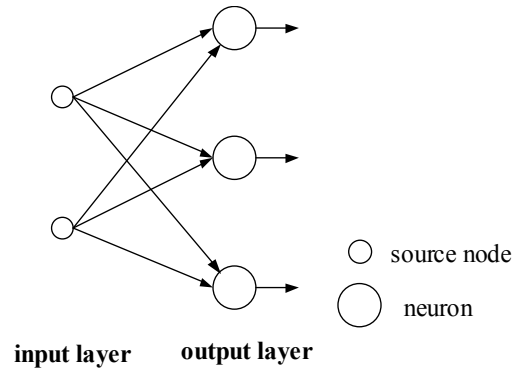


Figure 3.8: Single-layer feedforward networks

2. Multi-Layer Feedforward Networks (MFNs): In contrast to SFNs, MFNs have one or more hidden layers besides an input layer and an output layer. The function of neurons in the hidden layers is to intervene between the external input and the network output to enable the network to extract higher-order statistics. Shown in Figure 3.9 are the fully connected feedforward MFNs as every node in each layer of the network is connected to every other node in the adjacent forward layer. The network is called partially connected if some of the links are missing from the network.

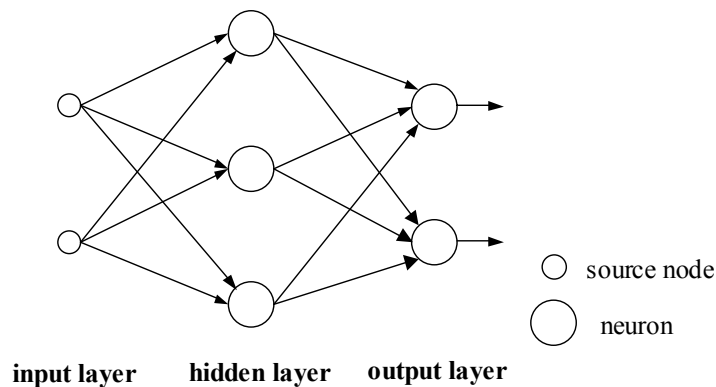


Figure 3.9: Multi-layer feedforward networks

3. Recurrent Networks (RNs): RNs differ from a feedforward neural network in that it has at least one feedback loop. The presence of feedback loops affects the learning capability of the network and its performance. RNs may be implemented differently

according to the number of layers and the type of feedback loops such as self-feedback, inter-layer feedback or intra-layer feedback loop.

3.3.1.3 Learning Processes

After the network is structured, a learning process is applied to adapt the neural network to the environments through adjusting the free parameters of the network such as synaptic weight and bias. The type of learning is determined by the manner in which the parameter changes take place (Mendel and McLaren, 1970). The common learning algorithms are categorized into two learning paradigms as follows (Haykin 1999):

1. Learning with a teacher: In this learning paradigm, a neural network is trained or adjusted by a teacher having knowledge of the environment, with that knowledge being represented by a set of input-output examples. When the teacher and the neural network are both exposed to a training example drawn from the environment, the teacher is able to provide the neural network with a desired response that represents the optimum action to be performed by the neural network for that training example. Then the network parameters are adjusted according to the combined influence of the training example and the difference between the desired response and the actual response of the network, also called error signal. This adjustment is carried out iteratively until the neural network optimally emulates the teacher in some statistical sense. This kind of learning paradigm is also referred to as supervised learning.
2. Learning without a teacher: In this learning paradigm, there is no teacher to oversee the learning process. The learning process is basically performed through continued interaction with the environment. Two types of learning structures can be implemented.
 - (a). Reinforcement learning: Instead of under the tutelage of a teacher, the reinforcement learning system is built around a critic that converts a primary reinforcement signal received from the environment into a high quality

reinforcement signal called the heuristic reinforcement signal (Barto et al., 1983). The network parameters are adjusted under observing this heuristic reinforcement signal. The goal of learning is to minimize a cost-to-go function, which is the expectation of the cumulative cost of actions taken over a sequence of steps (Haykin, 1999).

- (b). Self-organized learning: Without an external teacher or critic to oversee the learning process, the self-organized learning process is performed through observing a task-independent measure of the quality of representation that the network is required to learn. Once the network has become tuned to the statistical regularities of the input patterns, it is capable of forming internal representations to encode features of the input in a more explicit or simple form (Becker, 1991). The self-organized learning is also referred to as unsupervised learning.

3.3.1.4 Benefits of Neural Networks

A neural network is a massively parallel distributed processor that has ability to learn about its environment. It can be used for solving complex problems that are intractable to model-based approaches. The use of neural networks provides many useful properties and capabilities. Some of the neural network benefits are described as follows (Haykin 1999):

1. Nonparametric statistical inference: Neural networks can provide a model-free input-output nonlinear mapping that doesn't require prior statistical model for the input data.
2. Generalization: Neural networks can produce reasonable outputs for inputs not encountered during training (learning).

3. Nonstationary environment operation: Neural networks that have been trained to operate in a specific environment can be retrained to deal with minor changes in the operating environmental conditions.

3.3.2 Multilayer Feedforward Neural Networks

As mentioned previously, a multilayer feedforward neural network (MFNN) contains one or more hidden layer and the neuron in the network has the nonlinear activation function inside and high degree of connectivity. The combination of these characteristics together with the ability to learn from experience through supervised training makes the MFNN capable of performing a nonlinear mapping between many inputs and outputs. The most popular learning algorithm for MFNNs is the error back-propagation algorithm developed by Rumelhart et al. (1986). The back-propagation is a gradient decent algorithm in which the network parameters are moved along the negative of the gradient of the performance function. This algorithm consists of two passes through different layers of the network: a forward pass and a backward pass. In the forward pass, the synaptic weights of the network are all fixed and a set of outputs is produced forward through the network as the actual response of the network. During the backward pass, the synaptic weights of the network are all adjusted backward through the network in accordance with an error-correction rule seeking a direction for weight change that reduces the value of the cost function.

The training of the network is repeated for many examples in a training set until the networks reach a steady state so that a proper input-output mapping is constructed. For a given training set, the back-propagation learning may proceed in one of two basic ways: sequential training or batch training. In the sequential mode, weight updating is performed immediately after the presentation of each training example and continued until the last training example. In the batch mode, the weights of the network are updated only after the entire training set has been applied to the network. The advantages of the sequential training over the batch training are the better efficiency for on-line operation and resistance to convergence of learning to a local minimum. In contrast, the batch

training provides an accurate estimate of the gradient vector for better convergence of the learning algorithm. The relative effectiveness of the two training modes depends in the problem at hand. In general, the sequential mode of the back-propagation learning is highly popular because of its simplicity for implementation and effectiveness for solving large and difficult problem.

The signal flow of back-propagation learning applied to a multilayer feedforward neural network is shown in Figure 3.10. The forward and backward computations of sequential training processes are summarized in the following.

1. Forward computation: In the forward computation the synaptic weights remain unchanged and the signals are processed forward through the network, layer by layer, to consequently compute the actual response of the network. In the presence of a training sample in the epoch denoted by $(\mathbf{x}(n), \mathbf{d}(n))$ ($\mathbf{x}(n)$ is the input vector and $\mathbf{d}(n)$ is the desired response vector), the forward-proceeded local field $v_j^{(l)}(n)$ for neuron j in layer l is computed as follows:

$$v_j^{(l)}(n) = \sum_{i=0}^{m_{l-1}} w_{ji}^{(l)}(n) y_i^{(l-1)}(n) \quad (3-30)$$

where $y_i^{(l-1)}(n)$ is the output of neuron i in the previous layer $l-1$ at iteration n and $w_{ji}^{(l)}(n)$ is the synaptic weight of neuron j on layer l that is fed from neuron i in layer $l-1$. m_{l-1} is the total number of neuron in the previous layer $l-1$.

The output of neuron j in layer l is obtained from the transformation of the local field using the activation function $\varphi_j(\cdot)$ as follows:

$$y_j^{(l)}(n) = \varphi_j(v_j^{(l)}(n)) \quad (3-31)$$

For the input layer (i.e., $l = 0$), $y_j^{(0)}(n)$ is equal to $x_j(n)$, which is the j th element of the input vector $\mathbf{x}(n)$. For the neuron in the output layer (i.e., $l = L$, where L is the depth of the network), $y_j^{(L)}(n)$ is equal to $o_j(n)$, which is the j th element of the actual response vector $\mathbf{o}(n)$ of the network.

The error signal at the output of neuron j at iteration n is defined by:

$$e_j(n) = d_j(n) - o_j(n) \quad (3-32)$$

where $d_j(n)$ is the j th element of the desired response vector $\mathbf{d}(n)$.

The cost function $E(n)$ as a measure of learning performance is defined as the sum of the squares of the error signals for all the output neurons.

$$E(n) = \frac{1}{2} \sum_{j \in C} e_j^2(n) \quad (3-33)$$

where the set C includes all the neurons in the output layer of the network.

For the batch training in which the weights are updated on a pattern-by-pattern basis until one epoch, the cost function is obtained by summing $E(n)$ over all n and then normalizing with respect to the set size N , as shown by:

$$E_{av} = \frac{1}{N} \sum_{n=1}^N E(n) \quad (3-34)$$

where E_{av} is also called the average squared error energy.

2. Backward computation: In the backward computation the synaptic weights of the network are all adjusted backward through the network. The adjustment of the synaptic weights is performed in the following linear form.

$$w_{ji}^{(l)}(n+1) = w_{ji}^{(l)}(n) + \Delta w_{ji}^{(l)}(n) \quad (3-35)$$

where $\Delta w_{ji}^{(l)}(n)$ is the correction of the weight that connects neuron i and j on layer l at iteration n . $w_{ji}^{(l)}(n+1)$ and $w_{ji}^{(l)}(n)$ denote the corrected and uncorrected weights, each connects neuron i and j on layer l at iteration n .

The correction of the synaptic weight is determined by minimizing the cost function with respect to the synaptic weight using the gradient decent algorithm. Thus the correction of the synaptic weight is proportional to the partial derivative $\partial E(n)/\partial w_{ji}^{(l)}(n)$ and is defined as follows:

$$\Delta w_{ji}^{(l)}(n) = -\eta \frac{\partial E(n)}{\partial w_{ji}^{(l)}(n)} \quad (3-36)$$

where the minus sign indicates the direction for weight change that reduces the value of $E(n)$ and η is the learning-rate parameter of the back-propagation algorithm.

The smaller the learning-rate parameter, the smaller the changes to the synaptic weights between each training iteration. Increasing the value of the learning-rate parameter can speed up the rate of learning but may result in an unstable network with large changes in the synaptic weights.

Since $E(n)$ is the sum of the squares of the error signals for all the output neurons, the correction of the synaptic weight is a function of all synaptic weights and activation functions. Applying the chain rule of calculus to $\partial E(n)/\partial w_{ji}^{(l)}(n)$ and including a momentum term, a general form of the correction of the synaptic weight called the generalized delta rule is obtained as follows:

$$\Delta w_{ji}^{(l)}(n) = \alpha [\Delta w_{ji}^{(l)}(n-1)] + \eta \delta_j^{(l)}(n) y_i^{(l-1)}(n) \quad (3-37)$$

where α is usually a positive number called the momentum constant which is used for increasing the rate of learning yet avoiding the danger of instability. $y_i^{(l-1)}(n)$ is the output of neuron i in the previous layer $l-1$ at iteration n and $\delta_j^{(l)}(n)$ is the local gradient defined by $\delta_j^{(l)}(n) = -\partial E(n) / \partial v_j^{(l)}(n)$.

The local gradient is computed backward through the network and thus the correction of the synaptic weight is also proceeded backward through the network, layer by layer. The back-propagation formula of the local gradient in the output and hidden layer is described in Eq. (3-38). Details of the derivation of Eq. (3-38) are available in Rumelhart et al. (1986) or Haykin (1999).

$$\delta_j^{(l)}(n) = \begin{cases} e_j^{(L)}(n) \varphi_j'(v_j^{(L)}(n)) & \text{for neuron } j \text{ in output layer } L \\ \varphi_j'(v_j^{(l)}(n)) \sum_{k=0}^{m_{l+1}} \delta_k^{(l+1)}(n) w_{kj}^{(l+1)}(n) & \text{for neuron } j \text{ in hidden layer } l \end{cases} \quad (3-38)$$

where the prime in $\varphi_j'(\cdot)$ denotes differentiation with respect to the argument and m_{l+1} is the total number of neuron in the next layer $l+1$.

In summary, the back-propagation training algorithm starts with the forward pass in which the neuron outputs are computed forward through the network based on Eq. (3-30) and Eq. (3-31) and finally the error signals of the neurons in the output layer are obtained by Eq.(3-32). Then the backward pass starts at the output layer by passing the error signals backward through the network and recursively computing the local gradient for each neuron based on Eq. (3-38). Moving along the negative of the local gradient, the synaptic weights are corrected backward through the network, layer by layer, based on Eq. (3-35) and Eq. (3-37). The forward and backward computations are iterated with the presentation of new epochs of training examples to the network until the stopping criterion is met. The stopping criterion could be: The Euclidean norm of the gradient vector reaches a sufficiently small gradient threshold; the absolute rate of change in the

average squared error per epoch is sufficiently small; the weight updates are sufficiently small; or simply the number of iterations reaches to a predetermined value.

It should be noted that the MFNN should be well designed to ensure that reasonable outputs can be obtained even when inputs are not encountered during training. The factors affecting the performance of the input-output mapping include the number of the hidden neurons and the size of the training set. Basically, they are designed according to the physical complexity of the problem at hand and mostly decided empirically. More details about the design of the MFNN are available in Hush and Horne (1993).

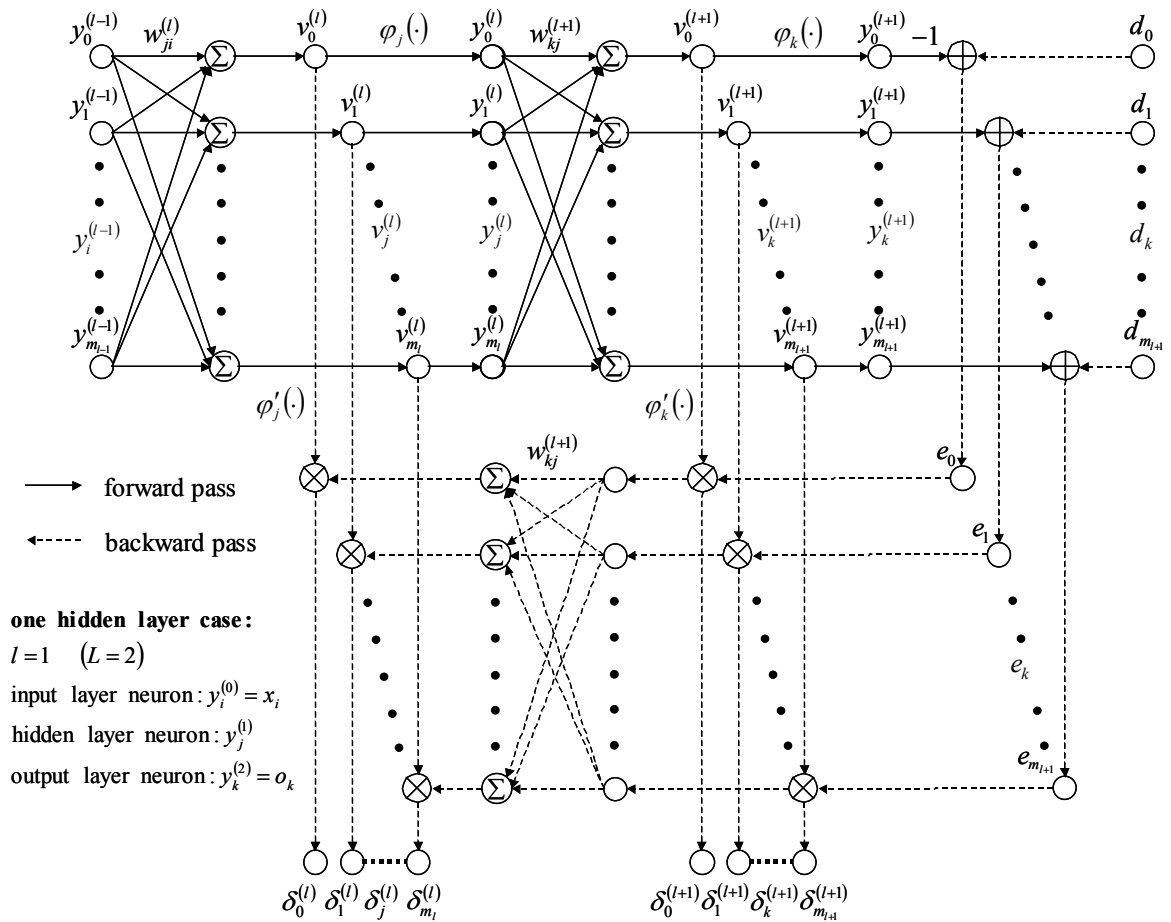


Figure 3.10: Signal flow of the back-propagation learning applied to a multilayer feedforward neural network

Chapter 4

Development of AI-Based Methods for Integration Enhancement

Chapter 3 has described the fundamentals of the model-based Kalman filter and the model-free AI methodologies. For low-cost MEMS INS/GPS integration, the Kalman filter will suffer significant performance degradation from the use of poor quality measurements because of its model dependency. In contrast, capable of handling imprecise and ambiguous information, AI methods are considered particularly suitable for dealing with low quality data since they are model-free. Using human-like reasoning and intelligence, AI methods can provide knowledge-based information to improve the adaptability and robustness of the low-cost integration system. This chapter first gives a comprehensive analysis of the limitation of the Kalman filter applied to the processing and fusion of low quality data, followed by the motivation of applying AI methods for integration enhancement. Finally, the design and development of AI-based methods, including a fuzzy logic rule-based GPS data classification system, a dynamics knowledge aided inertial navigation algorithm, and a neural networks compass calibration algorithm, are presented.

4.1 Limitation of MEMS INS/GPS Integration Using Kalman Filter

As described in Chapter 3, the Kalman filter in a loosely coupled INS/GPS integration system is applied to estimate INS navigation and sensor errors using GPS velocities and positions. It will rely on the last estimates and error dynamics models to predict navigation errors during GPS outages. Therefore, the system performance is mainly determined by the Kalman filter estimation and prediction accuracy. The Kalman filter estimation accuracy depends on the fidelity of the system and measurement models as

well as the noise statistics (Gelb, 1974). In a low-cost MEMS INS/GPS integration system, however, the quality of inertial data are poor which have large bias variation, high noise level, and large random error due to flicker noise, random walk etc. In this case, sensor errors are very difficult to realistically model using stochastic processes, thus the imperfect modelling resulted from mis-modelling, non-modelling and non-white properties of input data is obvious. In addition, when navigation systems operate in GPS challenging environments such as urban canyons, GPS solutions are characterized by large noises and multipath errors and GPS accuracy is more difficult to assess properly. As a result of using inaccurate dynamics and statistical models, the Kalman filter will suffer degraded estimation accuracy and even divergence problems for low-cost MEMS INS/GPS integration.

Similarly, the Kalman filter prediction performance is strongly associated with the quality of inertial sensors. The Kalman filter prediction accuracy is mainly defined by the accuracy of the system model (input noise) and the accuracy of the last estimate in filtering mode (Salychev, 1998). As stated previously, for low-cost MEMS INS/GPS integration the Kalman filter has degraded estimation performance in filtering mode. Moreover, in the presence of high input noise and large non-modelling sensor errors due to bias variations and random errors, it is difficult to accurately predict INS sensor errors using the Kalman filter. After time integration of the IMU measurements, the unidentified sensor errors will result in a rapid error growth in velocity and position during GPS outages. This is the major challenge to the integration of low-cost MEMS inertial sensors with GPS using the Kalman filter.

Since the traditional Kalman filter methodology was found insufficient for low-cost MEMS INS/GPS integration, the enhanced data fusion and data processing methods are needed in order to obtain satisfactory integration performance. In reasoning about a system, the precision inherent in our models of the system depends on the degree of complexity (uncertainty) of the system and the understanding about the problem (precision of measurement) (Ross, 1995). For the complex systems with only ambiguous or imprecise information available, the AI-based methods provide a nonlinear, adaptive,

and knowledge-based approach to understand the system's behaviour by using human reasoning and intelligence. AI technologies including expert systems, fuzzy logic and neural networks have found successful applications in a wide variety of fields, such as nonlinear mapping, data classification, and decision analysis (Kandel, 1992; Jang et al., 1997; Haykin, 1999). AI methods can be seen as the advanced versions of the estimation, classification and inference methods (Luo et al., 2002). As mentioned previously, the major limitation of using the model-based Kalman filter for low-cost MEMS INS/GPS integration is its significant performance degradation in the presence of low quality INS data and corrupted GPS data. If a magnetic compass, commonly embodied in a low-cost MEMS IMU, is used to provide external heading information, the compass data, likely to be disturbed and biased in vehicular environments, are also difficult to calibrate using model-based estimation methods such as the Kalman filter.

Thus, with the advantages of processing ambiguous or imprecise data and the capabilities of formulating human intelligence, AI methods have been applied in this dissertation to enhance the Kalman filter-based data fusion performance by adding functionalities of data quality assessment, navigation error compensation, sensor error modelling, and fusion scheme optimization. Linked to human reasoning and concept formation, fuzzy logic and expert systems have been implemented for GPS data classification and vehicle dynamics identification so that GPS solutions can be more properly weighted in various GPS environments and INS errors can be more effectively controlled with the aiding from dynamics knowledge. In addition, neural networks with learning and adaptation capabilities have been applied for compass error modeling and calibration so that compass biases and scale factor errors can be correctly removed even in strong disturbance environments. The rest of this chapter will present the design and development of these AI-based methods for integration enhancement.

4.2 Fuzzy Logic Rule-Based GPS Data Classification

As mentioned in Chapter 2, GPS is a satellite-based radio navigation system, which uses line-of-sight ranges between the navigation satellites and receivers to derive positioning

solutions. GPS signals therefore are subject to severe degradation in the presence of multipath, diffraction, attenuation or blockage. GPS positioning solutions in this case would have degraded accuracy and should be identified before they are used for navigation or integrated with other sensors such as INS. Traditionally, the receiver autonomous integrity monitoring (RAIM) method, which is based on self-consistency check among the available measurements, has been applied for fault detection and exclusion (FDE) in GPS data (Lee, 1986; Parkinson and Axelrad, 1988; Parkinson and Spilker, 1996). In GPS unfavourable environments, however, RAIM methods were found limited due to the violation of normally distributed zero-mean measurement errors, multiple blunders and the lack of redundancy (Collin et al., 2003; Kuusniemi, 2004).

For land vehicle applications low-cost GPS or HSGPS receivers are typically used with the code or pseudorange measurement as the principal observable for position determination. Code-based GPS position errors are determined by satellite geometry and pseudorange measurement errors. The user-to-satellite pseudorange measurement errors are transferred into position errors in local navigation frame according to the satellite geometry strength. The pseudorange measurements contain errors of satellite orbit and clock, atmosphere, multipath, receiver clock offset and measurement noise (Parkinson and Spilker, 1996 and Misra and Enge, 2001). In signal-degraded environments, the major pseudorange errors are due to multipath and other signal deteriorations such as diffraction and attenuation especially for HSGPS receivers. In various signal-degraded environments such as urban and suburban areas, therefore, it is possible to assess GPS performance by monitoring GPS signal quality and satellite geometry strength.

Previous researches have applied fuzzy logic or neuro-fuzzy soft computing to derive a quality indicator for GPS code based positioning solutions using the carrier-to-noise density ratio (C/N_0) and the Dilution of Precision (DOP) number (Lin et al., 1996; Ghalehnoe et al., 2002 and Wang and Gao, 2003a). But the resultant performance was still limited because the simple use of C/N_0 is not sufficient to reliably assess the pseudorange errors. Wang and Gao (2004d) have applied a fuzzy inference system to classify GPS position solutions using the DOP number and the fading C/N_0 value which

is the difference between the measured and expected C/N0. When a HSGPS receiver is used, however, the DOP number becomes less sensitive to the degree of signal degradation since weak and low-power signals can be acquired and tracked with higher satellite availability. Wang and Gao (2006) have further applied the receiver-satellite geometry matrix, namely in Eq. (2-4), to assess the effects of an individual satellite's measurement errors on the position solutions instead of using a single DOP number which is a geometric strength measure for all observed satellites. This modified system has shown improved classification performance and is suitable for both non-high sensitivity (conventional) and high sensitivity GPS data classification. The design and development of this system is described in the following sections.

4.2.1 GPS Signal Quality Measures

Carrier-to-noise density ratio (C/N0) is the most commonly used measure of the GPS signal quality. C/N0 is an instantaneous measure of the ratio of carrier present to noise per Hertz of bandwidth (dB-W/Hz) and can be computed as follows (Lachapelle, 2002):

$$C/N0 = S_R + G_a - 10\log(K_B T_0) - NF \quad (4-1)$$

where S_R is the received signal power;
 G_a is the antenna gain;
 $10\log(K_B T_0)$ is the ambient noise density; and
 NF is the receiver noise figure

C/N0 value depends upon the received signal strength, receiver antenna gain and the correlation process used by the receiver. Thus, for a given combination of a GPS antenna and receiver, C/N0 represents the received signal strength, i.e., the signal quality present at the input to a GPS receiver. The GPS signal power broadcast at the satellite is attenuated due mostly to the loss of propagation from the satellites to the receivers. The propagation loss is mainly dependent on the length of the path and the attenuation effects on the path, such as atmospheric attenuation, depolarization, shadowing by an object or

constructive and destructive interference by multipath. In an open-sky environment, the received signal strength is mainly dependent on the atmospheric attenuation and depolarization loss which are normally proportional to the length of the propagation path. Thus, in this case the received signal from the lower-elevation satellite usually has lower power than the signal from the higher-elevation satellite. In a signal-degraded environment, the received signal strength is relative to not only satellite elevation but also environmental attenuation conditions. Thus, the C/N_0 measured in open-sky environments can be used to represent the strength of the clear signal, called expected C/N_0 . The difference between the measured and the expected C/N_0 , called fading C/N_0 , therefore has a certain correlation to the strength of signal degradation (Brunner et al., 1999; Wieser and Brunner, 2000).

As mentioned previously, the strength of the received signal is changing with satellite elevation, thus the expected C/N_0 is a function of satellite elevation. To establish the C/N_0 scatter describing how the expected C/N_0 changes with satellite elevation and to study the signal degradation effects on C/N_0 , several static tests using a SiRF Star II Xtrac high sensitivity GPS receiver and a conventional SiRF Star II GPS receiver were performed in open-sky and various signal-degraded environments. The specifications of the SiRF Star II GPS receiver can be found in Table 6.1 of Chapter 6. Figure 4.1 through Figure 4.3 show the test environments to represent typical low, medium, and high signal-degraded conditions, respectively. In each environment test we logged the satellite elevation angle and the corresponding C/N_0 data of all observed satellites for a period of about 24 hours at 1 Hz sampling rate. All of the data collected from the high sensitivity GPS receiver under open-sky (clear signal) and different signal-degraded environments (deteriorated signal) are shown in Figure 4.4 through Figure 4.6, respectively. The results of the conventional GPS receiver are shown in Figure 4.7 through Figure 4.9.



Figure 4.1: Test set-up in a low signal-degraded environment



Figure 4.2: Test set-up in a medium signal-degraded environment



Figure 4.3: Test set-up in a high signal-degraded environment

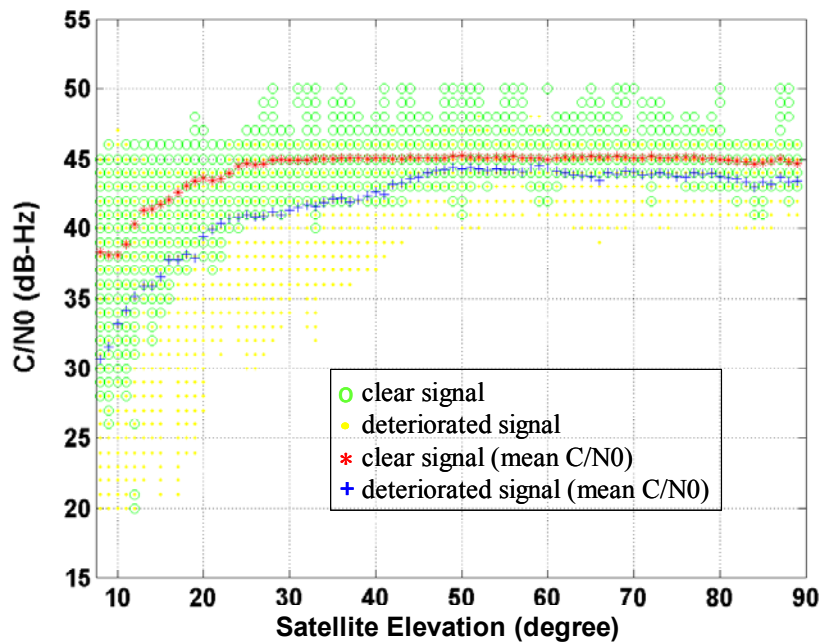


Figure 4.4: C/N_0 scatter diagram under open-sky and low signal-degraded environments (SiRF Star II Xtrac HSGPS)

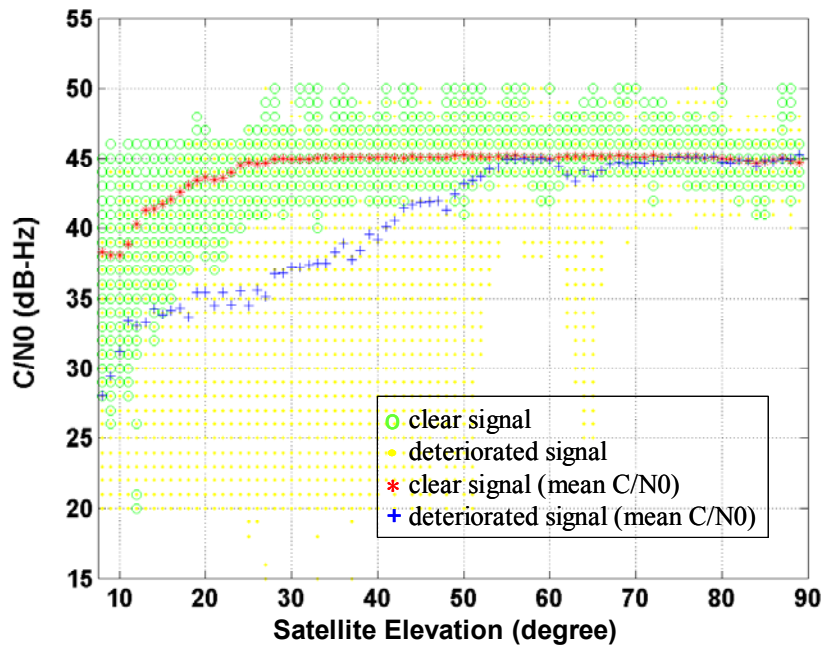


Figure 4.5: C/N0 scatter diagram under open-sky and medium signal-degraded environments (SiRF Star II Xtrac HSGPS)

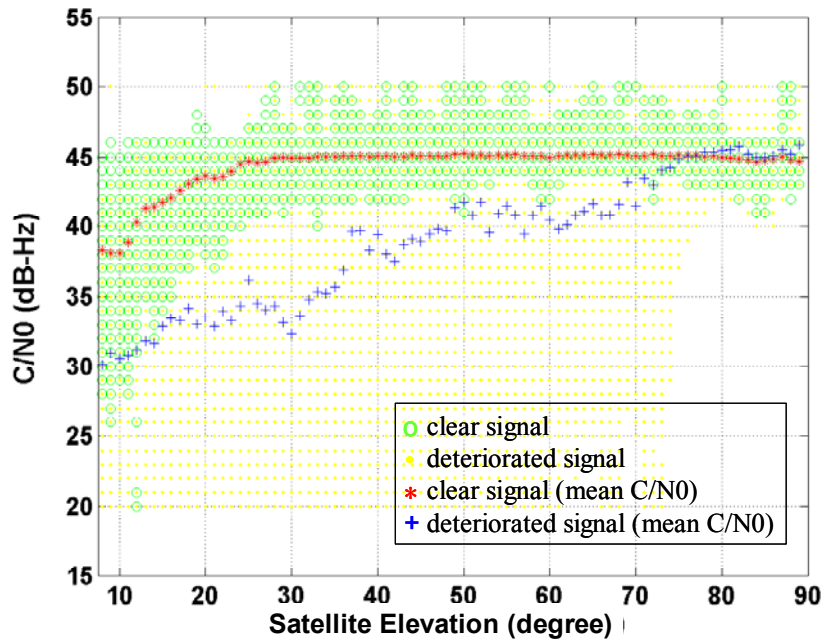


Figure 4.6: C/N0 scatter diagram under open-sky and high signal-degraded environments (SiRF Star II Xtrac HSGPS)

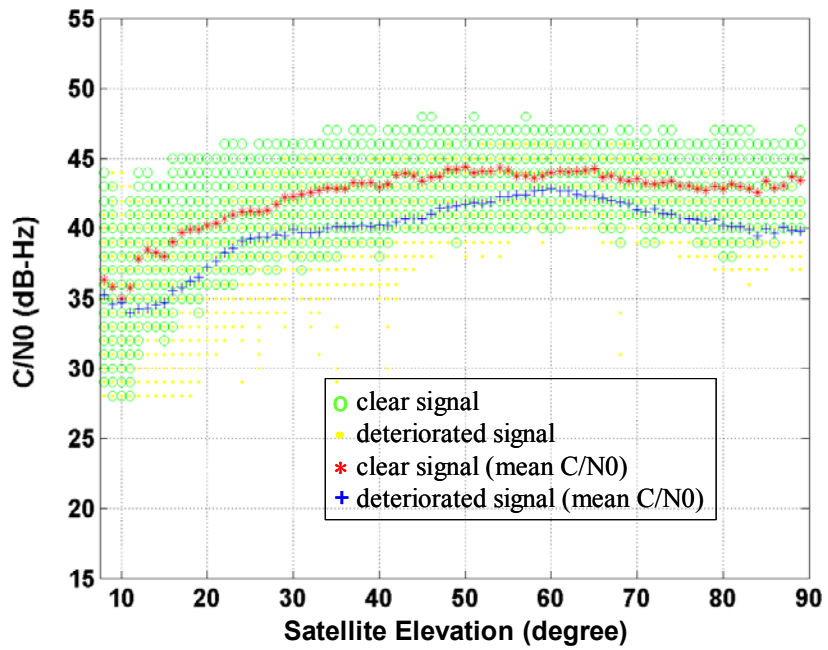


Figure 4.7: C/N0 scatter diagram under open-sky and low signal-degraded environments (SiRF Star II conventional GPS)

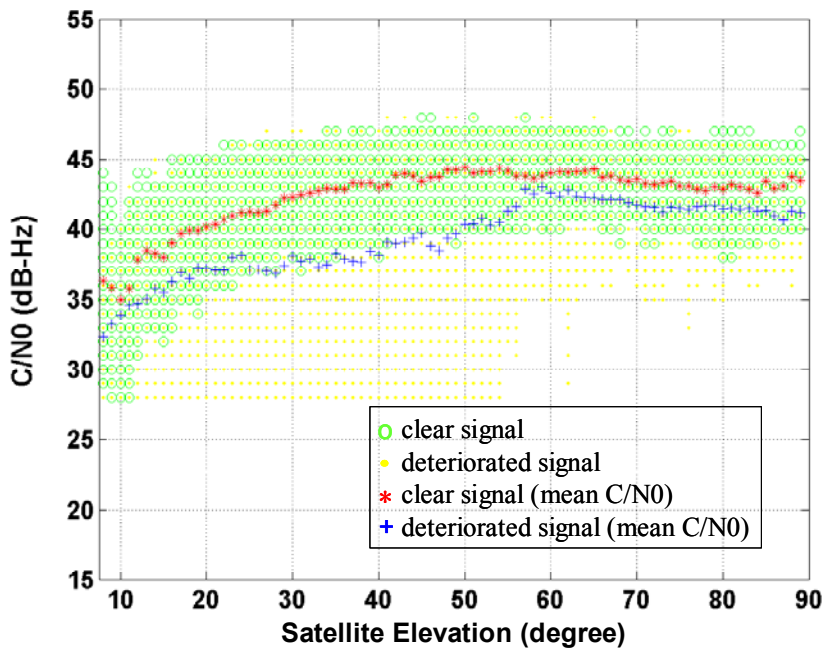


Figure 4.8: C/N0 scatter diagram under open-sky and medium signal-degraded environments (SiRF Star II conventional GPS)

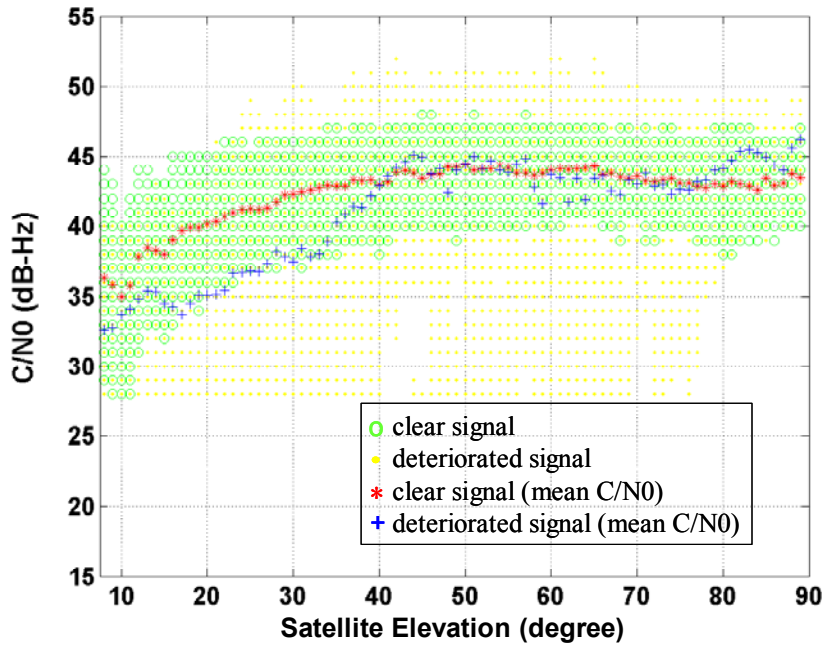


Figure 4.9: C/N0 scatter diagram under open-sky and high signal-degraded environments (SiRF Star II conventional GPS)

The results indicate that the data collected in signal-degraded environments generally have lower C/N0 than the data collected in the open-sky environment. However, it is possible to have similar C/N0 values in open-sky and signal-degraded environments, i.e., obtaining very small fading C/N0 under signal-degraded environments. There are two reasons for this occurrence. First, there is a low probability of having signal deterioration when the satellite is at high elevation and the receiver is under low and medium signal-degraded environments. In this case, the fading C/N0 correctly reflects the strength of signal degradation. Second, when the signal deteriorations are contributed by multipath, the measured C/N0 would be strengthened when the reflected signal arrives in-phase or weakened when it arrives out-of-phase (Misra and Enge, 2001). This case can be particularly found in the high signal-degraded environment tests as shown in Figure 4.6 and Figure 4.9. This is a dilemma for using fading C/N0 to indicate the magnitude of multipath errors (Wieser and Brunner, 2000). In general, signal deteriorations are the combination of multipath, diffraction, and attenuation. As indicated in Wieser and Brunner (2000), fading C/N0 is highly correlated with the degree of signal diffraction and

attenuation. Thus, fading C/N0 can still represent a certain degree of signal degradation for an individual satellite but not a one-on-one functional mapping to the pseudorange errors.

To compute the fading C/N0, the expected C/N0 scatter over satellite elevation for the selected GPS receiver and antenna should be determined first. Based on the 24-hour open-sky static test results, in this dissertation we form the expected C/N0 scatter by using the mean C/N0 at each satellite elevation angle as shown in Figure 4.4 through Figure 4.9. For the selected HSGPS receiver and antenna, we observed that the expected C/N0 scatter can be modeled using three linear reference functions shown in Figure 4.10: two constant functions and one linear ascending function. The corresponding parameters for the reference functions are listed in Table 4.1. For the conventional GPS receiver and antenna, the expected C/N0 scatter can be modeled using three linear reference functions shown in Figure 4.11: one linear ascending function, one constant functions and one linear descending function. The corresponding parameters for the reference functions are listed in Table 4.2. As expected, the profile of the expected C/N0 scatter is receivers and antennas dependent.

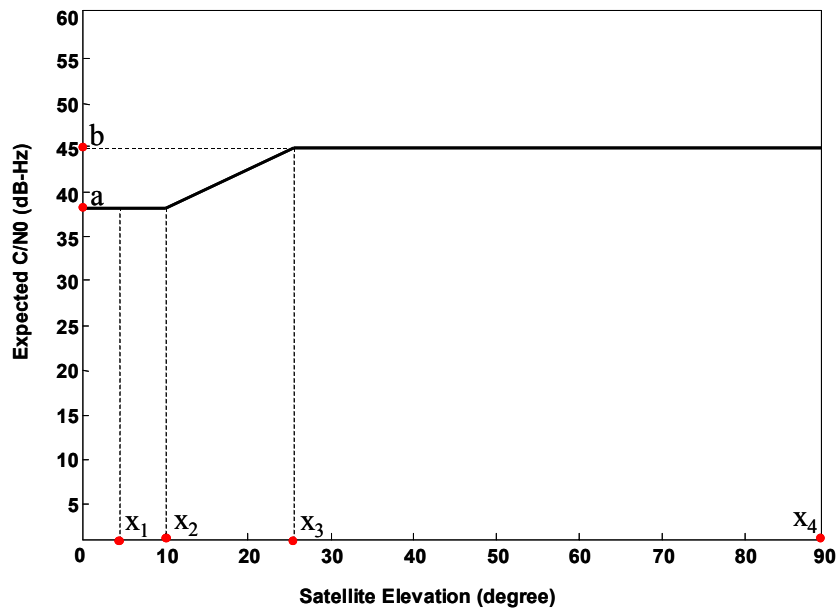


Figure 4.10: Profile of reference functions of the expected C/N0 (SiRF Star II Xtrac HSGPS)

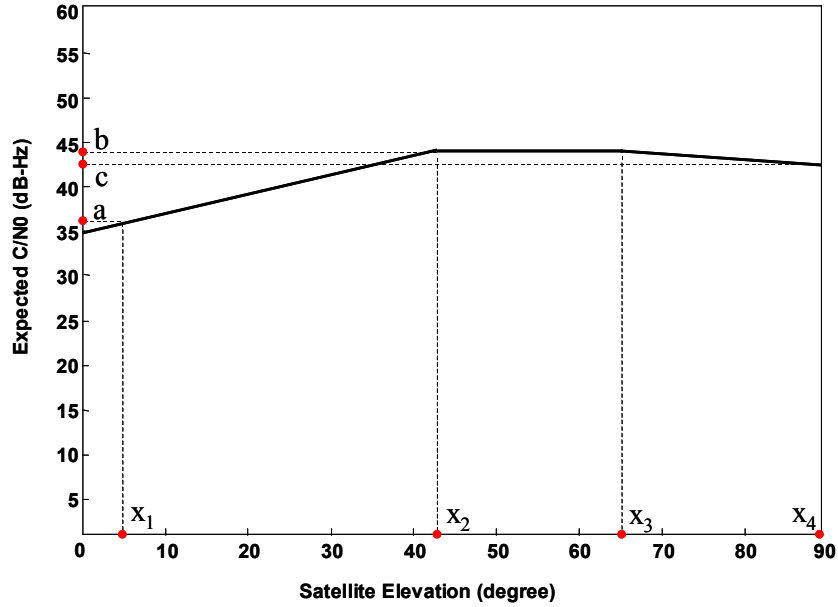


Figure 4.11: Profile of reference functions of the expected C/N0 (SiRF Star II conventional GPS)

Table 4.1: Parameters of reference functions of the expected C/N0 (SiRF Star II Xtrac HSGPS)

a (dB-Hz)	b (dB-Hz)	X ₁ (deg.)	X ₂ (deg.)	X ₃ (deg.)	X ₄ (deg.)
38	45	5	10	25	90

Table 4.2: Parameters of reference functions of the expected C/N0 (SiRF Star II conventional GPS)

a (dB-Hz)	b (dB-Hz)	c (dB-Hz)	X ₁ (deg.)	X ₂ (deg.)	X ₃ (deg.)	X ₄ (deg.)
36	44	43	5	42	65	90

4.2.2 Geo-Signal Degradation Measures

In the previous section, we have demonstrated the correlation between the fading C/N0 and the degree of signal degradation. To study the effects of signal degradation on GPS positioning solutions, the satellite geometry strength should be introduced. In this dissertation we incorporate the fading C/N0 of all observed satellites with the receiver-satellite geometry matrix to assess the effects of signal degradation in position domain, i.e., we project all user-to-satellite fading C/N0s on the local east-north-up (ENU) coordinate frame. We expected that an improved performance could be obtained

compared to using a single geometric strength measure, namely the DOP number, for all observed satellites (Wang and Gao, 2004d). Following the same model for position estimation using least-squares method (Misra and Enge, 2001), we project the user-to-satellite fading C/N0 of the observed satellites on the local ENU coordinate frame and calculate their average fading C/N0, \mathbf{F}_{ENU} , in the following manner.

$$\mathbf{F}_{\text{ENU}} = \begin{bmatrix} f_E \\ f_N \\ f_V \\ f_T \end{bmatrix} = \frac{1}{k} (\tilde{\mathbf{G}}^T \tilde{\mathbf{G}})^{-1} \tilde{\mathbf{G}}^T \begin{bmatrix} f_R^{S(1)} \\ \vdots \\ f_R^{S(k)} \end{bmatrix} \quad (4-2)$$

where k is the number of observed satellites; f_E , f_N , f_V , and f_T represent the average fading C/N0 projected to the east position, north position, vertical position, and time domain, respectively; $f_R^{S(1)}$, ..., $f_R^{S(k)}$ represent the user-to-satellite fading C/N0 of all observed satellites; $\tilde{\mathbf{G}}$ is the user-to-satellite geometry matrix in the local ENU coordinate frame as defined in Eq. (2-4):

Representing the fading C/N0 effects on the horizontal position, the average fading C/N0 in the horizontal, f_H , is chosen as the first geo-signal degradation measure and it can be obtained from the following equation:

$$f_H = \sqrt{f_E^2 + f_N^2} \quad (4-3)$$

Considering the overall signal quality of the tracked satellites, we take the number of fading satellites into account. A fading satellite is identified when the satellite's fading C/N0 is larger than a threshold value. The threshold value is determined by the quantity between the lower limit and the mean of the expected C/N0 obtained from the field tests as shown in Figure 4.4 for the high sensitivity GPS and Figure 4.7 for the conventional GPS. Then we calculate the fading satellite ratio, FR , as the second geo-signal degradation measure for the assessment of signal degradation conditions as follows:

$$FR = \frac{N_F}{N_U} \quad (4-4)$$

where N_F is the number of fading satellites; and N_U is the number of satellites used for navigation.

To test how the geo-signal degradation measures, f_H and FR , can be used to classify signal degradation conditions, the data acquired under various environment tests that already shown in the previous section were used. Figure 4.12 and Figure 4.13 show the distribution of the geo-signal degradation measures (f_H and FR) for different signal-degraded environment tests when the high sensitivity GPS and the conventional GPS are used, respectively. The black marks indicate the centre of each data set, representing the mean of the geo-signal degradation measures for the corresponding 24-hour signal-degraded environment test. As shown, for each test the geo-signal degradation measures cluster together. As expected, for both HSGPS and GPS tests, the data collected in a harsher signal-degraded condition have a larger average fading C/N0 in the horizontal and a higher fading satellite ratio. We also observed that there is an overlap of the geo-signal degradation measures between different environment tests. This is because the signal degradation condition is changing with time according to the user-to-satellite geometry relative to the around-receiver obstacles. Thus, during the 24-hour test it is possible to have similar geo-signal degradation measures under the near signal-degraded environments. Comparing the distribution of the geo-signal degradation measures between HSGPS and GPS under the same testing environment, we observed that relatively larger f_H and FR were obtained from HSGPS than GPS. This can be explained by the fact that more weak and degraded signals can be tracked by the high sensitivity GPS but not the conventional GPS. In general, the correlation between the geo-signal degradation measures and the signal-degraded conditions has been demonstrated and confirmed.

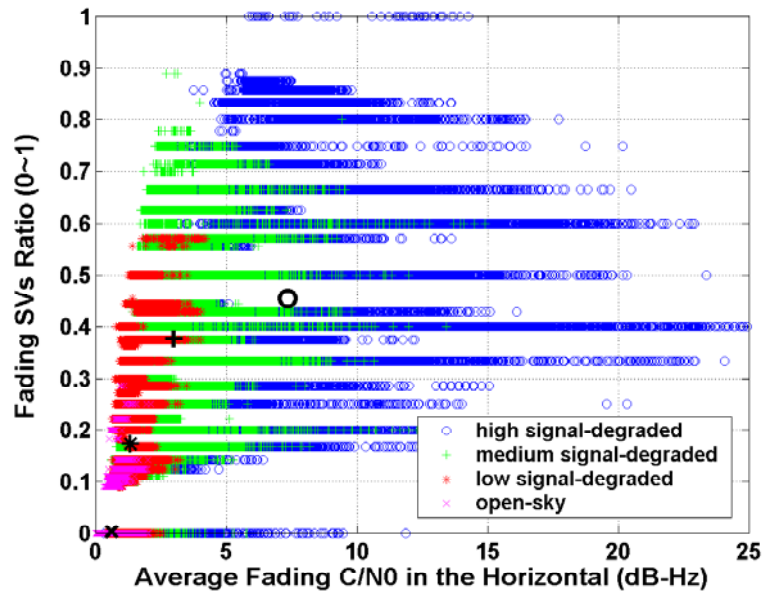


Figure 4.12: Distribution of the geo-signal degradation measures in various signal-degraded environments (SiRF Star II Xtrac HSGPS)

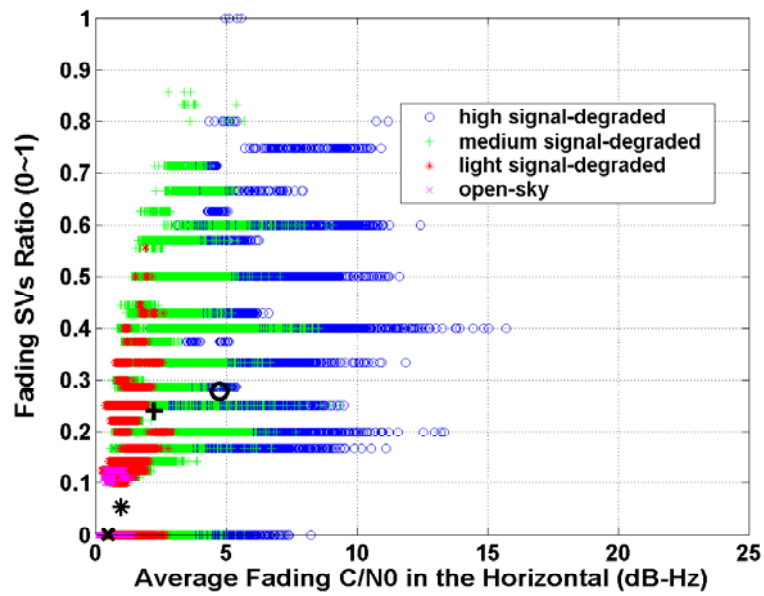


Figure 4.13: Distribution of the geo-signal degradation measures in various signal-degraded environments (SiRF Star II conventional GPS)

4.2.3 Design of Fuzzy Logic Rule-Based Data Classification System

Based on the results of various environment tests shown in Figure 4.12 and Figure 4.13, the geo-signal degradation measures can be used to classify GPS signal degradation conditions which highly affect the accuracy of GPS position. Thus, the geo-signal degradation measures can be used for GPS data classification. The common data classification method uses the similarity or distance measures between pairs of feature vectors in the feature space to partition the data into classes. In our application there is an overlap of the input feature vectors between different classes. In addition, as mentioned previously, there is a dilemma of using fading C/N0 to indicate the magnitude of multipath errors. Thus, the input data contain ambiguous and imprecise terms that have limited the applicability of the crisp or hard data classification method. As proposed by Zadeh in 1965, a fuzzy set that is a class of object with a continuum of grades of a membership provides a way to deal with imprecisely defined classes. Thus, the theory of fuzzy sets is used in our data classification system to deal with imprecise input data and to overcome the intrinsic limitations of crisp partitions.

As shown in Figure 4.12 and Figure 4.13, it is quite obvious that the larger the geo-signal degradation measures, the severer the signal degradation conditions. Thus, data classification can be accomplished by common sense reasoning. To perform the reasoning process of fuzzy or soft data classification, a fuzzy inference system that incorporates fuzzy sets theory, fuzzy if-then rules with fuzzy reasoning is employed in this study. The fuzzy inference system is a popular computing framework linked to human reasoning and concept formation dealing with ambiguous and imprecise information. Shown in Figure 4.14 is the architecture of the proposed fuzzy inference system for GPS data classification. The output of the fuzzy inference system is a numeric quality rating (QR) between 0 and 1. The QR value, which describes the degree of signal plus geometry degradation, is further applied to classify GPS data. A higher rating value indicates a higher likelihood of having a poor GPS solution. Because most GPS receivers use an internal filter to smooth position solutions, GPS position performance is less sensitive to the short-term or transient changing of signal degradation. To consider this filtering effect, we use the moving average of the geo-signal degradation measures as the

system input variables so that the QR value can reflect the performance of GPS position more appropriately. The size of moving average window was chosen as eight seconds based on the smoothing feature of the GPS position obtained from the field tests.

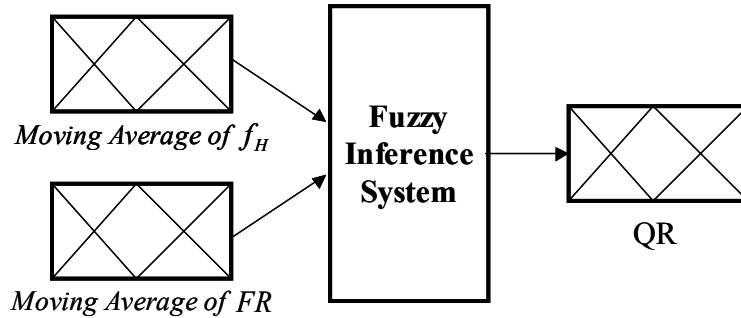
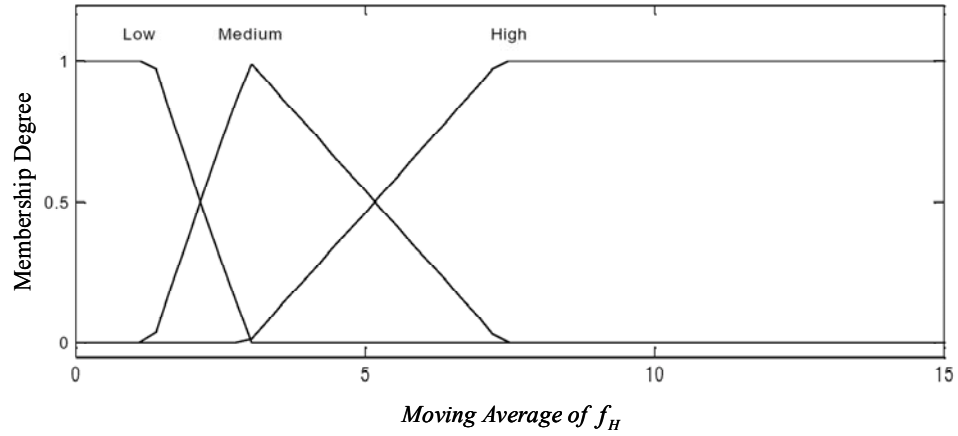
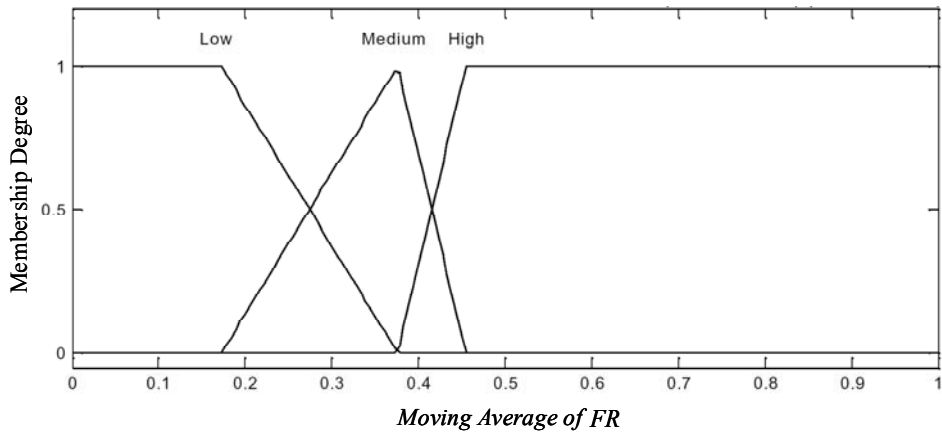


Figure 4.14: Architecture of the fuzzy logic GPS data classification system

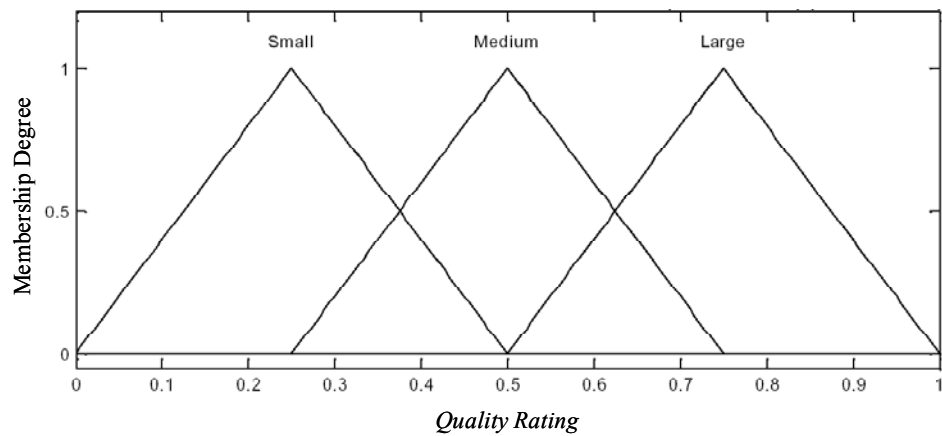
Once the system input and output variables are defined, the next step is to design the membership functions which characterize the fuzziness in a fuzzy set. The assignment of membership values or functions to fuzzy variables can be intuitive or based on some algorithm or logical operations (Ross, 1995). For the purpose of computational simplicity, the triangle membership functions are used. The parameters of input membership functions are determined based on the results of the various environment tests shown in Figure 4.12 and Figure 4.13. Three membership functions for each input variable are used and the mean of the geo-signal degradation measures under each signal degradation condition is assigned to the core value of the corresponding membership functions. These mean values are well representative of data clustering centres since they were calculated from large amount of sampling data. For the output membership functions, three triangles with even overlaps between sets and even segmentation from zero to one are used because in this study GPS data are intentionally classified into three classes. The applied membership functions of the fuzzy input and output variables for the high sensitivity GPS and the conventional GPS are illustrated in Figure 4.15 and Figure 4.16, respectively.



(a) the first input variable

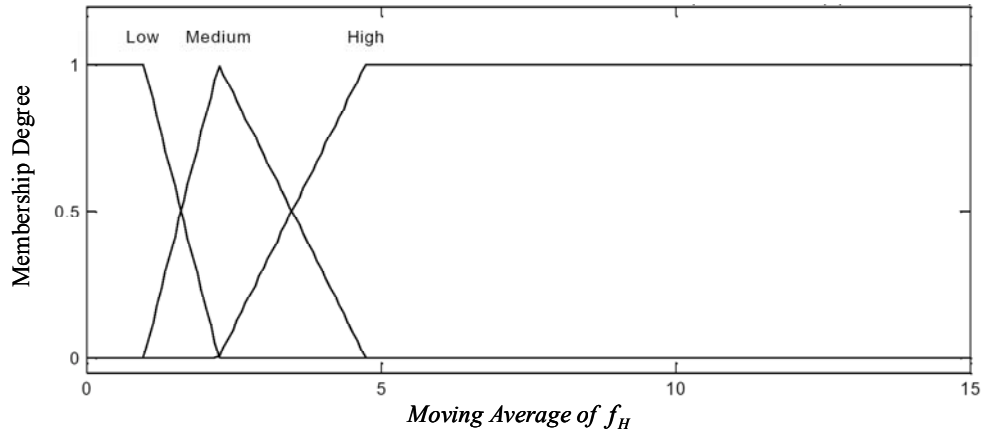


(b) the second input variable

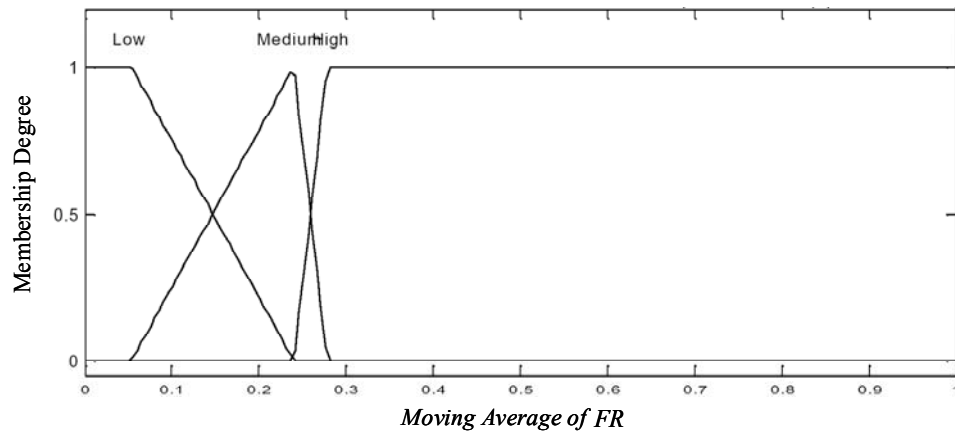


(c) the output variable

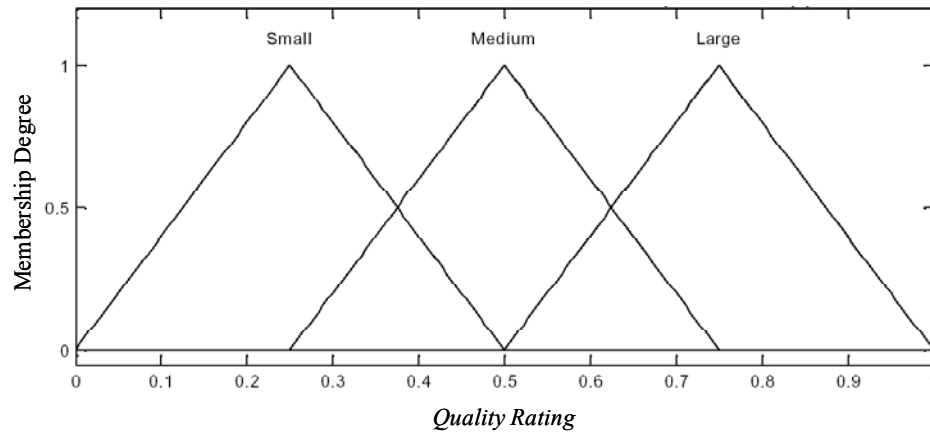
Figure 4.15: Membership functions used in the fuzzy inference system for HSGPS data classification



(a) the first input variable



(b) the second input variable



(c) the output variable

Figure 4.16: Membership functions used in the fuzzy inference system for GPS data classification

To describe the relationship between the input and the output, a set of rules is applied as shown in Table 4.3. Designed based on common sense reasoning and the field test results shown in Figure 4.12 and Figure 4.13, the rules are quite straightforward and identical for HSGPS and GPS data classification systems. For example, the GPS positioning solution would be poor (QR is large) if both the fading satellite ratio and the average fading C/N0 in the horizontal are high. After the membership functions and fuzzy if-then rules are defined, an inference procedure is applied to derive the output fuzzy set. In this dissertation, the Mamdani type fuzzy inference system with max-min composition, which is considered as the most commonly used fuzzy methodology, is used (Mamdani and Assilian, 1975). Then the centroid of area defuzzification is applied to extract a crisp value from the output fuzzy set as a representative value of the final fuzzy output. This crisp value in a range between 0.25 and 0.75 is further used for data classification. More specifically, if the value of quality rating is smaller than 3.75 (the medium between the core value of the ‘Small’ and ‘Medium’ membership functions), data are classified as low signal-degraded data. If the value of quality rating is larger than 6.25 (the medium between the core value of the ‘Medium’ and ‘Large’ membership functions), data are classified as high signal-degraded data.

Table 4.3: If-then rules used in the fuzzy inference system for GPS/HSGPS data classification

R ₁ :	If <i>Moving Average of f_H</i> is LOW and <i>Moving Average of FR</i> is LOW then QR is SMALL
R ₂ :	If <i>Moving Average of f_H</i> is LOW and <i>Moving Average of FR</i> is MED then QR is SMALL
R ₃ :	If <i>Moving Average of f_H</i> is MED and <i>Moving Average of FR</i> is LOW then QR is SMALL
R ₄ :	If <i>Moving Average of f_H</i> is MED and <i>Moving Average of FR</i> is MED then QR is MED
R ₅ :	If <i>Moving Average of f_H</i> is LOW and <i>Moving Average of FR</i> is HIGH then QR is LARGE
R ₆ :	If <i>Moving Average of f_H</i> is HIGH and <i>Moving Average of FR</i> is LOW then QR is LARGE
R ₇ :	If <i>Moving Average of f_H</i> is MED and <i>Moving Average of FR</i> is HIGH then QR is LARGE
R ₈ :	If <i>Moving Average of f_H</i> is HIGH and <i>Moving Average of FR</i> is MED then QR is LARGE
R ₉ :	If <i>Moving Average of f_H</i> is HIGH and <i>Moving Average of FR</i> is HIGH then QR is LARGE

4.3 Dynamics Knowledge Aided Inertial Navigation Algorithm

As stated previously, the major challenge to use low-cost MEMS inertial sensors for bridging GPS outages is the rapid error accumulation with the course of time. Traditionally, the Kalman filter is used to predict INS navigation errors based on the previously estimated sensor errors and the error dynamics models. When processing low quality data with high input noise and large random error, however, the conventional Kalman filter has found insufficient to provide accurate and acceptable prediction performance (Brown and Lu, 2004; Jaffe et al., 2004). Some neuro-fuzzy models and fuzzy inference systems have been proposed to predict INS drift errors and have shown their effectiveness on navigation error reduction (Chiang, 2004; El-Sheimy et al., 2004; Wang, 2004a). Their prediction performance, however, is proportional to the quality of instrument measurements and is difficult to be satisfactory when low-cost MEMS inertial sensors are used (Chiang, 2004).

Instead of predicting INS error, knowledge of vehicle dynamics could provide extra virtual measurements to correct INS navigation and sensor errors. ZUPTs have been used to provide effective INS error control when the stationary of a vehicle is available (Salychev, 1998; El-Sheimy, 2003). For automotive-grade and consumer-grade IMUs, the stationary outputs of gyroscopes themselves can be used for direct estimation of gyro biases (Sukkarieh, 2000). In addition, the nonholonomic constraints that govern the motion of a vehicle on a surface can provide velocity measurements in the transverse and vertical directions (Brandt and Gardner, 1998; Dissanayake et al., 2001; Shin, 2001). The complementary motion detection characteristics of accelerometers and gyroscopes can be applied to provide bounded tilt estimation (Collin et al., 2001; Ojeda and Borenstein, 2002; Wang and Gao, 2004c). That is, the accelerometer-derived tilt angle can be used as attitude measurements while vehicle is static or moving linearly at a constant speed. Moreover, Wang et al. (2005) have proposed to use certain vehicle dynamics such as stationary, straight-line motion, and cornering motion with its specific dynamics model to provide extra dynamics-based or dynamics-derived observations for INS error control. The following sections will describe the design and development of the overall dynamics

knowledge aided inertial navigation algorithm which includes a land vehicle motion model, vehicle dynamics-derived observations, and a fuzzy expert system for vehicle dynamics identification.

4.3.1 Land Vehicle Motion Model

Using the same idea proposed by Brandt and Gardner (1998), the first strategy of applying vehicle dynamics knowledge into inertial navigation algorithm is to incorporate the nonholonomic constraints with the INS navigation equations to derive the simplified state equations called land vehicle motion model. The derivation of the land vehicle motion model from the traditional INS navigation equations is described as below:

First, following the INS navigation equations for general three-dimensional motion described in Eq. (2-8), we further modify them by:

1. Assuming the Earth rotation is negligible and the gravity vector g is constant since the magnitude of their effects is at the sensor noise level for automotive-grade MEMS IMUs (Dissanayake et al., 2001).
2. Using the north-east-down (NED) coordinate system to express the navigation frame.
3. Using Euler angles to express the coordinate transformation and attitude propagation.

The INS navigation equations can now be written as:

$$\begin{bmatrix} \dot{\mathbf{P}}_N \\ \dot{\mathbf{V}}_N \\ \dot{\mathbf{A}}_N \end{bmatrix} = \begin{bmatrix} \mathbf{V}_N \\ \mathbf{R}_B^N \mathbf{A}_B - \mathbf{G}_N \\ \mathbf{C}_B^N \boldsymbol{\omega}_{IB}^B \end{bmatrix} \quad (4-5)$$

where the subscript N indicates the navigation frame represented by three orthogonal axes in local north (n), east (e) and down (d) directions; The subscript B indicates the body frame represented by three orthogonal axes in the forward (x), transverse (y) and

down (z) directions of the vehicle; $\mathbf{P}_N = [P_{Nn}, P_{Ne}, P_{Nd}]^T$ is the position of the vehicle in the navigation frame; $\mathbf{V}_N = [V_{Nn}, V_{Ne}, V_{Nd}]^T$ is the velocity of the vehicle in the navigation frame; $\mathbf{\Lambda}_N = [\phi, \theta, \psi]^T$ is the attitude of the vehicle expressed by three Euler angles, roll (ϕ), pitch (θ), and yaw (ψ), which are the rotation angles about the x , y and z axes, respectively; $\mathbf{A}_B = [A_{Bx}, A_{By}, A_{Bz}]^T$ is the measured acceleration in the body frame; $\boldsymbol{\omega}_{IB}^B = [\omega_{Bx}, \omega_{By}, \omega_{Bz}]^T$ is the measured angular velocity in the body frame; $\mathbf{G}_N = [0, 0, -g]^T$ is the gravity vector in which g is the gravitational constant; \mathbf{R}_B^N is the transformation matrix from the body frame to the navigation frame expressed by Euler angles as shown in Eq. (2-9); and \mathbf{C}_B^N is the transformation matrix describing the relationship between Euler rates and gyro measurements and is expressed as follows:

$$\mathbf{C}_B^N = \begin{bmatrix} 1 & \sin \phi \tan \theta & \cos \phi \tan \theta \\ 0 & \cos \phi & -\sin \phi \\ 0 & \frac{\sin \phi}{\cos \theta} & \frac{\cos \phi}{\cos \theta} \end{bmatrix} \quad (4-6)$$

The derivation of this transformation matrix can be found in Titterton and Weston (1997).

For land vehicle navigation, the nature of the vehicle's dynamics, if known, can provide extra information as constraints to reduce the navigation errors. In normal driving condition, the vehicle doesn't slide on and jump off the ground, i.e., there is no motion along the transverse direction and the direction normal to the road surface. The constraints on the motion of the land vehicles can be defined as follows:

$$V_{By} = 0 \quad (4-7)$$

$$V_{Bz} = 0 \quad (4-8)$$

In reality, because of the presence of sideslip due to turning or vibrations, these constraints are kind of transgressed. For the low-cost MEMS IMUs which cannot measure such movements, the constraint violation is negligible.

Based on these motion constraints, we can assume that the vehicle velocity vector in the navigation frame is coincided with the forward direction of the vehicle in the body frame, called velocity frame, i.e., $\mathbf{V}_F = V_f \bar{\mathbf{B}}_x$ where V_f is the speed of the vehicle and $(\bar{\mathbf{B}}_x, \bar{\mathbf{B}}_y, \bar{\mathbf{B}}_z)$ represents the body frame unit vectors. Then, by taking the first derivative of the velocity vector, we can calculate the motion acceleration of the vehicle in the velocity frame as follows:

$$\begin{aligned}
\mathbf{A}_F &= \dot{V}_f \bar{\mathbf{B}}_x + V_f \dot{\bar{\mathbf{B}}}_x \\
&= \dot{V}_f \bar{\mathbf{B}}_x + V_f \boldsymbol{\Omega}_B \times \bar{\mathbf{B}}_x \\
&= \dot{V}_f \bar{\mathbf{B}}_x + V_f \omega_{Bz} \bar{\mathbf{B}}_y - V_f \omega_{By} \bar{\mathbf{B}}_z
\end{aligned} \tag{4-9}$$

Rewriting the second equation in Eq. (4-5) by taking a transformation from the navigation frame to the body frame, we obtain:

$$\mathbf{R}_N^B \dot{\mathbf{V}}_N = \mathbf{A}_B - \mathbf{R}_N^B \mathbf{G}_N \tag{4-10}$$

The above equation implies that the vehicle motion accelerations are given by subtracting the gravity accelerations from the accelerometer outputs in the body frame. Replacing the vehicle motion acceleration term at the left-hand side of Eq. (4-10) by Eq. (4-9), we obtain:

$$\begin{bmatrix} \dot{V}_f \\ V_f \omega_{Bz} \\ -V_f \omega_{By} \end{bmatrix} = \begin{bmatrix} A_{Bx} \\ A_{By} \\ A_{Bz} \end{bmatrix} - \begin{bmatrix} \theta_c \psi_c & \theta_c \psi_s & -\theta_s \\ -\phi_c \psi_s + \phi_s \theta_s \psi_c & \phi_c \psi_c + \phi_s \theta_s \psi_s & \phi_s \theta_c \\ \phi_s \psi_s + \phi_c \theta_s \psi_c & -\phi_s \psi_c + \phi_c \theta_s \psi_s & \phi_c \theta_c \end{bmatrix} \begin{bmatrix} 0 \\ 0 \\ -g \end{bmatrix} \tag{4-11}$$

where the subscripts s and c refer to sine and cosine.

Rearranging the above equations, the relationship between vehicle motion accelerations, vehicle velocity and IMU measurements can be obtained as follows:

$$\dot{V}_f = A_{Bx} - g \sin \theta \quad (4-12)$$

$$V_f \omega_{Bz} = A_{By} + g \sin \phi \cos \theta \quad (4-13)$$

$$V_f \omega_{By} = -A_{Bz} - g \cos \phi \cos \theta \quad (4-14)$$

The above equations indicate that:

1. One x-axis accelerometer is enough to determine the forward velocity of the vehicle.
2. When a triad of accelerometers is used, the forward velocity of the vehicle can be directly computed if one of the angular velocities, ω_{By} or ω_{Bz} , is significant.
3. When the vehicle is stationary, the roll and pitch can be directly computed from the accelerometer measurements.

For the attitude dynamics, by rewriting and expanding the last equation in Eq. (4-5), we obtain the following equations describing the relationship between Euler rates and gyro measurements.

$$\dot{\phi} = \omega_{Bx} + \sin \phi \tan \theta \omega_{By} + \cos \phi \tan \theta \omega_{Bz} \quad (4-15)$$

$$\dot{\theta} = \cos \phi \omega_{By} - \sin \phi \omega_{Bz} \quad (4-16)$$

$$\dot{\psi} = \frac{\sin \phi}{\cos \theta} \omega_{By} + \frac{\cos \phi}{\cos \theta} \omega_{Bz} \quad (4-17)$$

Using the above three equations together with the initial attitude information, the current vehicle attitude represented by three Euler angles can be computed by direct integration. Although this approach may become indeterminate for roll and yaw when pitch equals to ± 90 degree, it will not occur in the case for land vehicle applications.

Finally, the vehicle's trajectory in the navigation frame can be computed by the forward velocity and attitude of the vehicle in the following manner.

$$\dot{P}_{Nn} = V_f \cos \theta \cos \psi \quad (4-18)$$

$$\dot{P}_{Ne} = V_f \cos \theta \sin \psi \quad (4-19)$$

$$\dot{P}_{Nd} = V_f \sin \theta \quad (4-20)$$

The land vehicle motion models comprise Eq. (4-12) through Eq. (4-20) which relate the IMU measurements to position, velocity and attitude information for a land vehicle. Allowing for the direct online estimation of the roll, pitch and the forward velocity of the vehicle from the accelerometer and gyroscope measurements, this model can be used to significantly reduce the error growth rate in position estimates especially for low-cost IMUs (Dissanayake et al., 2001; Wang et al., 2005).

4.3.2 Vehicle Dynamics-Derived Observations

Based on the land vehicle motion model and the specific physical characteristics of inertial sensors, under some specific vehicle dynamics it is possible to directly estimate some navigation states such as tilt angles and velocity of a land vehicle without using

external sensors. These dynamics-derived estimates can be used as the virtual measurement updates to the INS Kalman filter for navigation error control. The specific vehicle dynamics and the corresponding dynamics-based or dynamics-derived estimates are summarized into three categories: stationary, straight-line motion, and cornering motion.

4.3.2.1 Stationary Mode

When a vehicle is static, accelerometer measurements can be used to directly derive vehicle pitch and roll angles. Measuring only the local gravity field under this condition, the accelerometer outputs can be used to determine vehicle pitch and roll angles as follows (El-Sheimy, 2003):

$$\theta = \sin^{-1}\left(\frac{A_{Bx}}{g}\right) \quad (4-21)$$

$$\phi = -\sin^{-1}\left(\frac{A_{By}}{g}\right) \quad (4-22)$$

According to Eq. (4-21) and Eq. (4-22), no integration step in time is required and the accuracy of tilt estimation is mainly governed by accelerometer measurement error such as bias and noise. Using perturbation technique, we can derive the following equations to describe the relationship between accelerometer measurement error and tilt error.

$$\delta\theta = \sec\theta \frac{\delta A_{Bx}}{g} \quad (4-23)$$

$$\delta\phi = -\sec\phi \frac{\delta A_{By}}{g} \quad (4-24)$$

where $\delta\theta$ and $\delta\phi$ are pitch and roll errors; and δA_{Bx} and δA_{By} are the x-axis and y-axis accelerometer measurement errors, respectively.

In this dissertation, accelerometer biases are estimated by the INS Kalman filter and a statistical approach that will be described in Chapter 5. The performance of the bias estimation will be presented in Chapter 6. Theoretically, for land vehicle applications where the tilt angle is small, a 1 mg unidentified accelerometer bias will lead to tilt error of about 0.057 degree. For accelerometer noise effects, they can be reduced by averaging the tilt estimates over the stationary periods. Compared to the gyro-derived tilt with large drift errors, the accelerometer-derived tilt is accurate enough to provide direct correction and control of the tilt error. Another observation available during the stationary periods is the constant heading constraint. Since the vehicle is not moving, the heading of the vehicle can be considered unchanged and can be modeled by the following equation.

$$\psi(t_s) = \psi(t_s - 1) \quad (4-25)$$

where t_s denotes the sampling time during the stationary periods.

The fourth direct measurement during the stationary periods is the well-known ZUPT. ZUPT provides a very accurate velocity observation, as the vehicle is static. The last benefit from the stationary mode is the availability of gyro bias estimation. For automotive-grade and consumer-grade IMUs, the stationary outputs of gyroscopes themselves can be considered as measurement biases (Sukkarieh, 2000). This is because the Earth rotation is at the sensor noise level for automotive-grade MEMS IMUs and thus the true angular rate of the body frame during the stationary periods can be assumed as zero. By averaging all gyro measurements during the stationary periods, we can remove the noise effects and use this average value as the gyro bias estimate.

4.3.2.2 Straight-Line Motion Mode

When a vehicle is moving straight, no significant motion acceleration along the transverse direction exists. Thus, mostly the y-axis accelerometer measurement,

containing the local gravity field, can be used to determine the approximate roll angle based on Eq. (4-22). Although the approximation errors induced by sideslip or vibration may exist, they can be mostly reduced by moving average. Therefore, when the vehicle is moving straight, the accelerometer-derived roll still can be used as a direct roll update to reduce the drift error of the gyro-derived tilt. Similarly, to improve the accuracy of the accelerometer-derived roll, the y-axis accelerometer bias is estimated using the same method applied in the stationary mode and the noise effect is reduced by moving average.

4.3.2.3 Cornering Motion Mode

In addition to ZUPTs, the cornering motion with strong dynamics in transverse acceleration and yawing provides another occurrence for direct estimation of the vehicle velocity. Rearranging Eq. (4-13), the forward velocity of the vehicle can be directly estimated as follows:

$$V_f = \frac{1}{\omega_{Bz}} (A_{By} + g \sin \phi \cos \theta) \quad (4-26)$$

According to the above equation, the forward velocity is inversely proportional to the z-axis gyro measurement. Thus, the estimation of the forward velocity is not applicable if the signal-to-noise ratio of the z-axis gyro measurement is low. Only when the z-axis angular dynamics is significant, e.g. during the cornering motion, the estimation of the forward velocity becomes feasible. Using perturbation technique, we can derive the following equation to describe the error budget of the forward velocity estimate.

$$\begin{aligned} \delta V_f = & \frac{1}{\omega_{Bz}} (\delta A_{By} + g \cos \phi \cos \theta \delta \phi - g \sin \phi \sin \theta \delta \theta) \\ & - \frac{1}{\omega_{Bz}^2} (A_{By} + g \sin \phi \cos \theta) \delta \omega_{Bz} \end{aligned} \quad (4-27)$$

where δV_f and $\delta \omega_{Bz}$ are the errors of the forward velocity and the z-axis gyro measurement, respectively.

According to the above equation, the accuracy of the forward velocity estimate depends on the accuracy of the y-axis accelerometer measurement, the z-axis gyro measurement and the tilt estimate. The effect of the pitch error on the forward velocity estimate is negligible since tilt angles are generally small during the cornering motion of a land vehicle and thus the term $\sin\phi\sin\theta$ in Eq. (4-27) becomes very small. In addition, because the accelerometer-derived roll is always used to update the roll estimate when the vehicle is stationary or moving straight, the accuracy of the roll estimate during cornering is mainly governed by the accelerometer bias. Therefore, we can replace $\delta\phi$ in Eq. (4-27) with Eq. (4-24) and rewrite Eq. (4-27) as follows:

$$\begin{aligned}\delta V_f &= \frac{1}{\omega_{Bz}} \left(\delta A_{By} - g \cos\phi \cos\theta \sec\phi \frac{\delta A_{By}}{g} - g \sin\phi \sin\theta \delta\theta \right) \\ &\quad - \frac{1}{\omega_{Bz}^2} (A_{By} + g \sin\phi \cos\theta) \delta\omega_{Bz} \\ &\cong \frac{1}{\omega_{Bz}} (1 - \cos\theta) \delta A_{By} - \frac{1}{\omega_{Bz}^2} (A_{By} + g \sin\phi \cos\theta) \delta\omega_{Bz}\end{aligned}\tag{4-28}$$

Based on Eq. (4-28), the accuracy of the forward velocity estimate is mainly determined by IMU measurement errors such as bias and noise of the y-axis accelerometer and the z-axis gyro. In general, ω_{Bz} is large and the tilt angles are small during cornering motion of a land vehicle, thus the impact of δA_{By} and $\delta\omega_{Bz}$ on the velocity estimation error is diminished. For example, in a typical cornering motion where A_{By} is 1.5 m/s^2 , ω_{Bz} is 15 deg/sec, ϕ is 2 degree, and θ is 2 degree, $1 \text{ m/s}^2 \delta A_{By}$ will lead to 0.0023 m/s error in the velocity estimate and $1 \text{ deg/sec } \delta\omega_{Bz}$ will lead to -0.294 m/s error in the velocity estimate. To further improve the estimation accuracy, the y-axis accelerometer bias and the z-axis gyro bias are estimated using the same approach applied in the stationary mode. For the measurement noise effects, it is mainly caused by sensor noise, vibration and road ruggedness during the cornering motion. Similar to the stationary mode, moving average of the velocity estimates over a time window is used for noise reduction.

4.3.2.4 Summary

The vehicle dynamics-derived observations under different dynamics are summarized in Table 4.4. We find that the stationary dynamics provides the most dynamics-derived observations for INS error estimation and correction including attitude error, velocity error and gyro bias. During the straight-line motion direct estimation of the roll angle is possible and roll error can be well bounded and controlled by accelerometer measurements. When the vehicle makes a turn, a direct estimation of the forward velocity is available and the velocity error drift can be reduced. The accuracy of the dynamics-derived observations is mainly governed by the unidentified accelerometer and gyro biases. In general, the drift-free dynamics-derived observations are more accurate than the stand-alone INS navigation states and can provide effective INS error correction and reduction without the aiding from external sensors.

Table 4.4: Vehicle dynamics aided observations

Vehicle Dynamics	Direct Estimation of INS Navigation States and Sensor Errors				
	Pitch	Roll	Yaw	Forward Velocity	Gyro Bias
Stationary	$\theta = \sin^{-1}\left(\frac{A_{Bx}}{g}\right)$	$\phi = -\sin^{-1}\left(\frac{A_{By}}{g}\right)$	$\psi(t_s) = \psi(t_s - 1)$	$V_f = 0$	$b_{\omega_{Bx}} = \omega_{Bx}$ $b_{\omega_{By}} = \omega_{By}$ $b_{\omega_{Bz}} = \omega_{Bz}$
Straight-line Motion	N/A	$\phi = -\sin^{-1}\left(\frac{A_{By}}{g}\right)$	N/A	N/A	N/A
Cornering Motion	N/A	N/A	N/A	$V_f = \frac{A_{By} + g \sin \phi \cos \theta}{\omega_{Bz}}$	N/A

4.3.3 Design of Fuzzy Expert Vehicle Dynamics Identification System

In order to implement the aforementioned dynamics-dependent estimation for INS error control, the vehicle dynamics such as stationary, straight-line motion, and cornering motion must be correctly identified. Inertial measurements such as acceleration and angular velocity strongly relative to vehicle dynamics can be used for vehicle dynamics identification. In real-life applications, however, these raw measurements are corrupted with noise and vibration effects especially for low-cost MEMS IMUs. Therefore, the identification system must be capable of dealing with imprecision of inertial

measurements. As mentioned in Chapter 3, the fuzzy set theory provides a natural method for dealing with linguistic term that is a very effective knowledge representation format for imprecise and ambiguous information (Kandel, 1992). Thus, a fuzzy inference system that incorporates fuzzy sets and fuzzy logic into its reasoning process and knowledge representation scheme is applied to convert the INS raw measurements into a more appropriate measure for vehicle dynamics identification.

To consider both linear and angular dynamics, we define the input variables of the fuzzy inference system, $J(t_k)$ and $W(t_k)$, as follows:

$$J(t_k) = \sum_{t_i=t_k-n}^{t_k} |A_{norm}(t_i) - A_{norm}(t_i-1)| \quad (4-29)$$

$$W(t_k) = \sum_{t_i=t_k-n}^{t_k} |\omega_{norm}(t_i)| \quad (4.30)$$

where $A_{norm} = \sqrt{A_{Bx}^2 + A_{By}^2 + A_{Bz}^2}$ is the norm of the three-axis accelerations; $\omega_{norm} = \sqrt{\omega_{Bx}^2 + \omega_{By}^2}$ is the norm of the x-axis and y-axis angular velocities; t_k denotes the current discrete time; and n is the size of time window for statistical smoothing.

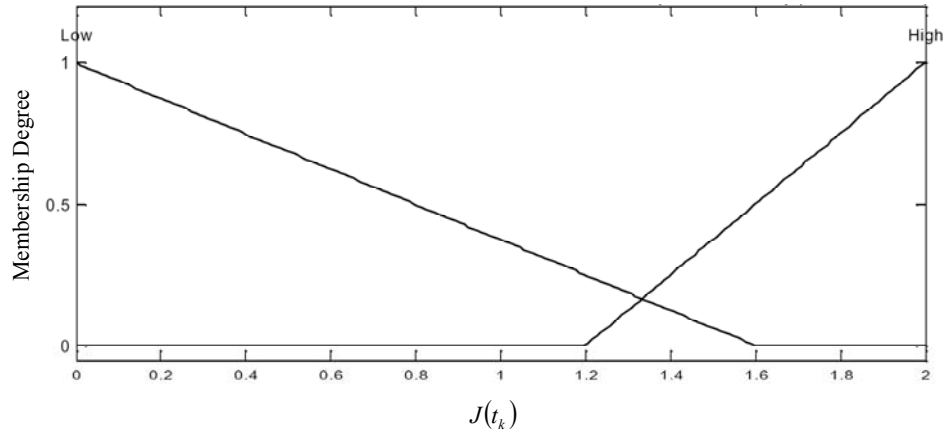
The first input variable $J(t_k)$ indicates the overall linear jerk dynamics over a fixed time interval ($t_k - n$ to t_k). The second input variable $W(t_k)$ indicates the pitching and rolling dynamics over a fixed time interval ($t_k - n$ to t_k). The output of the fuzzy inference system, namely the dynamics indicator $DI(t_k)$, is the combination of these two input dynamics measures through a fuzzy inference. As mentioned in Chapter 3, a fuzzy inference system is accomplished by fuzzy set membership functions, a set of if-then rules and a defuzzification process. The membership functions mapping input data into the fuzzy set degrees are used to handle the ambiguity of input data. In the considered problem, two membership functions, ‘Low’ and ‘High’, representing the low and high

linear/angular dynamics are used for each input variable. For the purpose of computational simplicity, the triangle membership functions are used. The parameters of input membership functions are empirically determined based on the field test data. Specifically, we use the values of $J(t_k)$ and $W(t_k)$ under the stationary and non-stationary dynamics to define the scope of the input membership functions. For the output membership functions, three triangles with full overlaps between each set and even segmentation from zero to one are used. The linguistic term ‘Large’ in the output membership functions means the higher likelihood for the vehicle being moving and so on. A set of if-then rules mapping the input fuzzy sets into the output fuzzy set is established by common sense reasoning and expert knowledge to the problems, e.g., the larger $J(t_k)$ and $W(t_k)$, the higher likelihood for the vehicle being moving. The designed membership functions and fuzzy rules are shown in Figure 4.17 and Table 4.5, respectively.

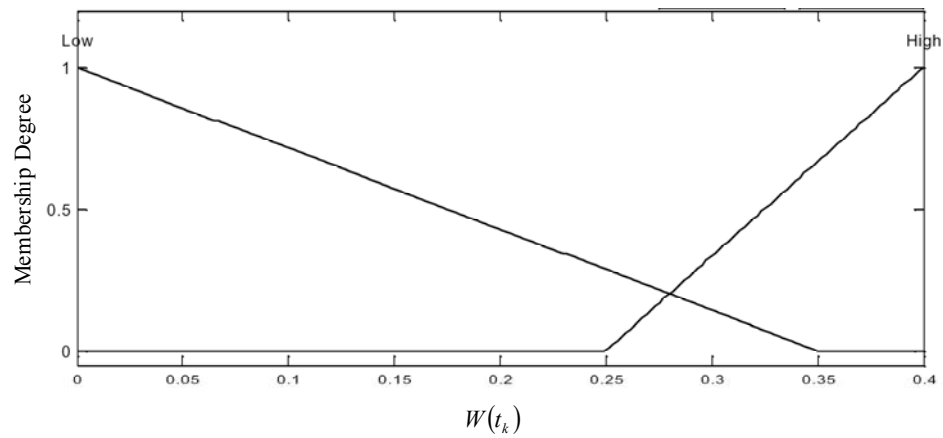
To complete the inference procedure and to generate the output fuzzy set, the Mamdani type fuzzy inference method with max-min composition, which is considered as the most commonly seen fuzzy methodology, is used (Mamdani and Assilian, 1975). The output fuzzy set is defuzzified into a crisp value using the centre of the area method. According to the designed output membership functions, the final crisp output, i.e., the dynamics indicator $DI(t_k)$, is in a range between 1/6 and 5/6 and it is straightforward to distinguish between stationary and non-stationary dynamics using a cut-off value of 0.5.

Table 4.5: If-then rules used in the fuzzy inference system for vehicle dynamics identification

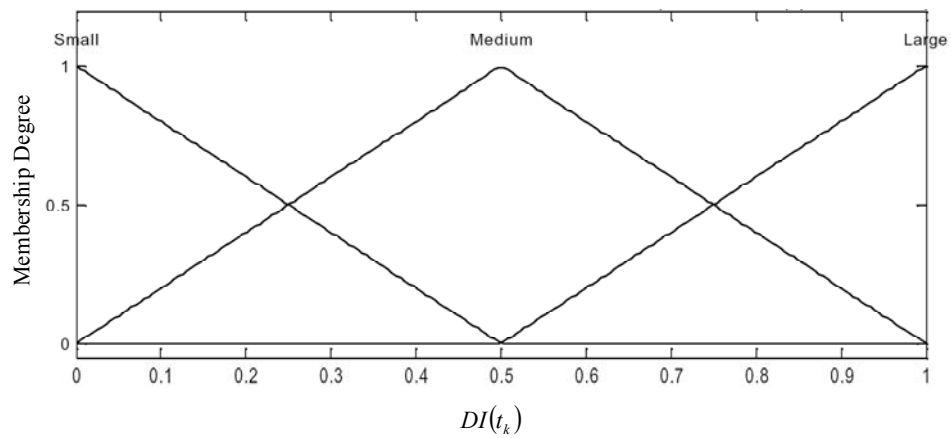
R ₁ :	If $J(t_k)$ is LOW and $W(t_k)$ is LOW then $DI(t_k)$ is SMALL
R ₂ :	If $J(t_k)$ is HIGH and $W(t_k)$ is LOW then $DI(t_k)$ is MEDIUM
R ₃ :	If $J(t_k)$ is LOW and $W(t_k)$ is HIGH then $DI(t_k)$ is MEDIUM
R ₄ :	If $J(t_k)$ is HIGH and $W(t_k)$ is HIGH then $DI(t_k)$ is LARGE



(a) the first input variable



(b) the second input variable



(c) the output variable

Figure 4.17: Membership functions used in the fuzzy inference system for vehicle dynamics identification

When the dynamics indicator $DI(t_k)$ is used for stationary and non-stationary identification, there however exists the detection delay because the fuzzy input variables, $J(t_k)$ and $W(t_k)$, are formed by a set of data from the previous epoch to current epoch. To overcome this problem, we define another linear dynamics parameter, $DA_x(t_k)$, to measure the instant forward dynamics as follows:

$$DA_x(t_k) = \sum_{t_i=t_k-p}^{t_k} |A_{Bx}(t_i) - A_{Bx}(t_k - p)| \quad (4-31)$$

where p is the time lag for the computation of acceleration difference.

When the vehicle begins to move from a stationary status, a dramatic dynamics change occurs in the forward direction. In this case, $DA_x(t_k)$ becomes significant and can be used to instantly indicate the dynamics transition from stationary to move. Based on the conditions of $DI(t_k)$ and $DA_x(t_k)$, a set of if-then rules shown in Table 4.6 are constructed to distinguish the status of vehicle dynamics, stationary or non-stationary.

When the vehicle dynamics is identified as non-stationary, the next task is to distinguish the vehicle dynamics between straight-line motion and cornering motion. Since pitch and roll angles are generally small during the cornering motion of a land vehicle, the z-axis gyro measurement, ω_{Bz} , can be directly used to represent the yawing dynamics. By simply averaging ω_{Bz} over a fixed time interval to reduce noise effects, a cornering dynamics measure is computed as follows:

$$M\omega_z(t_k) = \frac{1}{m} \sum_{t_i=t_k-m}^{t_k} \omega_{Bz}(t_i) \quad (4-32)$$

where m is the size of time window for moving average.

Based on the conditions of $M\omega_z(t_k)$, a set of if-then rules shown in Table 4.7 are constructed to classify the non-stationary dynamics as straight-line motion or cornering

motion. In Table 4.6 and Table 4.7, the if-then rules used for identifying stationary, straight-line motion and cornering motion are easily formulated by common sense reasoning and expert knowledge to the problems. The criterion value used in each rule is heuristically determined based on the real data and is vehicle dependent and sensitive to the installation locations of the sensors. The decision flow of the designed vehicle dynamics identification system is shown in Figure 4.18.

Table 4.6: Expert rules for stationary/non-stationary identification

R ₁ :	When the vehicle was in stationary at the last epoch: If $DA_x(t_k)$ is larger than a criterion value then the vehicle is in non-stationary
R ₂ :	When the vehicle was in non-stationary at the last epoch: If $DA_x(t_k)$ is smaller than a criterion value and $DI(t_k)$ is smaller than 0.5 then the vehicle is in stationary

Table 4.7: Expert rules for straight-line/cornering motion identification

R ₁ :	When the vehicle was in straight-line motion at the last epoch: If $M\omega_z(t_k)$ is larger than a criterion value then the vehicle is in cornering motion.
R ₂ :	When the vehicle was in cornering motion at the last epoch: If $M\omega_z(t_k)$ is smaller than a criterion value then the vehicle is in straight-line motion.

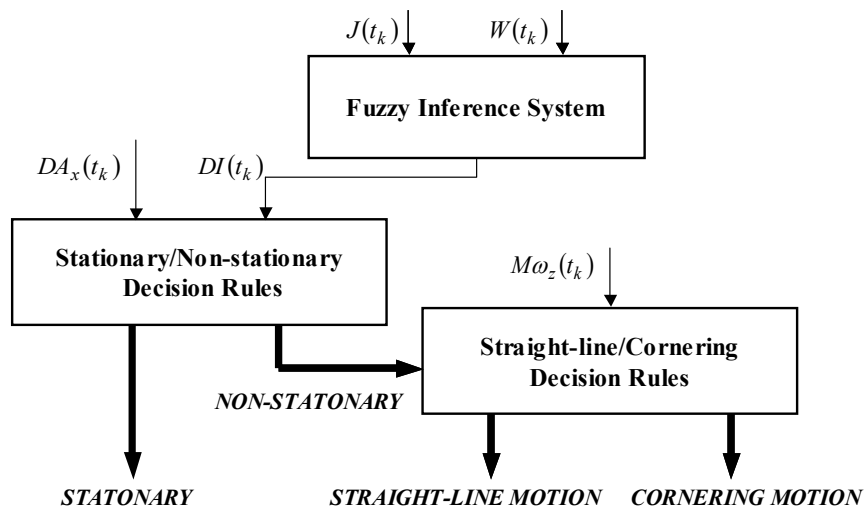


Figure 4.18: Decision flow of the vehicle dynamics identification system

4.4 Neural Networks Compass Calibration

As stated in Chapter 2, a magnetic compass can provide heading direction by measuring the Earth's magnetic field. In practical applications there usually exist unwanted local magnetic fields that will distort magnetometer measurements, hence a calibration procedure is essential. Two types of methods, one requiring true (reference) headings while another not, have been successfully used for compass calibration. When true headings are unavailable, a simple calibration method is to level and rotate the compass on a horizontal surface and to find the maximum and minimum values of the x-axis and y-axis magnetic readings. Then these four values can be used to compute the magnetometer scale factors and biases based on the fact that the locus of error-free measurements on x and y axes is a circle (Caruso 1997). Another similar method developed by Gebre-Egziabher et al (2001) is to use a non-linear two-step estimator to resolve an ellipse locus equation and then to estimate the scale factors and biases. In addition, Crassidis et al (2005) developed a real-time approach for compass calibration using the extended Kalman filter and Unscented filter. This approach relies on a conversion of the magnetometer-body and geomagnetic-reference vectors into an attitude independent observation by using scalar checking (Crassidis et al 2005). On the other hand, if true headings are known during the calibration process, a traditional "swinging" procedure involving levelling and rotating the compass through a series of known headings can be used (Bowditch 1995). At each known heading, the heading error is computed and these known headings and heading errors will be used to estimate the unknown parameters in the heading error equation using a batch least squares estimation. Once the parameters are solved correctly, the heading error can be predicted based on the heading error equation as a nonlinear input-output mapping. However, the common drawback of the forementioned calibration methods is that the algorithm will diverge or fail when the magnetic measurements are deteriorated by large amounts of noise and/or blunders which are frequently present in land vehicle environments.

To overcome the above problem, we have proposed a new compass calibration algorithm by applying a neural networks nonlinear mapping between the compass heading and the

true heading based on the fact that the uncalibrated compass heading corrupted by the magnetometer biases, scale factors and declination angles has a nonlinear relationship with the true heading (Wang and Gao, 2005c). When external true headings are available, the neural networks are trained to model this nonlinear relationship. After that, the trained neural networks can be used to convert the compass heading into the correct heading. By properly selecting the architecture of the networks and the size of the training data set, the neural networks can neglect the spurious disturbances and will produce a correct input-output mapping (Haykin 1999), making the proposed calibration algorithm more robust in practical applications. In the following sections, the nonlinear relationship between the compass heading and the true heading will be analyzed first. The design of the neural networks for compass heading calibration will then be presented and verified by simulation tests.

4.4.1 Magnetic Compass Error Model

In land vehicle applications the magnetic compass is usually mounted inside a vehicle. In this case, the Earth's magnetic fields are inevitably coupled with unwanted local magnetic fields caused by nearby ferrous effects such as steel materials and external interference such as electrical currents. As a result, the magnetic compass will output incorrect headings by measuring the distorted and/or bended Earth's magnetic fields. If the compass is securely mounted inside the vehicle, the nearby ferrous effects on magnetometer measurements will remain stable and can be modeled as measurement biases and scale factor errors. In contrast, the magnetic noise and disturbance are unpredictable and changing randomly, thus they cannot be modeled systematically and instead they are usually dealt with by filtering techniques. In addition to these environmental magnetic effects, there exists misalignment which represents the imperfect alignment between the magnetometer triad and the body frame and will lead to cross coupling of the magnetic measurements. Comparing to nearby ferrous effects, in general, the heading error due to misalignment is much smaller and can be neglected. As a result, only biases and scale factor errors are dealt with by compass calibration in most

applications. The magnetometer measurements in a horizontal plane can be modeled as follows (Caruso, 1997):

$$\tilde{M}_{x_H} = S_{x_H} M_{x_H} + b_{x_H} \quad (4-33)$$

$$\tilde{M}_{y_H} = S_{y_H} M_{y_H} + b_{y_H} \quad (4-34)$$

where \tilde{M}_{x_H} and \tilde{M}_{y_H} are the Earth's magnetic fields projected on the x_H and y_H axes of the horizontal plane, respectively; M_{x_H} and M_{y_H} are the measured magnetic fields projected on the x_H and y_H axes of the horizontal plane, respectively; and S_{x_H} , S_{y_H} , b_{x_H} and b_{y_H} are the measurement scale factors and biases on the x_H and y_H axes of the horizontal plane, respectively.

As stated in Chapter 2, the magnetic fields are converted into magnetic headings based on the nonlinear heading computation equations given in Eq. (2-28). Based on this nonlinear mapping and the above magnetometer error model, the magnetometer measurement biases and scale factor errors will result in incorrect compass headings that have a nonlinear relationship with true headings. The curves shown in Figure 4.19 are some examples of such nonlinear relationship. The added bias on each axis is from -0.4 to 0.4 times of the magnitude of the reference magnetic field. The added scale factor on each axis is from 1 to 1.5. The declination angle, which can be considered as a heading bias, is chosen as from -20 to 20 degrees.

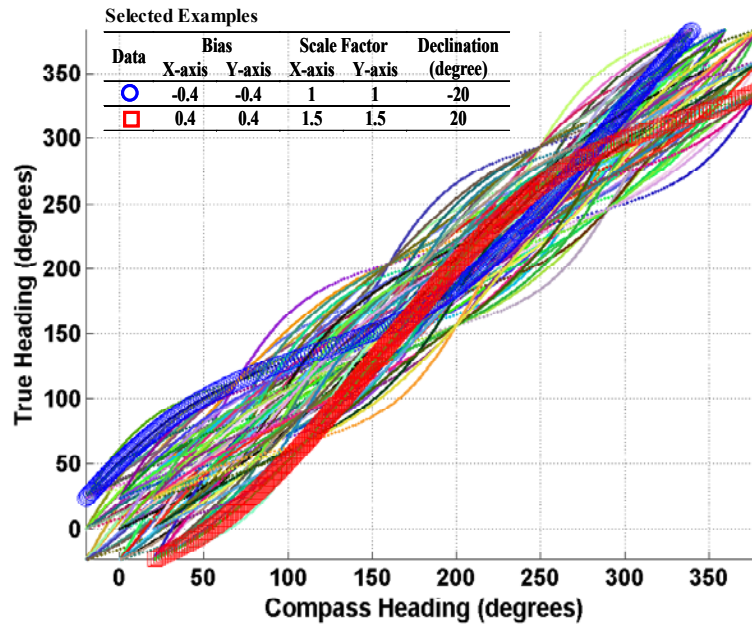


Figure 4.19: Nonlinear relationship between compass headings and true headings

4.4.2 Design of Neural Networks Compass Calibration System

As shown in Figure 4.19, we have demonstrated that there exists a nonlinear relationship between the compass heading and the true heading which describes the effects of biases, scale factors and declination angles in the heading domain. If we can properly model this nonlinear relationship or nonlinear functional mapping, we can convert the compass heading to the true heading based on it. In real applications, however, the sensor and environment noise, the blunder due to magnetic disturbances and the projection error of magnetic field vector due to tilt errors will corrupt and distort this nonlinear relationship. Therefore, the nonlinear functional mapping method should be capable of handling the corrupted data and modelling this nonlinear relationship effectively even in the presence of a large amount of noises, blunders and unknown errors. As described in Chapter 3, the neural networks can provide a model-free input-output nonlinear mapping that doesn't require prior statistical model for the input data. With the use of proper time constants of the mapping system, the neural networks can ignore spurious disturbances and respond to meaningful changes in the environment (Haykin 1999). In this dissertation the multilayer feedforward neural networks with a back-propagation learning algorithm which are

considered as the most commonly used networks for the nonlinear mapping are applied for modelling the nonlinear relationship between the compass heading and the true heading.

The architecture of the applied neural networks is shown in Figure 4.20. The input and output of the neural networks are compass heading and true heading. The compass heading is derived from magnetometer measurements based on the computation procedure described in Chapter 2. The true heading and tilt angles used for projecting magnetometer measurements on the horizontal plane are provided by the INS/GPS integration system which will be described in Chapter 5. When true headings are available, the neural networks are trained to model the input-output pattern. The training of the networks is repeated for many examples in the set until the networks reach a steady state so that a proper input-output mapping can be constructed. After the training process is completed, the trained neural networks are used to correct the compass heading. If the magnetometer errors or the operational environments change from the training data, the neural networks should be retrained to adapt to the up-to-date input-output relationship. It should be noted that the number of the neurons and the layers used will affect the performance of the input-output mapping. In general, the network architecture depends on the physical complexity of the problem at hand. In our application, by using a heuristic approach three-layer neural networks with twelve neurons in hidden layer are chosen for the nonlinear mapping between the compass heading and the true heading. More details about the neural networks algorithm are provided in Chapter 3.

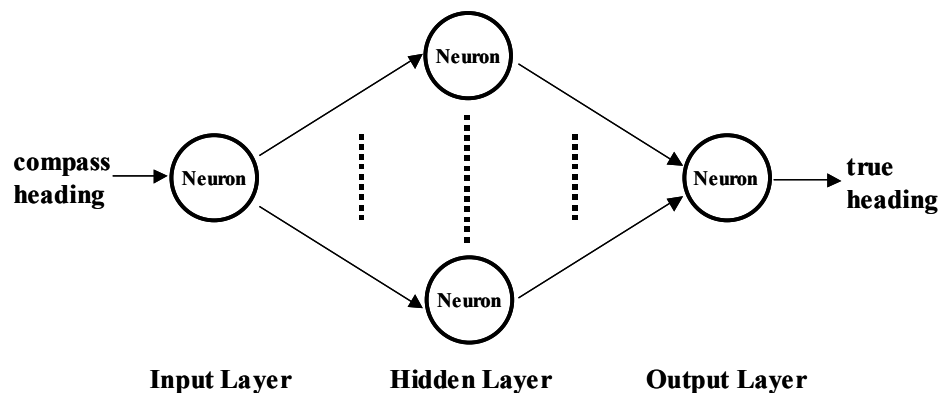


Figure 4.20: Architecture of the neural networks compass calibration system

4.4.3 Simulation Verification

In this section the performance of using neural networks for the nonlinear mapping between compass headings and true headings is examined by simulation data. Two-dimensional magnetic fields covering 360-degree directions on a horizontal plane are generated as reference data. Some biases, scale factors, noises, and disturbances are added into the reference data to produce distorted magnetometer measurements. The compass heading is then computed using the distorted magnetometer measurements and biased by a selected declination angle. Figure 4.21 shows an example of the true and distorted magnetic field measurement loci in 2-D. In this simulation data set, the added biases on x and y axes are randomly selected as 0.009 and 0.5 times of the magnitude of the reference magnetic field while the scale factors on x and y axes as 1.196 and 1.978, respectively. The Gaussian white sequences with a standard deviation of 3.5% of the magnitude of the reference magnetic field are also added as noise effects. The magnetic disturbances are simulated to bias the magnetic fields with a randomly selected magnitude of less than 60% of the reference magnetic field's magnitude. Twelve randomly selected data sets, evenly spreading over the entire reference data and accounting for 12.5% of the total reference data, are deteriorated by the simulated disturbances. Figure 4.22 shows the performance of using the neural networks for the nonlinear mapping between the true heading and the distorted compass heading that has been biased by a randomly selected declination angle of -9.59 degrees. The blue crosses represent the training data set and the green circles are the neural networks outputs from the processing of the disturbance-free testing data that have the same biases, scalar factors and declination angles as the training data. It can be seen that the neural networks have modeled the nonlinear relationship between the compass heading and the true heading properly although the training data are deteriorated by noise and disturbance.

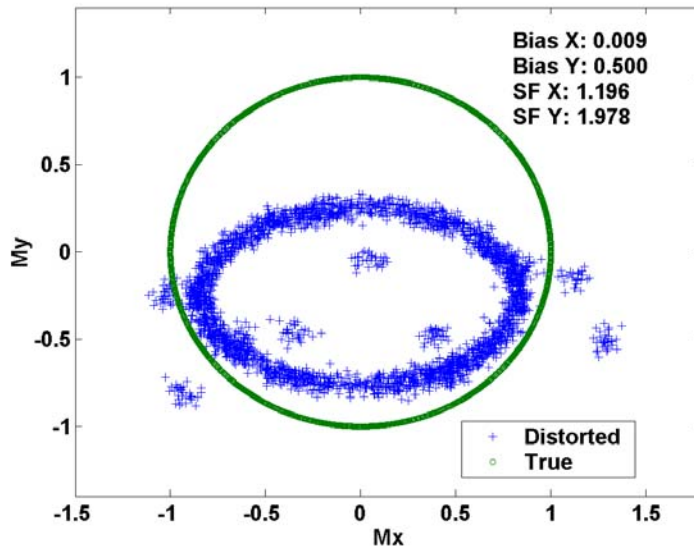


Figure 4.21: Magnetic field measurement locus in 2-D

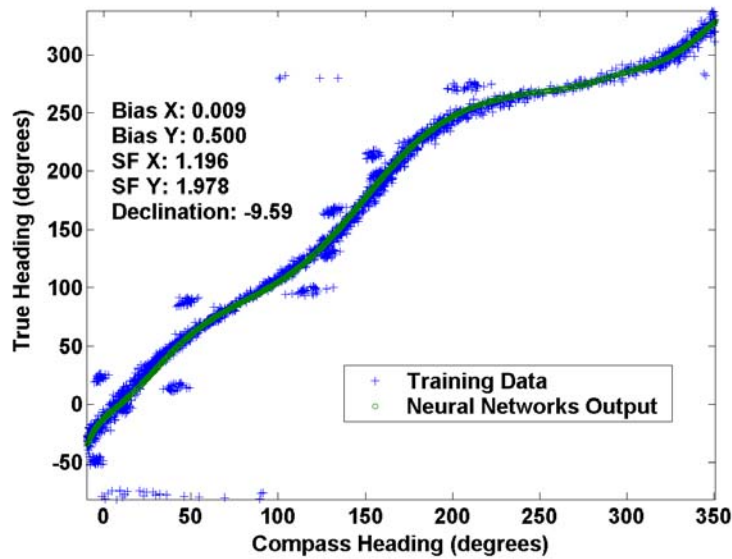


Figure 4.22: Performance of the neural networks nonlinear mapping

To assess the performance of the neural networks nonlinear mapping statistically, more simulation tests have been performed. The simulation results are summarized in Table 4.8. In each simulation test, the biases, scalar factors and declination angles are randomly selected. Noises and disturbances are then added in the same manner as described before to form the training data. After the training process, the neural networks first process the

disturbance-free testing data that have the same biases, scalar factors and declination angles as the training data and then output the calibrated headings. The calibration error is computed by taking the difference between the neural networks output and the true heading. As shown in Table 4.8, the average mean and RMS of the calibrated heading errors over these 10 simulation tests are -0.176 and 2.35 degrees, respectively. This shows the capability of the neural networks technique for the nonlinear input-output mapping in the presence of magnetic disturbances.

Table 4.8: Calibrated compass heading accuracy (12.5% data deteriorated by disturbances)

Test No.	Sensor Error				Calibrated Heading Error		
	Bias-x	Bias-y	SF-x	SF-y	Declination (degrees)	Mean (degrees)	RMS (degrees)
1	0.223	0.162	1.393	1.592	7.998	-0.621	2.059
2	0.13	-0.153	1.699	1.397	-7.777	-0.264	1.456
3	-0.478	-0.305	1.791	1.815	19.333	0.245	2.196
4	0.203	-0.005	1.565	1.767	5.964	0.672	2.827
5	-0.139	0.596	1.982	1.9	-4.725	-0.909	2.149
6	-0.331	-0.136	1.162	1.031	15.189	-0.94	3.503
7	0.009	0.5	1.196	1.978	-9.594	-0.252	2.777
8	0.297	0.175	1.743	1.651	5.419	-0.45	1.458
9	0.155	-0.248	1.168	1.814	9.688	0.904	2.466
10	-0.019	0.492	1.735	1.005	-20.873	-0.148	2.615

To further study the effects of magnetic disturbances on calibration performance, we have performed additional simulation tests with data deteriorated by different levels of disturbances. Table 4.9 and Table 4.10 summarized the simulation results with 6.25% and 25% of training data deteriorated by disturbances, respectively. The average mean and RMS of the calibrated heading errors are -0.236 and 1.907 degrees for the case with the less disturbances and -0.855 and 4.373 degrees for the case with the more disturbances. It can be seen that the calibration performance will degrade with the increment of the data deteriorated by disturbances. The results also demonstrate that the proposed calibration algorithm is still able to work under disturbance-rich environments, e.g. 25% data deteriorated by disturbances. This confirms the robustness of applying the neural

networks for compass calibration over other calibration algorithms that have failed to estimate biases and scalar factors under high disturbance environments.

Table 4.9: Calibrated compass heading accuracy (6.25% data deteriorated by disturbances)

Test No.	Sensor Error				Calibrated Heading Error		
	Bias-x	Bias-y	SF-x	SF-y	Declination (degrees)	Mean (degrees)	RMS (degrees)
1	-0.476	0.352	1.874	1.237	-20.44	1.059	2.673
2	0.193	-0.223	1.217	1.231	-5.706	0.713	1.156
3	-0.574	-0.189	1.727	1.489	-20.244	0.176	2.962
4	-0.038	-0.445	1.584	1.603	-6.591	0.211	1.9
5	0.109	-0.491	1.401	1.191	2.438	-0.501	1.162
6	0.276	-0.522	1.221	1.19	3.755	0.371	1.289
7	0.189	0.098	1.119	1.519	0.676	-0.027	2.986
8	-0.571	-0.022	1.543	1.379	3.928	-0.48	2.487
9	0.191	0.22	1.364	1.616	4.956	0.324	1.18
10	0.198	0.08	1.099	1.681	22.912	0.512	1.279

Table 4.10: Calibrated compass heading accuracy (25% data deteriorated by disturbances)

Test No.	Sensor Error				Calibrated Heading Error		
	Bias-x	Bias-y	SF-x	SF-y	Declination (degrees)	Mean (degrees)	RMS (degrees)
1	0.213	-0.281	1.411	1.4	-19.832	0.336	4.137
2	0.035	0.421	1.136	1.532	3.132	-2.476	4.437
3	-0.244	-0.099	1.509	1.074	2.09	2.327	4.574
4	-0.016	-0.091	1.287	1.893	-6.269	0.001	4.105
5	-0.463	-0.555	1.77	1.368	-19.414	-2.51	6.216
6	-0.163	-0.517	1.461	1.513	-11.922	-2.538	3.553
7	-0.19	0.598	1.982	1.412	3.95	-0.569	2.94
8	-0.544	-0.257	1.647	1.447	23.494	-0.911	4.62
9	-0.078	-0.268	1.24	1.49	-11.57	-1.471	5.241
10	-0.153	-0.037	1.989	1.303	-13.005	-0.737	3.909

Chapter 5

Development of An Intelligent Integration

Algorithm

In Chapter 4 the limitations of the low-cost MEMS INS/GPS integration using a traditional Kalman filter have been addressed. The methods to enhance the integration performance using AI techniques, including a fuzzy logic rule-based GPS data classification system, a dynamics knowledge aided inertial navigation algorithm, and a neural networks compass calibration algorithm, have also been developed. This chapter describes how these AI-based methods can be integrated with the Kalman filter to develop an intelligent integration algorithm for land vehicle applications. A cascaded loosely coupled integration scheme in which the intelligent integration methodology is implemented is described first. The design of the Kalman filters enhanced by the AI-based methods is then presented. Finally, the construction and operation procedure of the intelligent integration algorithm are illustrated.

5.1 Cascaded Integration Scheme

As stated in Chapter 3, a loosely coupled closed-loop integration scheme is considered as a more suitable approach for low-cost INS/GPS integration in land vehicle applications and has been applied in this dissertation. In general, one INS Kalman filter is used to model and estimate all navigation states including velocity, attitude and position to provide optimal estimation performance. For land vehicle applications in GPS challenging environments, the Doppler-derived velocity is more reliable than the code-derived position because multipath and signal degradation have much more impact on the pseudorange measurements than the Doppler measurements. Given this, the Doppler-

derived velocity is considered more useful for updating the inertial system and the code-derived position would even deteriorate the velocity and attitude estimation. Since the accurate modelling of the error-corrupted GPS position in signal-degraded conditions is difficult, the use of incorrect measurement covariance is likely to cause huge estimation error in velocity and attitude solutions. To maintain system stability, two cascaded Kalman filters, namely the velocity and attitude filter and the position filter, have been employed in this dissertation and implemented separately in a loosely coupled closed-loop integration scheme as shown in Figure 5.1. The INS velocity and attitude filter is designed to estimate INS sensor errors as well as velocity and attitude errors. The INS position filter is designed to integrate the corrected INS velocity and attitude with the GPS position to output an optimal position estimate.

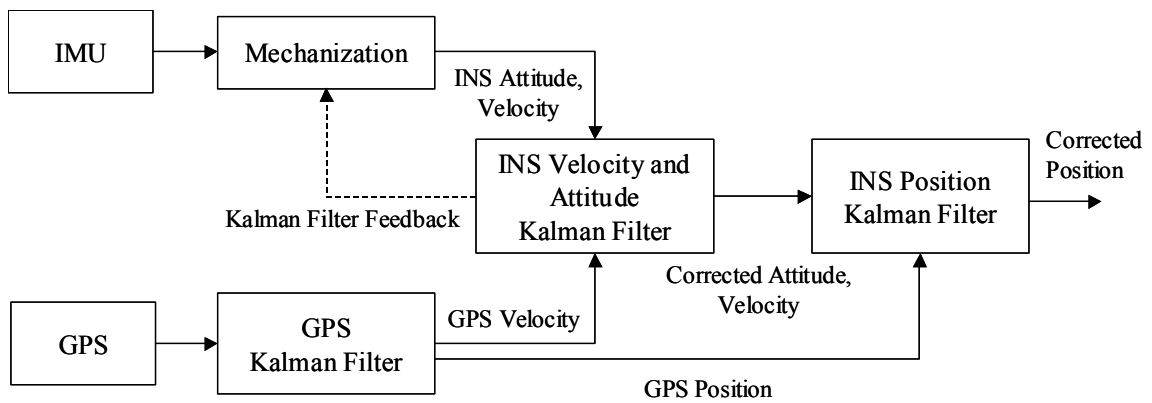


Figure 5.1: Cascaded INS/GPS integration scheme

5.2 Design of AI-Enhanced Velocity/Attitude and Position Filters

Traditionally, the design of the INS velocity and attitude filter and INS position filter is based on INS error dynamics models and measurement statistics. For low-cost INS/GPS integration in land vehicle applications, however, it is difficult to know accurate dynamics and statistical models and the Kalman filter will suffer degraded estimation accuracy and even divergence problems. This dissertation has applied the AI-based methods developed in Chapter 4 to improve the filter performance through simplifying the system models as well as extending and adapting the measurement updates.

Described in the following sections is the design of the AI-enhanced velocity and attitude filter and position filter in terms of the system and measurement models.

5.2.1 Velocity and Attitude Filter

5.2.1.1 Dynamics Model

The INS velocity and attitude filter is designed to estimate INS sensor errors and velocity and attitude errors based on the system error model and external measurement updates. The system error model can be derived based on perturbation analysis of the system dynamics. In this dissertation, the land vehicle dynamics model aided by nonholonomic constraints is utilized to describe the dynamics of a land vehicle as shown in Eq. (4-12) through Eq. (4-20). Using perturbation technique, we can derive the following error dynamics equations for vehicle velocity and attitude estimation from Eq. (4-12), Eq. (4-15), Eq. (4-16) and Eq. (4-17).

$$\delta \dot{V}_f = \delta A_{Bx} - g \cos \theta \delta \theta \quad (5-1)$$

$$\begin{aligned} \delta \dot{\phi} = & \delta \omega_{Bx} + \cos \phi \tan \theta \omega_{By} \delta \phi + \sin \phi \sec^2 \theta \omega_{By} \delta \theta + \sin \phi \tan \theta \delta \omega_{By} \\ & - \sin \phi \tan \theta \omega_{Bz} \delta \phi + \cos \phi \sec^2 \theta \omega_{Bz} \delta \theta + \cos \phi \tan \theta \delta \omega_{Bz} \end{aligned} \quad (5-2)$$

$$\delta \dot{\theta} = -\sin \phi \omega_{By} \delta \phi + \cos \phi \delta \omega_{By} - \cos \phi \omega_{Bz} \delta \phi - \sin \phi \delta \omega_{Bz} \quad (5-3)$$

$$\begin{aligned} \delta \dot{\psi} = & \cos \phi \sec \theta \omega_{By} \delta \phi + \sin \phi \sec \theta \tan \theta \omega_{By} \delta \theta + \sin \phi \sec \theta \delta \omega_{By} \\ & - \sin \phi \sec \theta \omega_{Bz} \delta \phi + \cos \phi \sec \theta \tan \theta \omega_{Bz} \delta \theta + \cos \phi \sec \theta \delta \omega_{Bz} \end{aligned} \quad (5-4)$$

where δV_f is forward velocity error;
 $\delta \phi$, $\delta \theta$, $\delta \psi$ are roll, pitch, and yaw errors;
 δA_{Bx} is the x-axis accelerometer measurement error; and
 $\delta \omega_{Bx}$, $\delta \omega_{By}$, $\delta \omega_{Bz}$ are the gyro measurement errors on each axis.

For the integration of automotive-grade MEMS INS with single point code-based GPS, only sensor biases and noises are modelled in the Kalman filter because other sensor errors such as misalignment and scale factor errors are weakly observable under operational conditions. On the other hand, the modelling of poor observable sensor errors will not only increase system complexity but also make the filter unstable. In addition, with the aiding from available vehicle dynamics knowledge, gyro biases can be estimated and removed from measurements directly if the vehicle is stationary. Thus, we model the sensor errors as follows:

$$\delta A_{Bx} = b_{A_{Bx}} + w_{A_{Bx}} \quad (5-5)$$

$$\delta \omega_{Bx} = w_{\omega_{Bx}} \quad (5-6)$$

$$\delta \omega_{By} = w_{\omega_{By}} \quad (5-7)$$

$$\delta \omega_{Bz} = w_{\omega_{Bz}} \quad (5-8)$$

where $b_{A_{Bx}}$ is the x-axis accelerometer bias;
 $w_{A_{Bx}}$ is the x-axis accelerometer noise; and
 $w_{\omega_{Bx}}, w_{\omega_{By}}, w_{\omega_{Bz}}$ are the gyro noises on each axis.

For the low-cost MEMS inertial sensor with large bias variations, the accurate modelling of the sensor bias is very difficult. We thus focus on the estimation of the constant part of the bias and model the accelerometer bias as a random walk process. Augmented with the above sensor error models, the final system error models can be constructed from Eq. (5-1) through Eq. (5-4) as follows:

$$\begin{aligned}
\underbrace{\begin{bmatrix} \delta \dot{V}_f \\ \delta \dot{\phi} \\ \delta \dot{\theta} \\ \delta \dot{\psi} \\ \dot{b}_{A_{Bx}} \end{bmatrix}}_{\dot{\mathbf{x}}} &= \underbrace{\begin{bmatrix} 0 & 0 & -g \cos \theta & 0 & 1 \\ 0 & f_{\phi\phi} & f_{\phi\theta} & 0 & 0 \\ 0 & f_{\theta\phi} & 0 & 0 & 0 \\ 0 & f_{\psi\phi} & f_{\psi\theta} & 0 & 0 \\ 0 & 0 & 0 & 0 & 0 \end{bmatrix}}_{\mathbf{F}} \underbrace{\begin{bmatrix} \delta V_f \\ \delta\phi \\ \delta\theta \\ \delta\psi \\ b_{A_{Bx}} \end{bmatrix}}_{\mathbf{x}} \\
&+ \underbrace{\begin{bmatrix} 1 & 0 & 0 & 0 & 0 \\ 0 & 1 & \sin \phi \tan \theta & \cos \phi \tan \theta & 0 \\ 0 & 0 & \cos \phi & -\sin \phi & 0 \\ 0 & 0 & \sin \phi \sec \theta & \cos \phi \sec \theta & 0 \\ 0 & 0 & 0 & 0 & 1 \end{bmatrix}}_{\mathbf{G}} \underbrace{\begin{bmatrix} w_{A_{Bx}} \\ w_{\omega_{Bx}} \\ w_{\omega_{By}} \\ w_{\omega_{Bz}} \\ w_b \end{bmatrix}}_{\mathbf{u}}
\end{aligned} \tag{5-9}$$

where $f_{\phi\phi} = \cos \phi \tan \theta \omega_{By} - \sin \phi \tan \theta \omega_{Bz}$;

$$f_{\phi\theta} = \sin \phi \sec^2 \theta \omega_{By} + \cos \phi \sec^2 \theta \omega_{Bz} ;$$

$$f_{\theta\phi} = -\sin \phi \omega_{By} - \cos \phi \omega_{Bz} ;$$

$$f_{\psi\phi} = \cos \phi \sec \theta \omega_{By} - \sin \phi \sec \theta \omega_{Bz} ;$$

$$f_{\psi\theta} = \sin \phi \sec \theta \tan \theta \omega_{By} + \cos \phi \sec \theta \tan \theta \omega_{Bz} ; \text{ and}$$

w_b is the driving noise for the accelerometer bias.

The spectral density matrix of the input white noise \mathbf{u} is given by

$$\mathbf{Q}(t) = \text{diag}(q_{A_{Bx}} \quad q_{\omega_{Bx}} \quad q_{\omega_{By}} \quad q_{\omega_{Bz}} \quad q_b) \tag{5-10}$$

where $q_{A_{Bx}}$ is the spectral density of the x-axis accelerometer noise;

$q_{\omega_{Bx}}, q_{\omega_{By}}, q_{\omega_{Bz}}$ are the spectral densities of the gyro noises on each axis;

q_b is the spectral density of the x-axis accelerometer bias.

The spectral density of the accelerometer and gyro noises can be estimated based on the standard deviation of short periods of static measurements or obtained from the manufacturer provided specifications. The variation of the accelerometer bias can be calculated by using Allan variance analysis of long periods of static data or obtained from

the manufacturer specifications (IEEE, std. 952-1997). In real applications under dynamic manoeuvres, however, sensor noises and bias variations are strongly coupled with vibration, dithering, dynamics, and environment effects especially for low-cost MEMS IMUs. To take these effects into account, a larger spectral density of the input noise should be used and in this dissertation they are determined empirically based on field test data.

After the system error dynamics and the spectral density of the input noise are determined, the discrete error model, i.e., the transition matrix and the process noise covariance matrix, can be calculated using Eq. (3-7) and Eq. (3-9).

5.2.1.2 Measurement Model

5.2.1.2.1 GPS Observations

For land vehicle applications, GPS velocities can be used to derive the forward velocity and heading information of the vehicle in the following manner.

$$V_f^{GPS} = \sqrt{(V_{Nn}^{GPS})^2 + (V_{Ne}^{GPS})^2 + (V_{Nd}^{GPS})^2} \quad (5-11)$$

$$\psi^{GPS} = \arctan\left(\frac{V_{Ne}^{GPS}}{V_{Nn}^{GPS}}\right) \quad (5-12)$$

where V_f^{GPS} is the GPS-derived forward velocity of the vehicle;

ψ^{GPS} is the GPS-derived heading of the vehicle; and

V_{Nn}^{GPS} , V_{Ne}^{GPS} , V_{Nd}^{GPS} are GPS velocities in the North, East and down directions.

The difference between the INS and GPS forward velocity and heading can be used as the Kalman filter measurement updates and the measurement model can be formed as follows:

$$\underbrace{\begin{bmatrix} V_f - V_f^{GPS} \\ \psi - \psi^{GPS} \end{bmatrix}}_{\mathbf{z}} = \underbrace{\begin{bmatrix} 1 & 0 & 0 & 0 & 0 \\ 0 & 0 & 0 & 1 & 0 \end{bmatrix}}_{\mathbf{H}} \underbrace{\begin{bmatrix} \delta V_f \\ \delta \phi \\ \delta \theta \\ \delta \psi \\ b_{A_{Bx}} \end{bmatrix}}_{\mathbf{x}} + \underbrace{\begin{bmatrix} v_{v_f^{GPS}} \\ v_{\psi^{GPS}} \end{bmatrix}}_{\mathbf{v}} \quad (5-13)$$

where $v_{v_f^{GPS}}$ and $v_{\psi^{GPS}}$ represent the measurement noises in the GPS-derived forward velocity and heading, respectively.

The covariance matrix of the measurement noise is given by

$$\mathbf{R} = \text{diag}\left(\sigma_{\delta V_f^{GPS}}^2 \quad \sigma_{\delta \psi^{GPS}}^2\right) \quad (5-14)$$

where $\sigma_{\delta V_f^{GPS}}$ is the standard deviation of the GPS-derived forward velocity error; and $\sigma_{\delta \psi^{GPS}}$ is the standard deviation of the GPS-derived heading error.

The standard deviation of the GPS-derived forward velocity error is basically determined based on GPS performance. For example, a typical value of $\sigma_{\delta V_f^{GPS}}$ in open-sky environments is about 0.1~0.2 m/s. For land vehicle applications under different GPS environments, the accuracy of GPS velocity is changing with signal degradation conditions and should be adjusted accordingly. Therefore, the fuzzy logic rule-based GPS data classification system developed in Chapter 4 is applied here to adapt the covariance of GPS velocity error based on the identified signal degradation conditions. Table 5.1 lists the standard deviation of the GPS velocity errors under different signal degradation conditions based on the field test data.

Since the GPS heading is derived from GPS velocities based on Eq. (5-12), its accuracy is highly correlated with the accuracy of GPS velocities. The standard deviation of the GPS heading error can be computed based on the following equation.

$$\sigma_{\delta\psi^{GPS}} = \frac{\sigma_{\delta V_f^{GPS}}}{V_f^{GPS}} \quad (5-15)$$

Under low speed dynamics and severe signal degradation conditions, however, the GPS heading is too noisy to be useful. Instead, it will deteriorate the Kalman filter heading estimation. In this dissertation, we have used a threshold to the GPS velocity and the difference between the GPS heading and the filter heading to eliminate this kind of measurements. More specifically, we will assign an extremely large value to $\sigma_{\delta\psi^{GPS}}$ when the GPS velocity is smaller than 1 m/s or the difference between the GPS heading and the filter heading is larger than 15 degrees.

Table 5.1: Adaptive $\sigma_{\delta V_f^{GPS}}$ values under different signal degradation conditions

Identified signal degradation condition	Low	Medium	High
$\sigma_{\delta V_f^{GPS}}$ (m/s)	0.1	0.5	2

5.2.1.2.2 Dynamics-Derived Observations

Besides the GPS updates, we can have additional dynamics-derived observations to correct the INS velocity and attitude by applying the dynamics knowledge aided inertial navigation algorithm developed in Chapter 4. These additional measurements are available to update the Kalman filter under certain vehicle dynamics such as stationary, straight-line motion, and cornering motion as follows:

1. Stationary mode: As summarized in Table 4.4, when the vehicle is stationary, a direct estimation of vehicle velocity and attitude information becomes feasible. In this mode, the measurement model can be formed as follows:

$$\underbrace{\begin{bmatrix} V_f - 0 \\ \phi - \phi^A \\ \theta - \theta^A \\ \psi - \psi^P \end{bmatrix}}_{\mathbf{z}} = \underbrace{\begin{bmatrix} 1 & 0 & 0 & 0 & 0 \\ 0 & 1 & 0 & 0 & 0 \\ 0 & 0 & 1 & 0 & 0 \\ 0 & 0 & 0 & 1 & 0 \end{bmatrix}}_{\mathbf{H}} \underbrace{\begin{bmatrix} \delta V_f \\ \delta \phi \\ \delta \theta \\ \delta \psi \\ b_{A_{Bx}} \end{bmatrix}}_{\mathbf{x}} + \underbrace{\begin{bmatrix} v_{V_f^{ZUPT}} \\ v_{\phi^A} \\ v_{\theta^A} \\ v_{\psi^P} \end{bmatrix}}_{\mathbf{v}} \quad (5-16)$$

where ψ^P is the yaw angle estimated by the Kalman filter at the previous epoch; ϕ^A and θ^A are the roll and pitch angles computed using accelerometer measurements after bias and noise removal; and $v_{V_f^{ZUPT}}$, v_{ϕ^A} , v_{θ^A} , and v_{ψ^P} represent the measurement noises for ZUPT, the accelerometer-derived roll and pitch, and the filter-derived yaw at the previous epoch, respectively.

The covariance matrix of the measurement noise is given by

$$\mathbf{R} = \text{diag}\left(\sigma_{\delta V_f^{ZUPT}}^2 \quad \sigma_{\delta \phi^A}^2 \quad \sigma_{\delta \theta^A}^2 \quad \sigma_{\delta \psi^P}^2\right) \quad (5-17)$$

where $\sigma_{\delta V_f^{ZUPT}}$ is the standard deviation of the ZUPT error; $\sigma_{\delta \phi^A}$ and $\sigma_{\delta \theta^A}$ are the standard deviation of the accelerometer-derived roll and pitch error; and $\sigma_{\delta \psi^P}$ is the standard deviation of the filter-derived yaw error at the previous epoch.

Since the vehicle has zero velocity and constant heading during stationary periods, we can assign a very small value to $\sigma_{\delta V_f^{ZUPT}}$. In order to constrain the heading estimate to the previously derived heading during stationary periods, we also assign a very small value to $\sigma_{\delta \psi^P}$. For the determination of $\sigma_{\delta \phi^A}$ and $\sigma_{\delta \theta^A}$, they are assigned small values of 0.2 degrees because the accelerometer-derived roll and pitch after bias compensation are much accurate compared to the gyro-derived roll and pitch which have large drift errors.

2. Straight-line motion mode: When the vehicle is moving straight, the accelerometer-derived roll is the only dynamics-derived measurement available to update the velocity and attitude filter. The measurement model is formed as follows:

$$\underbrace{\begin{bmatrix} \phi - \phi^A \end{bmatrix}}_{\mathbf{z}} = \underbrace{\begin{bmatrix} 0 & 1 & 0 & 0 & 0 \end{bmatrix}}_{\mathbf{H}} \underbrace{\begin{bmatrix} \delta V_f \\ \delta \phi \\ \delta \theta \\ \delta \psi \\ b_{A_{Bx}} \end{bmatrix}}_{\mathbf{x}} + \underbrace{\begin{bmatrix} v_{\phi^A} \end{bmatrix}}_{\mathbf{v}} \quad (5-18)$$

The covariance matrix of the measurement noise is given by

$$\mathbf{R} = \sigma_{\delta\phi^A}^2 \quad (5-19)$$

Similarly, we assign a small value of 0.2 degrees to $\sigma_{\delta\phi^A}$ because the accelerometer-derived roll after bias compensation is accurate enough to correct the drift errors of the gyro-derived roll.

3. Cornering motion mode: When the vehicle is making a turn, the forward velocity is the only dynamics-derived measurement available to update the velocity and attitude filter. The measurement model is formed as follows:

$$\underbrace{\begin{bmatrix} V_f - V_f^C \end{bmatrix}}_{\mathbf{z}} = \underbrace{\begin{bmatrix} 1 & 0 & 0 & 0 & 0 \end{bmatrix}}_{\mathbf{H}} \underbrace{\begin{bmatrix} \delta V_f \\ \delta \phi \\ \delta \theta \\ \delta \psi \\ b_{A_{Bx}} \end{bmatrix}}_{\mathbf{x}} + \underbrace{\begin{bmatrix} v_{V_f^C} \end{bmatrix}}_{\mathbf{v}} \quad (5-20)$$

where V_f^C is the dynamics-derived forward velocity after the bias and noise removal; and $v_{v_f^C}$ represents the measurement noise of V_f^C .

The covariance matrix of the measurement noise is given by

$$\mathbf{R} = \sigma_{\delta V_f^C}^2 \quad (5-21)$$

where $\sigma_{\delta V_f^C}$ is the standard deviation of the dynamics-derived forward velocity error.

As stated in Chapter 4, the accuracy of the dynamics-derived forward velocity is mainly dependent on the quality of the y-axis accelerometer and the z-axis gyro measurements as well as the vibration and road ruggedness effects during the cornering motion. Therefore, $\sigma_{\delta V_f^C}$ is defined empirically according to the field test data.

It should be noted that the x-axis and y-axis accelerometer biases must be determined first in order to correctly derive the above dynamics-based observations. As shown in Eq. (5-9), the x-axis accelerometer bias is already modeled in the filter and can be estimated when GPS velocity updates are available. For the y-axis accelerometer bias estimation, in this dissertation we have developed a statistical approach based on the forward velocity computation model described in Eq. (4-26). Arranging the y-axis acceleration term to the left-hand side of the equation, we rewrite Eq. (4-26) as follows:

$$A_{By} = \omega_{Bz} V_f - g \sin \phi \cos \theta \quad (5-22)$$

As mentioned previously, the bias term in the z-axis gyro measurement (ω_{Bz}) can be removed directly if the vehicle is stationary. The corrected V_f , ϕ , and θ can be estimated by the velocity and attitude Kalman filter when GPS updates are available.

After the Kalman filter reaches a steady-state condition, more accurate estimates can be obtained as well. Therefore, applying these corrected terms into Eq. (5-22), we can calculate the unbiased y-axis body acceleration. Furthermore, taking the difference between this unbiased acceleration and the y-axis accelerometer measurement, we can compute the acceleration error that is mainly contributed by the accelerometer bias and noise as well as the noises from ω_{Bz} , V_f , ϕ , and θ . A simple approach to resolve the accelerometer bias is to remove the noise effects by averaging a set of data and use this mean value as the constant part of the y-axis accelerometer bias. The estimate of the y-axis accelerometer bias, $\hat{b}_{A_{By}}$, using the statistical approach is given by the following equation.

$$\hat{b}_{A_{By}} = \frac{1}{M} \sum_{t_k=1}^M A_{By}(t_k) - \bar{\omega}_{Bz}(t_k) \hat{V}_f(t_k) + g \sin \hat{\phi}(t_k) \cos \hat{\theta}(t_k) \quad (5-23)$$

where A_{By} is the y-axis accelerometer measurement; $\bar{\omega}_{Bz}$ is the z-axis bias-removed gyro measurement; \hat{V}_f , $\hat{\phi}$, and $\hat{\theta}$ are the estimates of the velocity, roll and pitch given by the Kalman filter; and M is number of data used for averaging process.

In order to estimate the y-axis accelerometer bias more accurately, only the data obtained during the cornering motion and after the convergence of the Kalman filter are used for bias computation. This is because A_{By} and $\bar{\omega}_{Bz}$ have higher signal-to-noise ratio during the cornering motion and \hat{V}_f , $\hat{\phi}$ and $\hat{\theta}$ have better accuracy after the convergence of the Kalman filter. The obtainable accuracy of the accelerometer bias estimates and the dynamics-derived observations for a low-cost MEMS IMU are to be presented in Chapter 6.

It should be noted that the accuracy of some dynamics-derived observations, including stationary tilt, straight-line roll and cornering velocity, are correlated with inertial sensor biases and the estimated pitch and roll as shown in Eq. (4-23), Eq. (4-24) and Eq. (4-27). This will violate the assumption of the uncorrelated property between measurement noise

and process noise in the Kalman filter if using these dynamics-derived observations to estimate the inertial sensor biases and tilt. In this dissertation the x-axis and y-axis accelerometer biases are estimated by the Kalman filter and a statistical approach using only GPS data in open-sky environments while the gyro biases are estimated during the previous stationary period. In GPS challenging environments the accelerometer bias estimation is disabled and the previously estimated inertial sensor biases are applied to correct the dynamics-derived observations which are used to update the Kalman filter. This strategy not only ensures the stability of bias estimation but also avoids the dynamics-derived measurements to be correlated with the Kalman filter system state, i.e. the x-axis accelerometer bias. As the pitch and roll angles are generally small in land vehicle environments, the correlation between the dynamics-derived measurements and the tilt errors is not significant. Compared to the unaided INS navigation which has large error drift, it is worthy to use these dynamics-derived measurements to bound the INS velocity and tilt errors even they are slightly correlated.

5.2.1.2.3 Compass Observation

During GPS outages, although the dynamics-derived observations can control and correct the INS velocity and tilt errors, the heading error is still un-removed and will drift with time due to the lack of a direct heading measurement. If a magnetic compass is available, this problem can be solved by adding the calibrated compass heading into the measurement model. For example, in the straight-line motion mode the modified measurement model with both dynamics-derived and compass observations can be written as follows:

$$\underbrace{\begin{bmatrix} \phi - \phi^A \\ \psi - \psi^N \end{bmatrix}}_{\mathbf{z}} = \underbrace{\begin{bmatrix} 0 & 1 & 0 & 0 & 0 \\ 0 & 0 & 0 & 1 & 0 \end{bmatrix}}_{\mathbf{H}} \underbrace{\begin{bmatrix} \delta V_f \\ \delta \phi \\ \delta \theta \\ \delta \psi \\ b_{A_{Bx}} \end{bmatrix}}_{\mathbf{x}} + \underbrace{\begin{bmatrix} v_{\phi^A} \\ v_{\psi^N} \end{bmatrix}}_{\mathbf{v}} \quad (5-24)$$

where ψ^N is the compass heading after the neural networks calibration; and v_{ψ^N} represents the measurement noise of the calibrated compass heading.

The covariance matrix of the measurement noise is given by

$$\mathbf{R} = \text{diag}(\sigma_{\delta\phi^A}^2, \sigma_{\delta\psi^N}^2) \quad (5-25)$$

where $\sigma_{\delta\phi^A}$ and $\sigma_{\delta\psi^N}$ are the standard deviations of the accelerometer-derived roll error and the calibrated compass heading error, respectively.

With the aiding from the neural networks compass calibration developed in Chapter 4, the bias and scale factor error can be removed from the compass heading and the remained errors include only noise, disturbance and the projection error due to tilt compensation error. For land vehicle applications, these remained errors are related to vehicle dynamics. For example, when the vehicle is stationary, the projection error is much small because the tilt is corrected by the accurate accelerometer-derived tilt angles. Therefore, the dynamics knowledge is applied to adapt the standard deviation of the calibrated compass heading error as shown in Table 5.2. To avoid using the erroneous or disturbed compass heading to update the filter, a check on the difference between the compass heading and the filter heading is performed. When the difference is larger than 5 degrees, we assign an extremely large value to $\sigma_{\delta\psi^N}$ to skip the compass heading update.

Table 5.2: Adaptive $\sigma_{\delta\psi^N}$ values under different dynamics

Vehicle Dynamics	Stationary	Straight-line Motion	Cornering Motion
$\sigma_{\delta\psi^N}$ (deg.)	0.3	3	5

5.2.2 Position Filter

5.2.2.1 Dynamics Model

The INS position filter is designed to integrate GPS position with INS velocity to output an optimal position solution that combines the INS short-term accuracy with the GPS long-term accuracy. Because only the horizontal position is interested in land vehicle applications, the position and velocity in the North and East directions are modeled as the system states in the position filter. Obviously, the state of position is the integration of velocity and the state of velocity is the integration of acceleration. For simplicity, we model the vehicle velocity as a constant with an input noise driven by the vehicle acceleration. Therefore, the system model for the INS position filter is defined as follows:

$$\underbrace{\begin{bmatrix} \dot{P}_{Nn} \\ \dot{P}_{Ne} \\ \dot{V}_{Nn} \\ \dot{V}_{Ne} \end{bmatrix}}_{\dot{\mathbf{x}}} = \underbrace{\begin{bmatrix} 0 & 0 & 1 & 0 \\ 0 & 0 & 0 & 1 \\ 0 & 0 & 0 & 0 \\ 0 & 0 & 0 & 0 \end{bmatrix}}_{\mathbf{F}} \underbrace{\begin{bmatrix} P_{Nn} \\ P_{Ne} \\ V_{Nn} \\ V_{Ne} \end{bmatrix}}_{\mathbf{x}} + \underbrace{\begin{bmatrix} 0 & 0 \\ 0 & 0 \\ 1 & 0 \\ 0 & 1 \end{bmatrix}}_{\mathbf{G}} \underbrace{\begin{bmatrix} w_{V_{Nn}} \\ w_{V_{Ne}} \end{bmatrix}}_{\mathbf{u}} \quad (5-26)$$

where P_{Nn} and P_{Ne} are the North and East position states; V_{Nn} and V_{Ne} are the North and East velocity states; and $w_{V_{Nn}}$ and $w_{V_{Ne}}$ are the driving noise for the North and East velocity states.

The spectral density matrix of the input white noise \mathbf{u} is given by

$$\mathbf{Q} = \text{diag}(q_{V_{Nn}} \quad q_{V_{Ne}}) \quad (5-27)$$

where $q_{V_{Nn}}$ and $q_{V_{Ne}}$ are the spectral densities of the North and East velocities, respectively, which indicate the change of the vehicle velocity, i.e., the vehicle acceleration. Thus, they are determined based on the land vehicle dynamics.

After the system dynamics and the spectral density of the input noise are determined, the discrete error model in terms of transition matrix and process noise covariance matrix can be calculated using Eq. (3-7) and (3-9).

5.2.2.2 Measurement Model

5.2.2.2.1 Model with GPS

When GPS is available, the measurement updates for the position filter include the GPS position and the corrected INS velocity both in the North and East directions. The measurement model is defined as follows:

$$\underbrace{\begin{bmatrix} P_{Nn}^{GPS} \\ P_{Ne}^{GPS} \\ V_{Nn}^{INS} \\ V_{Ne}^{INS} \end{bmatrix}}_{\mathbf{z}} = \underbrace{\begin{bmatrix} 1 & 0 & 0 & 0 \\ 0 & 1 & 0 & 0 \\ 0 & 0 & 1 & 0 \\ 0 & 0 & 0 & 1 \end{bmatrix}}_{\mathbf{H}} \underbrace{\begin{bmatrix} P_{Nn} \\ P_{Ne} \\ V_{Nn} \\ V_{Ne} \end{bmatrix}}_{\mathbf{x}} + \underbrace{\begin{bmatrix} v_{P_{Nn}^{GPS}} \\ v_{P_{Ne}^{GPS}} \\ v_{V_{Nn}^{INS}} \\ v_{V_{Ne}^{INS}} \end{bmatrix}}_{\mathbf{v}} \quad (5-28)$$

where P_{Nn}^{GPS} and P_{Ne}^{GPS} are the North and East GPS positions; V_{Nn}^{INS} and V_{Ne}^{INS} are the corrected North and East INS velocities which are computed using the velocity and attitude filter outputs based on Eq. (4-18) and (4-19); $v_{P_{Nn}^{GPS}}$ and $v_{P_{Ne}^{GPS}}$ represent the measurement noises of the North and East GPS positions; and $v_{V_{Nn}^{INS}}$ and $v_{V_{Ne}^{INS}}$ represent the measurement noises of the corrected North and East INS velocities.

The covariance matrix of the measurement noise is given by:

$$\mathbf{R} = \begin{bmatrix} \mathbf{R}_{2 \times 2}^{GPS} & \mathbf{0}_{2 \times 2} \\ \mathbf{0}_{2 \times 2} & \mathbf{R}_{2 \times 2}^{INS} \end{bmatrix} \quad (5-29)$$

where $\mathbf{R}_{2 \times 2}^{GPS}$ and $\mathbf{R}_{2 \times 2}^{INS}$ are the covariance matrices of GPS position errors and corrected INS velocity errors, respectively.

Based on the above dynamics and measurement models, the position filter is actually performing a linear weighted combination of the GPS position and the corrected INS velocity using the Kalman gain. To compute the correct Kalman gain, the GPS position error and the corrected INS velocity error must be modeled properly. Since the corrected North and East INS velocities are computed using the outputs from the velocity and attitude Kalman filter based on Eq. (4-18) and (4-19), the accuracy of the corrected INS velocities is mainly determined by the filter performance. $\mathbf{R}_{2 \times 2}^{INS}$ can be determined by the propagation of error covariances of the forward velocity and heading obtained from the velocity and attitude Kalman filter. In terms of the GPS position error modelling, it is difficult to be accurate for land vehicle applications under various signal degradation conditions. This is because the GPS measurement is likely corrupted by multipath, echo-only signal and high code noise. Therefore, the GPS position errors vary with very short correlation time and the accurate estimation of a priori knowledge about the position errors and noise statistics becomes a challenge. To model the GPS position error more appropriately, the innovation-based adaptive filtering algorithm with unknown measurement noise covariance described in Chapter 3 and the fuzzy logic rule-based GPS data classification system developed in Chapter 4 have been integrated to adapt the covariance of the GPS position error.

The innovation-based adaptive measurement noise covariance $\hat{\mathbf{R}}_k$ is calculated based on Eq. (3-20). It should be noted that the window size in Eq. (3-20) needs to be properly determined so that the statistic of the innovation sequence is correctly estimated and in turn the computed $\hat{\mathbf{R}}_k$ is able to represent the actual measurement noise covariance. The choice of window size is usually application dependent. For land vehicle applications in urban areas the GPS position accuracy is changing rapidly as the vehicle is moving through various GPS environments. Therefore, a small window size should be used to enable the adaptive Kalman filter to correctly trace high-frequency changes of the GPS position accuracy. In this dissertation a window size of 5 epochs was chosen based on the GPS test performance in a typical North American urban area.

Ideally, the adaptive Kalman filter is expected to adapt the measurement noise covariance to environments to improve the estimation performance based on the residuals between the actual measurement from GPS and the predicted measurement from the integration filter. In GPS challenging environments, however, the adaptive filter might not work optimally due to the difficulty of separating the filter position error from GPS position error. This would happen in two cases. The first case is when the filter works without GPS position updates or with erroneous GPS position updates for certain periods of time. During GPS outages the filter position is basically the integration of the INS velocity which leads to a position drift. When erroneous GPS measurements last over several consecutive epochs, the innovation sequence is large and the Kalman gain becomes small, which leads to the filter working similarly to the GPS outage case. As a result, the filter position has a drift error and will bias the innovation sequence. The second case is when the GPS position is drifting and changing slowly over time. In this situation, this kind of GPS position errors is undetectable by the adaptive Kalman filter since the innovation sequence will remain relatively small. As a result, a large Kalman gain on measurements will cause the filter position to drift with the biased GPS position. When good GPS updates are available, for both cases, the innovation sequence becomes incorrect and unreliable because the predicted measurement from the integration filter is biased. Therefore, the adaptive Kalman filter cannot work appropriately because of using the exaggerated measurement noise covariance.

To remedy this problem and to improve the adaptive filtering performance, the GPS data classification system developed in Chapter 4 is used to modify the measurement noise covariance computed by the innovation-based adaptive estimation from Eq. (3-20). The basic idea behind this modification is to use the knowledge of the GPS signal degradation condition which is correlated to GPS statistical performance to weight the innovation-based adaptive measurement noise covariance. More specifically, for each channel (North and East), we decrease the innovation-based adaptive measurement noise covariance to the power of 0.5 and 0.75 when a GPS position is obtained under the low and medium signal-degraded conditions. Therefore, when a good GPS position is available, the adaptive measurement noise covariance is reduced to better characterize real GPS

performance and in turn to speed the convergence of the filter position to the GPS position. For example, if the filter position is biased by 45 m and a low signal-degraded GPS position with accuracy of 5 m is available to update the filter, according to Eq. (3-20) the traditional innovation-based adaptive measurement noise covariance will be around 1600~2500 m² which is incorrect and unreliable. With the proposed AI-enhanced method, the modified measurement noise covariance becomes around 40~50 m² which means the estimated GPS position accuracy is around 6~7 m close to the actual GPS position accuracy.

In addition to the information about GPS signal degradation conditions, the knowledge of vehicle dynamics can be used to modify the adaptive measurement noise covariance as well. When a vehicle is stationary, the vehicle position should be unchanged but the GPS position solution may drift and change slowly over time due to the smoothing feature provided by the in-receiver filter. As mentioned previously, this kind of GPS position errors are undetectable by the innovation-based adaptive Kalman filter and will subsequently lead to erroneous solutions. To resist the drift of the filter position, we assign an extremely large measurement noise covariance for the GPS position when the vehicle is stationary. Table 5.3 lists the AI-based modification of the adaptive measurement noise covariance for GPS positions based on the signal degradation condition and vehicle dynamics.

Table 5.3: AI-enhanced adaptive measurement noise covariance for GPS position

Vehicle dynamics	Non-stationary			Stationary
Signal degradation condition	Low	Medium	High	All
Modified measurement noise covariance	$\hat{\mathbf{R}}_k^{0.5}$	$\hat{\mathbf{R}}_k^{0.75}$	$\hat{\mathbf{R}}_k$	10^6

$\hat{\mathbf{R}}_k$: the innovation-based adaptive measurement noise covariance

5.2.2.2.2 Model without GPS

When GPS updates are unavailable due to signal blockages, only the corrected INS velocities are available to update the position filter. In this case the measurement model is reduced to

$$\underbrace{\begin{bmatrix} V_{Nn}^{INS} \\ V_{Ne}^{INS} \end{bmatrix}}_z = \underbrace{\begin{bmatrix} 0 & 0 & 1 & 0 \\ 0 & 0 & 0 & 1 \end{bmatrix}}_H \underbrace{\begin{bmatrix} P_{Nn} \\ P_{Ne} \\ V_{Nn} \\ V_{Ne} \end{bmatrix}}_x + \underbrace{\begin{bmatrix} v_{V_{Nn}^{INS}} \\ v_{V_{Ne}^{INS}} \end{bmatrix}}_v \quad (5-30)$$

The corresponding covariance matrix of the measurement noise is determined by the propagation of error covariances of the forward velocity and heading obtained from the velocity and attitude Kalman filter. In this case, the position filter will rely on the corrected INS velocity and the constant velocity model with the acceleration driven input noise to estimate the vehicle position.

5.3 Construction of An Intelligent Integration Algorithm

The previous two sections have described the cascaded integration scheme and the design of the AI-enhanced Kalman filters. This section presents the construction of the intelligent integration algorithm and explains the data processing flow. The intelligent integration algorithm employs two cascaded Kalman filters aided by three AI-based enhancement modules on a loosely coupled closed-loop integration scheme. The architecture of the intelligent integration algorithm is presented in Figure 5.2. Basically, the integration procedure is accomplished by two-step data processing: sensor-level data processing and filter-level data fusion. In the sensor-level data processing, the raw data from each sensor are processed independently to generate navigation states (attitude, velocity and position) and knowledge-based information (status of vehicle dynamics and GPS signal degradation condition). More specifically, the raw data from MEMS IMU are processed by the fuzzy expert vehicle dynamics identification system to provide the information of vehicle dynamics including stationary, straight-line motion and cornering motion. Such information is further applied to trigger the estimation of gyro biases and dynamics-derived observations and to adapt the velocity and attitude filter, as indicated by the dash line. Every time when the vehicle is stationary, the three-axis gyro biases can be estimated using raw gyro data. Thus, the gyro biases can be removed from the raw

measurements and the INS attitude and velocity are computed using the raw accelerometer data and the bias-removed gyro data based on the land vehicle motion model. In the meantime, the dynamics-based observations can also be computed by using IMU measurements and the outputs of the velocity and attitude filter under specific vehicle dynamics.

For compass data, the three-axis magnetic measurements are integrated with the tilt estimates provided by the velocity and attitude filter to generate the compass heading based on heading computation equations. Then, the computed compass heading is calibrated by the trained neural networks before they are used to the filter-level data fusion. For GPS data, GPS receiver velocity and position solutions are directly used. The signal strength measure and satellite geometry information are processed by the fuzzy logic rule-based GPS data classification system to provide the information of signal degradation condition. This information is further used for adapting the filter-level data fusion, as indicated by the dash line.

For the filter-level data fusion, the INS velocity and attitude filter will integrate the INS attitude and velocity with the GPS velocity and heading, the dynamics-derived observation and the calibrated compass heading to generate the corrected attitude and velocity. Dependent on GPS environments, the velocity and attitude filter works in two modes: GPS-only update mode and full update mode. The filter operates in the GPS-only update mode under open-sky environments and in the full update mode under signal-degraded and/or signal-blocked environments. Under open-sky environments, GPS can provide reliable and accurate measurement updates for the velocity and attitude filter. After reaching a steady-state condition, the Kalman filter can provide good estimation of the x-axis accelerometer bias and the vehicle attitude and velocity. Meanwhile, the y-axis accelerometer bias can also be estimated using the corrected velocity and tilt as well as the raw data from IMU. In addition, the corrected heading can be used as the reference heading to train the neural networks for the compass heading error modelling.

Under GPS challenging environments, GPS measurements are corrupted by multipath, signal degradation and signal cross-correlation. Accurate estimation of the accelerometer biases and the navigation errors using the Kalman filter is usually infeasible due to the lack of continuously accurate GPS velocity solutions. In this condition, the integration algorithm will stop the estimation of the accelerometer biases and the training of the neural networks. The last estimated accelerometer biases and the trained neural networks during open-sky navigation are used to correct dynamics-derived observations and to calibrate compass headings, respectively. Thus, the velocity and attitude filter can use the corrected dynamics-derived observations and the calibrated compass heading as the additional measurement updates to correct INS velocity and attitude. GPS velocity and heading solutions if available will still be used to update the velocity and attitude filter with adaptive measurement covariance.

In the position domain, the INS position filter is used to integrate the corrected attitude and velocity with the GPS position. As mentioned previously, the innovation-based adaptive filtering algorithm aided by the information of GPS signal degradation conditions and the knowledge of vehicle dynamics can be used to adapt the covariance of GPS position error, thus this filter can adaptively operate under various GPS environments. When GPS is unavailable, the position filter will rely on the corrected INS attitude and velocity to derive the dead-reckoning position solution.

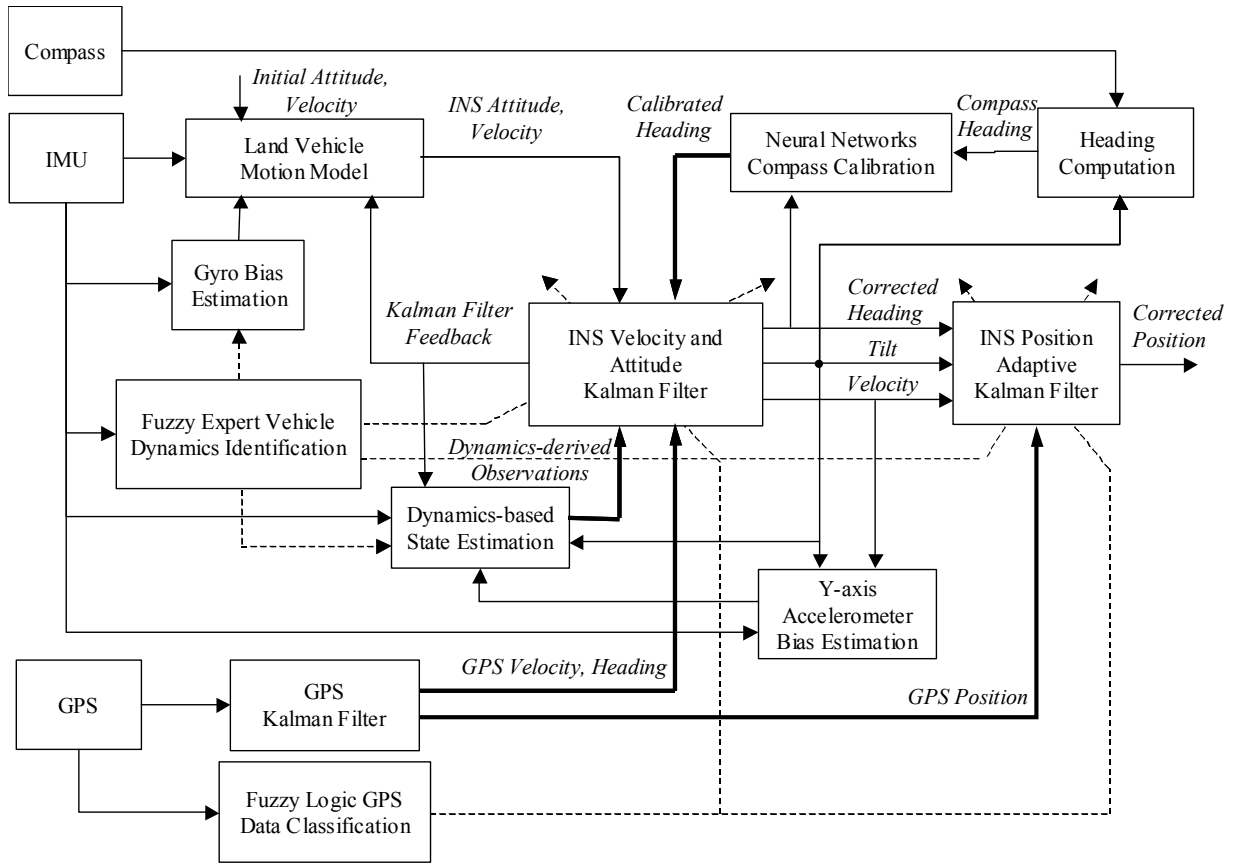


Figure 5.2: Architecture of the intelligent integration algorithm

Chapter 6

Test Results in Open Areas

This chapter describes the test and analysis results of the proposed intelligent integration algorithm under open area environments. The performance evaluation is carried out in a post-mission processing mode. A developed MATLAB-based program which implements the proposed integration algorithm with real-time processing routines has been used to process the data collected from the low-cost MEMS IMU and GPS in field tests and to generate the integrated navigation solutions. Details of test set-up as well as data collection and processing procedures are presented first, followed by two types of performance analysis: evaluation of the navigation performance with and without GPS updates.

6.1 Test Description

The test system set-up is shown in Figure 6.1. The low-cost sensors used in the test included an Xsens MT9 MEMS IMU and a SiRF Star II Xtrac high sensitivity GPS receiver. The MT9 is a miniature inertial measurement unit providing serial digital output of 3D acceleration, 3D rate of turn and 3D Earth-magnetic field data. The SiRF HSGPS receiver is a low-cost single-frequency 12-channel evaluation receiver which provides code-based single point positioning solutions. The specifications of the SiRF HSGPS and MT9 are shown in Table 6.1 and Table 6.2, respectively. A laptop running a C++ data acquisition program developed by the author was used to collect the data from the IMU and GPS through two serial ports. The data output rate was set as 20 Hz for the MT9 and 1 Hz for the HSGPS. The data acquisition software will tag IMU and GPS data with computer time when they were received at the serial ports, respectively. The tagged time is used for the time synchronization of IMU and GPS data. The time synchronization accuracy is at about the 10 ms level. For land vehicle applications, since general vehicle

dynamics is not too high, the estimation error due to the time synchronization error is negligible compared to the performance of the low-cost MEMS IMU. A high precise INS/GPS integration system consisting of a tactical-grade Honeywell HG1700 IMU and a high performance NovAtel OEM4 dual frequency GPS receiver was used to provide geo-reference solutions. A GIPSI data acquisition system (GIPSI DA) developed by the Terramatics Inc. was used to collect the 100 Hz IMU data from the HG1700 and 1 Hz GPS data from the OEM4. The GIPSI DA will time-tag IMU data with GPS 1PPS time to perform the time synchronization between the IMU and GPS data.

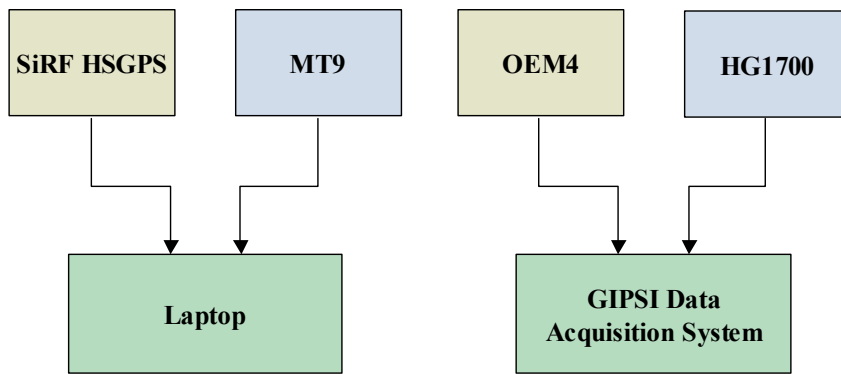


Figure 6.1: System set-up for open area tests

Table 6.1: SiRF HSGPS specifications (www.sirf.com)

Characteristic	Value
Position accuracy*	< 5m
Tracking	L1, C/A code
Channels	12
Tracking sensitivity**	16 dB-Hz
Hot start sensitivity**	23 dB-Hz
Warm start sensitivity**	28 dB-Hz
Cold start sensitivity**	32 dB-Hz

* A typical value based on 24-hour open sky static test.

** The sensitivity value is specified at the correlator. On a SiRFstarIIe/LP Evaluation Receiver with the supplied antenna, 32 dB-Hz is equivalent to -142 dBm or -172 dBW. Other board and antenna characteristics will vary.

Table 6.2: MT9 specifications (www.xsens.com)

Sensor	Gyro	Accelerometer	Magnetometer
Measurement unit	deg./s	m/s ²	MGauss
Operating range	+/- 900	+/- 20	+/- 750
Scale factor linearity (% of operating range)	0.1	0.2	1
Bias stability (1 σ)	5	0.02	0.5
Noise (RMS)	0.7	0.01	4.5
Alignment error (deg.)	0.1	0.1	0.1

The test system was installed on the University of Calgary's test van. The MT9 and HG1700 were mounted tightly on the floor of the test van. There are about half metre installation distance between each other to avoid interference between the MT9's magnetic sensors and the HG1700. The SiRF HSGPS antenna and OEM4 antenna were mounted on the roof of the van vertically above the MT9 and HG1700, respectively. Comparing to the obtainable position accuracy given by the low-cost MT9 and GPS, the position error due to this installation distance between the tested system and the geo-reference system is negligible. Pictures of the test van and the equipment set-up are shown in Figure 6.2.

The test was conducted at the University of Calgary Parking Lot #10 with an open-sky environment, on April 25, 2005. The purpose of the open area test is not only to assess the integration performance using clean GPS updates but also to examine how much the specific dynamics in urban driving conditions such as stationary, straight-line motion and cornering motion can improve the stand-alone inertial navigation performance. Thus, a test trajectory with eight cornering shapes and four virtual stop signs was chosen to mimic urban driving conditions as shown in Figure 6.3. Before tests on the selected trajectory, we performed an about 15-minute static initialization and then drove the vehicle on a S-turn trajectory couple times to make the geo-reference system reach a steady-state condition. After that, ten data collection runs on the selected trajectory were performed, each starting with about one minute static followed by about three minutes driving and ten seconds stop at each virtual stop sign.

The data collected from the HG1700 and OEM4 were processed by the P3-INS software package developed by the Positioning and Mobile Information System (PMIS) group in the Department of Geomatics Engineering at the University of Calgary to provide reference attitude, velocity and position information. The P3-INS integrates precise point positioning (PPP) with inertial technologies to generate geo-reference solutions without requiring the data from GPS reference stations. It determines position, velocity and attitude based on the integration of inertial data and un-differenced observations from a single GPS receiver. It can provide globally attainable accuracy for position at the centimetre to decimetre level and for attitude at the several arc min level (Zhang and Gao 2005). The data collected from the low-cost MT9 and SiRF HSGPS were processed by the MATLAB-based program which implements the proposed integration algorithm with real-time processing routines to generate the low-cost integrated navigation solutions. The geo-reference solutions were down sampled to 20 Hz and synchronized with the low-cost integrated navigation solutions based on GPS time using linear interpolation. By comparing the synchronized low-cost integrated solutions with the geo-reference solutions, we can assess the performance of the proposed integration algorithm in terms of attitude, velocity and position accuracy.

6.2 Results with GPS Updates

The first performance analysis is to assess the performance of the integration system when GPS is available. In this case, GPS data are used to update the INS Kalman filters to estimate accelerometer bias and to correct INS attitude, velocity and position. In the meantime, the corrected heading is used as the reference heading to train the neural networks for modelling the compass heading error. In the following sections, the performance analysis of the accelerometer bias estimation and the integrated navigation solutions are presented first, followed by the training performance of the neural networks for the compass heading error modelling.

6.2.1 Performance Analysis of Integrated Navigation

6.2.1.1 Accelerometer Bias Estimation Accuracy

The results of the x-axis accelerometer bias estimation from the sample run #4 are given in Figure 6.4. As shown, the estimates of the x-axis accelerometer bias converge to a constant value after the Kalman filter reaches a steady-state condition. The time for bias estimation convergence is mainly dependent on the degree of observability which is correlated to the vehicle dynamics change, usually the higher the dynamics change the shorter the convergence time. In our tests, the filter took about 1.5 minutes to reach a steady-state condition since the vehicle had frequent acceleration, deceleration and cornering motion on the selected test route. For the y-axis accelerometer bias estimation, as mentioned in Chapter 5, it has been assumed as a constant and is determined by averaging the estimates obtained during the cornering motion and after the convergence of the Kalman filter. Figure 6.5 shows the y-axis accelerometer bias estimation results from the same sample run. We notice that although the variation of the epoch-by-epoch bias estimates is large due to the high noise level presented in the MEMS measurements, the average value of all estimates over certain periods of time still can provide a reasonably good estimate of the y-axis accelerometer bias.

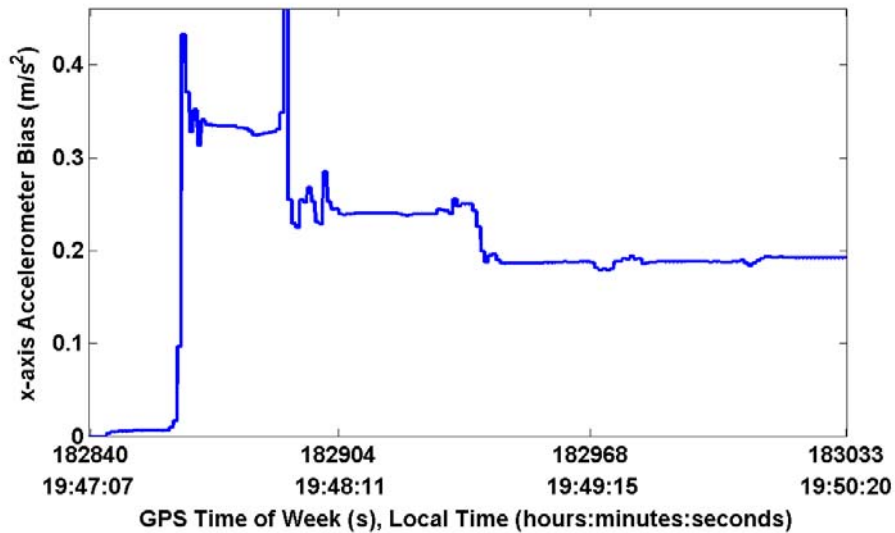


Figure 6.4: Estimation results of accelerometer bias (x-axis)

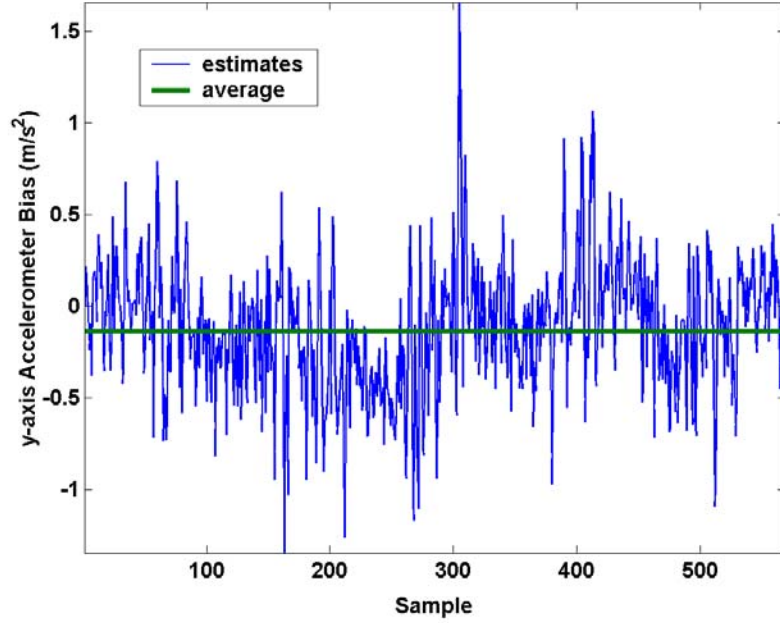


Figure 6.5: Estimation results of accelerometer bias (y-axis)

To assess the accuracy of the estimated accelerometer bias, the true bias should be determined first. Since it is very difficult to perform a lab calibration in the field test, we have developed an experimental approach to calculate the true bias by comparing the MT9 accelerometer measurements with the reference tilt provided by the HG1700/OEM4 geo-reference system when the vehicle is static. The equations for computing the true biases on the x-axis and y-axis accelerometers are given as follows:

$$\tilde{b}_{A_{Bx}} = g \sin^{-1} \left(\sin^{-1} \left(\frac{A_{Bx}^s}{g} \right) - \tilde{\theta}^s \right) \quad (6-1)$$

$$\tilde{b}_{A_{By}} = -g \sin^{-1} \left(-\sin^{-1} \left(\frac{A_{By}^s}{g} \right) - \tilde{\phi}^s \right) \quad (6-2)$$

where $\tilde{b}_{A_{Bx}}$ and $\tilde{b}_{A_{By}}$ are the computed true biases of the x-axis and y-axis accelerometers;

A_{Bx}^s and A_{By}^s are the stationary measurements from the x-axis and y-axis accelerometers;

$\tilde{\theta}^s$ and $\tilde{\phi}^s$ are the stationary pitch and roll provided by the HG1700/OEM4 geo-reference system; and g is the gravitational constant.

To remove the noise effects and to estimate the constant part of the bias, we calculate the mean value of all epoch-by-epoch bias estimates during the stationary periods and use it as the final estimate of the true bias. Shown in Figure 6.6 and Figure 6.7 are the estimation results of the true biases of the same sample run for the x-axis and y-axis accelerometers, respectively. We observed that the variation of the epoch-by-epoch estimates of the true bias is identical to the noise level of the MT9 accelerometers' stationary measurements and is affected by vehicle vibrations. After data averaging, the accuracy of the computed true bias mainly depends on the tilt accuracy obtained from the HG1700/OEM4 geo-reference system which is at several arc min level. Converted from this tilt accuracy, the accuracy of the computed true bias is at about 0.01 m/s^2 which is high enough for the reference.

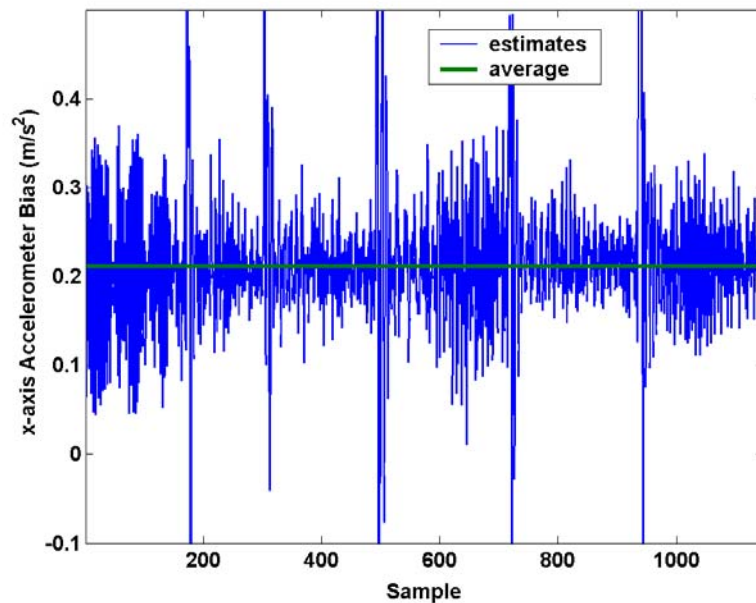


Figure 6.6: Estimation results of true accelerometer bias (x-axis)

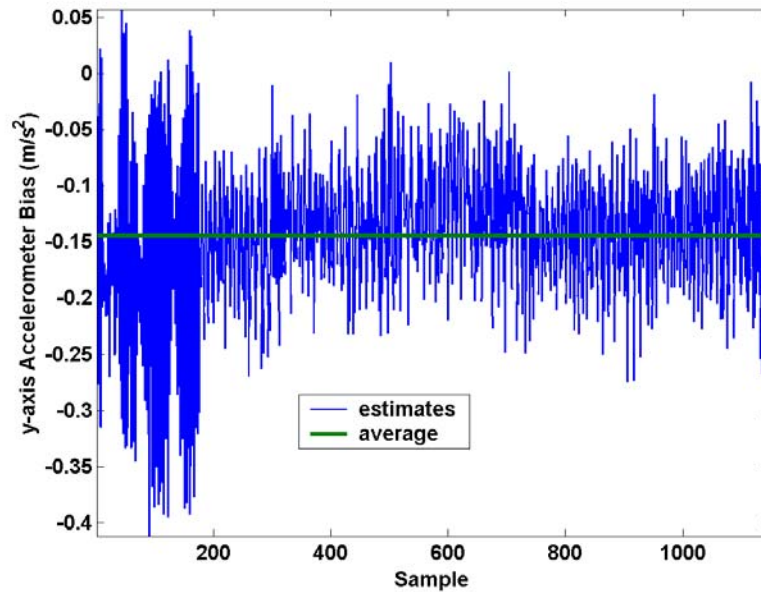


Figure 6.7: Estimation results of true accelerometer bias (y-axis)

Table 6.3 lists the estimated and true biases for each run of the test. The x-axis and y-axis accelerometer biases have been found properly estimated. The RMS error of the x-axis and y-axis estimated biases are about 0.032 m/s^2 and 0.038 m/s^2 , respectively. The x-axis bias estimation accuracy is better and more stable than the y-axis one. This could be explained by the fact that the y-axis bias is determined based on the average of a batch of accelerometer and gyro measurements as well as the Kalman filter velocity and tilt outputs. Thus, the accuracy of the y-axis bias estimation depends on not only the INS measurement quality but also the Kalman filter performance. On the other hand, the x-axis bias is estimated using the Kalman filter which is a recursive optimal estimator. If designed properly, the Kalman filter will converge and provide a steady-state estimate which is optimal in a statistical sense. In summary, the results demonstrate that the designed Kalman filter and the proposed systematic approach based on the land vehicle motion equation are able to provide good bias estimation for the low-cost MEMS inertial sensors.

Table 6.3: Accelerometer bias estimation accuracy

Test No.	X-axis Accelerometer Bias		Y-axis Accelerometer Bias	
	Reference (m/s ²)	Estimate (m/s ²)	Reference (m/s ²)	Estimate (m/s ²)
1	0.228	0.260	-0.124	-0.133
2	0.215	0.234	-0.136	-0.117
3	0.207	0.180	-0.144	-0.075
4*	0.211	0.192	-0.145	-0.137
5	0.206	0.204	-0.141	-0.215
6	0.201	0.216	-0.141	-0.157
7	0.202	0.228	-0.149	-0.174
8	0.198	0.253	-0.139	-0.117
9	0.199	0.241	-0.149	-0.122
10	0.203	0.186	-0.126	-0.120

* This is the sample run of test whose results are shown in Figure 6.4 and Figure 6.5.

6.2.1.2 Attitude Accuracy

Figure 6.8 through Figure 6.10 show the estimated and the reference pitch, roll and azimuth (heading) angles obtained from the same sample run #4. As shown in Figure 6.8 and Figure 6.9, the pitch and roll estimates converge to the reference pitch and roll respectively after the Kalman filter reaches a steady-state condition. As expected, the accuracy of the pitch and roll estimates degrade when the vehicle is stationary. This is because the estimation performance is proportional to the vehicle dynamics, i.e., the higher the vehicle dynamics the better the estimation performance. For the heading estimation, since it is directly observable from the measurements in the Kalman filter, the heading error can be instantly corrected when GPS heading updates are available. The heading accuracy of the integration system is therefore mainly dependent on the GPS heading accuracy.

Table 6.4 presents the statistical analysis of the attitude estimation accuracy based on the data from ten runs. It should be noted that only the data obtained after the convergence of the Kalman filter are used in the data analysis. As shown, the average RMS error is about 0.5 degrees for the pitch estimate and about 0.9 degrees for the roll estimate. The pitch accuracy is better than the roll accuracy because the roll state is less observable than the

pitch state in the applied Kalman filter. The heading accuracy is less than 1 degree which agrees with the theoretically obtainable performance provided by GPS. For example, considering the speed of the vehicle at 7 m/s and the typical GPS velocity accuracy at 0.1 m/s, we can calculate the corresponding GPS heading accuracy is equal to 0.81 degrees according to Eq. (5-15).

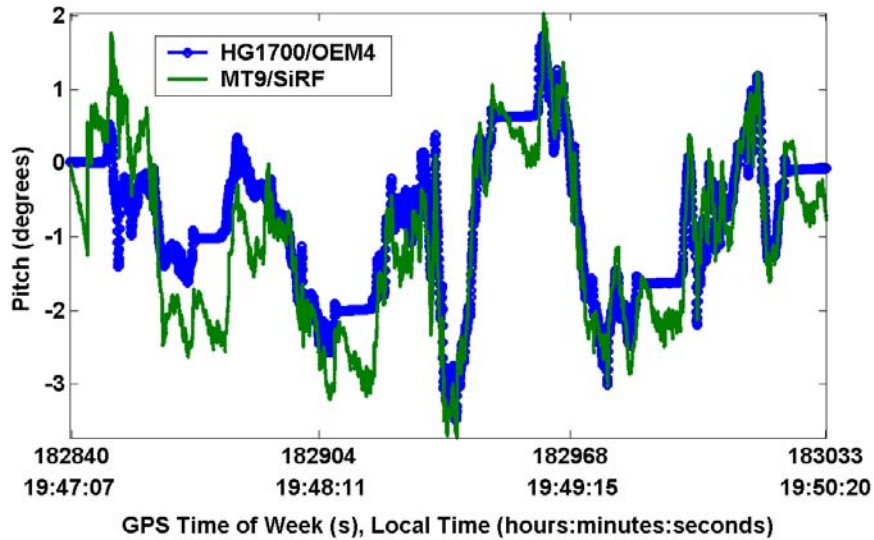


Figure 6.8: Estimation results of pitch (INS/GPS integration)

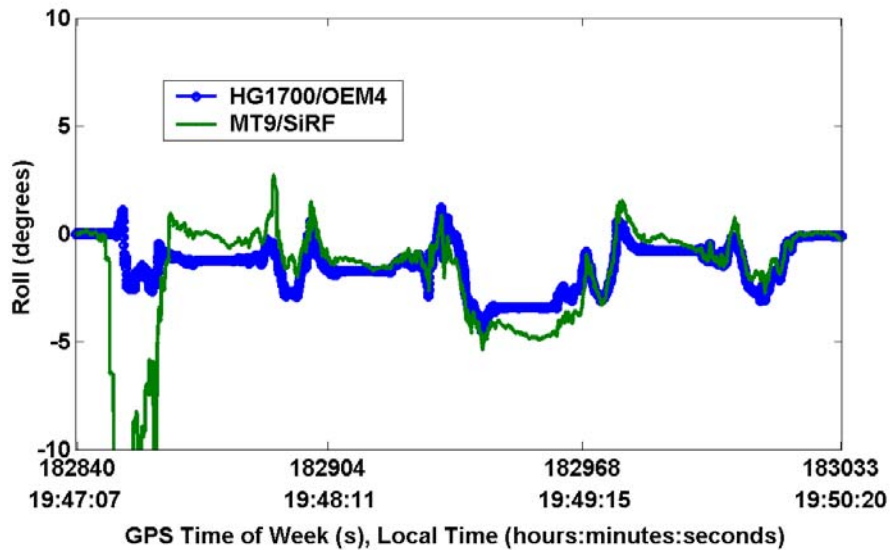


Figure 6.9: Estimation results of roll (INS/GPS integration)

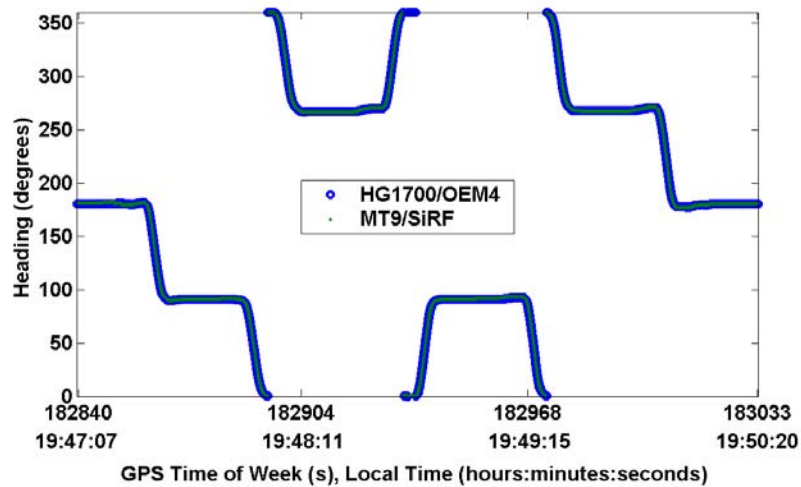


Figure 6.10: Estimation results of heading (INS/GPS integration)

Table 6.4: Attitude estimation accuracy (INS/GPS integration)

Test No.	Pitch Error (degrees)		Roll Error (degrees)		Heading Error (degrees)	
	Mean	RMS	Mean	RMS	Mean	RMS
1	-0.50	0.64	-0.30	0.81	0.39	0.95
2	-0.41	0.54	0.09	0.96	0.53	0.93
3	-0.03	0.38	0.16	0.73	0.26	0.83
4*	-0.23	0.42	-0.06	0.67	0.14	0.67
5	-0.25	0.46	-0.35	1.51	0.29	0.63
6	-0.35	0.48	-0.19	0.87	0.20	0.47
7	-0.27	0.46	-0.24	0.69	-0.03	0.54
8	-0.58	0.65	-0.01	0.98	0.38	0.64
9	-0.54	0.65	-0.05	0.92	0.28	0.53
10	-0.22	0.44	0.06	0.73	0.32	0.76
Average	0.34**	0.51	0.15**	0.89	0.28**	0.70

* This is the sample run of test whose results are shown in Figure 6.8 through Figure 6.10.

** This value is calculated by averaging the absolute value of each run of test.

6.2.1.3 Velocity and Position Accuracy

The velocity and position accuracy of the integration system is mainly dependent on the GPS velocity and position accuracy since the velocity and position states in the INS Kalman filter are directly observable from the measurements. Figure 6.11 and Figure

6.12 show the estimated and the reference velocity and position given by the same sample run #4. Due to the continuous and direct corrections of INS velocity and position errors from GPS, the integrated velocity and position performance is almost identical to the GPS velocity and position performance. The statistical analysis of the integrated velocity and position errors based on the ten-run data is presented in Table 6.5. In summary, the average RMS error is 0.13 m/s for the velocity estimate and about 3 m for the horizontal position estimate, which agrees with the code-based GPS performance in open areas.

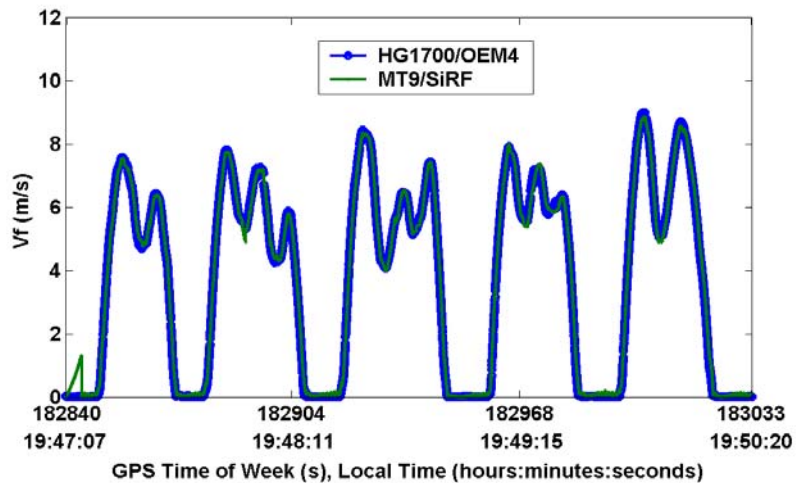


Figure 6.11: Estimation results of velocity (INS/GPS integration)

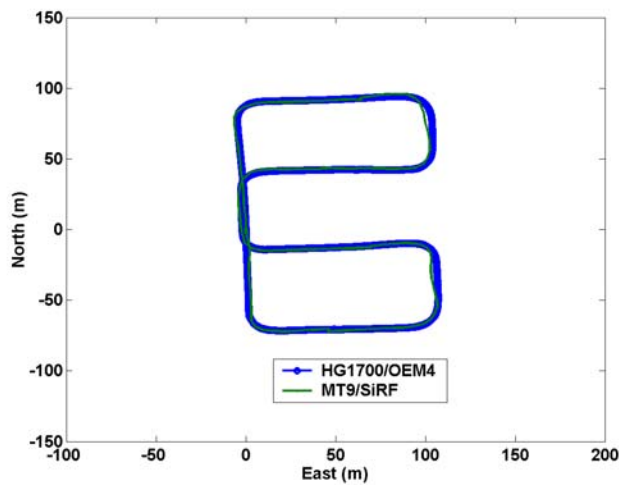


Figure 6.12: Estimation results of position (INS/GPS integration)

Table 6.5: Velocity and position estimation accuracy (INS/GPS integration)

Test No.	Velocity Error (m/s)		North Position Error (m)		East Position Error (m)		Horizontal Position Error (m)	
	Mean	RMS	Max	RMS	Max	RMS	Max	RMS
1	0.01	0.17	4.35	1.50	3.73	1.36	5.73	2.03
2	0.02	0.14	6.24	2.08	4.09	1.43	6.25	2.53
3	0.01	0.14	5.46	2.04	3.58	1.50	5.47	2.53
4*	0.01	0.13	4.11	1.72	4.42	1.83	5.42	2.51
5	0.02	0.14	4.63	2.28	4.74	2.16	5.51	3.14
6	0.03	0.13	6.17	2.21	4.98	2.40	6.18	3.26
7	0.02	0.12	6.49	2.23	4.98	2.51	6.49	3.36
8	0.04	0.12	6.40	2.17	5.15	2.44	6.42	3.26
9	0.02	0.12	6.10	2.76	4.17	2.01	6.10	3.41
10	0.02	0.13	6.63	2.81	4.57	2.08	6.65	3.50
Average	0.02**	0.13	5.66	2.18	4.44	1.97	6.02	2.95

* This is the sample run of test whose results are shown in Figure 6.11 and Figure 6.12.

** This value is calculated by averaging the absolute value of each run of test.

6.2.2 Performance Analysis of Compass Heading Error Modelling

As mentioned previously, the integrated heading solution is used as the reference heading to train the neural networks for modelling the compass heading error so that the trained neural networks can be used to correct the compass heading when GPS is unavailable. In this test, we trained the neural networks using the first run data with GPS updates and tested the calibration performance using the other nine-run data without GPS updates. Thus, the training data set is constructed by the compass heading and the true heading obtained from the first run test. The raw magnetometer measurements collected in the first run are shown in Figure 6.13. It can be seen that the Earth's magnetic fields have been biased, distorted and interfered by the local magnetic fields inside a land vehicle. These deteriorated magnetic measurements were first projected on a horizontal orientation based on the tilt angles outputted by the Kalman filter and then used to calculate the compass headings. The true headings were provided by the integrated heading solutions in the same run which have the mean error of 0.39 degrees and RMS error of 0.95 degrees as shown in Table 6.4.

Figure 6.14 shows the training data and the outputs of the trained neural networks while processing the same training data. It can be seen that although the training data have been deteriorated by noises, magnetic disturbances and projection errors, the neural networks still can properly model the nonlinear input-output relationship that describes the bias, scale factor and declination effects on the compass heading. However, because the perfect training data (without noise, magnetic disturbances and tilt compensation errors) are unavailable in real applications, the error modelling performance cannot be assessed specifically here. The compass calibration performance using the trained neural networks will be presented in the next section.

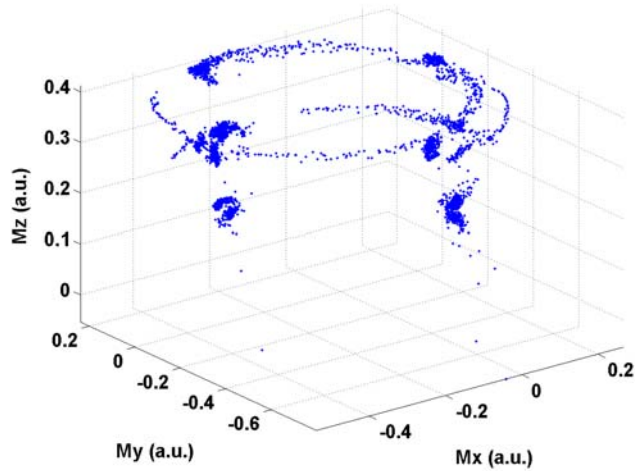


Figure 6.13: Measured magnetic fields for neural networks training

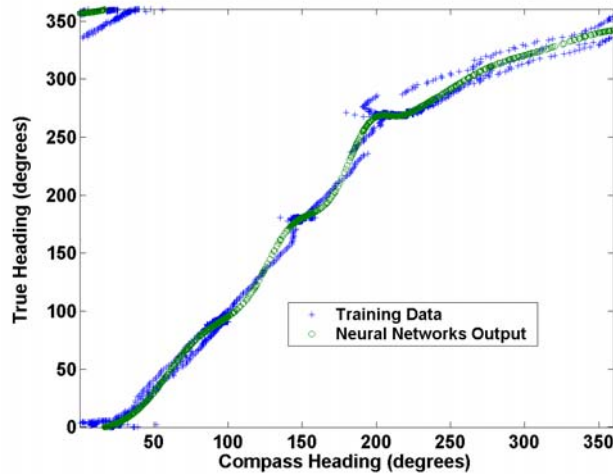


Figure 6.14: Results of neural networks training

6.3 Results without GPS Updates

The second performance analysis is to assess the performance of the integration system when GPS is unavailable, namely to assess the stand-alone inertial navigation performance during complete GPS outages. For the analysis purpose, GPS data are artificially disused and only the dynamics-derived observations with/without the calibrated compass headings are used to update the Kalman filters. To obtain the accurate dynamics-derived observations and the calibrated compass headings, as described in Chapter 4 and Chapter 5, the accelerometer biases should be known and the neural networks must be trained. In the following performance analysis, the biases estimated using full GPS updates in the previous run are applied in the current test and the filter is working without GPS updates. In addition, the neural networks trained by the first run data are applied to calibrate the compass heading in other nine-run tests. Thus, the total nine runs of stand-alone navigation results are assessed. The accuracy of the dynamics-derived observations is presented first, followed by the performance assessment of the compass heading calibration using the neural networks. Finally, the performance analysis of the stand-alone inertial navigation with/without compass aids is given.

6.3.1 Performance Analysis of Dynamics-Derived Observations

The dynamics-derived observations are directly computed using INS raw measurements and the Kalman filter outputs based on the status of vehicle dynamics. The incorrect dynamics identification will result in erroneous observations. Based on the designed fuzzy expert system described in Chapter 4, the results of vehicle dynamics identification for a sample run #7 are shown in Figure 6.15. By comparing the identified motion type with the reference velocity and yaw rate, we verify that the vehicle motion types including stationary, straight-line motion and cornering motion have been correctly identified. It should be noted that there exists a straight-line motion between the sixth and seventh cornering motions that was not identified by the designed fuzzy expert system. This is an expected and acceptable condition since the periods of the straight-line motion between two continuous cornering motions are too short to be recognizable by the

designed fuzzy expert system. Similar identification results for other runs have been also obtained but not shown here.

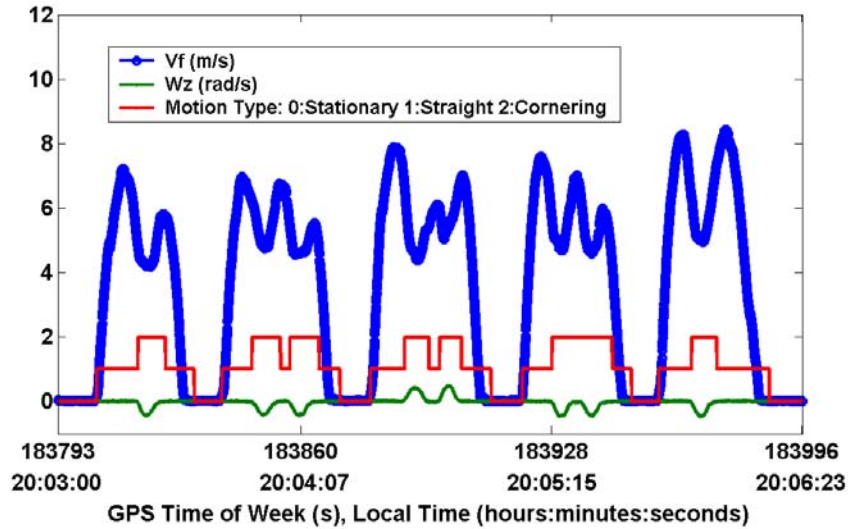


Figure 6.15: Results of vehicle dynamics identification

Figure 6.16 through Figure 6.18 show the dynamics-derived and reference pitch, roll and velocity using the data collected in the same sample run. As mentioned in Chapter 4, the dynamics-derived pitch and roll errors are mainly due to the unidentified accelerometer biases as the noise effects can be reduced by moving average. In this test, the x-axis and y-axis accelerometer biases estimated using full GPS updates in the previous run and used to correct the dynamics-derived observations are 0.202 m/s^2 and -0.149 m/s^2 while the reference biases are 0.216 m/s^2 and -0.157 m/s^2 for the x-axis and y-axis accelerometer, respectively. This shows the good bias estimation accuracy and therefore the dynamics-derived pitch and roll are considerably accurate, almost identical to the reference as shown in Figure 6.16 and Figure 6.17. Due to the approximation errors induced by sideslip or vibration, the dynamics-derived roll in the straight-line motion mode has relatively larger errors than the dynamics-derived roll in the stationary mode. For the cornering motion mode, as shown in Figure 6.18, the dynamics-derived velocities are close to the reference velocities so that they can be used to correct the stand-alone INS velocities and reduce the error drift. The errors of all dynamics-derived observations are shown in Figure 6.19 which demonstrates the error characteristics we have described

above. It should be noted that there exist some oscillatory errors in the stationary pitch and roll at the beginning of the stationary period. This is because the stationary pitch and roll are not smoothed at the beginning of the stationary period due to the lack of samples for moving average. As the samples for moving average increase, this type of error will be filtered and the stationary pitch and roll remain steady.

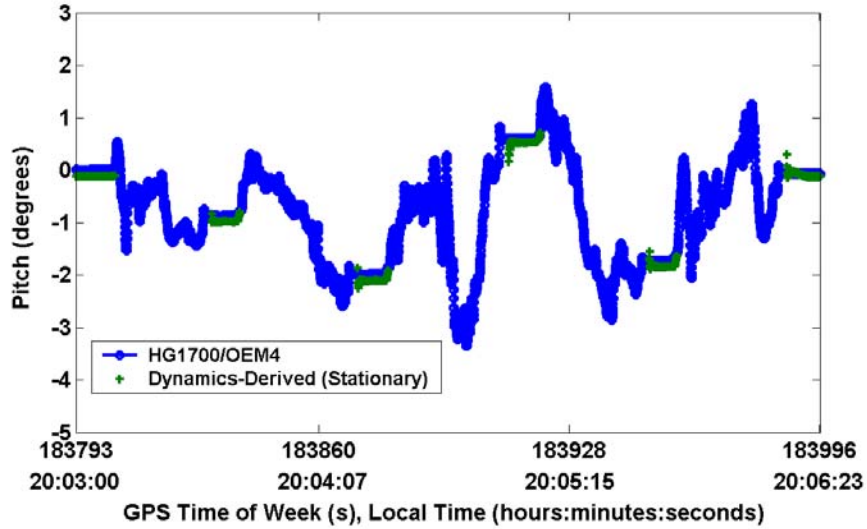


Figure 6.16: Dynamics-derived pitch observations

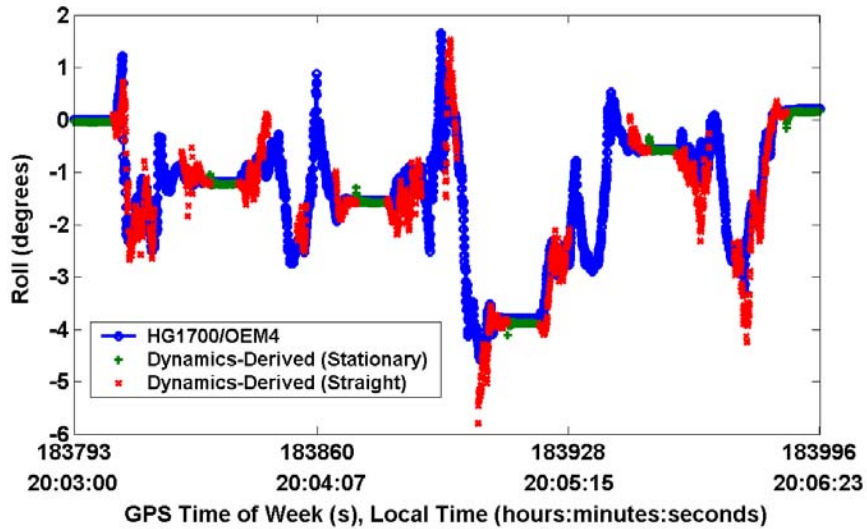


Figure 6.17: Dynamics-derived roll observations

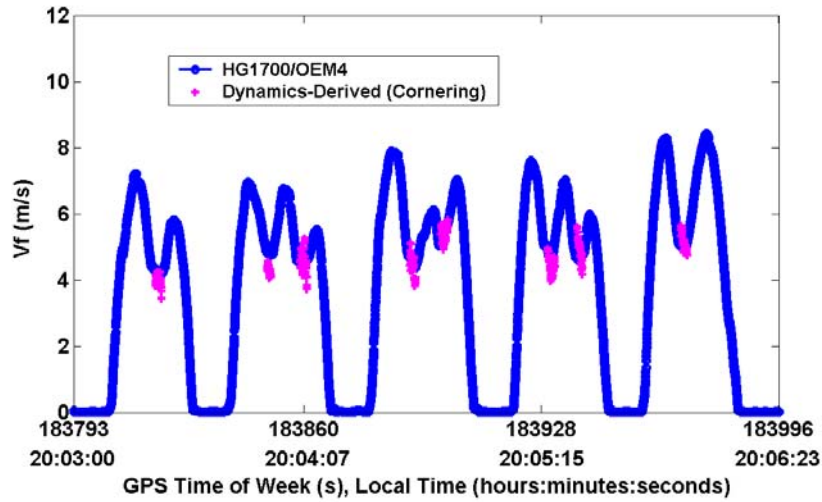


Figure 6.18: Dynamics-derived velocity observations

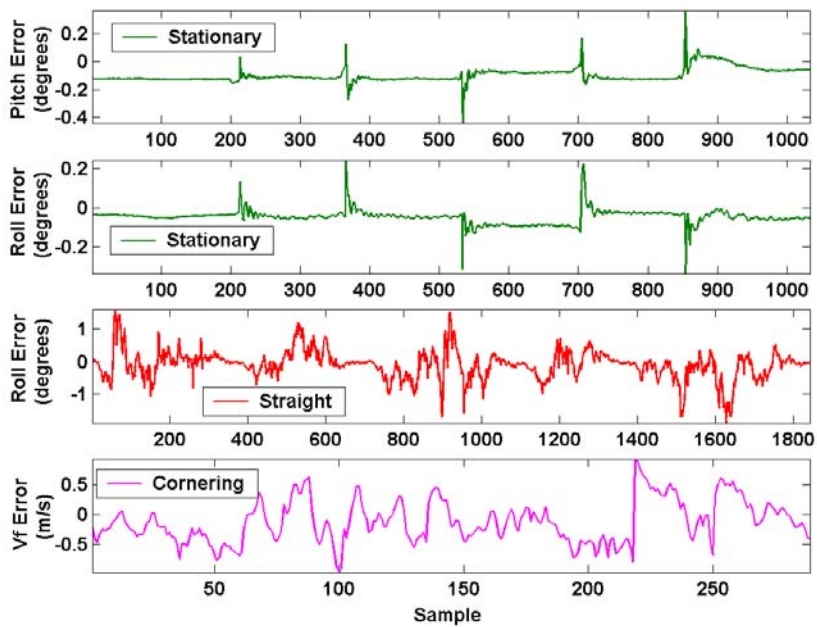


Figure 6.19: Errors of dynamics-derived observations

Table 6.6 demonstrates the accuracy of the dynamics-derived observations given by the nine-run data. As expected, the average mean of the dynamic-derived pitch and roll errors (about 0.16 degrees) is equivalent to the unidentified accelerometer bias (about 0.025 m/s^2) as shown in Table 6.3. We observed that in each test the RMS error of the dynamic-derived stationary pitch and roll is almost identical to the absolute value of the mean error.

This is because the stationary pitch and roll error is mainly due to the unidentified accelerometer bias after the noise effects have been removed by moving average. Due to the approximation errors induced by sideslip or vibration, the RMS error of the dynamics-derived roll in the straight-line motion mode is larger than the RMS error of the stationary roll. For the cornering motion mode, the accuracy of the dynamics-derived velocity is about 0.45 m/s and considerably stable for each test. Compared with the stand-alone INS navigation solutions, the dynamics-derived observations are accurate enough to provide pitch, roll and velocity corrections.

Table 6.6: Dynamics-derived observation accuracy

Test No.	Stationary Pitch Error (degrees)		Stationary Roll Error (degrees)		Straight-Line Roll Error (degrees)		Cornering Velocity Error (m/s)	
	Mean	RMS	Mean	RMS	Mean	RMS	Mean	RMS
2	-0.26	0.27	0.05	0.10	-0.01	0.46	-0.20	0.50
3	-0.13	0.14	0.16	0.17	0.15	0.44	-0.27	0.51
4	0.16	0.16	0.38	0.38	0.31	0.54	-0.18	0.42
5	0.04	0.06	0.01	0.06	0.01	0.45	-0.20	0.46
6	-0.03	0.04	-0.42	0.42	-0.45	0.68	-0.12	0.48
7*	-0.10	0.11	-0.05	0.06	-0.11	0.46	-0.13	0.38
8	-0.18	0.18	-0.20	0.20	-0.23	0.52	-0.25	0.42
9	-0.35	0.35	0.18	0.18	0.16	0.44	-0.19	0.42
10	-0.25	0.25	0.03	0.05	-0.05	0.42	-0.26	0.43
Average	0.17**	0.17	0.16**	0.18	0.16**	0.49	0.20**	0.45

* This is the sample run of test whose results are shown in Figure 6.16 through Figure 6.19.

** This value is calculated by averaging the absolute value of each run of test.

6.3.2 Performance Analysis of Compass Heading Calibration

Based on the test results from the sample run #7, the compass headings with and without the neural networks calibration compared to the reference headings are shown in Figure 6.20. As shown, the compass heading has been calibrated correctly, consistent with the reference heading. However, there exist some jump errors due to the magnetic disturbance and tilt compensation error. This type of error cannot be removed by compass calibration but can be filtered out by integration with gyro measurements. The accuracy of the calibrated heading for all runs is shown in Table 6.7. The average RMS error and mean error of the calibrated heading are 4.82 degrees and 0.26 degrees, respectively. The

large RMS value is due to the existence of jump errors as described above. Thus, the mean value is more suitable to represent the calibration performance. As shown in Table 6.7, the obtainable calibration accuracy using the neural networks in a typical land vehicle environment is about 0.2 degrees, which is accurate enough to provide corrections of the MEMS gyro-derived heading.

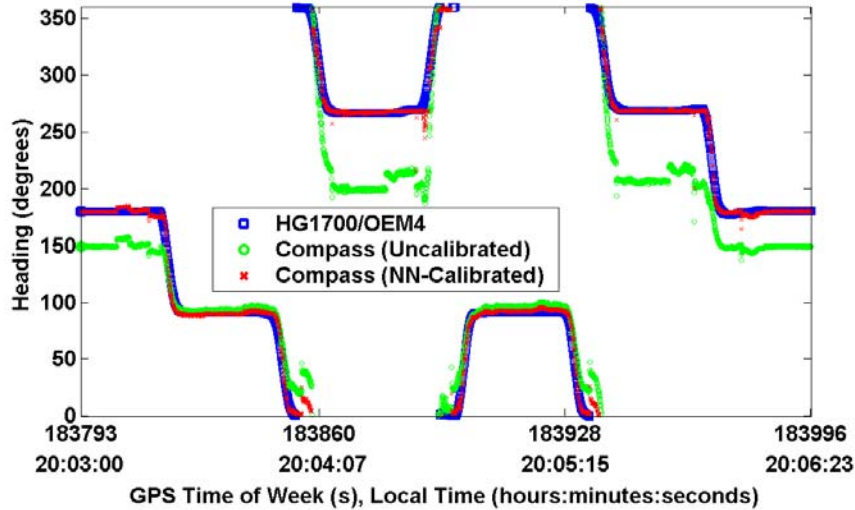


Figure 6.20: Calibrated and un-calibrated compass headings

Table 6.7: Calibrated compass heading accuracy

Test No.	Heading Error (degrees)	
	Mean	RMS
2	0.30	5.19
3	0.28	5.32
4	0.42	5.00
5	0.49	4.86
6	0.09	4.85
7*	0.17	4.70
8	0.20	4.61
9	0.26	4.16
10	0.16	4.71
Average	0.26**	4.82

* This is the sample run of test whose results are shown in Figure 6.20.

** This value is calculated by averaging the absolute value of each run of test.

6.3.3 Performance Analysis of Stand-Alone Inertial Navigation

Previous sections have demonstrated the obtainable accuracy of the dynamics-derived observations and the calibrated compass headings. In this section, the performance analysis of the stand-alone inertial navigation aided by these dynamics-derived observations with/without the calibrated compass headings is presented. The performance of the stand-alone inertial navigation aided by the dynamics-derived observations only is assessed first, followed by a discussion on the benefit of the compass aids.

6.3.3.1 Aiding from Dynamics-Derived Observations Only

6.3.3.1.1 Attitude Accuracy

The pitch, roll and heading estimates of the stand-alone inertial navigation aided by vehicle dynamics knowledge for the sample run #7 are shown in Figure 6.21 through Figure 6.23. To demonstrate the benefits of the dynamics aids, the unaided stand-alone inertial navigation solution is also displayed. In the unaided mode, no dynamics-derived observations are used to update the Kalman filter and thus it works in a full prediction mode. As shown in Figure 6.21 and Figure 6.22, the error of the dynamics-aided pitch and roll has been bounded and well controlled while the unaided pitch and roll have large error drifts. The dynamics-aided pitch estimates during the stationary periods as well as the roll estimates during the stationary and the straight-line motion periods are almost identical to the dynamics-derived pitch and roll shown in Figure 6.16 and Figure 6.17, respectively. This is because the pitch and roll states in the INS Kalman filter are directly observable from the dynamics-derived measurements and their covariances are very small. For the periods when the dynamics-derived pitch and roll updates are unavailable, the performance of the dynamics-aided tilt estimates degrades with time. The performance degradation is mainly dependent on the quality of inertial sensors and vehicle dynamics. Comparing Figure 6.21 with Figure 6.22, we observed that the dynamics-aided roll estimates are more accurate than the pitch due to the availability of roll measurement updates during the straight-line motion periods. For the heading performance, while zooming in the heading estimates at the end of the test, we found the error drifts of the dynamics-aided and unaided solutions are about one and two degrees,

respectively. The improvement in heading is not as significant as the improvement in tilt. This is because for the dynamics-aided system only the constant heading constraint during the stationary periods is available to control the heading error drift while the absolute tilt measurement updates are more frequently available to reduce the tilt error drift. In summary, the aiding from the vehicle dynamics knowledge enables the stand-alone MEMS INS to provide bounded tilt and heading solutions with reduced error drift rates.

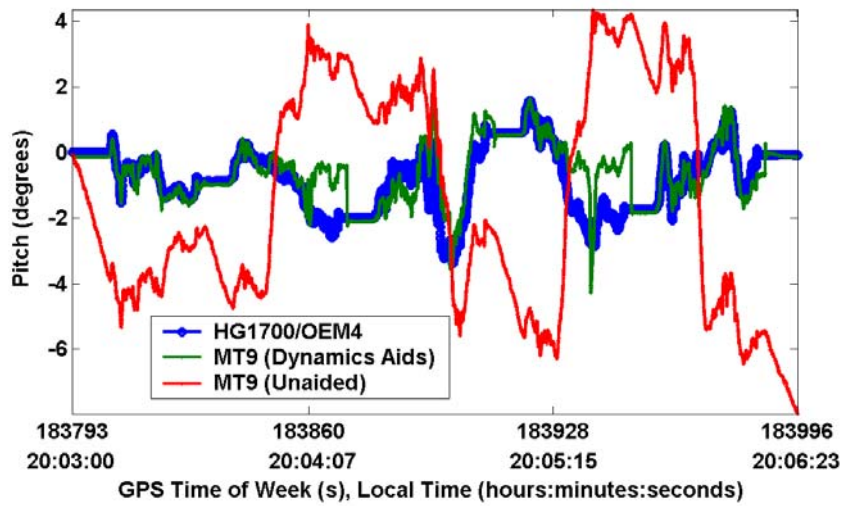


Figure 6.21: Estimation results of pitch (stand-alone INS with dynamics aid)

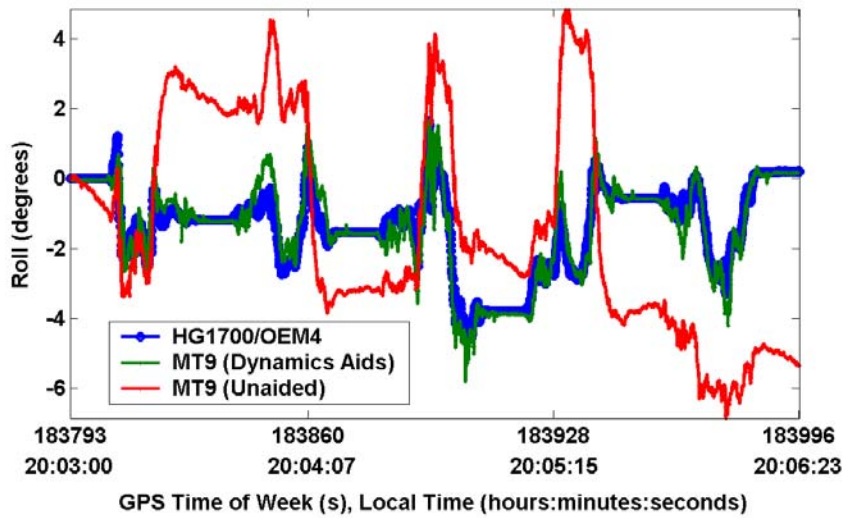


Figure 6.22: Estimation results of roll (stand-alone INS with dynamics aid)

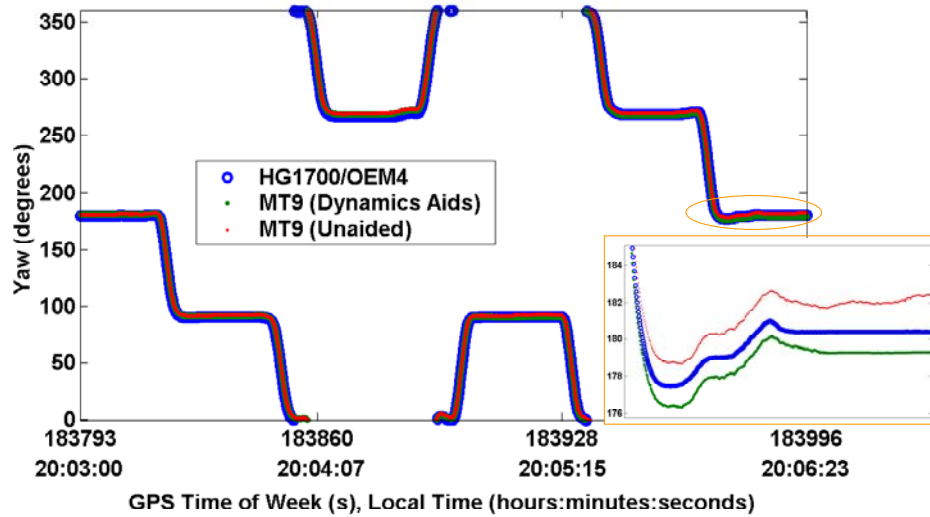


Figure 6.23: Estimation results of heading (stand-alone INS with dynamics aid)

Table 6.8 presents the accuracy of the stand-alone dynamics-aided attitude obtained from the nine-run tests. As shown, the average RMS error is about 0.8 for the pitch estimate degrees, about 0.5 degrees for the roll estimate and about 1.5 degrees for the heading estimate. From the performance comparisons of the integrated attitude (Table 6.4) and the stand-alone dynamics-aided attitude (Table 6.8), we found that the latter provides better roll accuracy while the former provides better pitch and heading accuracy. This could be explained by the following factors: the correction for the roll error from the direct dynamics-derived roll observations is more effective than the correction from the GPS velocity and heading updates based on the error dynamics model; on the other hand, the GPS velocity and heading updates provide the continuous correction for the pitch and heading errors with good observability while the dynamics-derived pitch observations and heading constraints are only available during the stationary periods. In summary, the accuracy of the stand-alone dynamics-aided attitude is dependent on the availability and the quality of the dynamics-derived attitude updates, i.e., the periods of the stationary and straight-line motion as well as the accuracy of the pre-estimated accelerometer biases.

Table 6.8: Attitude estimation accuracy (stand-alone INS with dynamics aid)

Test No.	Pitch Error (degrees)		Roll Error (degrees)		Heading Error (degrees)	
	Mean	RMS	Mean	RMS	Mean	RMS
2	0.18	0.71	0.10	0.54	1.17	1.70
3	0.41	1.11	0.29	0.58	-0.09	1.06
4	0.48	0.85	0.36	0.59	0.07	1.23
5	0.39	1.00	-0.01	0.58	-0.68	1.48
6	0.06	0.53	-0.38	0.60	0.95	1.10
7*	0.19	0.67	-0.01	0.45	0.62	1.36
8	-0.28	0.82	-0.14	0.48	2.30	2.47
9	-0.09	0.51	0.30	0.56	1.91	2.10
10	0.18	0.63	0.06	0.46	-0.62	1.19
Average	0.25**	0.76	0.18**	0.54	0.93**	1.52

* This is the sample run of test whose results are shown in Figure 6.21 through Figure 6.23.

** This value is calculated by averaging the absolute value of each run of test.

6.3.3.1.2 Velocity and Position Accuracy

Figure 6.24 and Figure 6.25 show the velocity and position solutions obtained from the stand-alone dynamics-aided and unaided MEMS INS and the geo-reference system from the sample run #7, respectively. As shown in Figure 6.24, the unaided velocity has large drifted errors and cannot be used for navigation while the dynamics-aided velocity error is well bounded by the ZUPTs and cornering velocity updates. During the straight-line motion, the dynamics-aided velocity error increases with time and the error growth rate is mainly dependent on the pitch accuracy. For the position performance, due to the lack of external position corrections in the stand-alone mode, the position error will accumulate with the course of time. In this test, with the aiding from the dynamics knowledge the stand-alone INS position solutions still keep on the track while the unaided solutions have drifted away from the track at the several hundred-metre level. The horizontal position error during about 3-minute GPS outages has been controlled to be within 27 m for the dynamics-aided system.

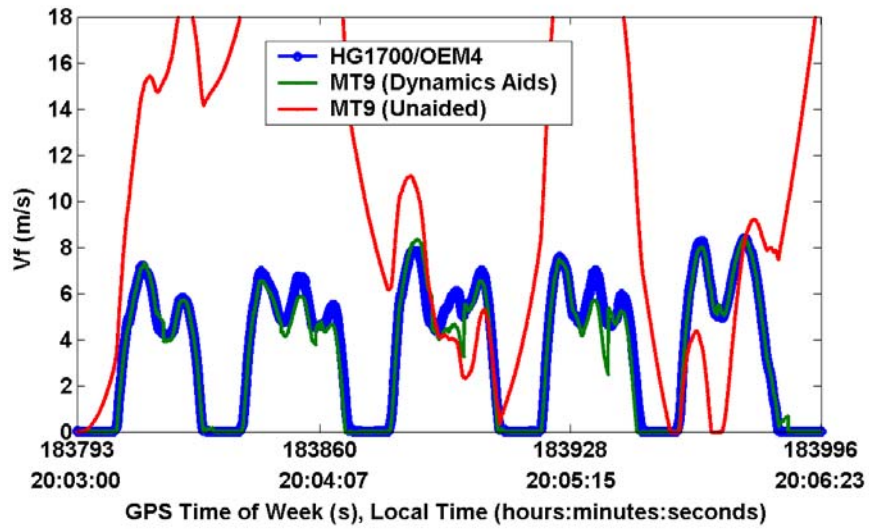


Figure 6.24: Estimation results of velocity (stand-alone INS with dynamics aid)

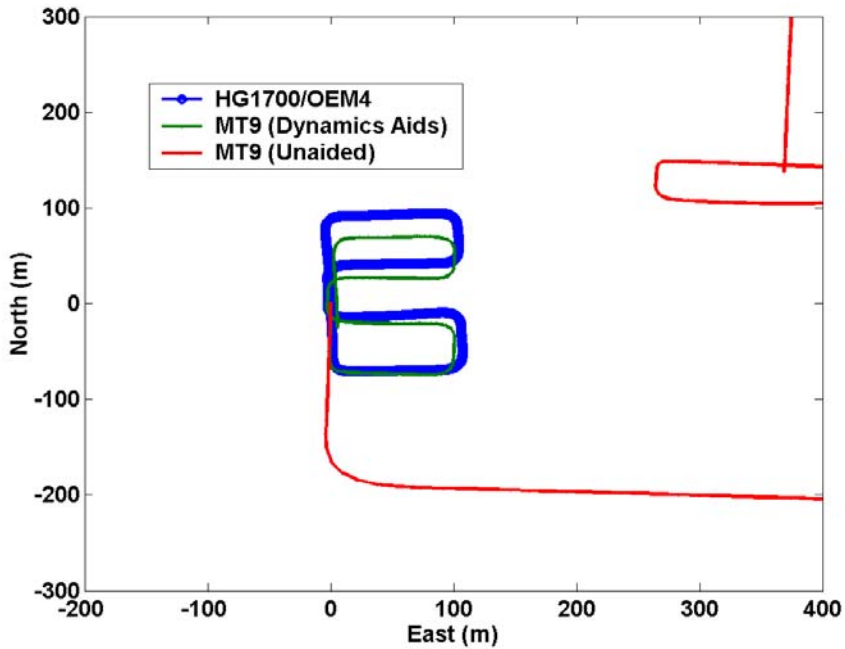


Figure 6.25: Estimation results of position (stand-alone INS with dynamics aid)

Table 6.9 further summarizes the dynamics-aided velocity and position accuracy obtained from the nine-run data. We found that the East position accuracy is better than the North because of the frequent stops available during the eastward/westward driving. In summary, during about 3 minutes stand-alone navigation the average RMS error of 0.66

m/s for velocity and of 16.25 m for horizontal position are obtainable while the average maximum horizontal position error has been maintained within 30 m. The achieved performance is much better than the performance supplied by the manufacturer specifications which demonstrates the effectiveness of the dynamics knowledge aids for low-cost MEMS INS navigation in the stand-alone mode.

Table 6.9: Velocity and position estimation accuracy (stand-alone INS with dynamics aid)

Test No.	Velocity Error (m/s)		North Position Error (m)		East Position Error (m)		Horizontal Position Error (m)	
	Mean	RMS	Max	RMS	Max	RMS	Max	RMS
2	-0.37	0.62	18.72	7.41	16.83	7.62	20.18	10.63
3	-0.38	0.75	18.37	8.51	25.36	13.14	29.19	15.65
4	-0.29	0.56	19.90	10.80	12.49	6.23	20.65	12.46
5	-0.30	0.82	33.15	19.22	32.05	16.78	43.93	25.51
6	-0.14	0.47	20.73	9.84	19.04	9.81	23.32	13.89
7*	-0.21	0.52	26.75	15.00	11.15	5.19	26.75	15.87
8	0.05	0.92	40.82	15.00	21.92	12.55	46.33	19.56
9	-0.22	0.56	22.39	11.53	19.95	9.78	26.55	15.12
10	-0.44	0.70	28.16	15.29	18.84	8.64	30.37	17.57
Average	0.27**	0.66	25.44	12.51	19.74	9.97	29.70	16.25

* This is the sample run of test whose results are shown in Figure 6.24 and Figure 6.25.

** This value is calculated by averaging the absolute value of each run of test.

6.3.3.2 Aiding from Dynamics-Derived and Calibrated Compass Observations

6.3.3.2.1 Attitude Accuracy

Table 6.10 lists the attitude estimation performance for all nine runs when both dynamics-derived observations and calibrated compass headings are used to correct the stand-alone INS attitude. Comparing these results with Table 6.8 where only the aiding from the dynamics knowledge is applied, we noticed that only the heading accuracy is improved while the pitch and roll accuracy remains the same. This is because the heading state in the Kalman filter is directly observable from the heading measurement; meanwhile, the pitch and roll states in the Kalman filter are very weakly observable from the heading measurement especially for land vehicle applications where the pitch and roll

of the vehicle are generally small. Thus, the calibrated compass heading can directly correct the INS heading error but only slightly improve the INS pitch and roll estimation.

Table 6.10: Attitude estimation accuracy (stand-alone INS with dynamics aid and compass aid)

Test No.	Pitch Error (degrees)		Roll Error (degrees)		Heading Error (degrees)	
	Mean	RMS	Mean	RMS	Mean	RMS
2	0.18	0.71	0.10	0.54	0.54	1.76
3	0.41	1.11	0.29	0.58	0.34	1.45
4	0.48	0.85	0.36	0.59	0.51	1.56
5	0.39	1.00	-0.01	0.58	0.41	1.24
6	0.06	0.53	-0.38	0.60	0.01	1.32
7	0.19	0.67	-0.01	0.45	0.19	1.53
8	-0.28	0.81	-0.14	0.48	0.50	1.40
9	-0.09	0.51	0.30	0.55	0.35	1.35
10	0.18	0.63	0.06	0.46	0.37	1.28
Average	0.25*	0.76	0.18*	0.54	0.36*	1.43

* This value is calculated by averaging the absolute value of each run of test.

Focusing on the assessment of the heading estimation accuracy, we found that with the aiding from the calibrated compass headings the average mean of the heading error has been reduced from 0.93 degrees to 0.36 degrees while the improvement in the average RMS error is slight, from 1.52 degrees to 1.42 degrees. The reason becomes clear when we examined the performance of the calibrated compass headings shown in Table 6.7. As mentioned previously, the compass calibration can remove bias and scale factor error but noise, magnetic disturbance and projection error. Thus, the mean error of the calibrated compass heading is usually smaller than the RMS error. As shown in Table 6.7, the average mean and RMS errors of the calibrated heading are 0.26 degrees and 4.82 degrees, respectively. With the small mean error, the calibrated compass headings can reduce the error drift of the gyro-derived heading. However, the noise, disturbance and projection error inherited in the compass heading may deteriorate the gyro-derived heading. The impact of these errors can be reduced by properly adjusting the measurement covariances of the compass heading using the adaptive method developed in Chapter 5.

To demonstrate this, shown in Figure 6.26 is a zoom-in version of the heading estimation results obtained from the run #8 test. This figure compares the performance between the calibrated compass heading, the stand-alone dynamics-aided INS heading and the dynamics-aided plus compass-aided heading. As shown, the dynamics-aided plus compass-aided approach provides smooth and drift-free heading estimation while the stand-alone dynamics-aided INS heading has a significant bias and the calibrated compass heading has significant jump errors.

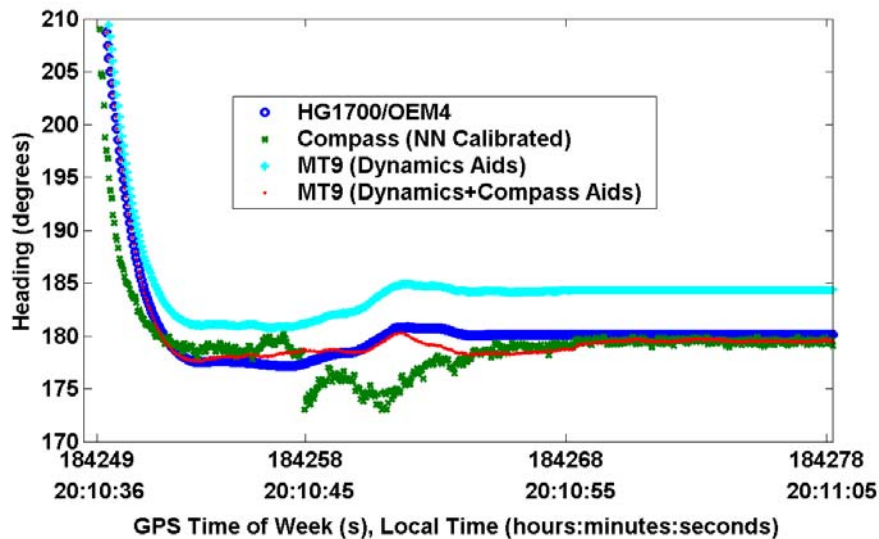


Figure 6.26: Comparison of heading estimation using different approaches (zoom-in)

6.3.3.2.2 Velocity and Position Accuracy

The estimation accuracy of the dynamics-aided plus compass-aided velocity and position solutions for all nine runs is summarized in Table 6.11. As expected, the aiding from the compass heading didn't show significant improvement in the velocity and position accuracy compared with no compass-aided solutions as shown in Table 6.9. This is because the accuracy of the forward velocity is mainly dependent on the pitch accuracy. As demonstrated previously, the aiding from the compass heading has only very slight improvement in the pitch estimation so that the velocity accuracy cannot be improved much. As the velocity improvement is very small and the heading improvement is not obvious during the short-time test, the performance improvement is also limited in the

position domain. It is expected to have greater performance improvement in the position domain with the aiding from the compass heading over longer period of time.

Table 6.11: Velocity and position estimation accuracy (stand-alone INS with dynamics aid and compass aid)

Test No.	Velocity Error (m/s)		North Position Error (m)		East Position Error (m)		Horizontal Position Error (m)	
	Mean	RMS	Max	RMS	Max	RMS	Max	RMS
2	-0.37	0.62	21.55	8.82	18.75	8.51	23.29	12.26
3	-0.38	0.74	20.20	8.49	25.80	12.94	29.63	15.47
4	-0.29	0.56	22.10	10.93	15.83	7.08	23.49	13.02
5	-0.30	0.82	36.15	19.34	32.87	16.87	45.52	25.66
6	-0.14	0.48	19.22	8.69	20.49	11.01	23.66	14.03
7	-0.21	0.52	27.91	14.75	11.38	5.34	28.03	15.69
8	0.05	0.92	44.83	15.87	24.99	15.10	48.86	21.91
9	-0.22	0.56	22.68	11.35	14.78	7.44	24.45	13.57
10	-0.44	0.70	28.95	14.17	20.13	9.15	30.59	16.87
Average	0.27*	0.66	27.07	12.49	20.56	10.38	30.84	16.50

* This value is calculated by averaging the absolute value of each run of test.

6.4 Summary of Test Results

In this chapter, the proposed intelligent integration algorithm has been tested and analyzed with open area data. Two types of performance analysis, namely integration performance and stand-alone inertial navigation performance, have been presented. The first analysis, with the use of GPS updates, demonstrated the obtainable accuracy of the accelerometer bias estimation and integrated navigation solutions as well as the performance of the compass heading error modelling using neural networks. The results showed that the bias estimation accuracy of about 0.03 m/s^2 is obtainable. In addition, the integrated solutions have provided attainable accuracy for attitude less than 1 degree and for velocity and position at about 0.1 m/s and 3 m level, respectively.

The second analysis, without the use of GPS updates, demonstrated the accuracy of the dynamics-derived observations and the calibrated compass headings as well as the stand-alone dynamics-aided INS navigation performance with/without compass aids. The

results showed that the mean error of the dynamics-derived tilt is less than 0.2 degrees equivalent to the bias estimation accuracy and the dynamics-derived velocity accuracy is less than 0.5 m/s, both accurate enough to provide corrections for the stand-alone INS pitch, roll and velocity. Meanwhile, the obtainable compass calibration accuracy using the neural networks in a typical land vehicle environment is about 0.2 degrees, also good enough to provide corrections for the stand-alone INS heading. For the stand-alone inertial navigation performance, with the aiding from the dynamics knowledge, the bounded tilt and heading with reduced error drift rates are attainable. The average horizontal position error is controlled within 30 m during about 3 minutes GPS outages. On the other hand, with the aiding from the calibrated compass headings, a smooth and drift-free heading estimation is also obtainable.

Chapter 7

Test Results in Urban Areas

Chapter 6 has demonstrated the performance of the proposed AI-enhanced integration algorithm applied under two operational conditions: with full GPS updates and complete GPS outages. This chapter presents the test results and performance analysis under realistic urban environments. The test set-up and test environments are described first. Then, the GPS-only position accuracy and the GPS data classification performance using the designed fuzzy inference system are evaluated. Finally, the attainable position accuracy of the AI-enhanced integrated solutions is presented.

7.1 Test Description

The test system set-up is similar to the one used in the open area test as described in Chapter 6, except a SiRF Star II conventional GPS receiver that has standard signal tracking sensitivity was added into the test system. The MT9 MEMS IMU, SiRF HSGPS and SiRF GPS were connected to a laptop through three serial ports to conduct data logging and time tagging as same as the process applied in the open area test. The test system was installed on the same test van used in the open area test. The MT9 was mounted tightly on the floor of the test van while the SiRF HSGPS and SiRF GPS antennas were mounted on the roof of the van vertically above the MT9. A digital map of the downtown Calgary provided by the City of Calgary was used as the reference for position accuracy analysis. The map provides the coordinates of a road centre-line with the several metre level accuracy.

A series of tests were conducted in the downtown Calgary, on April 23 and 26, 2005. Two test routes, both having a variety of spatial urban characteristics, were chosen as shown in Figure 7.1 and Figure 7.2. As shown, a variety of medium (60 – 100 m) to tall

(150 – 200 m) buildings and several underpasses (on 3rd Street and 5th Avenue) are located on each test route. Figure 7.3 and Figure 7.4 show the number of satellites tracked by the SiRF high sensitivity and conventional GPS receivers in a sample run of the route-A and route-B tests, respectively. Both tests started in a nearly open-sky area where the number of satellites tracked by either the HSGPS or GPS receiver was larger than eight. When the vehicle moved into the core downtown areas, the number of tracked satellites dropped and the conventional GPS may suffer from frequent signal outages. In general, the route-B test experienced severer signal degradation conditions than the route-A test. Eight data collection runs on each route were performed, each starting in a nearly open-sky area for one-minute static initialization to obtain good position fix. The test vehicle took about 10 minutes to finish the route-A loop of about 2 km in length and about 15 minutes to finish the route-B loop of about 3 km in length. In both routes, the vehicle frequently stopped on the traffic lights and had the speed varied from 0-40 km/h.

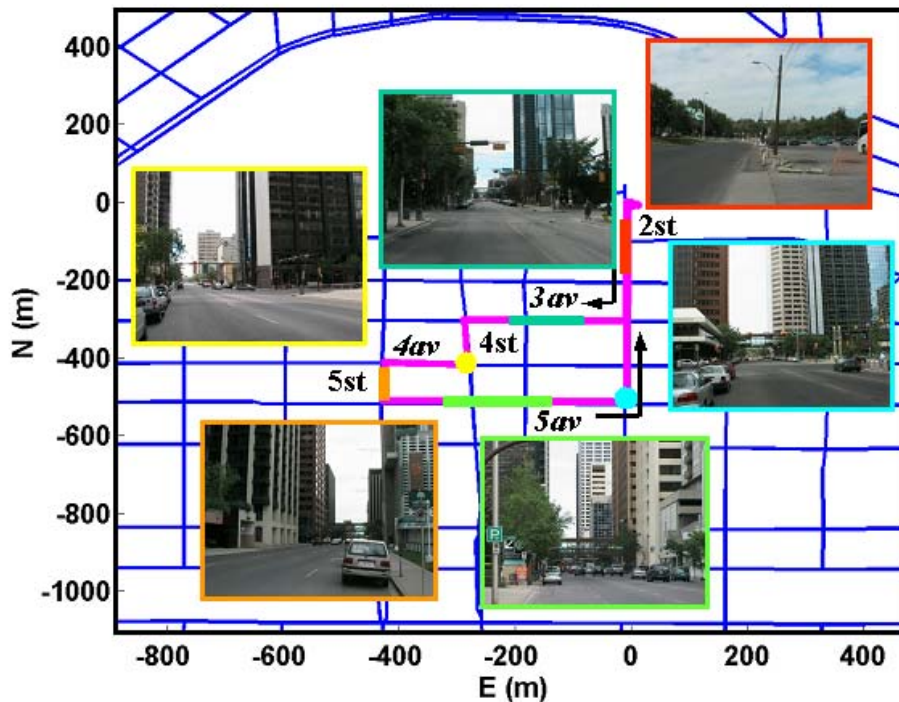


Figure 7.1: Urban area test trajectory (route-A)

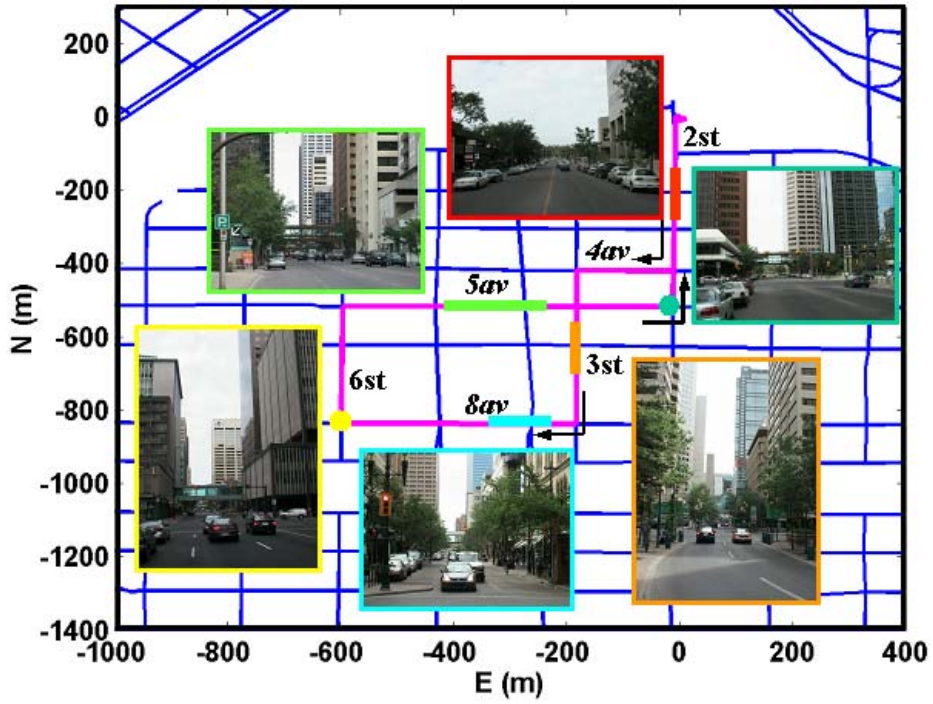


Figure 7.2: Urban area test trajectory (route-B)

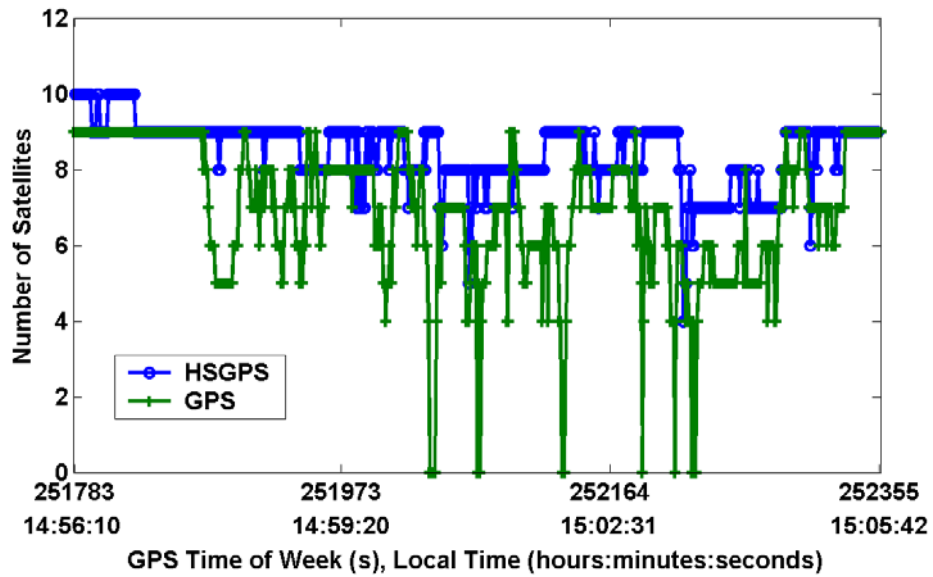


Figure 7.3: Satellites tracked in a route-A test

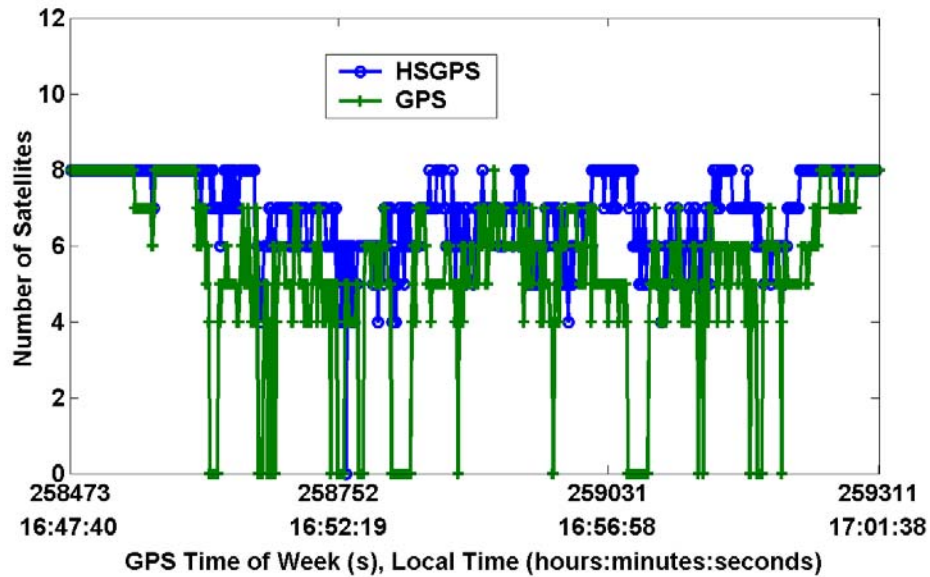


Figure 7.4: Satellites tracked in a route-B test

7.2 GPS Data Classification Performance

In urban area applications, GPS position is subject to performance degradation due to multipath, large noise and other signal deterioration. It is therefore crucial to check the quality of GPS data before they are used for navigation or integration with other sensors. This section examines the accuracy and availability of the single point code-based position solutions from the SiRF conventional and high sensitivity GPS receivers as well as their data classification performance using the designed fuzzy inference system. The results of the HSGPS are presented first, followed by the results of the conventional GPS.

7.2.1 Results of HSGPS

Figure 7.5 and Figure 7.6 illustrate the HSGPS positions obtained from the route-A tests on April 23 and 26, 2005 respectively. For the route-B tests, the HSGPS positions obtained on April 23 and 26, 2005 are illustrated in Figure 7.7 and Figure 7.8 respectively. In all figures, the HSGPS positions are marked with different colours and symbols according to the data classification results. As shown, the HSGPS can provide high availability of position solutions in urban areas, but the position performance is

inconsistent and unstable, i.e., some on the track and some off the track by the hundred-metre level especially for the route-B tests with severer signal degradation conditions. Using the fuzzy data classification, we have identified the erroneous GPS positions as high signal-degraded data. Other more accurate and stable position solutions have been identified as low or medium signal-degraded data as shown in Figure 7.5 through Figure 7.8. However, the high signal-degraded data may have good position accuracy. This is due to the heavy filtering of GPS position performed inside the receiver and this filtering effect is difficult to assess by using signal and geometry degradation information only.

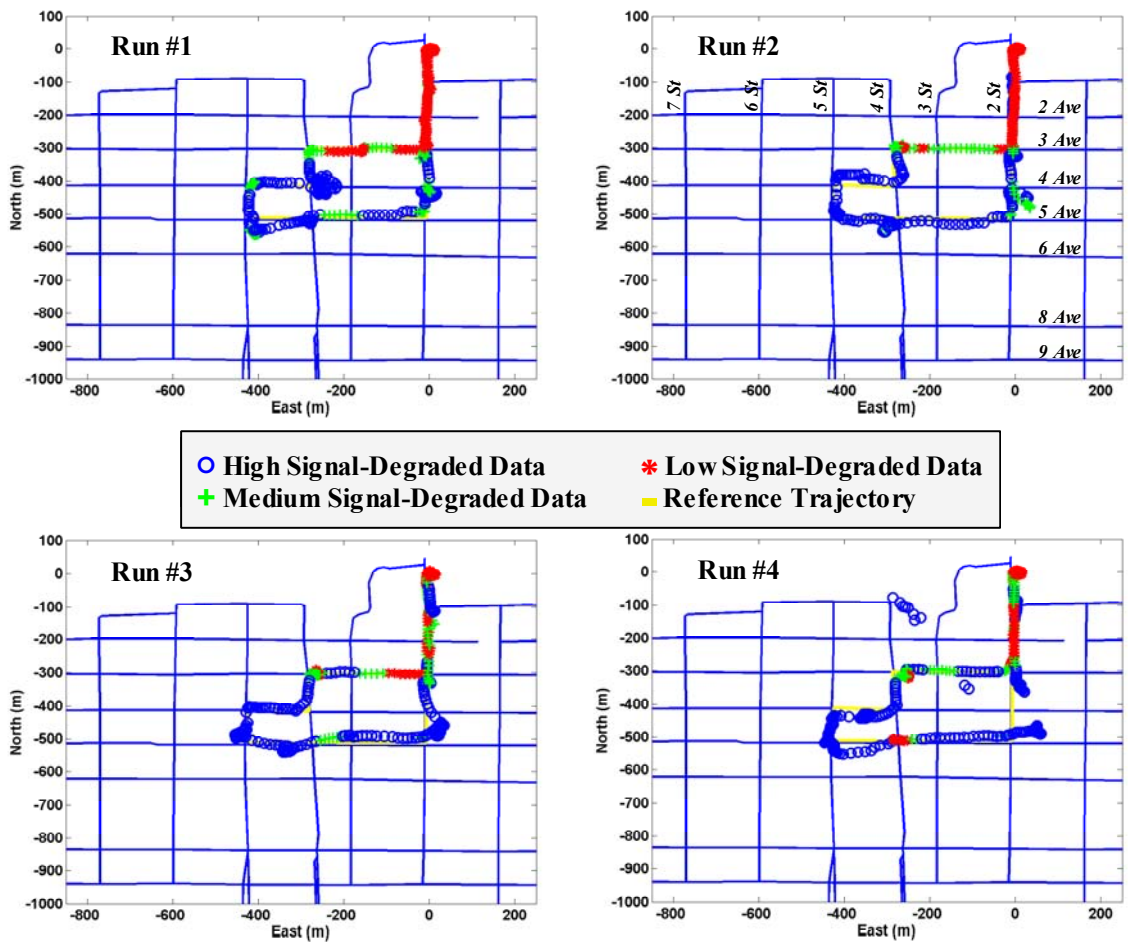


Figure 7.5: HSGPS positions and classification results, route-A tests, April 23, 2005

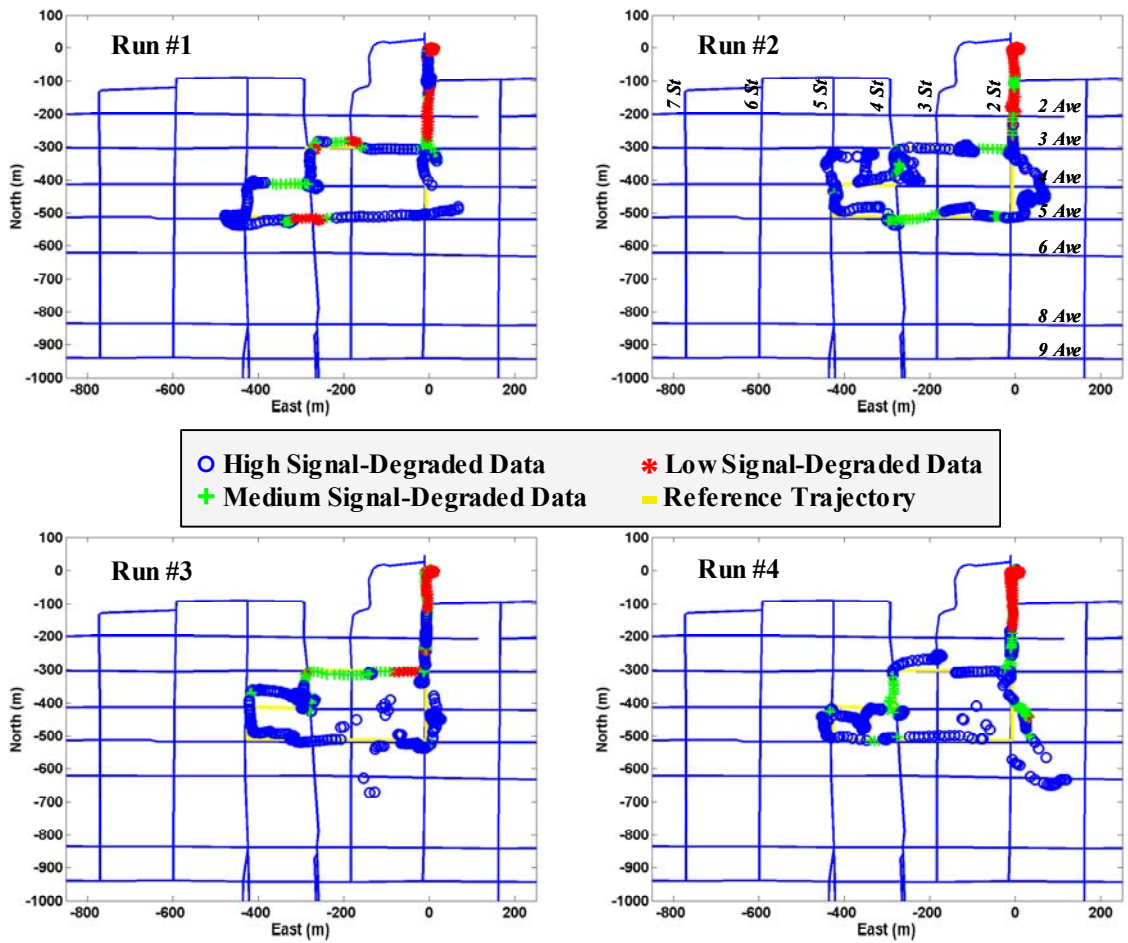


Figure 7.6: HSGPS positions and classification results, route-A tests, April 26, 2005

Comparing data classification results with the test environments in both route-A and route-B tests, we found that most of the identified low or medium signal-degraded data in the core downtown areas are located at or close to the intersections. This demonstrates the consistency between the data classification results with the actual signal and geometry conditions. Comparing data classification results between different runs, we observed that the data classification results are not identical from run to run. This is expected because the signal degradation condition is changing with time according to the user-to-satellite geometry relative to obstacles around the receiver. For example, in Figure 7.8 the HSGPS positions between 5th and 6th Street on 8th Avenue have been identified as low signal-degraded data in the run #1 test but as high signal-degraded data in the run #3 test. As shown, the identified low signal-degraded data overlapping the reference trajectory

indicates good position accuracy while the identified high signal-degraded data are off the track by the hundred-metre level. This demonstrates the correlation between the position performance and the signal degradation condition and the effectiveness of the designed fuzzy data classification system.

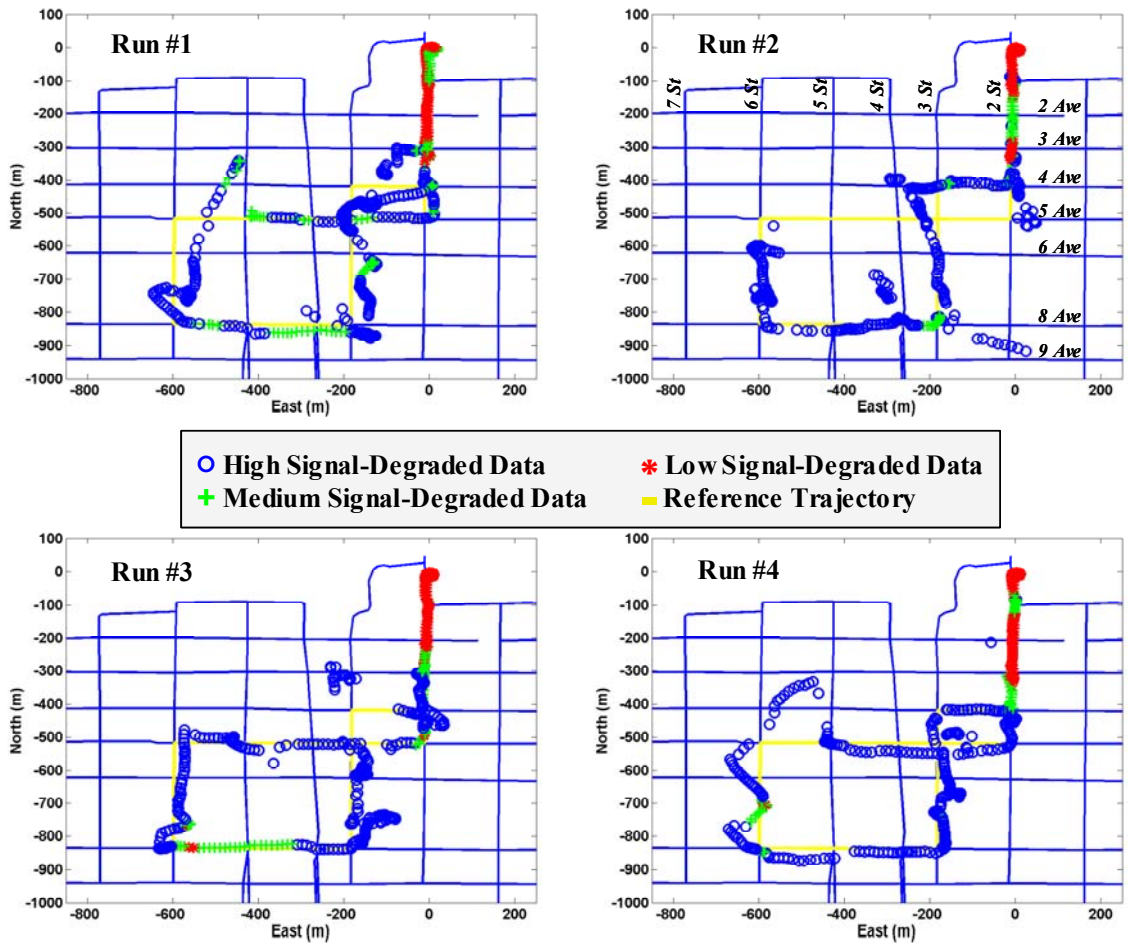


Figure 7.7: HSGPS positions and classification results, route-B tests, April 23, 2005

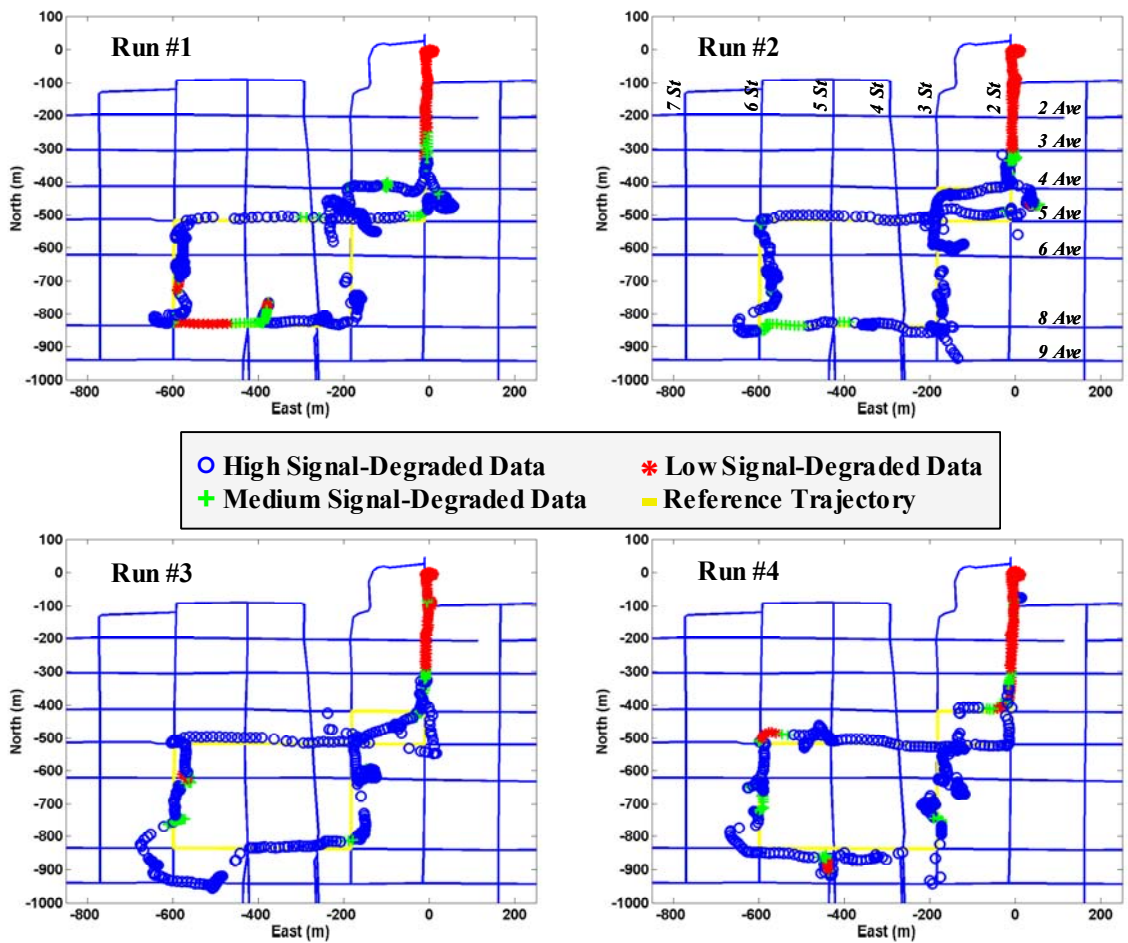


Figure 7.8: HSGPS positions and classification results, route-B tests, April 26, 2005

Table 7.1 and Table 7.2 list the accuracy and availability of the HSGPS position as well as the data classification performance obtained from the route-A and route-B tests, respectively. Because in our test the digital map is the only available reference, the across-track errors are computed for position accuracy analysis. As shown, although the availability of the HSGPS position in a typical North American urban area is considerably high (above 95% for both route-A and route-B tests), the position performance is unsatisfactory for land vehicle applications (with maximum across-track errors at the hundred-metre level). For data classification performance, we see that most of the data classification results agree with the conclusion that the high signal-degraded data have larger mean, RMS, and maximum across-track errors than the medium signal-degraded data and so on. However, because of the in-receiver filter effects, there exist

few exceptions that the position accuracy between different signal-degraded data set is similar. Statistically, based on the results of the eight run tests, the good HSGPS data classification for both route-A and route-B tests is still achievable. For the route-A tests, the average maximum across-track error is at around the 15 metre level for the low signal-degraded data, around the 30 metre level for the medium signal-degraded data, and around the 100 metre level for the high signal-degraded data. For the route-B tests with severer signal degradation conditions, the average across-track maximum error is at around the 35 metre level for the low signal-degraded data, around the 60 metre level for the medium signal-degraded data, and around the 150 metre level for the high signal-degraded data.

Table 7.1: HSGPS position accuracy after data classification (route-A)

Classified HSGPS Data		Test Run # (April 23, 2005)				Test Run # (April 26, 2005)				Average
		1	2	3	4	1	2	3	4	
Low Signal- Degraded	MAX (m)	10.70	7.62	10.14	19.99	21.58	12.30	8.47	36.76	15.95
	Mean (m)	3.02	3.01	4.78	4.23	3.34	2.76	2.00	2.96	3.26
	RMS (m)	4.04	3.52	5.37	5.45	4.98	3.55	2.48	6.77	4.52
	Av. (%)	47.75	37.55	30.87	36.49	29.79	22.39	15.65	14.42	29.36
Medium Signal- Degraded	MAX (m)	29.20	42.33	20.56	18.71	26.32	31.18	42.06	40.89	31.41
	Mean (m)	8.15	9.02	6.64	5.82	9.38	6.17	4.79	11.47	7.68
	RMS (m)	10.32	15.07	7.94	7.51	12.49	8.26	7.54	16.91	10.76
	Av. (%)	17.98	14.38	21.70	11.71	21.25	15.37	24.73	22.57	18.71
High Signal- Degraded	MAX (m)	65.04	43.61	40.64	279.81	73.93	94.58	199.89	126.60	115.51
	Mean (m)	15.12	10.86	14.22	26.84	14.80	29.97	20.29	22.95	19.38
	RMS (m)	20.11	14.97	17.36	53.68	21.58	41.38	31.17	35.24	29.43
	Av. (%)	33.33	47.00	46.09	50.00	47.91	61.64	56.18	49.84	49.00
Total	MAX (m)	65.04	43.61	40.64	279.81	73.93	94.58	199.89	126.60	115.51
	Mean (m)	8.02	7.61	9.60	15.93	10.19	20.16	13.35	16.65	12.69
	RMS (m)	12.78	12.00	12.79	38.53	16.32	32.79	24.10	28.19	22.19
	Av. (%)	99.06	98.93	98.66	98.20	98.95	99.40	96.56	86.83	97.07

Av. denotes Availability.

Table 7.2: HSGPS position accuracy after data classification (route-B)

Classified HSGPS Data		Test Run # (April 23, 2005)				Test Run # (April 26, 2005)				Average
		1	2	3	4	1	2	3	4	
Low Signal- Degraded	MAX (m)	11.22	5.98	33.05	14.56	67.41	59.94	31.57	64.80	36.06
	Mean (m)	2.82	1.63	3.74	3.31	3.74	4.55	3.24	5.17	3.53
	RMS (m)	3.73	2.11	5.10	3.90	10.34	11.03	6.77	11.03	6.75
	Av. (%)	31.38	23.34	31.94	37.04	26.46	26.09	28.68	28.33	29.16
Medium Signal- Degraded	MAX (m)	174.42	9.27	38.81	20.04	71.37	67.42	42.64	70.10	61.76
	Mean (m)	21.22	3.36	8.14	7.50	15.88	19.65	17.02	12.97	13.22
	RMS (m)	38.93	4.09	13.18	8.75	23.29	29.49	22.12	16.62	19.56
	Av. (%)	19.01	14.41	11.32	11.13	12.99	11.61	12.75	14.85	13.51
High Signal- Degraded	MAX (m)	175.04	397.57	131.97	207.04	70.45	62.19	120.78	115.75	160.10
	Mean (m)	36.35	38.73	27.48	27.25	23.17	19.32	33.40	25.94	28.95
	RMS (m)	47.14	83.23	39.01	42.73	28.46	24.99	45.92	36.26	43.47
	Av. (%)	47.30	48.85	52.25	50.00	58.64	60.11	55.54	53.79	53.31
Total	MAX (m)	175.04	397.57	131.97	207.04	71.37	67.42	120.78	115.75	160.87
	Mean (m)	22.63	22.84	17.25	15.98	16.96	15.42	22.32	17.89	18.91
	RMS (m)	37.09	62.54	29.35	30.73	24.18	22.79	35.86	28.41	33.87
	Av. (%)	97.68	86.60	95.50	98.17	98.09	97.81	96.97	96.97	95.97

Av. denotes Availability.

7.2.2 Results of GPS

For the SiRF conventional GPS that has standard signal tracking sensitivity, the position solutions obtained from the route-A tests on April 23 and 26, 2005 are illustrated in Figure 7.9 and Figure 7.10 and the position solutions from the route-B tests are shown in Figure 7.11 and Figure 7.12, respectively. Similar to the results from the HSGPS data classification, more accurate and stable position solutions have been identified as low or medium signal-degraded data while the erroneous and biased position solutions have been identified as high signal-degraded data. In addition, most of the identified low or medium signal-degraded data in the core downtown areas are located at or close to the intersections, demonstrating the consistency between the data classification results and the actual signal and geometry conditions. However, similar to the limitation presented in the HSGPS data classification, some solutions with good position accuracy were identified as high signal-degraded data and vice versa. This is because the single point code-based position solution from the GPS receiver is affected by not only the quality of the GPS signal and geometry but also the performance of the in-receiver filter. An unexpected example shown in the run #4 test in Figure 7.12 demonstrates that under low

and medium signal degradation conditions (at the corner of 5th Avenue and 6th Street) the GPS receiver could provide poor position solutions with error at the hundred-metre level. Looking at the HSGPS solution at the same location of the same run test shown in Figure 7.8, we found that the HSGPS solutions at the same corner were identified as low and medium signal-degraded data with good position accuracy. The HSGPS case is an expected result showing that the position performance is inversely proportional to the degree of signal degradation. Thus, by comparing the GPS with HSGPS position performance under the same location at the same time, it is clear that the performance difference is due to in-receiver filter effects. The unexpected GPS position solutions are obtained from the overweighting of the previous filtered positions and the underweighting of the current GPS measurements performed by the in-receiver filter.

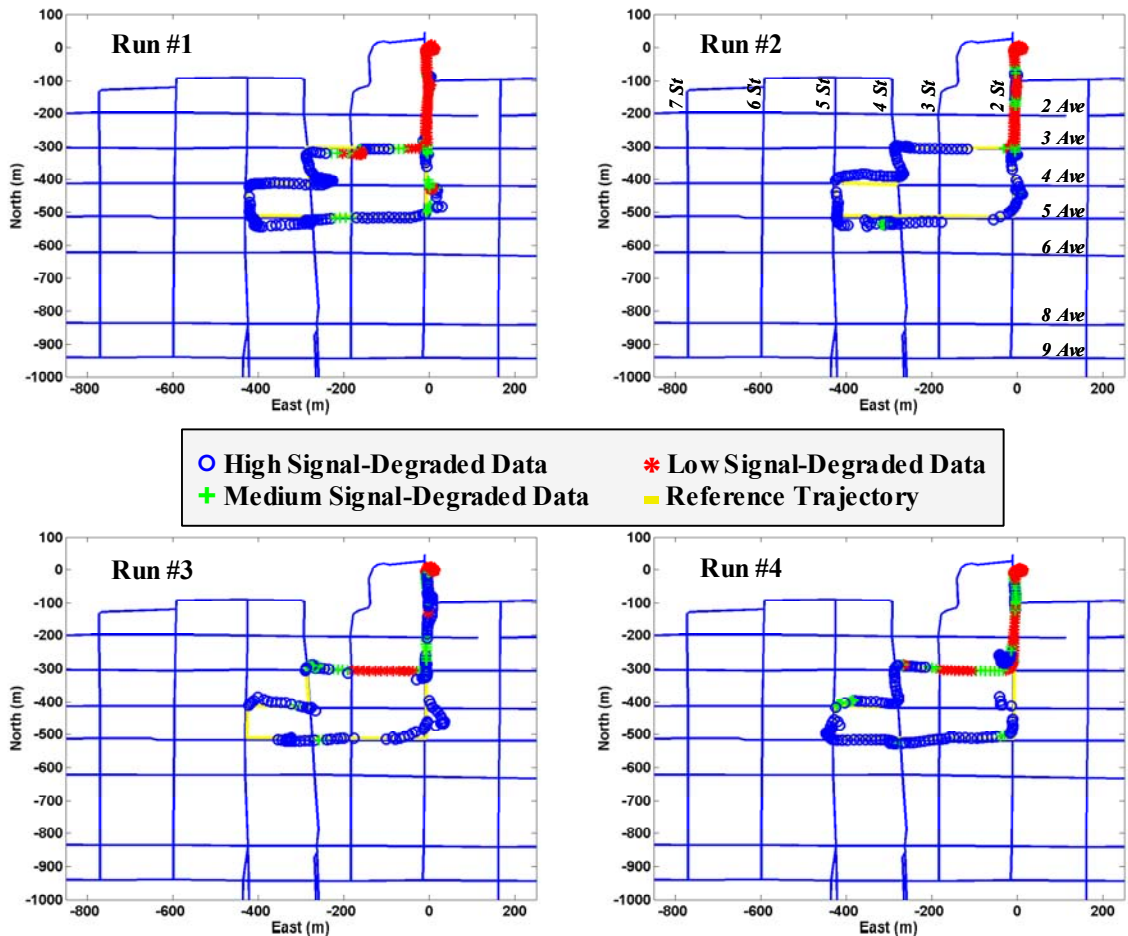


Figure 7.9: GPS positions and classification results, route-A tests, April 23, 2005

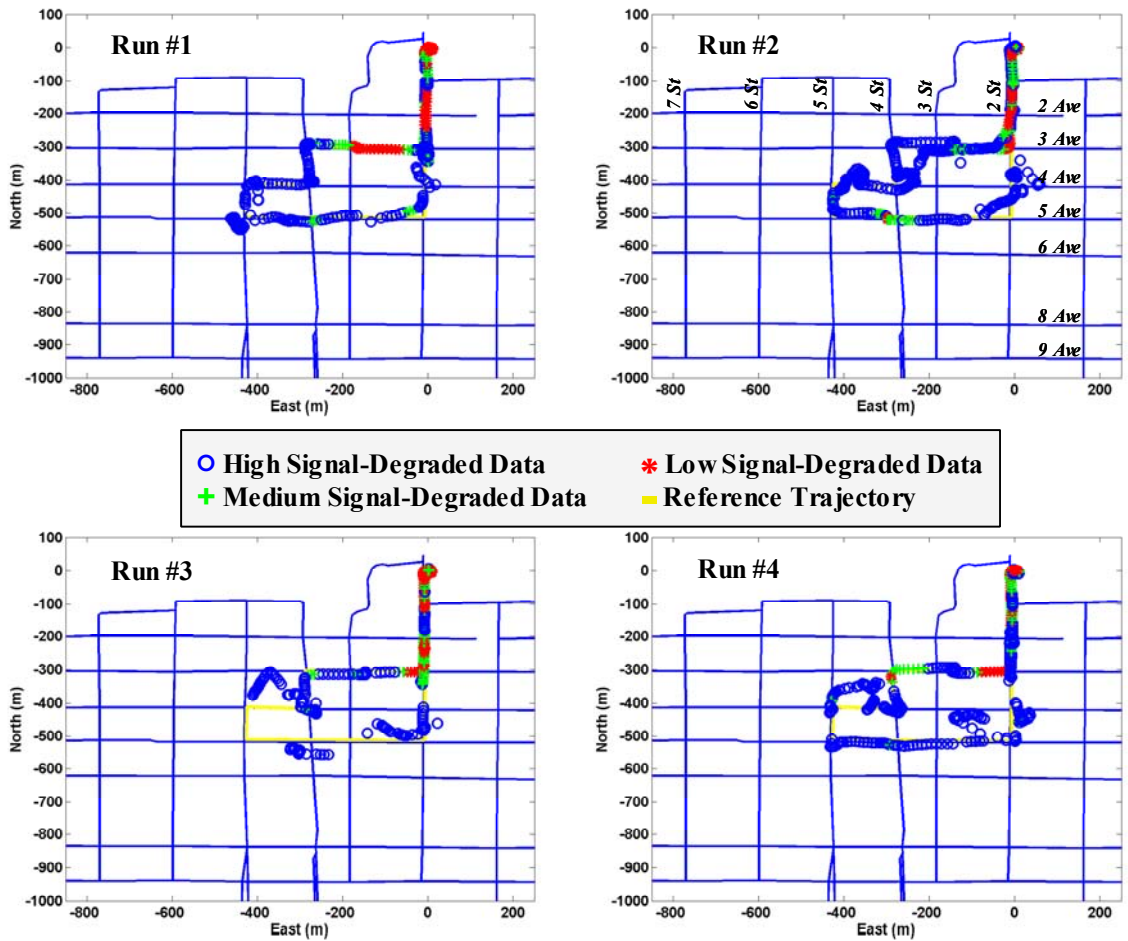


Figure 7.10: GPS positions and classification results, route-A tests, April 26, 2005

Table 7.3 and Table 7.4 list the across-track errors and the data availability of the conventional GPS solutions for each classified signal-degraded data in the route-A and route-B tests, respectively. As shown, the availability of GPS positions in urban areas is degraded, averagely about 87% for the route-A tests and about 76% for the route-B tests. The position performance is also unsatisfactory for land vehicle applications, averagely with the maximum across-track error at the hundred-metre level. For the data classification performance, the statistical results are similar to the HSGPS case. In general, the position accuracy is inversely proportional to the degree of signal degradation condition, i.e., the severer the signal degradation condition, the poorer the position accuracy. For the route-A tests, the average maximum across-track error is at around the 10 metre level for the low signal-degraded data, around the 35 metre level for

the medium signal-degraded data, and around the 95 metre level for the high signal-degraded data. For the route-B tests that have severer signal degradation conditions, the average maximum across-track error is at around the 20 metre level for the low signal-degraded data, around the 60 metre level for the medium signal-degraded data, and around the 150 metre level for the high signal-degraded data.

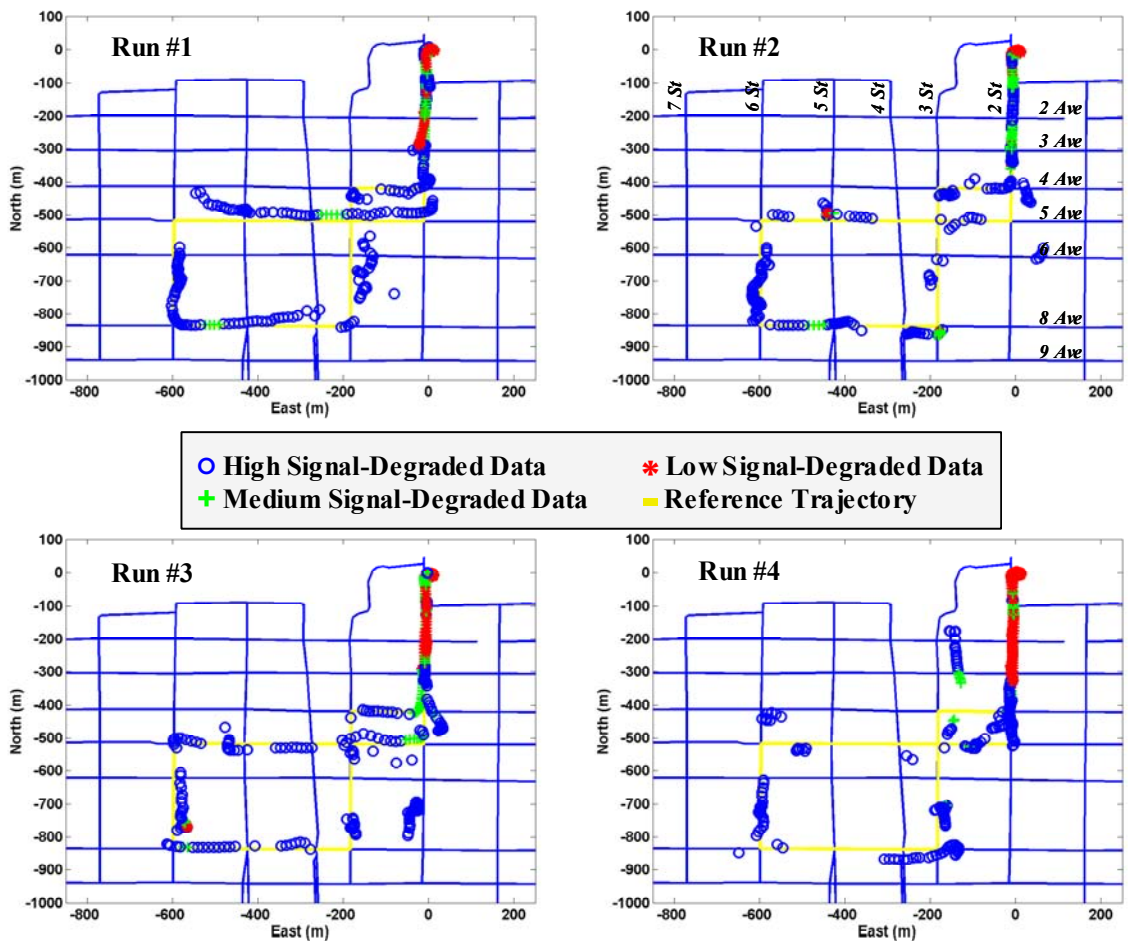


Figure 7.11: GPS positions and classification results, route-B tests, April 23, 2005

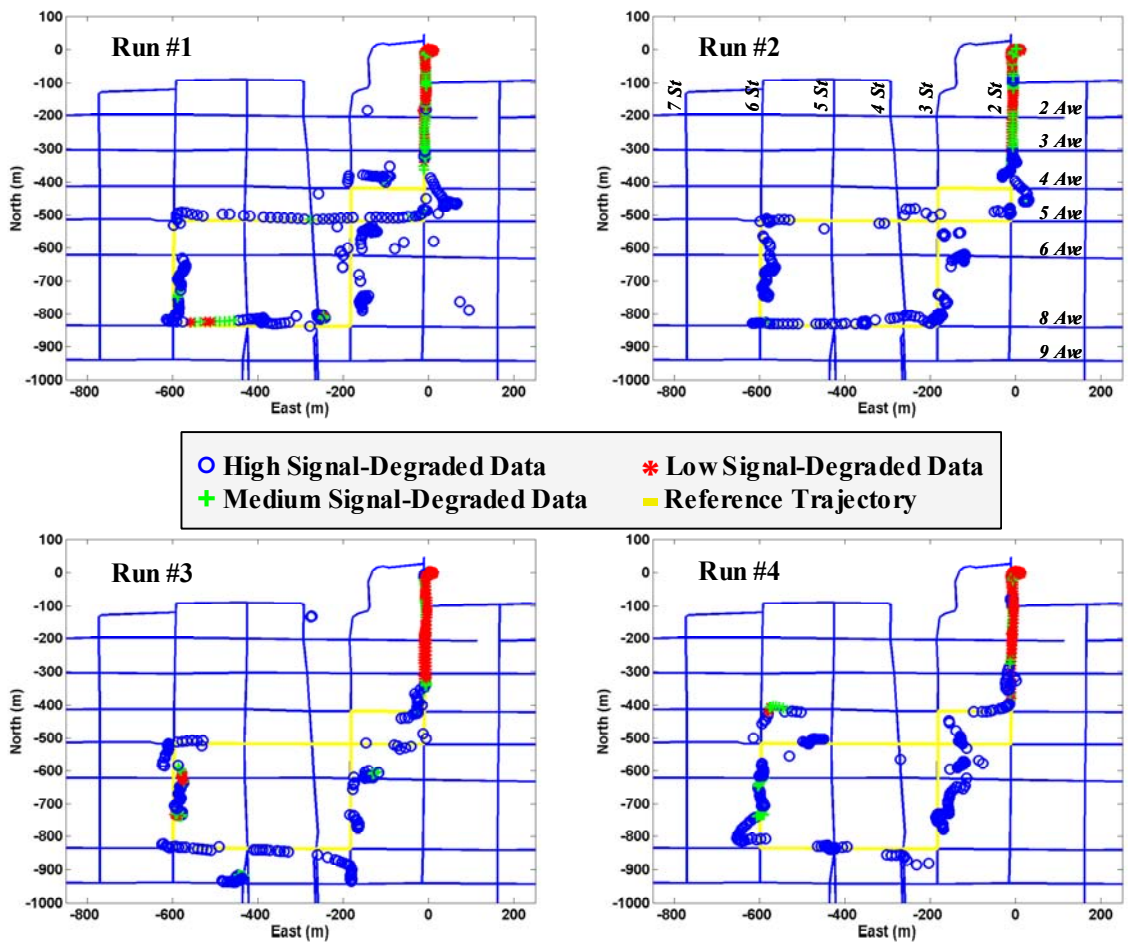


Figure 7.12: GPS positions and classification results, route-B tests, April 26, 2005

Comparing the overall performance of the conventional GPS position with the high sensitivity GPS position, we found that the high sensitivity GPS provides higher availability but lower reliability than the conventional GPS. For the route-A tests, the availability of the conventional and high sensitivity GPS solutions is about 87% and 97% while the average RMS across-track error is about 19 m and 22 m, respectively. For the route-B tests, the availability of the conventional and high sensitivity GPS solutions is about 76% and 96% while the average RMS across-track error is about 27 m and 34 m, respectively. The obtained performance difference is considered reasonable as the high sensitivity GPS receiver is specially designed to track low-power signals which are generally noisy and have large outliers due to multipath and echo-only signals.

Table 7.3: GPS position accuracy after data classification (route-A)

Classified GPS Data		Test Run # (April 23, 2005)				Test Run # (April 26, 2005)				Average
		1	2	3	4	1	2	3	4	
Low Signal- Degraded	MAX (m)	23.59	7.30	10.99	14.70	7.14	9.98	8.60	5.98	11.04
	Mean (m)	4.94	2.75	5.25	3.14	2.49	3.13	2.09	2.13	3.24
	RMS (m)	7.10	3.45	5.98	4.41	2.92	4.26	2.66	2.58	4.17
	Av. (%)	43.07	35.62	23.27	34.23	27.00	8.06	21.91	9.40	25.32
Medium Signal- Degraded	MAX (m)	22.58	26.68	13.48	16.88	28.56	133.06	14.88	20.43	34.57
	Mean (m)	7.25	10.37	5.30	6.48	7.29	10.96	2.56	3.59	6.73
	RMS (m)	9.74	14.43	6.86	8.32	8.98	29.22	3.74	6.16	10.93
	Av. (%)	9.93	6.44	14.99	14.41	15.51	12.99	14.55	16.77	13.20
High Signal- Degraded	MAX (m)	56.53	30.57	184.39	36.10	48.62	216.80	105.55	80.18	94.84
	Mean (m)	14.26	9.15	9.60	12.98	9.46	24.90	18.64	16.36	14.42
	RMS (m)	19.86	12.41	18.89	16.51	12.88	50.28	28.09	26.70	23.20
	Av. (%)	43.45	46.57	45.41	41.67	47.74	68.36	38.81	54.70	48.34
Total	MAX (m)	56.53	30.57	184.39	36.10	48.62	216.80	105.55	80.18	94.84
	Mean (m)	9.37	6.67	7.62	8.22	7.00	20.91	10.72	12.06	10.32
	RMS (m)	14.49	10.04	14.57	12.00	10.21	45.37	20.29	22.16	18.64
	Av. (%)	96.44	88.63	83.67	90.32	90.24	89.40	75.27	80.88	86.86

Av. denotes Availability.

Table 7.4: GPS position accuracy after data classification (route-B)

Classified GPS Data		Test Run # (April 23, 2005)				Test Run # (April 26, 2005)				Average
		1	2	3	4	1	2	3	4	
Low Signal- Degraded	MAX (m)	15.65	23.77	33.96	6.36	30.08	7.68	23.35	20.10	20.12
	Mean (m)	5.78	2.10	5.27	1.90	3.12	2.02	4.67	2.59	3.43
	RMS (m)	7.56	4.71	9.97	2.37	5.41	2.64	7.65	3.74	5.51
	Av. (%)	14.53	16.43	20.31	32.77	21.22	11.48	18.97	23.03	19.84
Medium Signal- Degraded	MAX (m)	20.07	29.74	33.05	107.85	58.94	30.89	84.21	112.91	59.71
	Mean (m)	3.01	4.33	5.57	11.18	11.95	2.43	14.88	11.38	8.09
	RMS (m)	5.55	7.95	8.86	22.69	19.51	4.28	28.50	29.57	15.86
	Av. (%)	11.59	13.69	16.28	10.06	13.11	11.20	18.51	10.61	13.13
High Signal- Degraded	MAX (m)	102.22	77.03	157.99	112.15	277.12	64.04	287.89	105.25	147.96
	Mean (m)	14.83	11.09	31.69	22.03	29.25	20.58	26.69	20.61	22.10
	RMS (m)	20.98	16.73	58.46	35.45	40.69	27.08	46.73	31.74	34.73
	Av. (%)	48.69	39.05	38.29	34.45	45.89	51.23	40.36	44.24	42.78
Total	MAX (m)	102.22	77.03	157.99	112.15	277.12	64.04	287.89	112.91	148.92
	Mean (m)	11.24	7.62	18.85	12.08	19.51	14.95	18.51	14.03	14.60
	RMS (m)	17.39	13.26	42.33	25.09	31.89	22.63	36.60	26.37	26.94
	Av. (%)	74.81	69.16	74.88	77.29	80.21	73.91	77.85	77.88	75.75

Av. denotes Availability.

7.3 Integration System Performance

The previous section has demonstrated the performance of the fuzzy data classification for both the SiRF high sensitivity and conventional GPS in the urban environment. This section presents the performance of the AI-enhanced MEMS INS/GPS integration system in the same environment. To assess the impact of AI enhancements on the position filter performance, the integrated positions derived from the conventional adaptive Kalman filter are also presented. It should be noted that for both cases the velocity filters work exactly the same, both aided by land vehicle dynamics knowledge. In the following sections, the results of the MT9/HSGPS integrated positions are presented first, followed by the results of the MT9/GPS integrated positions.

7.3.1 Results of MT9/HSGPS

Figure 7.13 and Figure 7.14 illustrate the MT9/HSGPS trajectories derived from the conventional adaptive Kalman filter (AKF) and the AI-enhanced adaptive Kalman filter (AI+AKF) for the route-A tests on April 23 and 26, 2005, respectively. For the route-B tests, the MT9/HSGPS trajectories are illustrated in Figure 7.15 and Figure 7.16 for April 23 and 26 tests, respectively. In all figures, the trajectories obtained from the AKF and AI+AKF are marked with cyan squares and pink diamonds respectively while the reference trajectory is marked with a yellow line. As shown, in the beginning and the end of each test with better GPS signal conditions, the obtained trajectories from both the AKF and AI+AKF overlap the reference trajectory, indicating good position accuracy. In the core downtown areas with severer signal degradation conditions, the accuracy of the integrated positions degrades due to the use of the deteriorated GPS positions and the drifted INS positions in the absence of GPS.

Comparing the integrated positions shown in Figure 7.13 through Figure 7.16 with the HSGPS positions shown in Figure 7.5 through Figure 7.8, we found that the erroneous HSGPS positions have been filtered and smoothed by the adaptive Kalman filter. In addition, as shown in Figure 7.5 through Figure 7.8, in most cases the HSGPS data have been correctly classified, thus the innovation-based adaptive measurement noise

covariance can be properly modified according to the identified signal degradation condition. Consequently, the more accurate GPS data are characterized by smaller measurement noise covariances so that the filter positions can fast converge to the accurate GPS positions. A typical example can be found in the run #2 of route-B tests on April 23, 2005. As shown in the run #2 test in Figure 7.7, some GPS positions with good accuracy at the corner of 8th Avenue and 3rd Street have been classified as medium signal-degraded data. Thus, the AI-enhanced adaptive Kalman filter will trust these medium signal-degraded data more by using the decreased adaptive measurement noise covariances. As shown in the run #2 test in Figure 7.15, the AI-enhanced integrated positions at the same corner have been corrected back to the track while the positions derived from the conventional adaptive Kalman filter not.

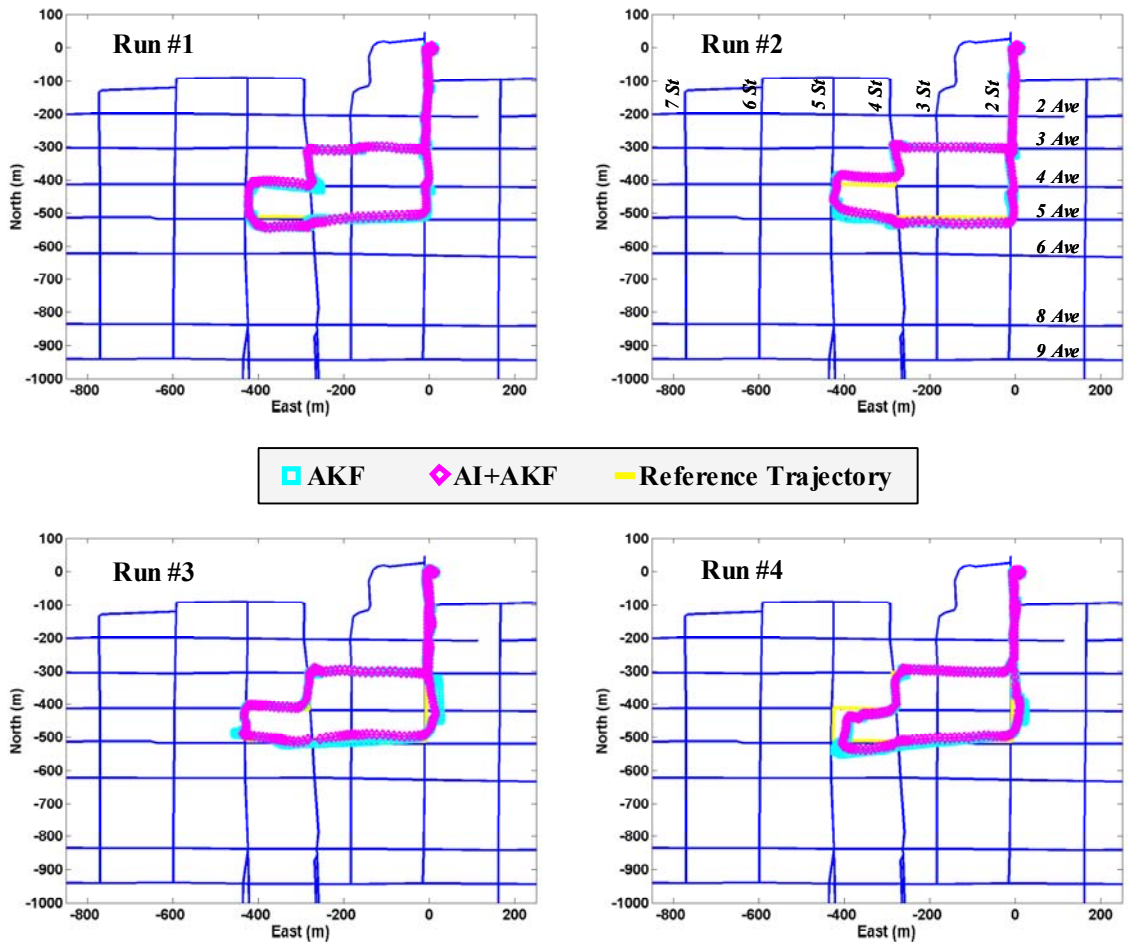


Figure 7.13: MT9/HSGPS integrated positions, route-A tests, April 23, 2005

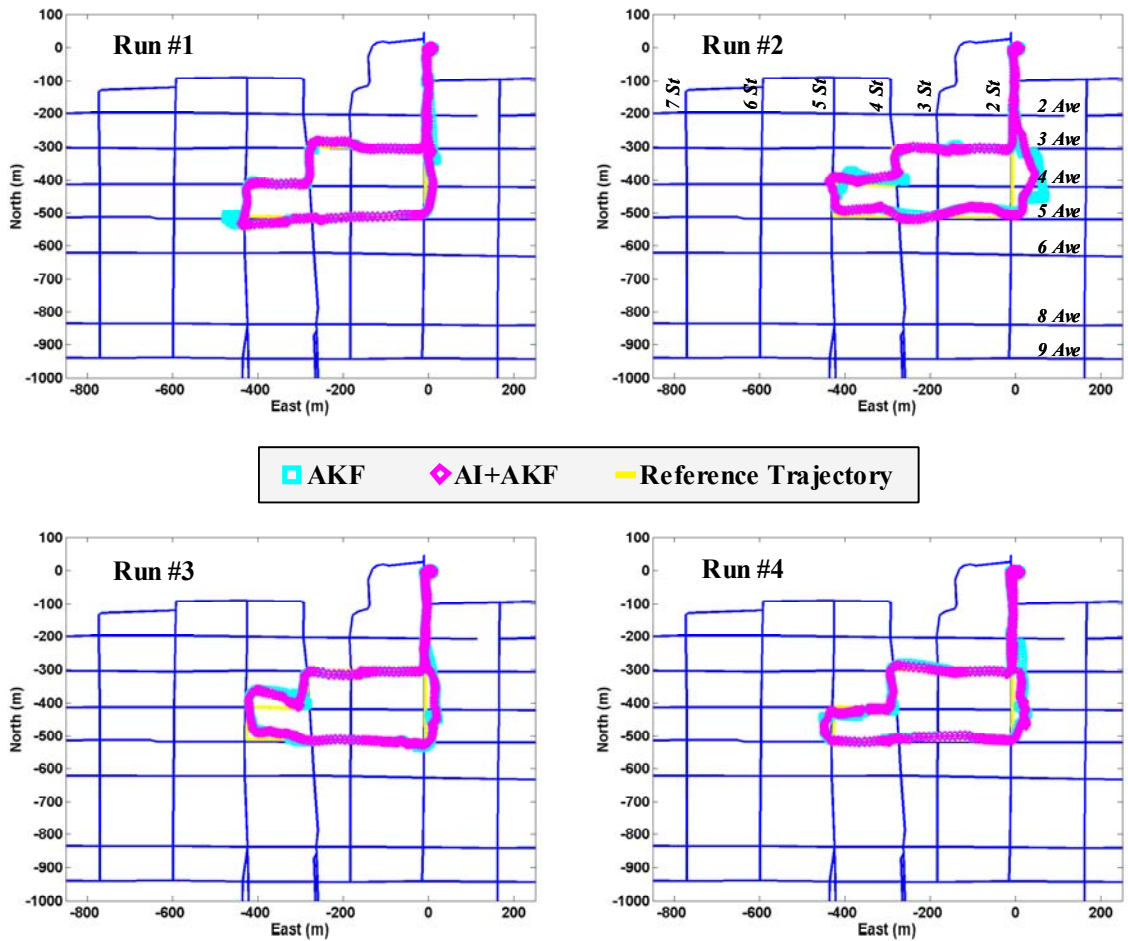


Figure 7.14: MT9/HSGPS integrated positions, route-A tests, April 26, 2005

Some test results have demonstrated the advantage of the AI-enhanced adaptive Kalman filter in terms of reducing position drifts induced by the slowly changing GPS position errors when the vehicle is stationary. A typical example can be found at the corner of 5th Avenue and 5th Street in the run #1 test in Figure 7.14. The trajectory provided by the AI+AKF remains on the track but the trajectory provided by the AKF drifts with erroneous GPS positions. As mentioned in Chapter 5, this performance improvement is contributed by the aiding from the vehicle dynamics knowledge. In summary, for both route-A and route-B tests, the results have demonstrated that the AI-enhanced adaptive Kalman filter can improve integration performance especially in GPS challenging environments. Table 7.5 and Table 7.6 list the integrated position accuracy versus the HSGPS-only position accuracy in terms of the across-track error for the route-A and

route-B tests, respectively. It can be seen that in each run the AI-enhanced AKF provides better position accuracy than the conventional one in terms of the mean, RMS and maximum across-track errors, which confirms the effectiveness of the designed AI-based enhancement. The average mean, RMS and maximum across-track errors of the AI+AKF solutions are 7.93 m, 10.97 m and 34.63 m for the route-A tests and 10.09 m, 14.38 m and 44.5 m for the route-B tests, respectively which shows significant improvement over the HSGPS solutions with the maximum across-track error at the hundred-metre level. As expected, better performance has been obtained from the route-A test, since there exist harsher GPS environments in the route-B test.

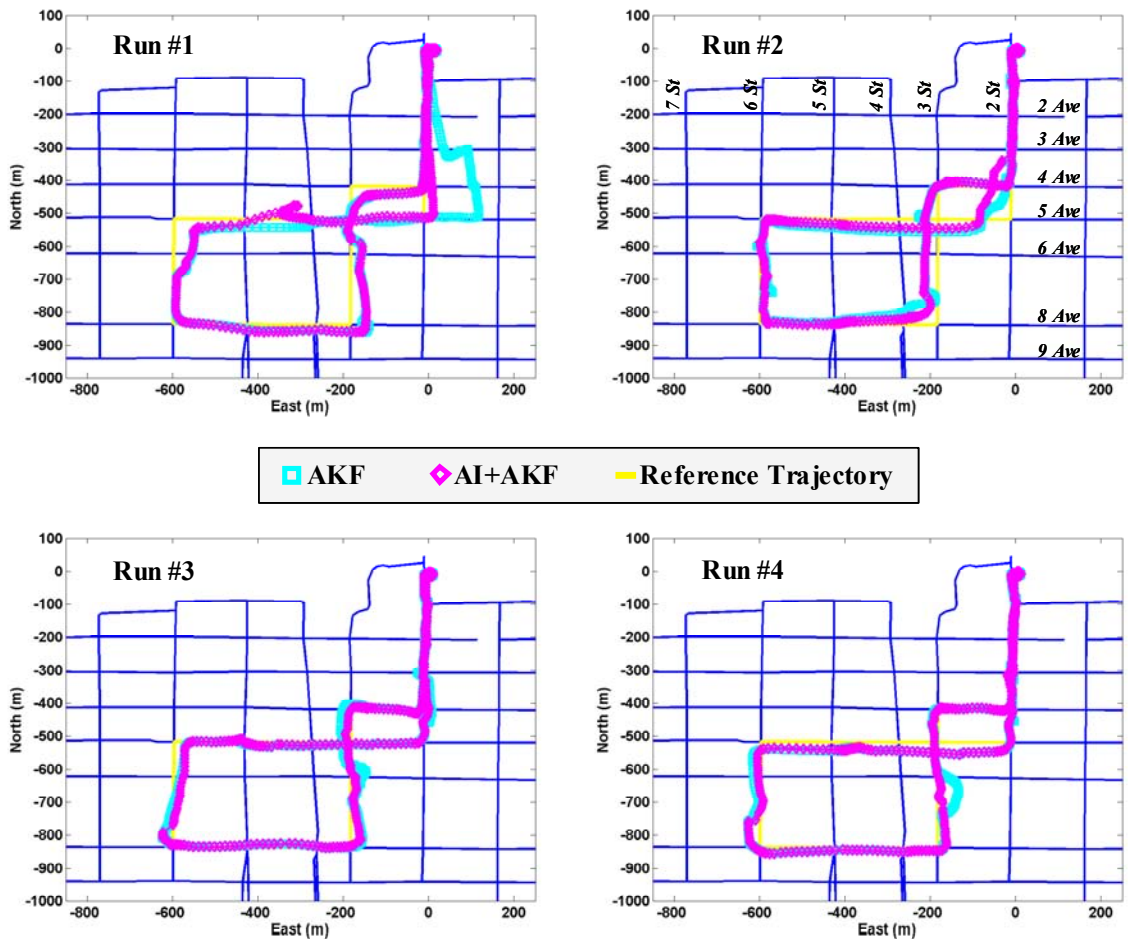


Figure 7.15: MT9/HSGPS integrated positions, route-B tests, April 23, 2005

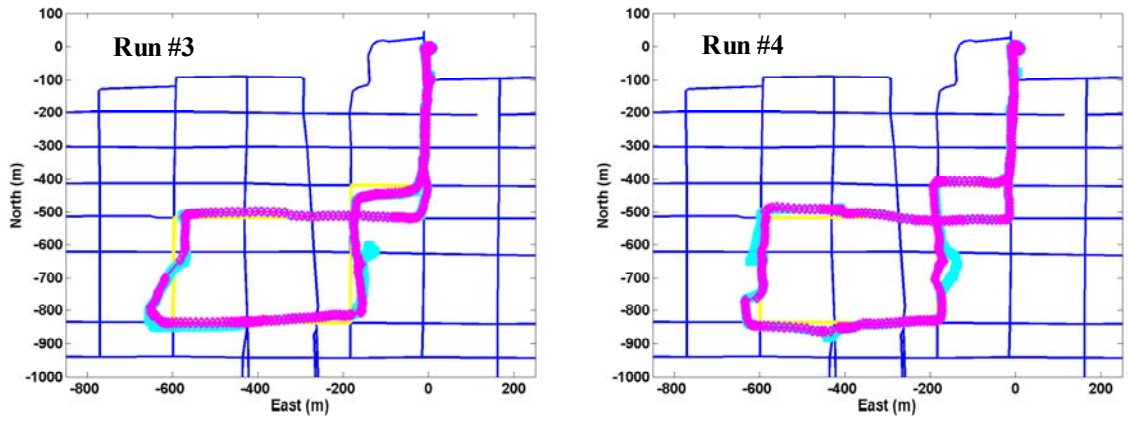
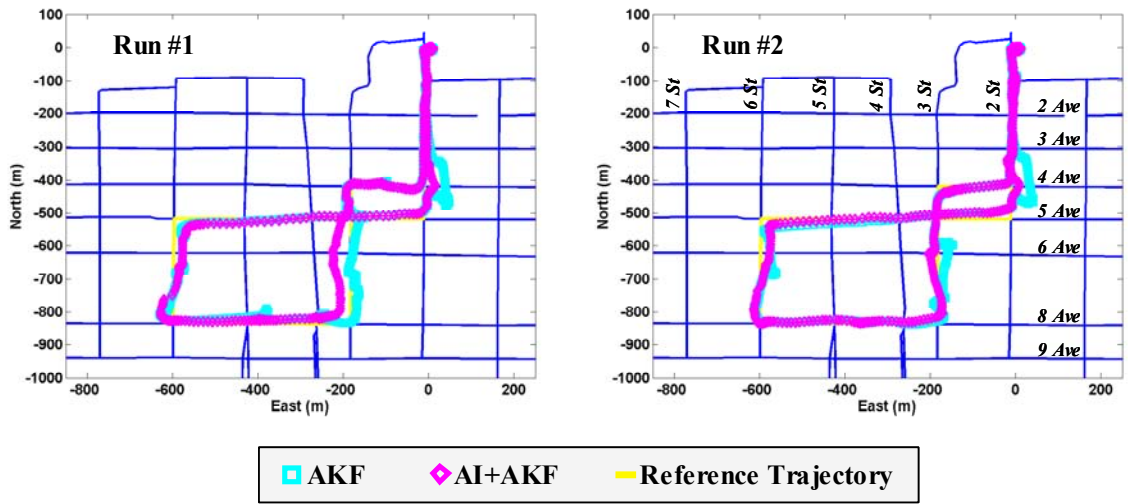


Figure 7.16: MT9/HSGPS integrated positions, route-B tests, April 26, 2005

Table 7.5: Integrated MT9/HSGPS vs. HSGPS position accuracy (route-A)

Across-Track Errors	Test Run # (April 23, 2005)				Test Run # (April 26, 2005)				Average	
	1	2	3	4	1	2	3	4		
HSGPS	MAX (m)	65.04	43.61	40.64	279.81	73.93	94.58	199.89	126.60	115.51
	Mean (m)	8.02	7.61	9.60	15.93	10.19	20.16	13.35	16.65	12.69
	RMS (m)	12.78	12.00	12.79	38.53	16.32	32.79	24.10	28.19	22.19
AKF	MAX (m)	32.99	31.72	33.70	40.65	47.64	77.05	52.72	36.33	44.10
	Mean (m)	6.48	5.97	8.74	11.63	9.37	18.62	11.17	9.28	10.16
	RMS (m)	9.74	8.70	11.51	15.84	14.20	26.68	16.86	13.24	14.59
AI+AKF	MAX (m)	31.78	28.99	22.39	32.61	26.89	52.02	50.58	31.82	34.63
	Mean (m)	5.25	5.82	7.03	10.17	5.33	12.75	9.23	7.86	7.93
	RMS (m)	8.46	8.08	8.45	13.10	7.39	17.83	12.91	11.59	10.97

Table 7.6: Integrated MT9/HSGPS vs. HSGPS position accuracy (route-B)

Across-Track Errors		Test Run # (April 23, 2005)				Test Run # (April 26, 2005)				Average
		1	2	3	4	1	2	3	4	
HSGPS	MAX (m)	175.04	397.57	131.97	207.04	71.37	67.42	120.78	115.75	160.87
	Mean (m)	22.63	22.84	17.25	15.98	16.96	15.42	22.32	17.89	18.91
	RMS (m)	37.09	62.54	29.35	30.73	24.18	22.79	35.86	28.41	33.87
AKF	MAX (m)	129.34	76.65	36.39	50.17	58.44	51.98	58.12	48.98	63.76
	Mean (m)	23.29	14.22	8.66	11.17	15.21	13.04	15.62	12.65	14.23
	RMS (m)	38.88	21.16	11.67	15.92	20.72	18.79	22.63	17.68	20.93
AI+AKF	MAX (m)	48.12	73.76	31.96	36.45	42.32	34.89	52.59	35.90	44.50
	Mean (m)	12.17	13.20	5.89	8.08	12.31	7.15	13.11	8.81	10.09
	RMS (m)	17.39	20.05	8.50	11.53	16.37	9.28	19.19	12.71	14.38

7.3.2 Results of MT9/GPS

For the MT9/GPS integrated solutions, the trajectories obtained from the route-A tests on April 23 and 26, 2005 are illustrated in Figure 7.17 and Figure 7.18 and from the route-B tests in Figure 7.19 and Figure 7.20, respectively. Similar to the results of the MT9/HSGPS system, for both route-A and route-B tests the integrated positions are good in the nearly open areas and degraded in the core downtown areas. In addition, the AI-enhanced adaptive Kalman filter has provided better position performance than the conventional one in general. However, an undesirable result was found in the run #4 of the route-B test on April 26, 2005. As shown in the run #4 test in Figure 7.20, the AI-enhanced adaptive Kalman filter solutions are poorer than the conventional ones. This is because in this case the AI+AKF approach has used the incorrect data classification result to modify the adaptive measurement noise covariance. From the GPS data classification results in the same run test as shown in Figure 7.12, we found that the GPS receiver provided poor position solutions under the low and medium signal degradation conditions (at the corner of 5th Avenue and 6th Street) due to in-receiver filter effects. As a result, the poor GPS solutions were overweighted in the AI-enhanced adaptive Kalman filter which subsequently degraded the integration performance.

The accuracy of the integrated position and the GPS-only position for route-A and route-B tests is shown in Table 7.7 and Table 7.8, respectively. Similar to the MT9/HSGPS results, the AI-enhanced adaptive Kalman filter provides better position accuracy than the

conventional one for the MT9/GPS integration system. The average mean, RMS and maximum across-track errors for the AI-enhanced integration solutions are 7.1 m, 10.5 m and 40.1 m for the route-A tests and 11.11 m, 16.85 m and 52.43 m for the route-B tests. Obviously, a better performance has been obtained from the route-A tests since there exist harsher GPS environments in the route-B tests.

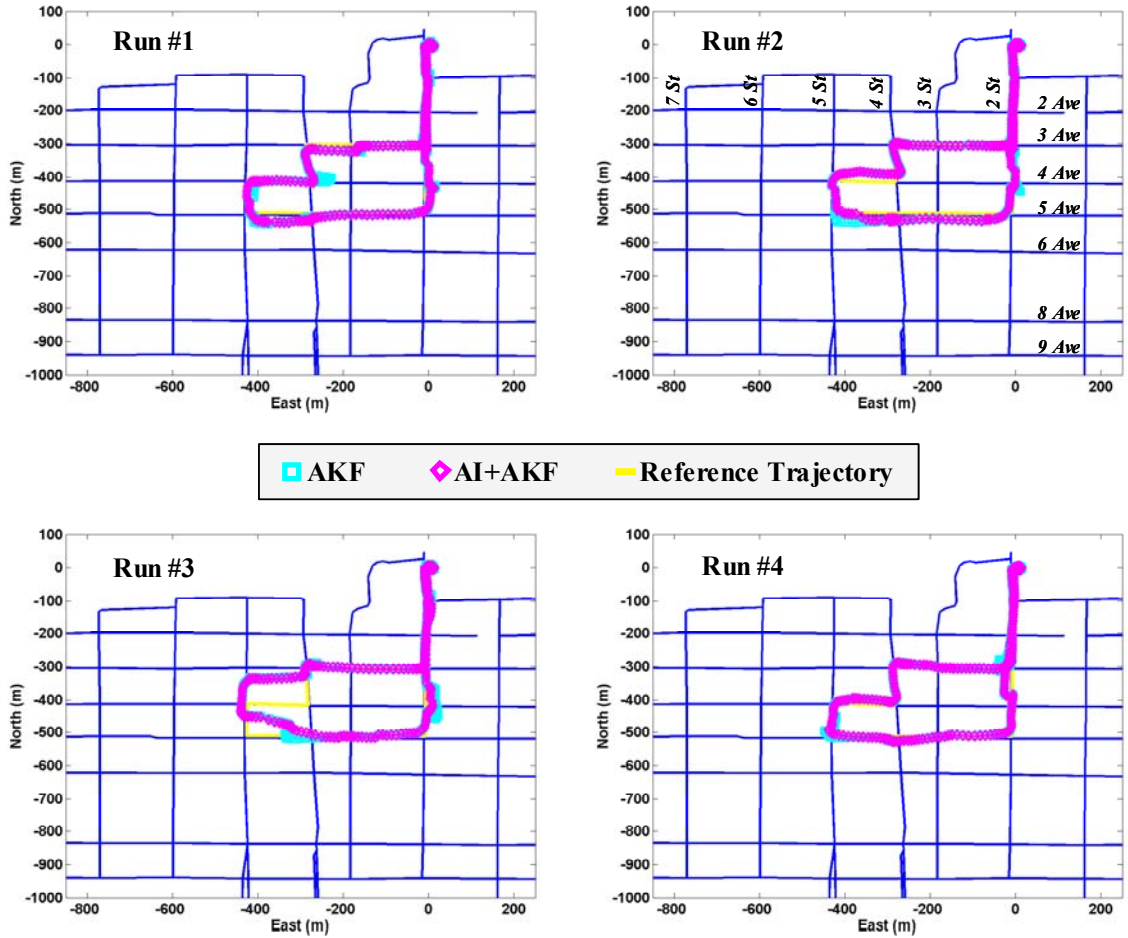


Figure 7.17: MT9/GPS integrated positions, route-A tests, April 23, 2005

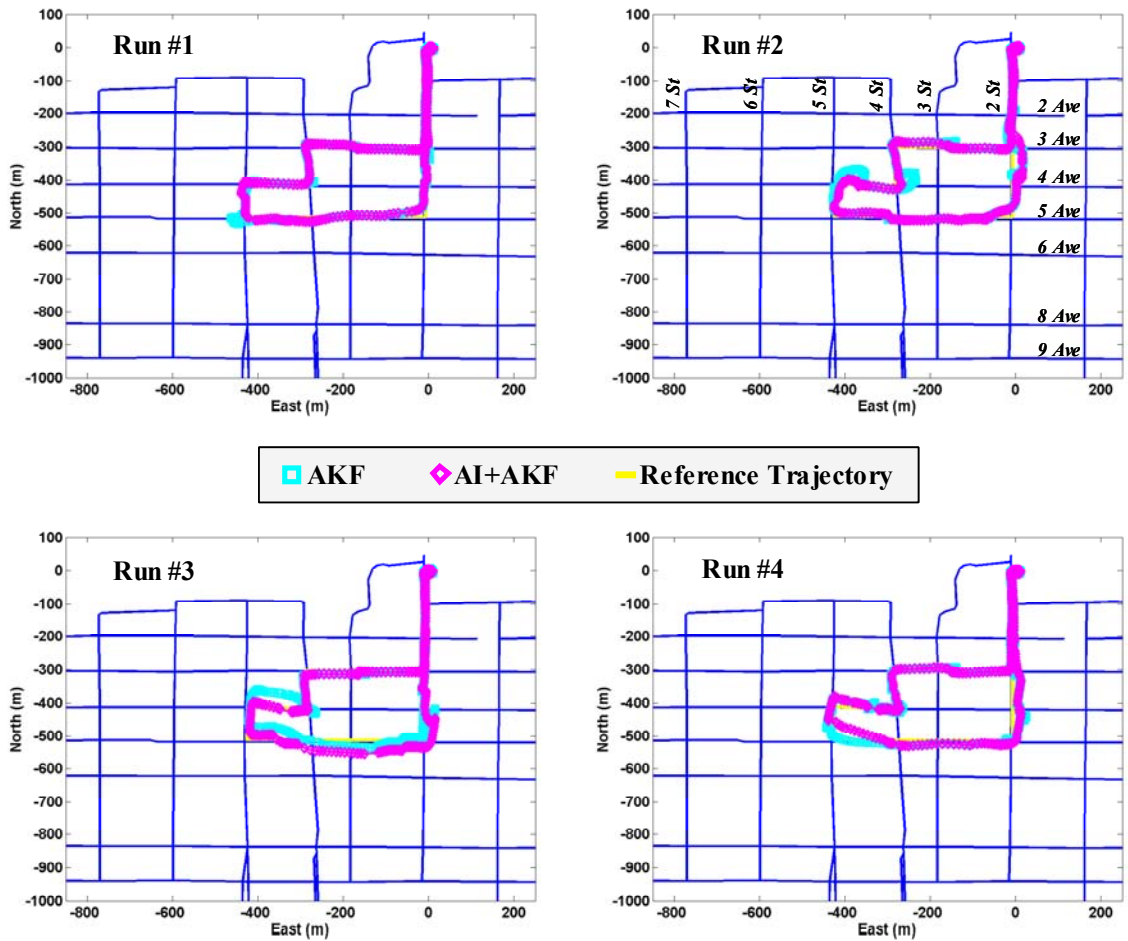


Figure 7.18: MT9/GPS integrated positions, route-A tests, April 26, 2005

Comparing the results of the MT9/HSGPS with that of the MT9/GPS, we observed that the MT9/HSGPS AI+AKF approach provides better position accuracy than the MT9/GPS AI+AKF approach. However, when the AKF-only is applied, the MT9/HSGPS system provides poorer position accuracy than the MT9/GPS system. This could be explained by the error behavior difference between the HSGPS and GPS positions. Based on the results of the HSGPS positioning shown in Figure 7.5 through Figure 7.8, we found that the HSGPS provides more available data but the obtained positions may gradually drift away from the track under severe signal degradation conditions. As mentioned in Chapter 5, the gradually drifted HSGPS position errors are undetectable by the innovation-based AKF, which will lead to biased position estimation. In contrast, the conventional GPS provides less available but more reliable positions as shown in Figure 7.9 through Figure

7.12. Although there exist some GPS position outliers, they have been easily detected by the innovation-based AKF. Thus, the conventional AKF works more properly in the MT9/GPS integration than in the MT9/HSGPS integration. Accordingly the MT9/GPS AKF positions are more accurate. When the AI-enhanced AKF is applied for data fusion, the measurement noise covariance is modified to better characterize the real GPS performance and thus the integrated position accuracy can be improved. As shown in Table 7.5 through Table 7.8, the improvement for the MT9/HSGPS integration is more significant than the MT9/GPS integration. This is because more drifted position errors from the HSGPS have been successfully removed by the AI enhancement and more low and medium geo-signal-degraded HSGPS data are available to modify the measurement noise covariance. As a result, the MT9/HSGPS AI+AKF solution is better than the MT9/GPS AI+AKF solution.

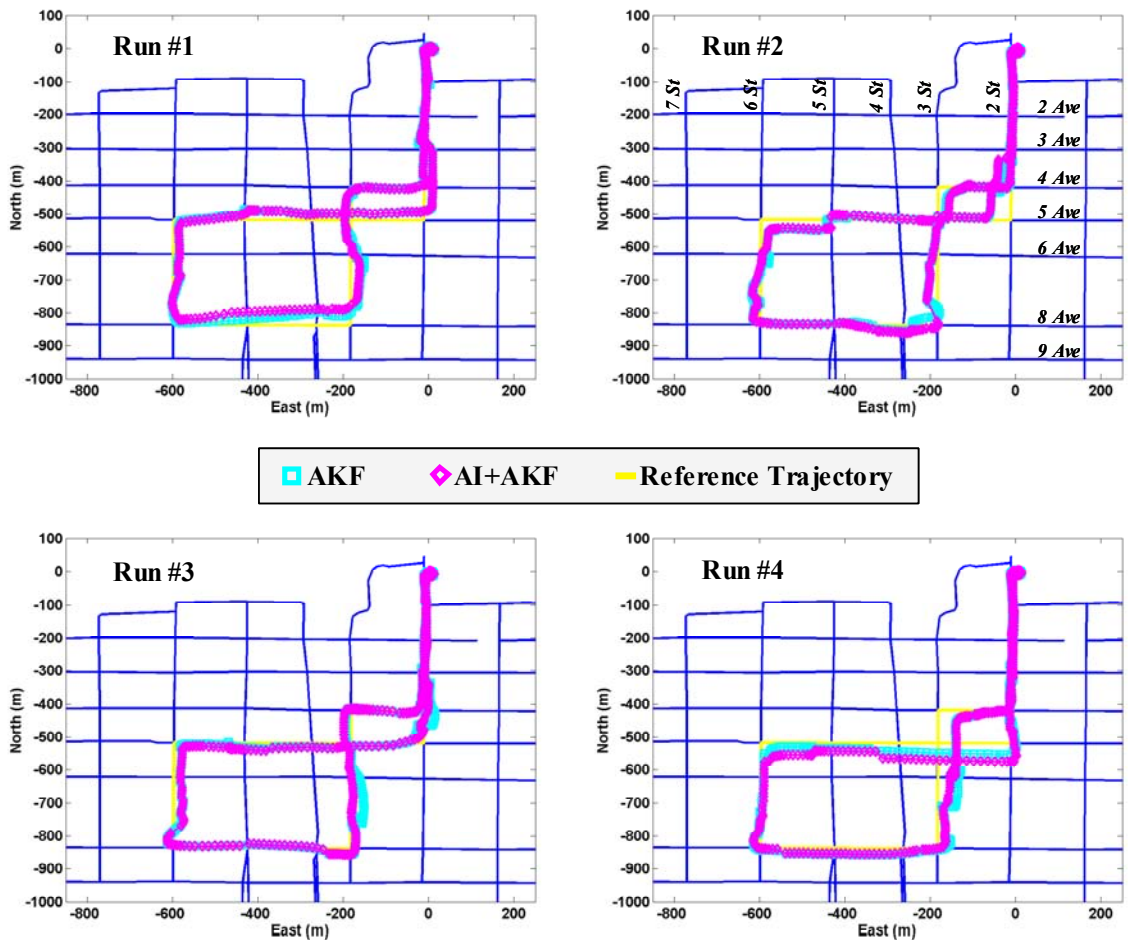


Figure 7.19: MT9/GPS integrated positions, route-B tests, April 23, 2005

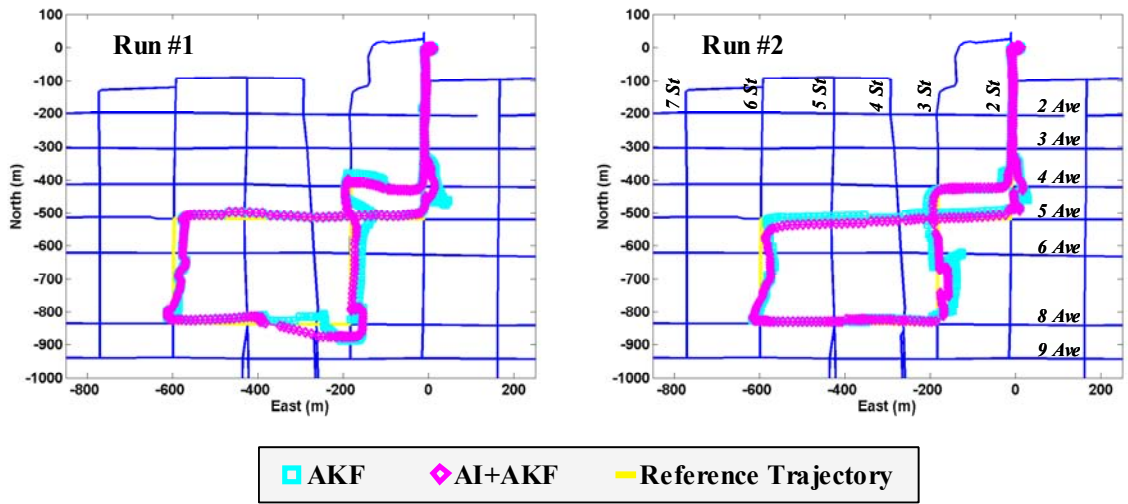


Figure 7.20: MT9/GPS integrated positions, route-B tests, April 26, 2005

Table 7.7: Integrated MT9/GPS vs. GPS position accuracy (route-A)

Across-Track Errors		Test Run # (April 23, 2005)				Test Run # (April 26, 2005)				Average
		1	2	3	4	1	2	3	4	
GPS	MAX (m)	56.53	30.57	184.39	36.10	48.62	216.80	105.55	80.18	94.84
	Mean (m)	9.37	6.67	7.62	8.22	7.00	20.91	10.72	12.06	10.32
	RMS (m)	14.49	10.04	14.57	12.00	10.21	45.37	20.29	22.16	18.64
AKF	MAX (m)	55.72	30.65	89.28	35.68	35.54	50.23	51.53	31.37	47.50
	Mean (m)	9.28	6.84	11.68	7.37	6.32	10.63	9.37	7.34	8.60
	RMS (m)	14.18	10.29	20.90	11.11	9.08	15.62	15.10	10.51	13.35
AI+AKF	MAX (m)	29.64	28.62	86.67	25.76	34.72	33.02	42.58	39.75	40.10
	Mean (m)	6.99	5.86	11.27	5.96	4.05	7.49	8.36	6.79	7.10
	RMS (m)	9.80	8.85	19.78	8.31	5.73	9.64	12.14	9.73	10.50

Table 7.8: Integrated MT9/GPS vs. GPS position accuracy (route-B)

Across-Track Errors		Test Run # (April 23, 2005)				Test Run # (April 26, 2005)				Average
		1	2	3	4	1	2	3	4	
GPS	MAX (m)	102.22	77.03	157.99	112.15	277.12	64.04	287.89	112.91	148.92
	Mean (m)	11.24	7.62	18.85	12.08	19.51	14.95	18.51	14.03	14.60
	RMS (m)	17.39	13.26	42.33	25.09	31.89	22.63	36.60	26.37	26.94
AKF	MAX (m)	56.46	56.29	32.02	54.65	56.42	56.77	66.12	58.27	54.62
	Mean (m)	10.36	8.58	8.17	12.17	15.37	14.54	14.47	10.05	11.71
	RMS (m)	13.56	13.54	11.37	18.81	21.02	20.10	21.37	15.81	16.95
AI+AKF	MAX (m)	60.61	52.84	24.85	57.48	39.68	37.64	49.70	96.64	52.43
	Mean (m)	10.70	9.46	6.33	13.26	10.59	7.91	12.75	17.89	11.11
	RMS (m)	14.91	14.84	8.57	20.77	15.04	10.38	17.47	32.85	16.85

7.4 Summary of Test Results

In this chapter, the performance of the stand-alone GPS and the AI-enhanced integration system in the urban environment has been evaluated. Two types of GPS receivers, the conventional and high sensitivity GPS, and two types of low-cost integration systems, the MEMS INS/GPS and MEMS INS/HSGPS have been tested on two downtown routes. The HSGPS provided higher availability but lower reliability of position solutions than the conventional GPS. In severe signal degradation conditions, both GPS solutions were subject to large position errors at the hundred-metre level. Using the proposed fuzzy data classification system, more accurate position solutions have been identified successfully. For the route-A test, the average maximum across-track errors for the identified low signal-degraded HSGPS and GPS data were around 15 m and 10 m, respectively. For the route-B test which has severer signal degradation conditions, the average maximum across-track errors for the identified low signal-degraded HSGPS and GPS data increased to around 35 m and 20 m, respectively. However, there still existed few disagreements between the obtained position performance and the signal degradation condition because of the smoothing feature of the position solution from the GPS receivers.

Compared to the stand-alone GPS, the AI-enhanced integration system can improve the position performance significantly. Based on the average result of the route-A and route-B tests, the MT9/HSGPS integration provided about 71% improvement in the average maximum across-track error over the HSGPS and the MT9/GPS integration provided

about 61% improvement in the average maximum across-track error over the GPS. With the capabilities of better characterizing the real GPS performance and identifying the slowly changing GPS position error, the AI-enhanced adaptive position filter provided better position performance than the conventional adaptive position filter. About 26% improvement in the average maximum across-track error for the MT9/HSGPS integration and 10% for the MT9/GPS integration were obtained. Overall, the AI-enhanced MEMS INS/HSGPS integration system provided the best position performance because of the use of more available and properly weighted GPS data.

Chapter 8

Conclusions and Recommendations

The contribution of this research work is in the development of AI-based algorithms and their incorporation with the conventional/adaptive Kalman filter for the integration of low-cost MEMS INS with SPP GPS for land vehicle applications. Three AI-based methods have been developed to deal with the corrupted GPS data in signal-degraded environments, the large instrument errors experienced with a low-grade MEMS IMU and the distorted magnetic measurements from an electronic compass, respectively. Specifically, a fuzzy logic rule-based system has been developed to identify GPS signal degradation conditions based on the combination of signal quality and geometry information so that GPS solutions can be classified in terms of their quality and subsequently can be more properly weighted in data fusion under various GPS environments. A dynamics knowledge aided inertial navigation algorithm along with a fuzzy expert vehicle dynamics identification system has been created to simplify system models and to extend measurement update schemes of the Kalman filter so that INS errors can be more effectively controlled especially during GPS outages. A neural-networks-based compass calibration algorithm has been developed to correctly remove the systematic measurement errors even in disturbance-rich environments so that the compass heading can benefit the integration system in land vehicle environments. Finally, these AI-based methods have been incorporated with the conventional/adaptive Kalman filter in a loosely coupled integration scheme to build up an intelligent data fusion and processing algorithm for low-cost MEMS INS/SPP GPS integration. The developed algorithms have been tested and evaluated in various GPS conditions (open areas, complete GPS outages and urban areas) using a low-cost Xsens MT9 MEMS IMU with SiRF Star II conventional/high sensitivity GPS receivers. The following sections outline the major conclusions drawn from this research and the recommendations for future improvements.

8.1 Conclusions

This dissertation has demonstrated the advantages and effectiveness of the developed AI-based methods applied to the enhancement of low-grade MEMS INS/SPP GPS data fusion and processing. Such AI-enhanced integration system can provide continuous and satisfactory navigation solutions for land vehicle applications in all operational environments. In the following, major conclusions are summarized in terms of various GPS conditions.

Navigation in open areas

1. With continuous and reliable GPS updates in open areas, the dynamics-aided Kalman filter can estimate the constant part of the accelerometer bias with estimation accuracy of about 0.03 m/s^2 . This enables the accurate estimation of the dynamics-derived observations to provide INS error control during GPS outages. In general, the x-axis bias estimation accuracy is better and more stable than the y-axis one because the x-axis bias is estimated directly using the Kalman filter while the y-axis bias estimation involves a statistical approach affected by more error sources. Under signal-degraded conditions, however, GPS accuracy will be degraded and in turn the Kalman filter cannot provide stable and reasonable bias estimation. In this case, the bias estimation process should be suspended and the last estimated bias is used for error compensation.
2. The low-cost MEMS INS/SPP GPS integration system can provide accuracy for attitude less than 1 degree and for horizontal velocity and position at accuracy about 0.1 m/s and 3 m in open-sky environments, respectively. The pitch and roll accuracy is affected by the filter observability which varies with vehicle dynamics changes while the heading accuracy is mainly determined by the accuracy of the GPS heading update which is proportional to the vehicle velocity. The integrated velocity and position performance is almost identical to the GPS velocity and position performance.

3. The heading information provided by the integration system in open areas has been successfully used for compass error modelling. With sufficient training data, the neural networks can properly model the nonlinear input-output relationship that describes the bias, scale factor and declination effects on the compass heading even in the presence of significant noise and disturbance. The neural networks should be retrained once the bias, scale factor and declination effects change.

Navigation with complete GPS outages

1. The dynamics-aided inertial navigation algorithm can provide sufficiently accurate attitude and velocity observations to control the stand-alone INS error drift. The bias of the dynamics-derived tilt is about 0.16 degrees and the attainable accuracy of the dynamics-derived velocity is about 0.45 m/s. The performance of the dynamics-derived observations is mainly determined by the accuracy of the accelerometer bias estimate and thus will degrade when the constant part of the accelerometer bias changes.
2. The neural networks trained in open areas have been successfully used to calibrate compass heading during the sequential GPS outages. The calibration accuracy using the neural networks in a typical land vehicle environment is about 0.26 degrees which is good enough to correct the MEMS gyro-derived heading. This calibration method doesn't require declination information and magnetometer bias and scale factor estimation. In addition, it can provide robust calibration performance in the presence of large noise and disturbance while other traditional approaches may fail or diverge.
3. During complete GPS outages, the dynamics-aided MEMS INS can provide bounded attitude and improved velocity and position information while the unaided solutions will drift over time rapidly and cannot be used for navigation. During about 3-minute stand-alone inertial navigation on the test trajectory with eight cornering shapes and four virtual stop signs, the attainable accuracy of the

dynamics-aided roll, pitch and heading is about 0.8, 0.5 and 1.5 degrees, on average, respectively. The performance difference between each axis is due to the variations in frequency and availability of the dynamics-derived information with respect to pitch, roll and heading channels. The accuracy of the dynamics-aided horizontal velocity and position solutions is about 0.66 m/s and 16.25 m, respectively and the maximum horizontal position error has been maintained within 30 m, on average. The achieved performance is therefore much better than the performance supplied by the manufacturer specifications which demonstrates the capability of using the dynamics-aided MEMS INS to bridge longer GPS outages. The limitation of the proposed method is the requirements of frequent stationary and/or cornering dynamics of the vehicle. In urban area applications, however, these requirements can be easily fulfilled by the dense traffic lights, traffic jam and the grid road layout.

4. When the calibrated compass heading is added to enhance the stand-alone dynamics-aided INS navigation, no significant improvement in tilt, velocity and position but heading accuracy only has been found. This is because the heading state in the Kalman filter is direct observable from the compass heading measurement while others are not. The improvement of the heading solution in terms of biasness is more significant than preciseness because the calibrated compass heading is nearly unbiased but is still corrupted with random errors due to noise, magnetic disturbance and projection error. In summary, the dynamics-aided plus compass-aided approach is able to provide smooth and drift-free heading estimation with mean error of 0.36 degrees and RMS error of 1.42 degrees, on average, during the GPS outage of about 3 minutes.

Navigation in urban areas

1. In urban areas, the stand-alone GPS position is subject to degraded availability and accuracy with occasional outliers of the hundred-metre level. The in-receiver filter smoothes the position but at the same time may introduce large biases when GPS measurements are corrupted by large noise and multipath. The HSGPS provides

higher availability but lower reliability in position solutions than the conventional GPS.

2. The developed fuzzy data classification system can properly classify GPS data quality in the statistical sense based on the identified signal degradation conditions for both conventional and high sensitivity GPS. However, the proposed method cannot provide a systematic assessment of epoch-by-epoch positional accuracy because of the unknown proprietary of the in-receiver filter and the dilemma of using the fading C/N_0 to indicate the magnitude of multipath error. The proposed method could be applied to notify users the quality of GPS data under various GPS environments and to improve the performance of GPS/INS integration system by properly adapting the GPS data in data fusion as implemented in this research.
3. The intelligent MEMS INS/SPP HSGPS integration system can provide continuous and satisfactory position solutions for land vehicle navigation in the typical North American urban canyons. The average RMS and maximum across-track errors are around 10.97 m and 34.63 m for the route-A tests and 14.38 m and 44.5 m for the route-B tests where there exist harsher GPS environments. The intelligent MEMS INS/SPP GPS integration system provides similar position performance, with the average RMS and maximum across-track errors of around 10.5 m and 40.1 m for the route-A test and 16.85 m and 52.43 m for the route-B test, respectively. In harsher GPS environments such as in the core downtown area, HSGPS is recommended for the integration system in order to provide better navigation performance.
4. The AI-enhanced adaptive Kalman filter has shown better performance than the conventional adaptive Kalman filter because of its capability to reject the slowly changing GPS position error and to fast recover from the biased estimation once good GPS data are available. This improvement is found more significant in the MEMS INS/HSGPS integration than the MEMS INS/GPS integration because the HSGPS solution has more gradually drifted type of position error that can be detected by the AI-enhanced adaptive Kalman filter but not by the conventional one.

However, the degraded position performance could be introduced by the AI-enhanced adaptive Kalman filter when the performance of the GPS filter output doesn't correspond to the signal degradation condition such as poor GPS outputs in a low signal-degraded condition. Based on the experimental results, this rarely happens and is difficult to detect due to the latency of the in-receiver filter.

In summary, the proposed AI-based methods suggest a powerful approach to process the imprecise and ambiguous data obtained from low quality instruments and in unfavourable environments that are difficult to deal with by traditional model-based algorithms. The intelligent integration algorithm increases the potential of using a low-cost MEMS INS/SPP GPS system to provide continuous and satisfactory navigation solution for land vehicle applications.

8.2 Recommendations

Based on the results and conclusions of this dissertation, the following recommendations for further research are proposed:

1. The velocity and attitude filter is designed to operate in GPS-only update mode under open-sky environments and in full update (updates from GPS, dynamics-derived observation and calibrated compass heading) mode under signal-degraded and/or signal-blocked environments. In this research, the integration system was tested in open-sky and urban areas respectively but not in a more realistic situation such as from open-sky/suburban to urban areas or vice versa. In practical applications, it is required to develop an expert system to automatically switch the operation mode of the velocity and attitude filter according to GPS data quality and filter performance.
2. The parameters of the neural networks used for compass calibration such as the number of hidden neuron are decided empirically in this research. For optimization purpose, an intelligent mechanism to adjust the structure and parameters of the

neural networks according to the complexity of the problem is recommended and should be investigated in the future.

3. For testing purpose, the neural networks used for compass calibration are trained and tested using the data collected by different runs on the same route during a couple-hour experiment. In practical applications, as the compass is installed in a moving vehicle, the nonlinear relationship between compass heading and true heading may change with environments such as geographic location. Thus, it is required to retrain the neural networks occasionally to adapt the environmental changes. An intelligent mechanism to determine the size of the training data and the frequency of the training in accordance with the actual field environments should be investigated.
4. Under signal-degraded and/or signal-blocked environments, the proposed integration algorithm stops the estimation of accelerometer biases and uses the last estimated biases to correct dynamics-derived observations to provide additional measurement updates for INS error control. However, the estimated bias may differ from the true bias with time according to operational environments and in turn the dynamics-derived observations could be biased. The impact of the biased dynamics-derived updates on INS error control should be investigated.
5. The parameters used in the fuzzy expert vehicle dynamics identification system are vehicle dependent and sensitive to the installation locations of the sensors. In his research they were empirically determined based on the real data. To reduce the cost of the design process and to optimize the identification system, a self-learning fuzzy system is recommended.
6. When the vehicle is moving in a straight line during long periods of GPS outage, only the accelerometer-derived roll is available to update the Kalman filter and it provides very small corrections for the pitch and forward velocity error. In this case, the pitch and forward velocity error will drift to a large extent and thus additional

error control or prediction techniques are required to maintain the stand-alone MEMS INS with reasonable performance.

7. The fuzzy data classification system can properly classify GPS data quality in the statistical sense based on the identified signal degradation conditions. However, few exceptions such as poor GPS outputs in a low signal-degraded condition could happen due to the latency of the in-receiver filter. Investigating a fault detection method to monitor these exceptions is beneficial to improve the robustness of the data classification system.
8. The position accuracy of the proposed integration system can be further improved by using map-matching techniques which provide additional map-derived observations to constrain position errors.
9. Incorporating the dynamics knowledge aided inertial navigation algorithm and fuzzy GPS data classification system with the Kalman filter in a tightly coupled integrated scheme should be investigated for possible performance improvement when the computational loading is not a major concern.

References

- Aleksander, I. and H. Morton (1990). *An Introduction to Neural Computing*. London: Chapman and Hall.
- Anderson, R., D. Hanson and A. Kourepenis (2001). Evolution of low-cost MEMS inertial system technologies, *Proceedings of ION GPS 2001*, 11-14 September, Salt Lake City, UT, USA, pp. 1332-1342.
- Ashkenazi, V., T. Moore, C. J. Hill, W. Y. Ochieng and W. Chen (1995). Design of a GNSS: coverage, accuracy and integrity, *Proceedings of ION GPS 1995*, 12-15 September, Palm Springs, CA, USA, pp. 463-472.
- Barto, A.G., R.S. Sutton and C. W. Anderson (1983). Neuronlike adaptive elements that can solve difficult learning control problems, *IEEE Transactions on Systems, Man and Cybernetics*, Vol. 13, pp. 835-846.
- Becker, S. (1991). Unsupervised learning procedures for neural networks, *International Journal of Neural Systems*, Vol. 2, pp. 17-33.
- Bezdek, J. C., R. Ehrlich and W. Full (1984). FCM: the fuzzy c-means clustering algorithm, *Computers and Geosciences*, Vol. 10, pp. 191-203.
- Bowditch, N. (1995). *The American Practical Navigator*. Bethesda, Maryland: Defense Mapping Agency, Hydrographic/Topographic Centre.
- Braasch, M. S. (1996). Multipath effects, in *Global Positioning System: Theory and Applications*, Vol. 1, chapter 14, pp. 547-569. Washington D.C.: American Institute of Aeronautics and Astronautics.
- Brandt, A. and J. F. Gardner (1998). Constrained navigation algorithms for strapdown inertial navigation systems with reduced set of sensors, *Proceedings of the American Control Conference*, 24-26 June, Philadelphia, PA, USA, pp. 1848-1852.
- Brown, A., and Y. Lu (2004). Performance test results on an integrated GPS/MEMS inertial navigation package, *Proceedings of ION GNSS 2004*, 21-24 September, Long Beach, CA, USA, pp. 825-832.
- Brown, R. G. and Y. C. Hwang (1997). *Introduction To Random Signals and Applied Kalman Filtering*. John Wiley & Sons Inc., third edition.
- Brunner, F.K., H. Hartinger and L. Troyer (1999). GPS signal diffraction modelling: the stochastic SIGMA- Δ Model, *Journal of Geodesy*, Vol. 73, pp. 259-267.

- Cannon, M. E. (1991). *Airborne GPS/INS with an Application to Aerotriangulation*. PhD Thesis, UCGE Report No. 20040, The Department of Geomatics Engineering, University of Calgary, Canada.
- Caruso, M. J. (1997). Application of magnetoresistive sensors in navigation systems, *Sensors and Actuators*, SAE SP-1220, pp. 15-21.
- Caruso, M. J. (2000). Application of magnetic sensor for low cost compass systems, *Honeywell SSEC*, from <http://www.magneticsensors.com/datasheets/lowcost.pdf>
- Chiang, K.W. (2004) *INS/GPS Integration Using Neural Networks for Land Vehicular Navigation Applications*. PhD Thesis, UCGE Report No. 20209, Department of Geomatics Engineering, University of Calgary, Canada.
- Collin, J., J. Käppi and J. Saarinen (2001). Unaided MEMS-based INS application in a vehicular environment, *Proceedings of ION GPS 2001*, Salt Lake City, UT, USA, 11-14 September, pp. 1343-1348.
- Collin, J., H. Kuusniemi, O. Mezentsev, G. MacGougan, and G. Lachapelle (2003). HSGPS under heavy signal masking - accuracy and availability analysis. *Proceedings of 6th Nordic Radio Navigation Conference and Exhibition*, 2-4 December, Stockholm-Helsinki, Sweden-Finland.
- Connelly, J., A. Kourepenis and T. Marinis (2000). Micromechanical sensors in tactical GN&C applications, *Proceedings of AIAA Guidance, Navigation, and Control*, 6-9 August, Montreal, QB, Canada, pp. 561-567.
- Crassidis, J. L., K-L. Lai and R. R. Harman (2005). Real-time attitude-independent three-axis magnetometer calibration, *Journal of Guidance, Control, and Dynamics*, Vol. 28, No. 1, pp. 115-120.
- Dissanayake, G., S. Sukkarieh, E. Nebot and H. Durrant-Whyte (2001). The aiding of a low-cost strapdown inertial measurement unit using vehicle model constraints for land vehicle applications, *IEEE Transactions on Robotics and Automation*, Vol. 17, No. 5, pp. 731-747.
- El-Sheimy, N., A-H. Walid and G. Lachapelle (2004). An adaptive neuro-fuzzy model for bridging GPS outages in MEMS-IMU/GPS land vehicle navigation, *Proceedings of ION GNSS 2004*, 21-24 September, Long Beach, CA, USA, pp. 1088-1095.
- El-Sheimy, N. (2003). *Inertial Techniques and INS/DGPS Integration*. ENGO 623 Lecture Notes, The Department of Geomatics Engineering, University of Calgary, Canada.
- El-Sheimy, N. and K. P. Schwarz (1999). Navigating urban areas by VISAT - a mobile mapping system integrating GPS/INS/digital cameras for GIS applications, *Journal of The Institute of Navigation*, Vol. 45, No. 4, pp. 275-286.

- Farrell, J.L. (2005). Inertial instrument error characterization, *Proceedings of ION AM 2005*, 27-29 June, Cambridge, MA, USA, pp.1020-1025.
- French, R. L. (1987). The evolving roles of vehicular navigation, *Journal of The Institute of Navigation*, Vol. 34, No. 3., pp. 212-228.
- French, R. L. (1995). From Chinese chariots to smart cars: 2,000 years of vehicular navigation, *Journal of The Institute of Navigation*, Vol. 42, No. 1, Special Issue, pp. 235-258.
- Gao, Y, E. J. Krakiwskv and M.A. Abousalem (1993). Comparison and analysis of centralized, decentralized, and federated filters, *Journal of The Institute of Navigation*, Vol. 40, No. 1, pp. 69-86.
- Gebre-Egziabher, D., G. H. Elkaim, J. D. Powell and B. W. Parkinson (2001). A non-linear, two-step estimation algorithm for calibrating solid-state strapdown magnetometers, *Proceedings of the International Conference on Integrated Navigation Systems*, 28-30 May, St. Petersburg, Russia, pp. 290-297.
- Gelb, A. (1974). *Applied Optimal Estimation*. Cambridge, Massachusetts: The Massachusetts Institute of Technology Press.
- Ghalehnoe, A., K. Mohammadi and M. R. Mosavi (2002). Improve determining the location of a moving body on map by low cost GPS receiver, *Proceedings of 2002 Student Conference on Research and Development*, 16-17 July, Shah Alam, Malaysia, pp. 242-244.
- Godha, S. (2006). *Performance Evaluation of Low Cost MEMS-Based IMU Integrated with GPS for Land Vehicle Navigation Application*. M.Sc. Thesis, UCGE Report No. 20239, Department of Geomatics Engineering, University of Calgary, Canada.
- Greenspan, R. L. (1996). GPS and inertial integration, in *Global Positioning System: Theory and Applications*, Vol. 2, chapter 7, pp. 187–220. Washington D.C.: American Institute of Aeronautics and Astronautics.
- Ham, F. M. and I. Kostanic (2001). *Principles of Neurocomputing for Science and Engineering*. McGraw-Hill.
- Haykin, S., *Neural Networks: A Comprehensive Foundation*. Upper Saddle River, NJ: Prentice Hall, 1999.
- Hellendoorn, H. and C. Thomas (1993). Defuzzification in fuzzy controllers, *Intelligent and Fuzzy Systems*, Vol. 1, pp. 109-123.
- Hide, C. and T. Moore (2005). GPS and low cost INS integration for positioning in the urban environment, *Proceedings of ION GPS 2005*, 13-16 September, Long Beach, CA, USA, pp. 1007-1015.

- Hide, C., T. Moore and M. J. Smith (2003). Adaptive Kalman filtering for low-cost INS/GPS, *The Journal of Navigation*, Vol. 56, No. 1, ISSN 0373-4633, pp. 143-152.
- Hofmann-Wellenhof, B., H. Lichtenegger and J. Collins (2001). *GPS Theory and Practice*. New York: Springer-Verlag, fifth edition.
- Hofmann-Wellenhof, B., K. Legat and M. Wieser (2003). *Navigation - Principles of Positioning and Guidance*. New York: Springer Wien.
- Huff, M.A. (1999). Position paper: MEMS manufacturing, *The MEMS Exchange*. Reston, Virginia, USA.
- Hush, D.R. and B.G. Horne (1993). Progress in supervised neural networks: What's new since Lippmann?, *IEEE Signal Processing Magazine*, Vol. 10, pp. 8-39.
- Ibrahim, F., N. Al-Holou, T. Pilutii and A. Tascillo (2000). DGPS/INS integration using linear neurons. *Proceedings of ION GPS 2000*, 19-22 September, Salt Lake City, UT, USA, pp. 2455-2463.
- IEEE (1997). *IEEE Standard Specification Format Guide and Test Procedure for Single-Axis Interferometric Fiber Optic Gyros*. IEEE Standard 952-1997.
- IEEE (2001). *Standard for Inertial Sensor Terminology*. IEEE Standard IS 528-2001.
- Jaffe, R., S. Bonomi and A. M. Madni (2004) Miniature MEMS quartz INS/GPS description and performance attributes, *Proceedings of ION GNSS 2004*, 21-24 September, Long Beach, CA, USA, pp. 852-863.
- Jang, J-S. R., C.-T. Sun and E. Mizutani (1997). *Neuro-Fuzzy and Soft Computing*. Upper Saddle River, NJ: Prentice Hall.
- Jang, J-S. R. (1993) ANFIS: adaptive-network-based fuzzy inference systems, *IEEE Transactions on Systems, Man, and Cybernetics*, Vol. 23, No. 3, pp. 665-685.
- Jekeli, C. (2000). *Inertial Navigation Systems with Geodetic Applications*. New York, NY: Walter de Gruyter.
- Kalman, R. E. (1960). New approach to linear filtering and prediction problems, *Transactions on ASME, Journal of Basic Engineering*. Vol. 82, pp. 34-45.
- Kandel, A. (Editors) (1992). *Fuzzy Expert Systems*. Boca Raton, FL: CRC Press.
- Kaplan, E. D. (1996). *Understanding GPS Principles and Applications*, Boston: Artech House.
- Karatsinides, S. P. (1994) Enhancing filter robustness in cascaded GPS-INS integrations, *IEEE Transactions on Aerospace and Electronic Systems*, Vol. 30, No. 4, pp. 1001-1008.

- Karr, C. L. and E. J. Gentry (1993). Fuzzy control of pH using genetic algorithms, *IEEE Transactions on Fuzzy Systems*, Vol. 1, No. 1, pp. 46-53.
- Klobuchar, J. A. (1996). Ionospheric effects on GPS, in *Global Positioning System: Theory and Applications*, Vol. 1, chapter 12, pp. 485–513. Washinton D.C: American Institute of Aeronautics and Astronautics.
- Kraft, M. (1997). *Closed Loop Digital Accelerometer Employing Oversampling Conversion*. Ph.D. Thesis, School of Engineering, Coventry University, UK.
- Kuusniemi, H. (2005) *User-Level Reliability and Quality Monitoring in Satellite-Based Personal Navigation*. Ph.D. Thesis, Department of Information Technology, Tampere University of Technology, Finland.
- Lachapelle, G. (2002). *NAVSTAR GPS: Theory and Applications*. ENGO 625 Lecture Notes, Department of Geomatics Engineering, The University of Calgary, Canada.
- Ladetto, Q., V. Gabaglio and B. Merminod (2001a). Two different approaches for augmented GPS pedestrian navigation, *International Symposium on Location Based Services for Cellular Users*, 5-7 February, Munich, Germany
- Ladetto Q., V. Gabaglio and B. Merminod (2001b) Combining gyroscopes, magnetic compass and GPS for pedestrian navigation, *International Symposium on Kinematic Systems in Geodesy, Geomatics and Navigation (KIS)*, 5-8 June, Banff, AB, Canada, pp. 205-212.
- Langley, R.B. (2003). The magnetic compass and GPS, *GPS World*, September.
- Lee, Y. C. (1986). Analysis of range and position comparison methods as a means to provide GPS integrity in the user receiver. *Proceedings of ION AM 1986*, 24-26 June, Seattle, WA, USA, pp. 1–4.
- Leick, A. (1995). *GPS Satellite Surveying*. John Wiley & Sons, Inc., second edition.
- Lin, C-J., Y-Y. Chen and F-R. Hang (1996). Fuzzy processing on GPS data to improve the position accuracy, *1996 Asian Fuzzy Systems Symposium*, 11-14 December, Kenting, Taiwan, pp. 557-562.
- Loebis, D., R. Sutton and J. Chudley (2003). A fuzzy Kalman filter optimized using a genetic algorithm for accurate navigation of an autonomous underwater vehicle, *Proceedings of MCMC 2003 conference*, 17-19 September, Girona, Spain, pp. 19-24.
- Luo, R. C., C-C. Yih and K. L. Su (2002). Multisensor fusion and integration: approaches, applications, and future research directions, *IEEE Sensors Journal*, Vol. 2, No. 2, pp. 107-119.

- MacGougan, G. D. (2003). *High Sensitivity GPS Experiments in Degraded Signal Environments*. MSc Thesis, UCGE Report No. 20176, The Department of Geomatics Engineering, University of Calgary, Canada.
- Magill, D. T. (1965). Optimal adaptive estimation of sampled stochastic processes, *IEEE Transactions on Automat Control*, Vol. AC-10, No. 4, pp. 434-439.
- Mamdani, E. H. and S. Assilian (1975). An experiment in linguist synthesis with fuzzy logic controller, *International Journal of Man-Machine Studies*, Vol. 7, No. 1, pp. 1-13.
- Maybeck, P. (1979). *Stochastic Models, Estimation, and Control*, Vol. 1. Academic Press.
- Mehra, R. K. (1972). Approaches to adaptive filtering, *IEEE Transactions on Automatic Control*, Vol. AC-17, pp. 693-698.
- Mehra, R. K. (1970). On the identification of variance and adaptive Kalman filtering, *IEEE Transactions on Automatic Control*, Vol. 4C-15, No. 2, pp. 175-184.
- Mendel, J. M., and R. W. McLaren (1970). Reinforcement-learning control and pattern recognition systems, in *Adaptive, Learning, and Pattern Recognition Systems: Theory and Applications*, vol. 66, J. M. Mendel and K. S. Fu (eds.), pp. 287-318, New York: Academic Press.
- Misra, P. and P. Enge (2001). *Global Positioning System: Signal, Measurement, and Performance*. Lincoln, MA: Ganga-Jamuna Press.
- Mohamed, A. H. and K. P. Schwarz (1999). Adaptive Kalman filtering for INS/GPS, *Journal of Geodesy*, Vol. 73, pp.193-203.
- Ochieng, W. Y., P. J. Shardlow and G. Johnston (1999). Advanced transport telematics positioning requirements: An assessment of GPS performance in greater London, *Journal of Navigation*, Vol. 52, pp. 342-355.
- Ojeda, L. and J. Borenstein (2002). FLEXnav: fuzzy logic expert rule-based position estimation for mobile robots on rugged terrain, *Proceedings of the 2002 IEEE International Conference on Robotics and Automation*, 10-17 May, Washington DC, USA, pp. 317-322.
- Olynik, M.C. (2002). *Temporal Characteristics of GPS Error Sources and Their Impact on Relative Positioning*. MSc Thesis, UCGE Report No. 20162, Department of Geomatics Engineering, The University of Calgary, Canada.
- Pal, S. and R. King (1981). Image enhancement using smoothing with fuzzy sets, *IEEE Transactions on Systems, Man and Cybernetics*, Vol. SMC-11, pp. 494-501.

- Park, M. (2004). *Error Analysis and Stochastic Modeling of MEMS based Inertial Sensors for Land Vehicle Navigation Applications*. MSc Thesis, UCGE Report No. 20194, Department of Geomatics Engineering, University of Calgary, Canada.
- Parkinson, B. W. and J. Spilker (eds.) (1996). *Global Positioning System: Theory And Applications*, Vol. 1 and 2. Washington D.C.: American Institute of Aeronautics and Astronautics.
- Parkinson, B. W. and P. Axelrad (1988). Autonomous GPS integrity monitoring using the pseudorange residual, *Journal of The Institute of Navigation*, Vol. 35, No. 2, pp. 49-68.
- Petovello, M. (2003). *Real-time Integration of a Tactical-Grade IMU and GPS for High-Accuracy Positioning and Navigation*. PhD Thesis, UCGE Report No. 20173, Department of Geomatics Engineering, University of Calgary, Canada.
- Petovello, M., O. Mezentsev, G. Lachapelle and M.E. Cannon (2003). High sensitivity GPS velocity updates for personal indoor navigation using inertial navigation systems, *Proceedings of ION GPS/GNSS 2003*, 9-12 September, Portland, OR, USA, pp. 2886-2896.
- Rahbari, R., B. W. Leach, J. Dillon and C. W. de Silva (2005). Expert system for an INS/DGPS integrated navigator installed in a Bell 206 helicopter, *Engineering Applications of Artificial Intelligence*, Vol.18, Issue 3, pp. 353-361.
- Ray, J. (2000). *Mitigation of GPS Code and Carrier Phase Multipath Effects Using a Multi-antenna System*. PhD Thesis, UCGE Report No. 20136, Department of Geomatics Engineering, University of Calgary, Canada.
- Ray, J. (2002). *Advanced GPS Receiver Technology*. ENGO 699.73 Lecture Notes, Geomatics Engineering, University of Calgary, Canada.
- Ross, T. J. (1995). *Fuzzy Logic with Engineering Applications*. McGraw-Hill Inc..
- Rumelhart, D. E., G. E. Hinton and R. J. Williams (1986). Learning internal representations by error propagation, In *Parallel Distributed Processing: Explorations in the Microstructure of Cognition*, Volume 1: Foundations, D. E. Rumelhart and J. L. McClelland (eds.). Cambridge, MA: MIT Press.
- Salychev, O. (1998). *Inertial Systems in Navigation and Geophysics*. Bauman MSTU Press.
- Salychev, O., V. V. Voronov, M. E. Cannon, R. A. Nayak and G. Lachapelle (2000). Low cost INS/GPS integration: concepts and testing, *Proceedings of ION NTM 2000*, 26-28 January, Anaheim, CA, USA, pp. 98-105.
- Salycheva, A. (2004). *Medium Accuracy INS/GPS Integration in Various GPS Environments*. MSc Thesis, UCGE Report No. 20200, Department of Geomatics Engineering, University of Calgary, Canada.

- Sasiadek, J. Z., Q. Wang and M. B. Zeremba (2000). Fuzzy adaptive Kalman filtering for INS/GPS data fusion, *Proceedings of the 15th IEEE International Symposium on Intelligent Control*, 17-19 July, Rio, Patras, Greece, pp.181-186.
- Scherzinger, B. M. (2000). Precise robust positioning with inertial/GPS RTK, *Proceedings of ION GPS 2000*, 19-22 September, Salt Lake City, UT, USA, pp. 155-162.
- Schwarz, K. P. and M. Wei (2001). *INS/GPS Integration for Geodetic Applications*. ENGO 623 Lecture Notes, Department of Geomatics Engineering, The University of Calgary, Canada.
- Seeber, G. (1993). *Satellite Geodesy: Foundations, Methods, and Applications*. Berlin: Walter de Gruyter.
- Shin, E-H. (2001). *Accuracy Improvement of Low Cost INS/GPS for Land Applications*. MSc. Thesis, UCGE Report No. 20156, Department of Geomatics Engineering, University of Calgary, Canada.
- Shin, E-H. (2005). *Estimation Techniques for Low-Cost Inertial Navigation*. PhD Thesis, UCGE Report No. 20219, Department of Geomatics Engineering, University of Calgary, Canada.
- Skaloud, J. (1999). *Optimizing Georeferencing of Airborne Survey Systems by INS/DGPS*, PhD Thesis, UCGE Report No. 20127, The Department of Geomatics Engineering, University of Calgary, Canada.
- Spilker, J. J. (1996). Tropospheric effects on GPS, in *Global Positioning System: Theory and Applications*, Vol. 1, chapter 13, pp. 517–546. Washington D.C.: American Institute of Aeronautics and Astronautics.
- Stephen, J. (2000). *Development of a Multi-Sensor GNSS Based Vehicle Navigation System*. M.Sc. Thesis, UCGE Report No. 20140, Department of Geomatics Engineering, University of Calgary, Canada.
- Sukkarieh, S. (2000). *Low Cost, High Integrity, Aided Inertial Navigation Systems for Autonomous Land Vehicles*. Ph.D. Thesis, Australian Centre for Field Robotics, Department of Mechanical and Mechatronic Engineering, The University of Sydney, Sydney, Australia.
- Swanson, S. R. (1998). A fuzzy navigational state estimator for GPS/INS integration, *IEEE Position Location and Navigation Symposium*, 20-23 April, Palm Springs, CA, USA, pp. 541-548.
- Tanaka, H., T. Okuda and K. Asai (1976). A formulation of fuzzy decision problems and its application to an investment problem, *Kybernetes*, Vol. 5, pp. 25-30.

- Telematics Update (2005). World News: Navigation systems to grow at 66% in 5 years, from <http://www.telematicsupdate.com/homepage2.asp?news=46124>.
- Titterton, D. H. and J. L. Weston (1997). *Strapdown Inertial Navigation Technology*. Peter Peregrinus Ltd., UK.
- Tung, S. (2000). Position Paper: An Overview of MEMS Inertial Sensors, from www.eas.asu.edu/~nsf2000/Table_of_Contents/ST.pdf.
- Vadiee, N. (1993). Fuzzy rule-based expert systems-I, in *Fuzzy Logic and Control: Software and Hardware Applications*, pp. 51-85, M. Jamshidi, N. Vadiee, and T. Ross (eds.). Englewood Cliffs, N.J: Prentice Hall.
- Van Dierendonck, A., P. Fenton and T. Ford (1992). Theory and performance of narrow correlator spacing in a GPS receiver, *Journal of The Institute of Navigation*, Vol. 39, No. 3, pp. 265–283.
- Wang J., M. Stewart and M. Tsakiri (1999). Online stochastic modelling for INS/GPS integration, *Proceedings of ION GPS 1999*, 14-17 September, Nashville, Tennessee, USA, pp. 1901-1906.
- Wang, J., H. K. Lee and S. Hewitson (2003). Influence of dynamics and trajectory on integrated GPS/INS navigation performance, *Journal of Global Positioning Systems*, Vol. 2, No. 2, pp. 109-116.
- Wang, J-H. and Y. Gao (2003a). Evaluating the accuracy of GPS positions under severe signal-degradation using adaptive-network-based fuzzy inference systems (ANFIS), *Proceedings of The 50th CASI Annual General Meeting and Conference*, 28-30 April, Montréal, QB, Canada.
- Wang, J-H. and Y. Gao (2003b). Performance improvement of a low-cost gyro-free INS for land vehicle navigation by using constrained navigation algorithm and neural network, *Proceedings of ION GPS/GNSS 2003*, 9-12 September, Portland, Oregon, USA, pp. 762-768.
- Wang, J-H. (2004a). The aiding of a low-cost MEMS INS for land vehicle navigation using fuzzy logic expert system, *Proceedings of ION GNSS 2004*, 21-24 September, Long Beach, California, USA, pp. 718-728.
- Wang, J-H. and Y. Gao (2004b). GPS-based land vehicle navigation system assisted by a low-cost gyro-free INS using neural network, *The Journal of Navigation*, Vol. 57, No. 3, pp. 417-428.
- Wang, J-H. and Y. Gao (2004c). Fuzzy logic expert rule-based multi-sensor data fusion for land vehicle attitude estimation, *Proceedings of 19th International CODATA Conference*, 7-10 November, Berlin, Germany.

- Wang, J-H. and Y. Gao (2004d). Identification of GPS positioning solutions deteriorated by signal degradations using a fuzzy inference system, *GPS Solutions*, Vol. 8, No. 4, pp. 245-250.
- Wang, J-H., Y. Gao and Y. Zhang (2005). An intelligent MEMS IMU-based land vehicle navigation system enhanced by dynamics knowledge, *Proceedings of ION AM 2005*, 27-29 June, Cambridge, MA, USA.
- Wang, J-H. and Y. Gao (2005a). An intelligent MEMS IMU/HSGPS integration system for vehicular navigation in urban canyons, *Proceedings of ION GNSS 2005*, 13-16 September, Long Beach, California, USA, pp. 941-948.
- Wang, J-H. and Y. Gao (2005b). Multi-sensor data fusion for land vehicle attitude estimation using fuzzy expert system, *Data Science Journal*, Vol. 4, pp. 127-139.
- Wang, J-H. and Y. Gao (2005c). A new magnetic compass calibration algorithm using neural networks, *Measurement Science and Technology*, Vol. 17, pp. 153-160.
- Wang, J-H. and Y. Gao (2006a). High sensitivity GPS data classification based on signal-degraded conditions, *IEEE Transactions on Vehicular Technology*. (accepted)
- Wang, J-H. and Y. Gao (2006b). Urban vehicular navigation using AI-enhanced MEMS INS/GPS integration systems, *8th GEOIDE Annual Scientific Conference*, May 31 to June 2, Banff, Alberta, Canada. (Poster)
- Wang, J-H. and Y. Gao (2006c). The aiding of MEMS INS/GPS integration using artificial intelligence for land vehicle navigation, *Proceedings of IMECS 2006*, 20-22 June, Hong Kong, China.
- Ward, P. (1996). Satellite signal acquisition and tracking, in *Understanding GPS Principles and Applications*, chapter 5, pp.128-207. Norwood, MA: Artech House Inc..
- Wei, M. and K. P. Schwarz (1990). Testing a decentralized filter for GPS/INS integration, *Proceedings of IEEE PLANS 1990*, 20-23 March, Las Vegas, Nevada, USA, pp. 429-435.
- Wells, D. (1987). *Guide to GPS Positioning*. Canadian GPS Associates.
- Whitcomb, L. (1989). Sensor compensation for vehicle magnetic signature, *IEEE Aerospace and Electronic Systems Magazine*, Vol. 4, No. 2, pp. 33-37.
- Wieser, A. (2003). Fuzzy logic and GPS, *GPS World*, March.
- Wieser, A. and F.K. Brunner (2000). An extended weight model for GPS phase observations, *Earth Planets Space*, Vol. 52, pp. 777-782.

Zhang, Y. and Y. Gao (2005). Performance analysis of a tightly coupled Kalman filter for the integration of undifferenced GPS and inertial data, *Proceedings of ION NTM 2005*, 24-26 January, San Diego, CA, USA.

Zadeh, L. A. (1965). Fuzzy sets, *Information and Control*, Vol. 8, pp. 338-353.